UNIVERSITY OF SOUTHAMPTON

Faculty of Engineering, Science and Mathematics

School of Chemistry

Photoionisation Studies of Reactive Intermediates with Synchrotron Radiation

by

Marie Eypper

Thesis for the degree of Doctor of Philosophy

December 2009

ABSTRACT

UNIVERSITY OF SOUTHAMPTON

FACULTY OF ENGINEERING, SCIENCE AND MATHEMATICS

SCHOOL OF CHEMISTRY

Doctor of Philosophy

Photionisation Studies of Reactive Intermediates with Synchrotron Radiation

by **Marie Eypper**

Reactive intermediates are currently receiving a great deal of attention both experimentally and theoretically as they play important roles in atmospheric, astrophysical and plasma sciences. During this project, the photoionisation behaviour of selected reactive species was studied in the gas phase using photoelectron spectroscopy at the synchrotron radiation source of Elettra, Trieste. IF was investigated by Photoelectron Spectroscopy (PES) and Threshold Photoelectron Spectroscopy (TPES), which led to the determination of improved adiabatic and vertical ionisation energies (AIEs and VIEs) of the $IF^+(X^2\Pi_{3/2}) \leftarrow IF(X^1\Sigma^+)$ and $IF^+(^2\Pi_{1/2}) \leftarrow IF(X^1\Sigma^+)$ ionisations and improved spectroscopic constants for the two IF ionic states $X^2\Pi_{3/2}$ and $^2\Pi_{1/2}$. Iodine atoms were also studied by Constant Ionic State (CIS) spectroscopy in the photon energy region of the $(5p)^{-1}$ ionisations. Rydberg series were observed and analysed. The ionisation energy and quantum defect of each observed series were determined. Beta parameter plots of iodine atoms as a function of photon energy were also derived for the first time and showed unexpected behaviour. The TPES technique was used for the study of non linear triatomics such as CF_2, SF_2 and HO_2. Extensive vibrational structure was obtained for the first PE bands of CF_2 and SF_2, which led to the determination of the AIEs and of the harmonic and fundamental vibrational frequencies. In the case of CF_2, the experimental spectra were supported by *ab initio*/Franck–Condon simulations, which allowed the upper state vibrational quantum numbers associated with each observed vibrational component to be determined.

Contents

Declaration of authorship

I, **Marie Eypper**, declare that this thesis entitled, "Photoionisation Studies of Reactive Intermediates with Synchrotron Radiation" and the work presented in it are both my own, and have been generated by me as a result of my own original research. I confirm that:

- This work was done wholly or mainly while in candidature for a research degree at this University;
- Where any part of this thesis has previously been submitted for a degree or any other qualification at this University or any other institution, this has been clearly stated;
- Where I have consulted the published work of others, this is always clearly attributed;
- Where I have quoted from the work of others, the source is always given. With the exception of such quotations, this thesis is entirely my own work;
- I have acknowledged all main sources of help;
- Where the thesis is based on work done by myself jointly with others, I have made clear exactly what was done by others and what I have contributed myself;
- Parts of this work have been published as:
  - F. Innocenti, M. Eypper, E. P. F. Lee, S. Stranges, D. K. W. Mok, F. T. Chau, G. C. King and J. M. Dyke, *Chem. Eur. J.*, **14**, 11452, 2008.
  - F. Innocenti, M. Eypper, S. Beccaceci, A. Morris, S. Stranges, J. B. West, G. C. King and J. M. Dyke, *J. Phys. Chem.*, **112**, 6939, 2008

Signed:

Date:

Acknowledgements

Firstly, I would like to express my gratitude towards my supervisor, Prof. J. M. Dyke for giving me the opportunity to carry out this project but also for his constant guidance and support throughout these years. He provided me with many helpful suggestions, important advice and constant encouragement during the course of this work. This project was held in collaboration with other groups in order to complete the 24 hours shifts when acquiring data at the synchrotron radiation source of Elettra, Trieste. I would therefore like to thank everyone that participated and made the acquisition of the data possible, starting with Prof. G. King and his wife Dr. M. Siggel King, for their precious help, suggestions and good moods; Prof. J. B. West and Dr. A. Morris for their valuable expertise in synchrotron radiation sources and in the operation of the spectrometer, and of course, Dr. S. Stranges for his help throughout the experiments conducted in Trieste and during the long night shifts. Special thanks to Fabrizio, for providing me with useful tips on the spectrometer and beamline operations during my first year. Even after his departure from the Southampton PES group, his help via emails and meetings has always been important to me. I am also grateful for having carried out my PhD in a very nice atmosphere. This was made possible by the friendship developed with the other group members, Grant, Otello, Nerina, Sonia and Ed. The office would not have been the same without the PhD students from "the other side", Quintin, Nikos, Alvaro and Stephen.

I am deeply grateful to my parents and family for being always there for me, whatever the time or circumstances. I feel very lucky to have such supportive parents who have always approved my choices, and tried to help me with them as much as they could.

My life in Southampton would not have been the same without the people I met outside of the office: Axel, Amaury and Florian with whom, many of my first year

evenings and week ends were spent. I need to have a special thought for 41 avenue road.....Nico, Suzanna, Chritina, H, Mari and Gareth. This was probably the best house I ever lived in and I think they'll agree that it will stay in our memories for long. And Patrick, who has been close to me since the day I started my PhD and without whom, life in Southampton would not have been the same. Finally I would like to mention all the party people I met in Southampton, and who made those three years extraordinary.

I have also have been lucky enough to meet someone special in Southampton, Sylvain, who makes me feel like never before. I would like to thank him for bringing sunshine, joy and happiness to my life and for always being by my side.

I am also grateful to the EU Early Stage Research Training Network (SEARCHERS) for financial support.

Table of Acronyms

PE : Photoelectron

PES : Photoelectron Spectroscopy

TPES : Threshold Photoelectron Spectroscopy

XPS : X-ray Photoelectron Spectroscopy

CIS : Constant Ionic State

AIE : Adiabatic Ionisation Energy

VIE : Vertical Ionisation Energy

KE : Kinetic Energy

IE : Ionisation Energy

UV : Ultra Violet

VUV : Vacuum Ultra Violet

FC : Franck Condon

MQDT : Multi Quantum Defect Theory

AO : Atomic Orbital

MO : Molecular Orbital

SCF : Self Consistent Field

HF : Hartree-Fock

UHF : Unrestricted Hartree-Fock

RHF : Restricted Hartree-Fock

STO : Slater Type Orbital

GTO : Gaussian Type Orbital

DZ : Double Zeta

TZ : Triple Zeta

PEF : Potential Energy Function

TOF : Time Of Flight

FWHM : Full Width at Half Maximum

CI : Configuration Interaction

MRCI : Multi Reference Configuration Interaction

MCSCF : Multi Configuration Self Consistent Field

CASSCF : Complete Active Space Self Consistent Field

CC : Coupled Cluster

CBS : Complete Basis Set

REMPI : Resonance Enhanced Multi Photon Ionisation

Chapter 1

Introduction

1.1 Photoelectron Spectroscopy

Unstable species are currently receiving a great deal of attention both experimentally and theoretically as they play important roles in atmospheric and astrophysical chemistry, and plasma and combustion science. Although they are often present at low partial pressures, reactive species can have a major influence on gas phase chemistry. The chemical properties of molecules are a consequence of their electronic structure; hence obtaining information on the electronic structure of reactive species is crucial. One way of obtaining such information is via a technique called Photoelectron Spectroscopy (PES) [1]. Photoelectron spectroscopy is based on the photoelectric effect, which was discovered experimentally by Hertz in 1887 [2], and later described from a theoretical point of view by Einstein [3]. Photoionisation occurs when a photon, $h\nu$, of sufficient energy interacts with an atom or a molecule, M. An electron is ejected, leaving the atom or molecule in an ionic state [4]:

$$M + h\nu \rightarrow M^+ + e^- \tag{1.1.1}$$

In atoms, the principle of conservation of energy implies that the kinetic energy of the ejected photoelectron, KE, is given by:

$$KE = h\nu - IE \tag{1.1.2}$$

where IE is the ionisation energy of the molecule under consideration. In molecules, this equation modifies to:

$$KE = h\nu - IE - \Delta E_{ROT,VIB} \tag{1.1.3}$$

where $\Delta E_{ROT,VIB}$ is the change in rotational and vibrational energy on ionisation. Photoelectron Spectroscopy (PES) is a technique that measures the kinetic energy of the ejected photoelectron in order to determine the ionisation energy, IE, of an atom or a molecule. Using a monochromatic photon source and recording the yield of the ejected photoelectrons as a function of their kinetic energies gives rise to a photoelectron spectrum, in which a band arises for ionisation to each ionic state accessed. A photoelectron spectrum thus provides a map of the ionic states obtained upon one-electron ionisation of the system under consideration. A wealth of information can be obtained from a photoelectron spectrum; for example, vibrational structure may be observed in a PE band, which can lead to the experimental determination of the vibrational constants, ω_e and $\omega_e\chi_e$ of the ionic state. Also, the band shape in a photoelectron spectrum can provide information on the nature of the orbital from which the ejected photoelectron originated and the change in the equilibrium bond length on ionisation [5].

Photoelectron spectroscopy techniques are classified in terms of the energy of the radiation used to ionise the molecule. When X-rays are used, the technique is called X-ray photoelectron spectroscopy (XPS) and both valence and core electrons can be ionised. In this project, vacuum ultraviolet radiation is used to ionise the system under consideration and the technique is called Vacuum Ultraviolet Photoelectron Spectroscopy or just PES. In this technique only valence electrons can be ionised.

In principle, Photoelectron Spectroscopy is a simple technique that only requires a source of monochromatic radiation, from, for example, a simple rare gas discharge photon source, a electron kinetic energy analyser and an electron detector [1]. However, there are several experimental difficulties, like the maintenance of low pressures throughout the apparatus and the presence of residual stray fields that affect the trajectories of the photoelectrons. These difficulties limit the resolution of PE bands, which is usually about 30–40 meV (240–320 cm^{-1}). This type of resolution is sufficient to resolve vibrational structure in most cases but only allows the observation of rotational structure for a few light molecules (e.g. molecular hydrogen [6]).

1.2 Synchrotron Radiation Sources

The development of synchrotron radiation sources in the last 50 years gave rise to new perspectives for photoelectron spectroscopy [7]. Synchrotron radiation sources are continuous, polarised sources of radiation. The radiation is emitted by electrons circulated in curved trajectories at a velocity close to the speed of light [8]. Synchrotron radiation can be monochromatised and tuned continuously from the far infrared to the hard x-ray region. Synchrotron radiation sources are also polarised, which allows PE angular distribution studies to be performed.

The tunability of synchrotron radiation sources allows Constant Ionic State (CIS) spectra to be recorded. In this type of spectra, the kinetic energy of the electrons is scanned simultaneously with the energy of the radiation while maintaining their difference equal to the ionisation energy of the process under investigation, thus monitoring a selected ionisation process. CIS spectra show resonances when the energy of the radiation is equal to the excitation energy to an excited neutral state that autoionises to the ionic state under investigation. In this way, Rydberg series converging to ionic thresholds above the first ionisation limit can be observed. A Rydberg state is a highly excited state where an electron is promoted to an orbital with large radius and high principal quantum number, n. Rydberg states are hydrogen-like in character and form series that converge to a particular ionisation limit of energy IE. The energy of a Rydberg state, E_n, is given by the Rydberg formula [9]:

$$E_n = IE - \frac{R}{(n-\delta)^2} \tag{1.2.1}$$

where R is the Rydberg constant and δ is the quantum defect, which reflects the magnitude of penetration of the Rydberg orbital into the ionic core. When the energy of the radiation matches exactly that of a transition to a Rydberg state, two processes may occur: direct ionisation or absorption of the photon by the molecule, which is excited to a neutral excited state (Rydberg state) and then autoionises back to the neutral ionic state. These two processes compete, which often gives rise to asymmetric resonances in CIS spectra, known as Fano profiles [10].

Threshold photoelectron (TPE) spectra provide complementary information to conventional PE spectra and can be recorded with Synchrotron Radiation sources. In order to obtain TPE spectra, the yield of threshold electrons is recorded while the energy of the radiation is swept. The detection of threshold electrons is achieved via

the application of a penetrating field which focusses low energy electrons towards the analyser of the spectrometer. The result is a significant improvement of the resolution (to about 5 meV) compared to conventional PE spectra resolution (about 30 meV) [11]. TPE molecular spectra are influenced by autoionisation processes and thus can show non Franck–Condon vibrational distributions and the observation of ionic vibrational components which are not normally observed in the Franck–Condon distributions.

Another main advantage of synchrotron radiation sources is their polarisation, which allows angular distribution studies to be performed. The angular distribution of photoelectrons is not usually isotropic, so that band intensities measured in PE or CIS spectra depend on the angle of detection of the electrons with respect to the polarisation axis of the radiation, θ. The intensity of a particular photoelectron band, measured at an angle θ with respect to the polarisation direction may be written as [12]:

$$I(\theta) = \frac{\sigma}{4\pi}\left[1 + \frac{\beta}{4}(1 + 3Pcos2\theta)\right] \tag{1.2.2}$$

where σ is the photoionisation cross section, β is the asymmetry parameter and P is the degree of polarisation of the incoming radiation. By measuring the intensity at two different angles θ, at a selected photon energy, the asymmetry parameter can be easily determined. β can take any value between -1 and +2. Knowing the beta value can provide information on the nature of the orbital involved in the ionisation and the angular momentum carried away by the free electron.

1.3 Reactive intermediates

Reactive intermediates are short–lived atoms or molecules in the gas–phase formed, for example, from a reaction, photolysis or pyrolysis. Their short lifetimes make them difficult to work with. The main experimental difficulty in studying reactive intermediates is that they must be produced *in situ* otherwise their partial pressures are reduced by reaction. Since the first successful photoelectron spectroscopic study of a reactive intermediate in 1970 [13], the Southampton PES group has concentrated on the study of short lived atoms and molecules by UV PES [14–16]. The spectrometer used for the present project was built by Dr. A. Morris [17] especially for the study of reactive intermediates with synchrotron radiation [18]. Initial studies were made at the Daresbury Synchrotron Radiation Source on short lived molecules [19] and later at the Synchrotron Radiation Source of Elettra, Trieste [20, 21]. The reason the research was transferred to Trieste is that Elettra is a third generation synchrotron source [22] whereas Daresbury is a second generation source [23], i.e., the Elettra source is much more intense. On the VUV beamlines at Daresbury and Elettra, the photon beam is more intense and the photon band width is narrower at Elettra.

1.4 Aim of the project

The overall aim of this project was to study the photoionisation behaviour of selected reactive species in the gas phase using photoelectron spectroscopy at the Synchrotron Radiation Source of Elettra, Trieste. In this way, information on the neutral as well as on the ionic states of the atoms and molecules studied can be obtained. The photoionisation dynamics of the molecules studied can also be investigated through angular distribution studies. The techniques used to study the reactive atoms and molecules were angle resolved photoelectron spectroscopy (PES), angle resolved

constant ionic state (CIS) spectroscopy and threshold photoelectron spectroscopy (TPES). The TPES technique allows very high collection efficiency and resolution, making it a very useful tool for the study of vibrational structure in photoelectron bands.

In this thesis, the fundamental principles underlying photoionisation are discussed in Chapter 2. Chapter 3 describes the apparatus used during this project and the basic characteristics of Synchrotron Radiation. The basic principles of *ab-initio* molecular orbital calculations are presented in Chapter 4. The results obtained from the PES and TPES study of iodine atoms and IF are given in Chapter 5 while Chapter 6 presents the results obtained from the CIS spectroscopy study of iodine atoms. Chapter 7 deals with the study of difluorocarbene by TPES, and Chapter 8 presents preliminary work on the SF_2 and HO_2 reactive intermediates. Finally Chapter 9 concludes the thesis with a summary of the project and outlines possibilities for further work.

Chapter 2

Relevant basic principles

Photoelectron spectroscopy involves the study of the electronic structure of atoms and molecules by application of the photoelectric effect, discovered by Hertz in 1887. In this chapter, the basic principles behind photoelectron spectroscopy will be presented. Direct ionisation and indirect processes are reviewed, with the Franck-Condon principle considered in both cases. The fundamental principles underlying PE angular distributions will also be presented.

2.1 Direct ionisation

When a photon, $h\nu$, of sufficient energy interacts with a molecule M, photoionisation can occur. An electron is ejected from an occupied molecular orbital, leaving the molecule in an ionic state: [4]:

$$M + h\nu \rightarrow M^{+} + e^{-} \tag{2.1.1}$$

Photoelectron spectroscopy (PES) is a technique that measures the kinetic energy, KE, of the ejected photoelectrons in order to determine the ionisation energy, IE, of the molecule under consideration. For an atom, the principle of conservation of energy requires that all the excess energy of the photon above the ionisation energy ($h\nu - IE$) is carried away as electron kinetic energy since the electron is much lighter than any atomic ion:

$$KE = h\nu - IE \tag{2.1.2}$$

For a molecule, this equation is modified to:

$$KE = h\nu - IE - \Delta E_{rot} - \Delta E_{vib} \tag{2.1.3}$$

where ΔE_{rot} and ΔE_{vib} are the changes in rotational and vibrational energy between the molecule and ion on ionisation. A PE spectrum is obtained by recording the yield of ejected photoelectrons as a function of their kinetic energies. The spectrum thus shows for a closed shell molecule, to a first approximation, a band for ionisation to each ionic state accessed.

The probability of a direct transition (or ionisation) between the molecular ground state, characterised by the eigenfunction Ψ'' and the final state (consisting of the ion plus the free electron), characterised by the eigenfunction Ψ' is proportional to the square modulus of the transition moment integral, M [5]:

$$M = \langle \Psi'' | \Sigma p | \Psi' \rangle \tag{2.1.4}$$

where p is the dipole moment operator and the sum extends over all electrons i and

ions j. Ψ' and Ψ'' are functions of electron r and nuclear R coordinates. The Born-Oppenheimer approximation allows the separation of the wavefunctions into a product of electronic, $\Psi_e(r, R)$ and nuclear (vibrational, rotational), $\Psi_n(R)$ components. The dependence of Ψ_e on R retains the weak interaction between the electronic and nuclear motion [24]:

$$\Psi(r, R) = \Psi_e(r, R)\Psi_n(R) \tag{2.1.5}$$

Since the rotational structure of bands in a PE spectrum is usually unresolved, the nuclear wavefunction, Ψ_n can be treated as a vibrational function, neglecting the rotation, i.e. $\Psi_n = \Psi_v$. The electronic-nuclear separation of the wavefunction can also be applied to the dipole operator, $\Sigma_{i,j}p = \Sigma_i p_e + \Sigma_j p_n$, thus modifying the transition moment integral into:

$$M = \int\int \Psi_e^{''*}(r, R)\Psi_v^{''*}(R)|\Sigma_i p_e + \Sigma_j p_n|\Psi'_e(r, R)\Psi'_v(R)drdR \tag{2.1.6}$$

This integral can be separated according to the electronic and nuclear dipole operators:

$$\begin{aligned} M = &\int \Psi_v^{''*}(R)\Psi'_v(R)dR \int \Psi_e^{''*}(r, R)|\Sigma_i p_e|\Psi'_e(r, R)dr \\ &+ \int \Psi_v^{''*}(R)|\Sigma_j p_n|\Psi'_v(R)dR \int \Psi_e^{''*}(r, R)\Psi'_e(r, R)dr \end{aligned} \tag{2.1.7}$$

Since the electronic eigenfunctions belonging to different states are orthogonal to one another, the second term in equation 2.1.7 vanishes for electronic transitions.

Assuming that the matrix element of the electric dipole moment varies only slightly with R and if the dependence of Ψ_e on the nuclear coordinates is neglected, equation 2.1.7 becomes:

$$M = \int \Psi_v^{''*}(R)\Psi_v'(R)dR \int \Psi_e^{''*}(r, R_0)|\Sigma_i p_e|\Psi_e'(r, R_0)dr \tag{2.1.8}$$

where R_0 is the equilibrium ground state configuration. This equation therefore has one factor which depends on the nuclear motion and one factor which depends mainly on the electronic motion. The photoionisation transition probability can then be expressed as [24]:

$$P \propto |\langle \Psi_v^{''*}(R)|\Psi_v'(R)\rangle|^2 \, | \int \Psi_e^{''*}(r, R_0)|\Sigma_i p_e|\Psi_e'(r, R_0)dr|^2 \tag{2.1.9}$$

$$i.e. \qquad P \propto |\langle \Psi_v^{''*}(R)|\Psi_v'(R)\rangle|^2 |M_e(r, R_0)|^2 \tag{2.1.10}$$

The second term in equation 2.1.10 is the electric transition moment squared, M_e, while the first term is called the Franck-Condon factor and is responsible for the relative intensities of the vibrational components in a PE band in conventional PE spectra.

2.1.1 Electronic selection rules

An electronic transition is allowed only if the electric dipole transition moment, M_e, is different from zero. In other words, the product $\Psi_e^{''*} p_e \Psi_e'$ needs to be totally symmetric for at least one component of p_e. If the spin-orbit interactions are small,

the electronic eigenfunction including spin, Ψ_e, can be divided in the product of an orbital and a spin function [5]:

$$\Psi_e = \Psi_{e'} \times \Psi_s \tag{2.1.11}$$

As the dipole operator does not operate on the spin coordinates, the transition moment becomes:

$$M_e(r, R_0) = \langle \Psi_{e'}^{*''} | p_e | \Psi_{e'}' \rangle \langle \Psi_s^{*''} | \Psi_s' \rangle \tag{2.1.12}$$

The spin functions corresponding to different spin values are orthogonal to one another. The second integral is zero for states of different spin. Photoelectron ionisations are thus allowed only between initial and final states of the same spin, $\Delta S = 0$, where the final state wavefunction is a product of the ion and free electron wavefunctions. Closed-shell molecules with singlet neutral ground state have spin, $S_{mol} = 0$. The ejected photoelectron always has half-integral spin, $S_e = 1/2$; only doublet ionic states, $S_{ion} = 1/2$, are therefore accessible from singlet neutral ground states.

2.1.2 Vibrational selection rules and Franck-Condon factor for direct photoionisation

The probability of a vibrational transition during an ionisation process is given by the Franck-Condon factor (FCF), which can be written as:

$$FCF = |M_v|^2 = |\langle \Psi_v^{*''} | \Psi_v' \rangle|^2 \tag{2.1.13}$$

The FCF determines the relative intensities of the vibrational components in a photoelectron band. The Franck-Condon principle states that the intensity of a vibrational component in an electronically allowed transition (or ionisation) is proportional to the absolute square of the overlap integral of the vibrational wavefunctions of the initial and final states. The FC principle is illustrated in Figure 2.1, which shows potential energy curves for a molecule AB in its ground state and for the ion AB^+ in several ionic states. In most neutral molecules, in the ground electronic state, the separation ΔE between the lowest vibrational level $v'' = 0$ and the next vibrational level $v'' = 1$ is large with respect to $k_B T$, which is about 200 cm^{-1} at room temperature (300K). Only the lowest vibrational state $v'' = 0$ is therefore significantly populated in most neutral molecules. In Figure 2.1, the molecule AB is thus considered to be in the lowest vibrational state, $v'' = 0$. However, several ionic states are accessible during the ionisation process and a schematic photoelectron spectrum obtained from the various ionisations is shown on the right hand coordinate [5].

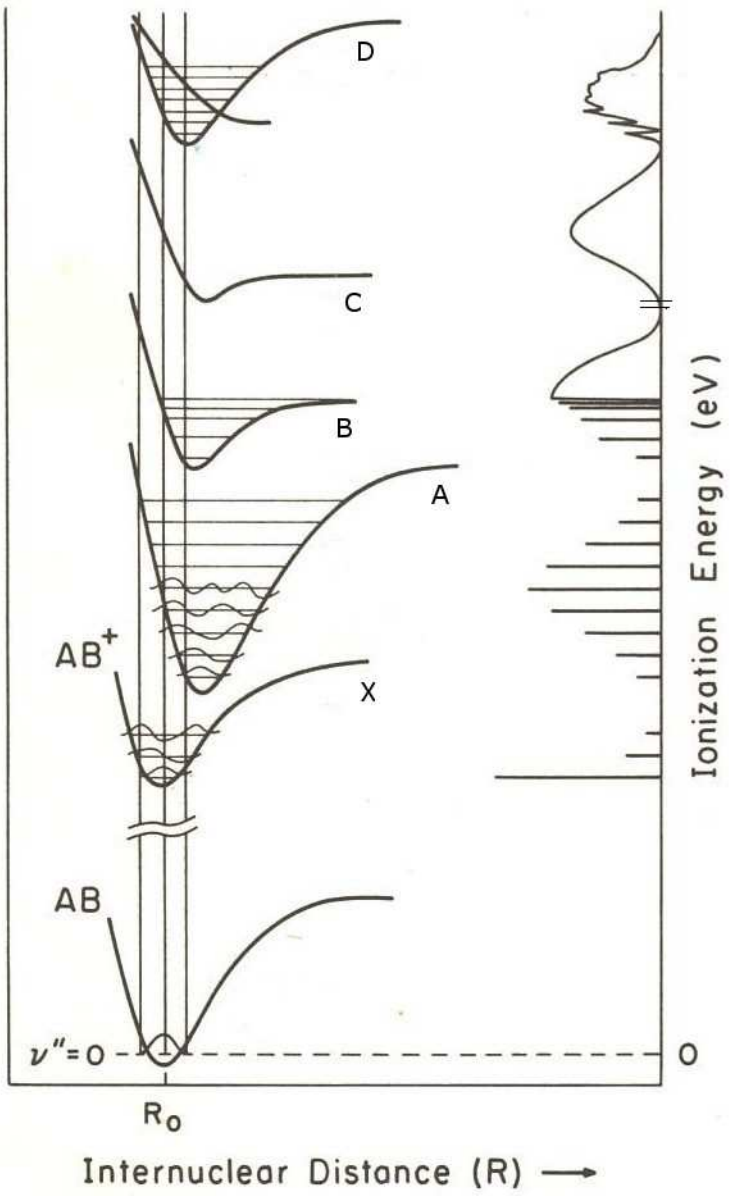

Figure 2.1: The Franck-Condon principle in direct ionisation [5]

In Figure 2.1, the vibrational wavefunction is drawn for the $v'' = 0$ vibrational level of the neutral $AB(X)$ state and for the vibrational levels of the first two ionic states, X and A. The wavefunctions for the $v = 0$ vibrational levels are bell shaped with maxima at the equilibrium internuclear separation of the electronic state while the wavefunctions of higher vibrational levels have broad maxima and minima near the classical turning points of the motion. The intermediate maxima and minima are smaller and their contributions to the overlap integral roughly cancel each other. Consider first the $v' = 0 \leftarrow v'' = 0$ ionisation to the first ionic state, AB^+X. This state has a similar equilibrium geometry to the ground molecular state AB. As a result, the maximum overlap is between the $v'' = 0$ vibrational state of the molecule and the $v' = 0$ vibrational state of the ion. The first vibrational component in the PE spectrum will therefore be the strongest. However, the second ionic state, AB^+A has its equilibrium internuclear distance shifted from the equilibrium internuclear distance of the molecular ground state. The overlap between the $v'' = 0$ and $v' = 0$ wavefunctions is reduced but the overlap of the $v'' = 0$ and $v' = 1$ wavefunctions increases. The maximum probability in the vibrational transition therefore shifts to a higher member of the series as the potential curves shift away from each other. Looking at the shape of the schematic PE spectrum drawn on the side of the potential curves can provide useful information. As just mentioned, the ionic state X has the same nuclear configuration as the molecular state. Consequently, the PE spectrum shows a very intense $v'' = 0$ to $v' = 0$ band followed by a relative short progression. This arises from the ejection of a non bonding electron. On the other hand, the second ionic state, A, has a larger equilibrium internuclear distance. The resulting PE spectrum shows a much longer vibrational progression with maximum intensity towards the middle of the progression. In this case, the photoelectron was ejected from a bonding orbital. Ionisation to the C state gives maximum intensity at internuclear distances which correspond to ionisation to above the dissociation limit of the C state, resulting in a broad featureless band. In considering the vibrational structure of a PE band, two terms are used, the Adiabatic Ionisation Energy (AIE)

and the Vertical Ionisation Energy (VIE). The AIE represents the energy required to ionise the molecule in the lowest vibrational level to the lowest vibrational level of the ionic state. The VIE is the energy required to ionise from the lowest vibrational level of the molecule to the vibrational level of the ionic state that gives the maximum overlap integral. The VIE is thus the most intense component of a vibrational progression. The AIE and VIE coincide when the $v'' = 0$ to $v' = 0$ band is the strongest, e.g. for the first PE band in Figure 2.1.

For an anharmonic oscillator, the energy of vibrational levels is given by [25]:

$$\varepsilon_v = (v' + 1/2)\omega_e - (v' + 1/2)\omega_e\chi_e \tag{2.1.14}$$

where v is the vibrational quantum number, ω_e is the vibrational constant and χ_e is the anharmonicity constant. It follows that the spacing between two vibrational levels is given by :

$$\Delta\varepsilon = \omega_e - 2\omega_e\chi_e(v' + 1) \tag{2.1.15}$$

From an experimental PE spectrum, it is thus possible to determine the vibrational constants ω_e and $\omega_e\chi_e$ of the ionic state by plotting the separation of vibrational components against $(v' + 1)$. A comparison of the ω_e value obtained in the ionic state with the usually well known value of ω_e in the molecular ground state can give an estimate of the bonding character of the orbital the electron occupied before ionisation. If ionisation occurred from a bonding electron, the bond strength is weakened in the ion and the internuclear bond length is increased. This lowers the vibrational constant ω_e of the ion. Once the vibrational constants $(\omega_e, \omega_e\chi_e)$ of the molecule and the ion are known, the Franck-Condon envelope for a given PE band can be computed using several trial values of the ionic bond length, r'_e. The equilibrium

bond length r_e and vibrational constants $(\omega_e, \omega_e\chi_e)$ of the neutral ground state are usually well known from other spectroscopic methods while the spectroscopic constants of the ion are determined from the PE spectrum, as just explained. The computed profile that fits best the experimental spectrum should corresponds to the most accurate value of the ionic bond length. The program used in this work is called FCF and the basic subroutine used was written by Cashion and Cooley [26, 27]. It computes the envelope of the first band in the photoelectron spectrum for different trial values of r'_e, thus allowing comparison between the experimental spectrum and the computed spectra. In the calculations, the vibrational wavefunctions for the neutral and ionic states are found from solution of the radial Schrödinger equation:

$$\frac{d^2\Psi_v}{dr^2} + [E_v - V(r)]\Psi(r) = 0 \tag{2.1.16}$$

where V(r) is assumed to be a Morse potential and is given by:

$$V(r) = D_e[1 - exp(-a(r - r_e))]^2 \tag{2.1.17}$$

In this equation, D_e is the dissociation energy and a is a constant. Both are related to the vibrational constants via:

$$D_e = \frac{\omega_e^2}{4\omega_e\chi_e} \tag{2.1.18}$$

and

$$a = \sqrt{\frac{8\pi^2 c\mu\omega_e\chi_e}{h}} \tag{2.1.19}$$

From ω_e, $\omega_e\chi_e$ and r_e the Morse potential of a particular state can thus be determined. The Schrödinger equation can then be solved for a given V(r) using the Numerov-Cooley method [28] to give the vibrational wavefunction Ψ_v and eigenvalues E_{vib} for the neutral and ionic states of the molecule. The FCF can then be calculated and the band envelope constructed, allowing the determination of the ionic bond length r'_e. This method has been used in this work to determine the bond length in the ground state of IF^+, as will be described in Chapter 5.

2.2 Indirect processes

2.2.1 Decay mechanisms

In contrast to a direct ionisation process where the incoming photon ejects an electron from the molecule, indirect processes can also occur when the energy of the incoming photon matches exactly the energy of a discrete neutral excited state above an ionisation limit. In this case, the photon is absorbed by the molecule, which is excited to a neutral excited state (Rydberg or valence state), with energy above the first ionisation limit. Once the molecule is in this excited state, it will decay by one of several mechanisms [29]:

(1) Re-radiation: $AB + h\upsilon \rightarrow AB^* \rightarrow AB + h\upsilon$

(2) Predissociation: $AB + h\upsilon \rightarrow AB^* \rightarrow A + B$

(3) Ion pair formation: $AB + h\upsilon \rightarrow AB^* \rightarrow A^+ + B^-$

(4) Autoionisation: $AB + h\upsilon \rightarrow AB^* \rightarrow AB^+ + e^-$

Fluorescent re-radiation is a rare mechanism as the time needed for an excited

molecule to radiate is in the order of 10^{-8} s. Autoionisation or predissociation are much faster processes and can be more rapid than one vibrational period, which is of the order of 10^{-13} s [30]. Consequently fluorescent decay is not competitive with the other decay mechanisms and will only occur when the other processes are unavailable.

Predissociation happens when a transition occurs to a bound state which interacts with an unbound one. The molecule dissociates after the radiationless transition between these states. However, the probability of such transition is so small that the molecule will have already decayed into a lower lying state with emission of radiation [30]. A special case of predissociation is the formation of ion-pair states where two ionic products are formed from the excited neutral state [31].

Autoionisation is also a radiationless transition where the excited neutral molecule spontaneously emits an electron. Autoionisation mechanisms can be of different types: rotational, vibrational, spin-orbit and electronic. Vibrationally and rotationally induced autoionisations happen when the excited state (usually a Rydberg state) lies above the first ionisation threshold due to vibrational or rotational excitation in the core. This type of autoionisation involves a breakdown of the Born-Oppenheimer approximation as strong interactions between the core and the Rydberg electron are required to transfer the excess energy of the core to the Rydberg electron. Vibrationally induced autoionisation has been observed in hydrogen [32] and it has been shown that it is most probable for the minimum change in vibrational quantum number, $\Delta\nu = -1$ [32, 33]. However, excitation to, and thus autoionisation from these states is weak. Vibrational autoionisation is therefore not considered to be an important process in most molecules. The same applies to rotational autoionisation. Spin-orbit autoionisation results from an exchange between Rydberg and core electrons and is primarily observed in the noble gases like Ar where the resonant series converging to $\mathrm{Ar}^2P_{1/2}$ can autoionise to the lower $\mathrm{Ar}^+\ ^2P_{3/2}$ state. Electronic autoionisation is a two-electron process that results from interactions

between a Rydberg state built upon an excited ionic state and a continuum corresponding to a lower state. It may happen in one of two ways. Either the excited core relaxes to a lower energy configuration and the energy so released is transferred to the Rydberg electron, or the Rydberg electron returns to its original orbital occupied in the neutral ground state and the excess energy is used to eject another electron, again leaving the ion in a less-excited state. Both cases require the close approach of the Rydberg electron to the core; only electronic motions are involved, so the Born-Oppenheimer approximation still holds. Electronic autoionisation appears to be the dominant autoionisation process in most molecules, where there are sufficient excited ionic states to yield fairly high densities of Rydberg states several eV above the first ionisation threshold.

A Constant Ionic State (CIS) spectrum, obtained by scanning simultaneously the energy of the photon source and the kinetic energy of the electrons while maintaining their difference equal to the ionisation energy of the process under investigation, will show a background level that depends on the cross-section for direct ionisation superimposed with discrete features that correspond to excited neutral states that electronically autoionise, as will be seen in Chapter 6.

2.2.2 Rydberg states

In atomic systems, the valence shell consists of a set of atomic orbitals with the same principal quantum number as that of the highest occupied orbital in the ground state. On the other hand, a Rydberg state is obtained when an electron is promoted outside the valence shell to an orbital with a higher principal quantum number. In most molecules, the distinction between a valence state and a Rydberg state is not clear as valence-Rydberg mixing can occur. However, Rydberg states are usually defined as highly excited states where an electron moves in an orbital with a large radius and a

high principal quantum number. The electronic configuration of the passive electrons corresponds to a state of the positively charged ion and is called the ionic core. Rydberg states are atomic-like in character and their excitation energy relative to the neutral ground state can be expressed as [34]:

$$E_n = IE - \frac{R}{(n-\delta)^2} \tag{2.2.1}$$

where n is the principal quantum number, E_n is the excitation energy to the nth level, IE is the ionisation energy towards which the series converges, δ is the quantum defect and R is the Rydberg constant (13.61 eV). The Rydberg constant varies slightly with the reduced mass of the electron-core system [9]. Rydberg states with successively higher principal quantum number form a series, converging to a particular ionisation limit of energy IE. The Rydberg electrons are at a distance so large from the ionic core that the core appears as a point charge, leading to the near hydrogenic behaviour of the Rydberg states. The deviation from this behaviour is determined by the effective quantum number n^*, which is given by $n^* = n - \delta$. The effective quantum number, n^*, is a measure of the effective nuclear charge seen by the excited electron and its magnitude reflects the degree of penetration of the Rydberg orbital into the electronic core. This penetration strongly depends on the radial distribution function of that orbital. Indeed, the greater the penetration of the wavefunction into the electronic core, the larger is the effective nuclear charge seen and the larger the value of δ. Rydberg orbitals with the same angular momentum quantum number, l, tend to have very similar values of δ. ns orbitals tend to penetrate significantly into the ionic core and thus the Rydberg electron sees the highest effective nuclear charge. np orbitals are less penetrating and nd orbitals even less. This can be seen by looking at the radial distribution functions for ns, np and nd orbitals (for $n > 2$) for a first row atom [35]. The quantum defect for ns Rydberg orbitals is therefore high while those of np and nd orbitals are progressively lower as

the degree of penetration of those orbitals into the core decreases. The quantum defect tends to be greater for heavy atoms or molecules as the interactions between the electron and the core are stronger. Typical values of δ for the first and second rows of atoms are reported in Table 2.1 [36].

	δ (ns)	δ (np)	δ(nd)
1^{st} row	1.0	0.5	0.1
2^{nd} row	2.0	1.5	0.3

Table 2.1: Typical values of quantum defect δ for the first and second rows of atoms [36].

The ionic core interacts only weakly with the Rydberg electron. As a result, the core will closely resemble the ionic state produced at the series limit and the spectroscopic constants for a member of the Rydberg series will be similar to those of this ionic state. The similarity between the Rydberg states and the core ionic state increases as the principal quantum number of the Rydberg orbital increases, so that when the ionisation limit is reached there is a seamless transition into the continuum [37]. As n increases, the average radius of the orbital also increases rapidly. The electron spends more time away from the core than close to it, and interacts less strongly with the ionic core. The average radius of a Rydberg orbital is $(n^2\hbar)/(me^2Z)$, so that Rydberg molecules with high n values have average radii as large as 100 Angström [34]. These Rydberg states are expected to have large cross sections for collisional reactions such as collisional ionisation or charge transfer. Rydberg series are observed in absorption spectra and accurate ionisation energies can be determined by extrapolation to series limits.

Transitions to a Rydberg state follow the electric dipole selection rules for optical absorption. These rules are usually dependant on the particular Hund's coupling case to which the initial and final electronic states under consideration belong. Some rules though, hold for any system [30]. These are:

$$
\begin{aligned}
&I.\ \ \Delta J = 0, \pm 1, with\ the\ restriction\ \ J = 0 \nrightarrow J = 0 \\
&II.\ \ g \leftrightarrow u, g \nleftrightarrow g, u \nleftrightarrow u
\end{aligned}
\tag{2.2.2}
$$

Where J is the total angular momentum while g (gerade) and u (ungerade) represent the symmetry with respect to inversion about the center of symmetry of the molecule. Apart from these general selection rules, other selection rules hold only for particular Hund's cases. Hund's cases (a) and (b) are the most frequent for the upper and lower states and the following selection rules apply in these cases:

$$
\begin{aligned}
&III.\ \ \Delta\Lambda = 0, \pm 1 \\
&IV.\ \ \Sigma^+ \leftrightarrow \Sigma^+, \Sigma^- \leftrightarrow \Sigma^-, \Sigma^+ \nleftrightarrow \Sigma^- \\
&V.\ \ \Delta S = 0
\end{aligned}
\tag{2.2.3}
$$

Where the "+" and "-" signs represent the symmetry of the molecule about the plane of inversion. Rydberg states can be described by Hund's cases (a) and (b) except at high values of n where the Rydberg electron is no longer coupled to the internuclear axis and Hund's case (d) is then more appropriate [9].

A Rydberg orbital is characterised by a definite principal quantum number n and an azimuthal quantum number l, so that in a system there are ns, np, nd... series. Rydberg states are defined by the ionic core around which they are built and the symmetry of the Rydberg orbital. The experimental determination of the quantum defect for a state can define the orbital angular momentum of the Rydberg electron. Rydberg series were observed in this work in CIS spectra of iodine atoms. The quantum defects of the series have been determined, as will be presented in Chapter 6.

2.2.3 Autoionisation resonances

At energies above the first ionisation threshold of a molecule, electronic states of different configurations can coincide exactly in energy since some of them may belong to a continuum state. The mixing between a configuration belonging to discrete states and continuum states gives rise to the phenomena of autoionisation [10]. The interference between the amplitude of direct and indirect processes results in a characteristic Fano profile. This is usually seen as sharp asymmetric features in a photoionisation spectrum, which records the total cross-section as a function of photon energy, where the total cross section is expressed as [37]:

$$\sigma(\varepsilon) = \sigma_a \frac{(q+\varepsilon)^2}{1+\varepsilon^2} + \sigma_b \tag{2.2.4}$$

where σ_a and σ_b represent two portions of the cross section, which correspond respectively to transitions to states of the continuum that do and do not interact with the discrete autoionising neutral excited state. In equation 2.2.4, ε is the reduced energy parameter and is defined as:

$$\varepsilon = \frac{E - E_r}{\Gamma/2} \tag{2.2.5}$$

where E is the incident photon energy, E_r is the resonance energy and Γ is the natural width of the autoionising state. Finally, q, is the Fano line profile index and is expressed as [37]:

$$q = \sqrt{\frac{2}{\pi\Gamma}} \frac{\langle \Phi | z | \psi_0 \rangle}{\rho \langle \psi_E | z | \psi_0 \rangle} \tag{2.2.6}$$

where z is the component of the dipole moment of the atom in the direction of the

photon polarisation. ψ_0 is the wavefunction of the initial state while Φ and ψ_E are the final state wavefunctions for the indirect and direct process respectively. ρ^2 is a correlation coefficient, defined as:

$$\rho^2 = \frac{\sigma_a}{\sigma_a + \sigma_b} \tag{2.2.7}$$

The q parameter characterises the line profile; neglecting the background cross section, the resonance is expected to reach a maximum at $\varepsilon_{max} = 1/q$ and a minimum at $\varepsilon_0 = -q$. The sign of q thus determines whether the maximum occurs before or after the minimum. The magnitude of q indicates the relative probabilities of the transition to the Rydberg state and direct ionisation. Figure 2.2 shows typical Fano profiles as a function of ε for five different values of q. It can be seen that when $q = 0$, the resonance is symmetric and has low magnitude. The magnitude of the resonance increases with q, along with the asymmetric character of the resonance.

Using equation 2.2.7, equation 2.2.4 can be modified to give an expression of the cross section as a function of ρ:

$$\sigma(E) = \sigma_c \left(\frac{(q+\varepsilon)^2}{1+\varepsilon^2} \rho^2 + (1-\rho^2) \right) \tag{2.2.8}$$

where $\sigma_c = \sigma_a + \sigma_b$. Autoionising states can have strong effects on photoionisation, photoabsorption and photodissociation spectra as well as on the angular distribution parameter β. Fano's theory can be used to fit experimental line shapes and determine values of q, ρ^2 and Γ for an entire Rydberg series, as will be seen in Chapter 6 on the work on iodine atoms.

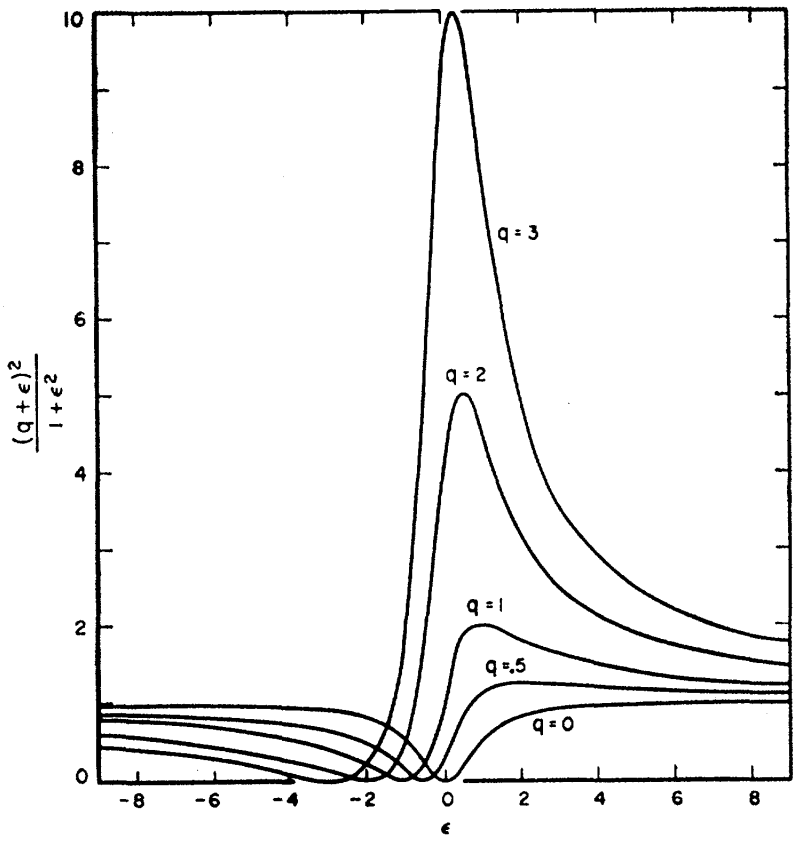

Figure 2.2: Typical Fano profiles for different values of q [10].

2.2.4 Multichannel quantum-defect theory (MQDT)

Fano's well known resonance formula shown in equation 2.2.4 considers isolated autoionising states coupled to degenerate continua. The development by Seaton [38] of the Multichannel Quantum Defect Theory (MQDT) extended Fano's configuration interaction theory to the case of many autoionising states interacting with degenerate continua and allowed the characterisation of interacting autoionising series. Variants of the MQDT were developed by Seaton [39], Giusti-Suzor and Fano [40] and Cooke [41]. A discussion of the method has been given by Connerade [42]. Dubau and Seaton [43] studied the case of a series of Rydberg levels autoionising into a

single continuum, which corresponds in MQDT language, to two interacting channels, one open and one closed. As previously seen, Fano's expression of the cross section is given by equation 2.2.4. In this equation, the reduced energy, ε, can also be given by [43]:

$$\varepsilon = \frac{tan[\pi(n^* + \delta)]}{\xi^2} \tag{2.2.9}$$

where δ is the quantum defect, n^* is the effective quantum number and the parameter ξ can be related to the resonance width Γ_n via [40]:

$$\Gamma_n = \frac{2\xi^2 R}{\pi(n^*)^3} \tag{2.2.10}$$

Equation 2.2.4 represents the case of one closed channel and one open channel. If more than one closed channel exists in the region of interest and if these channels do not interact either directly or through open channels, the photoionisation cross section has been given by Ueda [44] as a superimposition of equation 2.2.4 over the k closed channels:

$$\sigma_k(E) = \sum_k \sigma_{ak} \left(\frac{(q_k + \varepsilon_k)^2}{1 + \varepsilon_k^2} \right) + \sigma_b \tag{2.2.11}$$

If an energy region contains both open and closed channels and if all the closed channels are degenerate, equation 2.2.11 becomes:

$$\sigma(E) = \sigma_a \left(\frac{(1 + \Sigma_k q_k/\varepsilon_k)^2}{1 + (\Sigma_k q_k/\varepsilon_k)^2} \right) \tag{2.2.12}$$

During the course of this work, codes were written using the program Mathematica

to fit the experimental data of relative cross-sections recorded as a function of photon energy, obtained in CIS spectra, to Fano profiles. Equation 2.2.12 was used, as will be seen in Chapter 6 for the analysis of iodine atom resonances. In order to obtain an improved fit of the experimental data, a slow variation of the parameters σ_a, σ_b, δ, q and ξ with energy was introduced. This was achieved by using a set of parameters linear in the reduced energy $X = (I - E)/R$. The parameters (generically named p) are then written as $p = p_a + p_b X$.

2.2.5 Franck-Condon Factors for autoionisation processes

As mentioned in the previous section, autoionisation can cause deviations in the profile of a photoelectron band from the expected Franck-Condon envelope for direct ionisation. A single autoionising level, excited at a particular photon energy, can decay to several vibrational levels in the ionic state, thus extending the vibrational progression in the PE spectrum recorded at that photon energy. Irregular changes in the intensities of the vibrational components in the PE spectrum are also commonly observed. If the lifetime of the autoionising state is greater than one vibrational period, the photoelectron spectrum is expected to be dependent on the Franck-Condon factors for radiationless transitions from the autoionising state of the neutral molecule to the final state of the ion, as is illustrated schematically in Figure 2.3. This Figure shows a schematic PE spectrum on the right hand coordinate. The low-energy part of the PE spectrum is mostly dependent on direct ionisation. However, the PE spectrum is modified by the autoionisation process, which extends the vibrational progression outside of the Franck Condon envelope for direct ionisation. The intensity of the vibrational components are also modified and, as is observed on this Figure, it can happen that two maxima appear on a spectrum influenced by autoionisation.

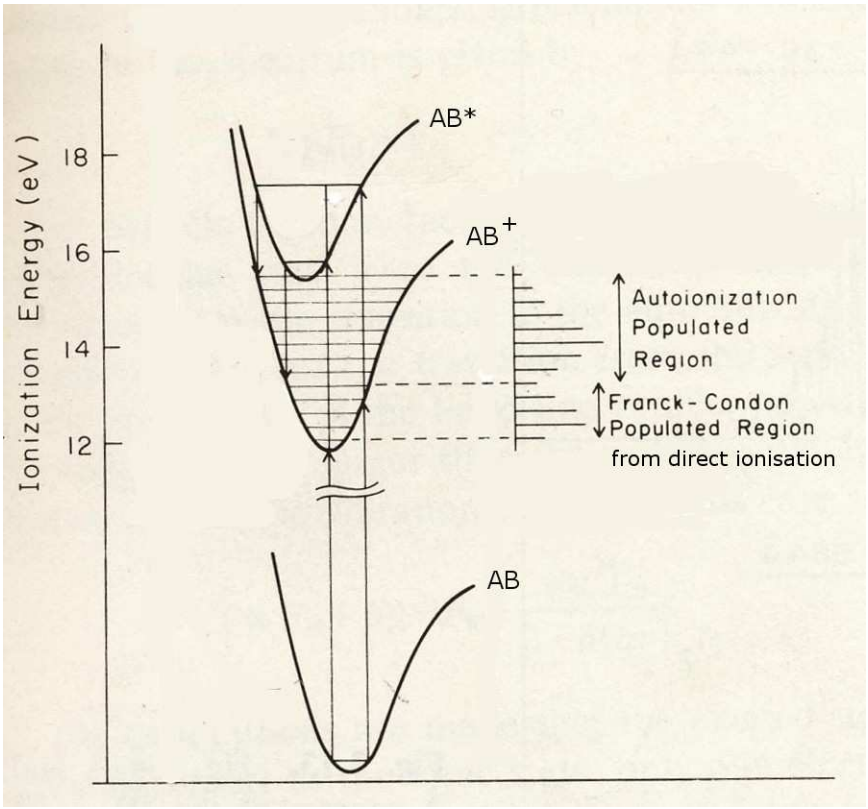

Figure 2.3: Schematic diagram illustrating the FCF in autoionisation [5].

The radiationless transition probability γ from the autoionsing level Ψ_a to the final ionic state Ψ_f is expressed as [5]:

$$\gamma = \frac{4\pi^2}{h}|\langle\Psi_f|W|\Psi_a\rangle|^2 \tag{2.2.13}$$

where W is the perturbation function and is totally symmetric. The selection rules for autoionisation can thus be derived as Ψ_f and Ψ_a must have common symmetry species for the radiationless transition probability γ to be nonzero, that is:

$$\Gamma(\Psi_f) = \Gamma(\Psi_a) \tag{2.2.14}$$

If the electronic, vibrational and rotational motion can be separated from the overall wavefunction, the selection rule becomes [5]:

$$\Gamma(\Psi_e\Psi_v\Psi_\tau)_f = \Gamma(\Psi_e\Psi_v\Psi_\tau)_a \tag{2.2.15}$$

Application of this selection rule may give information about the electronic states responsible for autoionising resonances when studying PE spectra perturbed by autoionisation. The intensities of vibrational components in a PE band can be predicted by the configuration interaction method, as developed by Fano [10, 37]. Two distinct cases are defined in this method. In case (1), the source has a width narrower than the width of the autoionisation line and is tuned to the maximum of the autoionising resonance, giving an intensity for the vibrational bands proportional to [5, 45]:

$$I \propto F_{if} + F_{ia} \cdot F_{af} \cdot q^2 \tag{2.2.16}$$

where F_{if} is the Franck-Condon factor for the direct ionisation from the initial ground molecular state i to the final ionic state f, F_{ia} is the Franck-Condon factor for the transition to the autoionising level a and F_{af} is the Franck-Condon factor for the transition from the autoionising level to the final ionic state. If the source linewidth $\delta(h\nu)$ is larger than the width of the autoionisation line Γ_n, as is likely to be the case in this work, then case (2) applies and the intensities of the vibrational components in a PE band is given by [5, 45]:

$$I \propto F_{if} + F_{ia} \cdot F_{af} \cdot \frac{\pi q^2 \Gamma_n}{2 \cdot \delta(h\nu)} \tag{2.2.17}$$

Both cases assume that the excited state has the same vibrational constants as the

ionic state on which it is built, that only one ionic state is populated in the decay of the autoionising level, and that only one autoionising state is involved in the ionisation process.

In Constant Ionic State (CIS) spectroscopy, the intensity of a single photoelectron feature is recorded as the photon energy is scanned. Discrete structure is observed only when the photon energy of the radiation coincides exactly with the energy of a transition to an autoionising state. Threshold Photoelectron (TPE) spectra are also affected by autoionisation, as will be described in Chapters 5 and 7.

2.2.6 Selection rules for autoionisation in atoms

In the Russell-Saunders coupling, the following selection rules apply for autoionising transitions between two states:

$$\begin{aligned}
&\Delta L = 0, \pm 1 \ \textit{with the exception} \ L = 0 \nleftrightarrow L = 0 \\
&\Delta l = \pm 1, \ \textit{for the promoted electron} \\
&\Delta S = 0 \\
&\Delta J = 0, \pm 1 \ \textit{with the exception} \ J = 0 \nleftrightarrow J = 0 \\
&\textit{no change of parity (Laporte rule)}
\end{aligned} \tag{2.2.18}$$

Parity is determined from the sum $\Sigma_i l_i$ over all electrons in each state These selection rules are not always followed and another coupling scheme, the $J_c l$ (JK) coupling scheme sometimes applies, as will be seen in Chapter 6 where the study of iodine atoms is described.

2.3 Angle resolved studies

The angular distribution of photoelectrons emitted with a polarised photon source is not usually the same in all directions. As a result, the band intensities in PE and CIS spectra depend on the angle of detection of the photoelectrons with respect to the direction of polarisation of the photon source. Synchrotron radiation, being strongly polarised, allows the study of the angular distribution of the photoelectrons. The differential cross section angular distribution ($d\sigma/d\Omega$, where σ is the cross section and Ω is the solid angle collected) for polarised radiation and randomly orientated molecules in the electric dipole approximation can be expressed as [5]:

$$\frac{d\sigma}{d\Omega} = \frac{\sigma}{4\pi}[1 + \beta P_2 cos\theta] \tag{2.3.1}$$

where θ is the angle between the direction of detection of the electron and the direction of the electric field, β is the asymmetry parameter and $P_2(cos\theta)$ is the second order Legendre polynomial:

$$P_2(cos\theta) = (3/2cos^2\theta - 1/2) \tag{2.3.2}$$

The electric dipole approximation also states that the selection rule $\Delta l = \pm 1$ applies for photoionisation where l is the azimuthal quantum number for the electron moved. As a result, photoionisation from an atomic orbital of angular momentum, $l > 0$, will give rise to two outgoing electron waves of angular momentum $(l + 1)$ and $(l - 1)$. Both waves can interfere with one another, as is manifested by the difference in phase shifts, $\cos(\delta_{l+1} - \delta_{l-1})$ in the Cooper Zare formula for β [34] :

$$\beta = \frac{l(l-1)R_{l-1}^2 + (l+1)(l+2)R_{l+1}^2 - 6(l+1)R_{l+1}R_{l-1}cos(\delta_{l+1} - \delta_{l-1})}{(2l+1)[lR_{l-1}^2 + (l+1)R_{l+1}^2]} \tag{2.3.3}$$

where $\delta_{l\pm1}$ are the phase shifts of the lth partial wave and R is the radial matrix element, expressed as:

$$R_{l\pm1}(\varepsilon) = \int_0^{\infty} P_{nl}(r) r P_{\varepsilon,l\pm1}(r) dr \tag{2.3.4}$$

Photoelectron emission is a two step process with 1) absorption of a photon by a neutral molecule and 2) the escape of the photoelectron. The escape can be accompanied by a transfer of angular momentum between the photoelectron and the ionic core. The photoelectron ejection can thus be schematically represented as:

$$X(J_0\pi_0) + h\nu(j_\gamma = 1, \pi_\gamma = -1) \rightarrow X^+(J_c\pi_c) + e^{-1}[lsj, \pi_e = (-1)^l] \tag{2.3.5}$$

where $X(J_0\pi_0)$ and $X^+(J_c\pi_c)$ represent the atom and resultant ion, with total angular momentum J and parity π. The angular momentum transferred between the molecule and the ion and photoelectron, j_t, is defined by:

$$j_t = j_\gamma - l = J_c + s - J_0 \tag{2.3.6}$$

The allowed values of j_t are those consistent with the conservation of the total angular momentum [34, 46]:

$$J_0 + j_\gamma = J_c + s + l \tag{2.3.7}$$

The conservation of parity π also implies:

$$\pi_\gamma \pi_0 = -\pi_0 = \pi_c(-1)^l \tag{2.3.8}$$

The values of j_t are thus either parity favoured or parity unfavoured. When j_t is parity favoured, $l = j_t \pm 1$ [47]. When j_t is parity unfavoured, $l = j_t$ and the asymmetry parameter, β_{unf} is -1; hence the angular distribution is energy independent. In general, the asymmetry parameter is given as a weighted average of the various $\beta(j_t)$:

$$\beta = \Sigma_{Jcs} \left(\frac{\Sigma_{j_t}^{fav} \sigma(j_t)_{fav} \beta(j_t)_{fav} - \Sigma_{j_t}^{unf} \sigma(j_t)_{unf}}{\sigma} \right) \tag{2.3.9}$$

where the expressions for $\beta(j_t)_{fav}$, $\sigma(j_t)_{fav}$ and $\sigma(j_t)_{unf}$ are given by Dill and co-workers [46, 48] in terms of scattering amplitudes. This expression of β is valid only in the absence of all anisotropic interactions between the departing electron and the ion. In this case, j_t is limited to the single value of l_0, which is the initial orbital angular momentum of the photoelectron. During the second stage of the photoionisation process, additional angular momentum transfer can arise, with the limitations expressed in equation 6.11. The Cooper Zare model does not consider the exchange between the ion core and escaping electron, hence parity unfavoured angular momentum transfers with values of $j_t \neq l_0$ are excluded. Dill et. al. [48] have studied the influence of these anisotropic interactions for the photoionisation of atomic sulfur (which is an open shell system) and found that angular momentum transfers $j_t \neq 0$ contribute by a small amount to the asymmetry parameter β and to the cross sections. The Cooper Zare model is thus most accurate for closed shell systems.

To ensure that $d\sigma/d\Omega$ is positive for all values of θ in the Cooper Zare formula, the β parameter can take values from $-1 \leq \beta \leq +2$. $\beta = +2$ corresponds to a pure $cos^2\theta$

distribution with preference of the photoelectrons to be along the vector axis, $\beta = -1$ corresponds to a pure $sin^2\theta$ distribution with preference of the photoelectrons to be perpendicular to the vector axis and $\beta = 0$ corresponds to an isotropic distribution. Using equation 2.3.3 the β values for some atomic ionisations can be derived and are given in Table 2.2 [12].

Transition	β value
s $\rightarrow$ p	β =2
p $\rightarrow$ s	β =0
p $\rightarrow$ d	β =1
d $\rightarrow$ p	β =0.2
p $\rightarrow$ f	β =0.8

Table 2.2: β values for some atomic ionisations obtained from the Cooper Zare formula [12].

Analogous behaviour is observed in molecules. For example, if a molecular orbital is composed primarily of atomic s orbitals, β is likely to be large and the outgoing electron wave will have predominately p character. The asymmetry parameter depends mostly on the character of the molecular orbital from which an electron is removed, and is therefore normally constant within a particular photoelectron band. However, it is seriously affected by autoionisation, so that the band intensities in PE and CIS spectra can be affected by the angle at which the spectra are measured. Experimentally, β values can be determined by using the following equation for the cross section:

$$\frac{d\sigma}{d\theta} = \frac{\sigma}{4\pi}\left[1 + \frac{\beta}{4}(3Pcos2\theta + 1)\right] \tag{2.3.10}$$

For linearly polarised radiation ($P = 1$), the intensities measured at $\theta = 0^\circ$ is:

$$I_0 = \frac{\sigma}{4\pi}(1+\beta) \tag{2.3.11}$$

and at $\theta = 54°44'$ (in which case the measured intensity is proportional to the total photoionisation cross section and independent of β):

$$I_{54°44'} = \frac{\sigma}{4\pi} \tag{2.3.12}$$

The ratio of these intensities R can be written as:

$$R = \frac{I_0}{I_{54°44'}} = (1+\beta) \tag{2.3.13}$$

This gives

$$\beta = R - 1 \tag{2.3.14}$$

Thus, by recording PE or CIS spectra at two angles, $\theta = 0°$ and $\theta = 54°44'$, it is possible to obtain the β values. In this way, further information can be obtained about the photoionisation process, mainly concerning the character of the initial orbital and the nature of the free electron wavefunction. β values have been calculated during the iodine atom study, as will be seen in Chapter 6.

2.4 Conclusion

In this Chapter, the relevant basic principles related to photoelectron spectroscopy have been reviewed. The principles of direct and indirect photoionisation were

considered along with their selection rules. The Franck Condon principle was presented with its applications to both direct and indirect ionisations, and the basic ideas of angularly resolved measurements were also briefly introduced. These principles have been applied to the analysis of the results obtained during this work, as will be seen in the following chapters.

Chapter 3

Experimental

This chapter describes the photoelectron spectrometer and the Synchrotron Radiation Source used in this work. A detailed description of the photoelectron spectrometer is given in section 3.1 while a description of the preparation of the reactive intermediates studied during this project is given in section 3.2. Section 3.3 presents the different modes of spectral acquisition allowed by the spectrometer and section 3.4 describes the Synchrotron Radiation Source and mode of operation.

3.1 The photoelectron spectrometer

The Southampton PES group has been studying short-lived molecules by photoelectron spectroscopy since the first successful photoelectron spectroscopic study of a reactive intermediate was performed, in 1970, by Jonathan et. al. [13]. Several spectrometers were designed and built to be used in laboratory-based experiments with discrete line sources of vacuum ultraviolet (VUV) radiation, obtained from a discharge in an inert gas, for the study of the electronic structure of

such molecules [14, 15]. However, the development of synchrotron radiation offered new possibilities and a new spectrometer was designed and built, by Dr A. Morris, especially for the study of reactive intermediates in the gas phase, using synchrotron radiation [17]. It was initially used at the UK Synchrotron Radiation Source (SRS) facility at Daresbury [16, 23] and later at ELETTRA, in Italy [22, 49, 50]. The spectrometer was built to utilise the fact that synchrotron radiation is tunable and polarised, and thus allows angular distribution measurements to be performed as a function of the photon energy. It has also recently been modified to allow Threshold Photoelectron Spectroscopy (TPES) measurements. This new feature was first tested during the course of this project [51].

The main components of the spectrometer are the ionisation chamber, a three-element lens system, an electron energy analyser, an electron detector and a radiation source. Each chamber is evacuated to sufficiently low pressure to allow electrons to be transmitted from the point of production to the detector. Also, sufficient pumping capacity is built in to allow rapid transportation of the reactive species from the point of production to the photoionisation region. Constraints were imposed on the design of the spectrometer to prevent contamination of the monochromator optics at the synchrotron radiation source. The degree of sample differential pumping was increased from that in a PE spectrometer at Southampton and each chamber is evacuated by a separate turbomolecular pump. The design also needed to allow for the alignment of the spectrometer with the photon beam. This was achieved by building in wheels for mobility and adjustable legs to align the interaction region with the photon beam. Fine adjustments are permitted by two plates that allow translation movements and one plate which allows rotation of the spectrometer . The spectrometer can thus be aligned so that the interaction region is at the focal point of the photon beam before connecting it with the beamline.

Figure 3.1 shows a schematic diagram of the spectrometer in the plane perpendicular

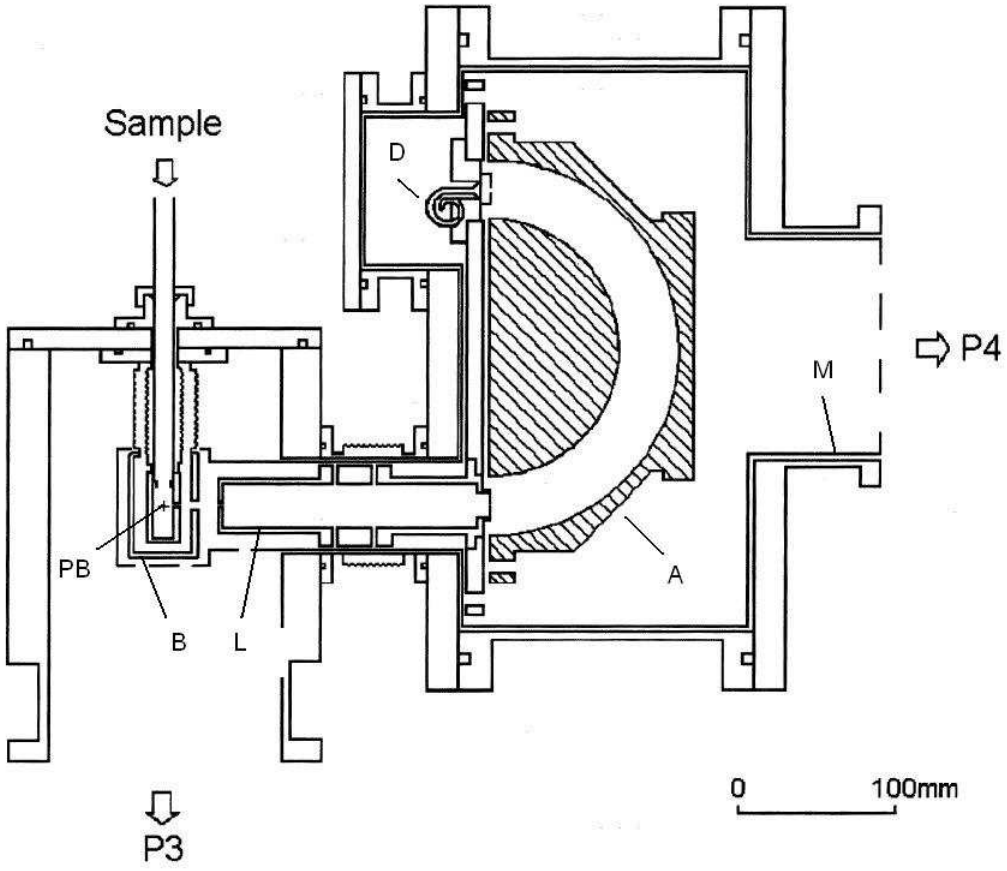

Figure 3.1: Cross section of the spectrometer in the direction of the photon beam. PB indicates the photon beam, B the boxes, L the lenses, A the 180° analyser, M the magnetic shielding and D the detector

to the photon beam which shows the principal features of the design. The sample gases are introduced via an inlet system into the ionisation region where they interact with the photon beam (labelled PB in Figure 3.1). To improve the pumping efficiency, the interaction region is enclosed by two metallic boxes (B in Figure 3.1) that are differentially pumped. A schematic diagram of the pumping system of the spectrometer is shown in Figure 3.2, which is described in the next section. Both boxes are coated with graphite in order to reduce any local electric fields that would

affect the trajectory of the electrons. The first box (closest to the ionisation region) is earthed. From the interaction region, the ejected photoelectrons travel through the lens system (L in Figure 3.1). This lens system allows the spectrometer to be used in constant pass energy mode. The first lens element is electrically connected to the outer box. It is usually earthed as well, except when TPES spectra are recorded, in which case an extraction voltage is applied. The third lens element accelerates (or decelerates) the electrons so that they enter the analyser (A in Figure 3.1) with appropriate energy while a voltage is applied to the second lens element that focusses the electrons onto the entrance slit of the analyser (this voltage is predetermined by a focus curve). The analyser consists of two concentric 180° hemispherical electrodes with a mean radius of 100 mm. The electrons are detected by a channeltron (D in Figure 3.1) which sends the signal to a standard electronic counting system. The spectrometer is mainly made of aluminium alloy and non-magnetic materials to avoid any local electric and magnetic fields that could affect the motion of the electrons. The box surrounding the ionisation region, as well as the lenses, analyser and detector are enclosed in thin shielding made of $\mu - metal$ (M in Figure 3.1) to avoid any local fields that would affect the trajectory of the photoelectrons. This alloy has a high magnetic permeability that constrains magnetic fields to pass within it rather than through it.

3.1.1 The vacuum system

The spectrometer needs to be kept at low pressure, $P \leq 1 \times 10^{-5}$ mbar, to ensure that the photoelectrons do not undergo inelastic collisions with the background gas between photoionisation and detection. Low pressure is also necessary to avoid absorption of the photons and contamination of the beamline optics. .

Figure 3.2 shows the differential pumping system [52] used on the spectrometer.

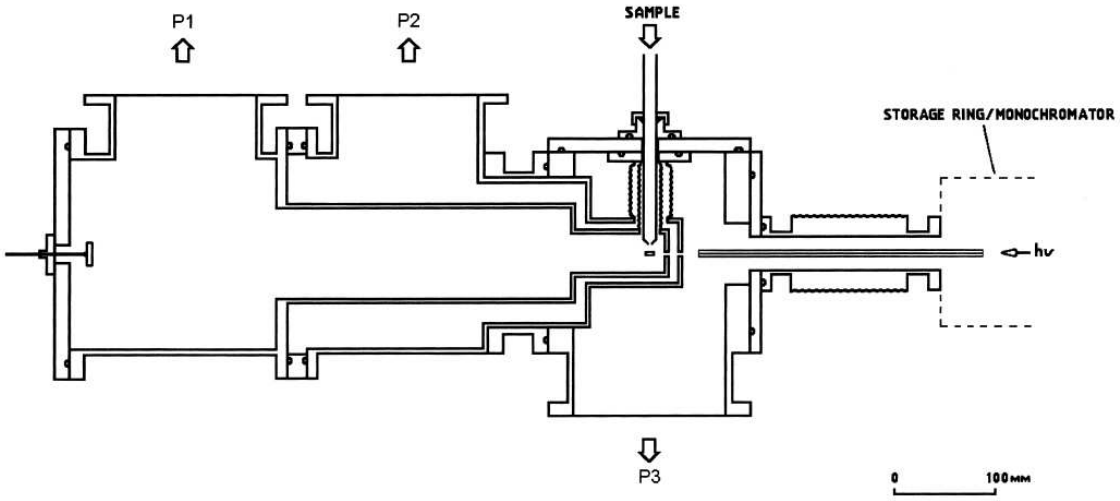

Figure 3.2: Cross section of the pumping system of the spectrometer

There are four turbomolecular pumps on the spectrometer, P1 to P4, each one backed by a rotary pump. P4 cannot be seen in Figure 3.2 as it is behind the ionisation region and pumps the analyser and detector region (see Figure 3.4 in section 3.1.5). It is a Leybold Turbovac 600 (600 $\mathrm{l.s^{-1}}$). As can be seen in Figure 3.2, the two boxes surrounding the interaction region are separately pumped by P1 and P2, thus increasing the pumping efficiency. These are 400 $\mathrm{l.s^{-1}}$ pumps (Leybold Turbovac 361C). The vacuum between the spectrometer and the synchrotron radiation source is maintained by P3, a 1000 $\mathrm{l.s^{-1}}$ pump (Leybold Turbovac 1000). P1 and P2 are fitted with purge valves, which reduce the bearings contamination when working with corrosive gases. There is also a Pirani gauge connected to each rotary pump to measure the pressure on the backing line in each part of the spectrometer. The base pressure of the spectrometer is about 2×10^{-7} mbar, as measured outside the boxes, on the wall of the ionisation chamber, by an ionisation gauge. This pressure rises when sample gas is admitted into the ionisation chamber. However, as long as the spectrometer pressure does not exceed 1×10^{-5} mbar, there is no significant change of pressure on the beamline pressure gauges. This indicates that the differential

pumping is sufficiently efficient to avoid contamination of the beamline optics.

3.1.2 The hemispherical electron analyser

The electron energy analyser, labelled A in Figure 3.1, consists of two concentric 180° hemispheres (inner and outer sectors) made of aluminium alloy. Both hemispheres are held at different voltages, V_i and V_o, and have different radii, R_i and R_o respectively. To select the mean pass energy, E_{pass}, of the electrons, the voltages applied to the hemispherical electrodes need to be selected. On this spectrometer, R_i = 80 mm and R_o = 120 mm; the inner separation is 40 mm. In order to obtain the required pass energy, E_{pass}, the hemispheres must be at voltages given by [1]:

$$V_i = E_{pass}\frac{R_o}{R_i} \tag{3.1.1}$$

$$V_o = E_{pass}\frac{R_i}{R_o} \tag{3.1.2}$$

The analyser is usually operated in constant pass energy mode (usually 5 eV). For that, the voltages applied to the hemispheres are floating with respect to the voltage of the third lens, thus keeping the pass energy constant throughout a spectrum. When photoelectron (PE) spectra are recorded, electrons are transmitted from the photoionisation point to the analyser entrance slits by a three element lens system (L in Figure 3.1). The total width of the entrance and exit slits of the analyser, ΔS, contributes to the base width, ΔE_b, of a photoelectron band, along with the radii of the hemispheres. ΔE_b is related to the pass energy, E_{pass}, via, [5]:

$$\Delta E_b = \frac{\Delta S}{R_i + R_o}E_{pass} \tag{3.1.3}$$

where $\Delta S = \Delta S_{entrance} + \Delta S_{exit}$. The full width at half maximum, $\Delta E_{1/2}$ is then related to the base width, ΔE_b by [53]:

$$\frac{\Delta E_b}{\Delta E_{1/2}} = 2.7 \tag{3.1.4}$$

In this work, the slits are each 1 mm wide which gives a $\Delta E_{1/2}$ of 18 meV for a pass energy of 5 eV. This resolution can be improved by decreasing the slits size or the pass energy but this is accompanied by a loss of intensity. Equation 3.1.3 neglects the angular acceptance of the analyser, α [53]. Other factors also contribute to the resolution of a photoelectron band like the radiation bandwidth, the Doppler broadening [25] and small fields that affect the motion of the electrons [54]. The last contribution is particularly important at small electron energies, as low energy electrons are much more affected by stray fields. The hemispheres, as well as the lens elements and boxes are coated with a conductive layer of graphite to minimise these potentials. However, the use of corrosive gases gradually reduces the efficiency of the spectrometer. The hemispheres, lenses and boxes then need to be taken apart for cleaning and replacement of the graphite coating. In practice, when a photoelectron spectrum of the $(3p)^{-1}$ ionisation of argon is recorded at 5 eV pass energy, the half width, $\Delta E_{1/2}$ is about 40 meV.

3.1.3 The lens system

As previously stated, a three-element lens system was inserted between the ionisation region and the electron energy analyser in order to operate this spectrometer in constant pass energy mode, E_{pass}. This allows constant resolution and transmission for electrons throughout a spectrum. The pass energy is usually 5 eV. The lenses are made of cylindrical aluminium elements, electrically insulated from each other. The

first element of the lens system (the elements nearest to the photon beam, PB in Figure 3.1) is usually earthed so that the ejected photoelectrons maintain their initial kinetic energy, E_i. The third lens element accelerates (or decelerates) the electrons so that they enter the analyser with the appropriate energy. The voltage of this lens is determined by the following equation:

$$V_3 = E_{pass} - E_i \tag{3.1.5}$$

The second lens element is at a voltage V_2 that focusses the electrons onto the entrance slit of the analyser. It acts as a focussing element so that the exit slit of the lens system becomes the optical image of the entrance slit. V_2 is generated experimentally by optimising this voltage for a particular photoelectron signal at different kinetic energies, at a selected pass energy. To obtain an energy shift of a particular photoelectron band in Southampton (where only the HeI(α) line source is available), an external voltage is applied to the inner box. The optimum values of V_2 that give the most intense and well-resolved PE band are recorded and a curve is generated by plotting $(E_i + V_2)/E_i$ vs E_{pass}/E_i [55]. This curve is fitted with a fourth order polynomial. The coefficients obtained are used as input in the controlling software which gives the optimum focussing voltage V_2 at a specific electron kinetic energy. This focus curve may change when the spectrometer is cleaned or when doing experiments with a microwave discharge on the inlet system. An example of a focus curve determined in this work with equation
$y = 1.22224 + 2.85281 \times x - 0.57852 \times x^2 + 0.04273 \times x^3 - 0.00111 \times x^4$, is given in Figure 3.3.

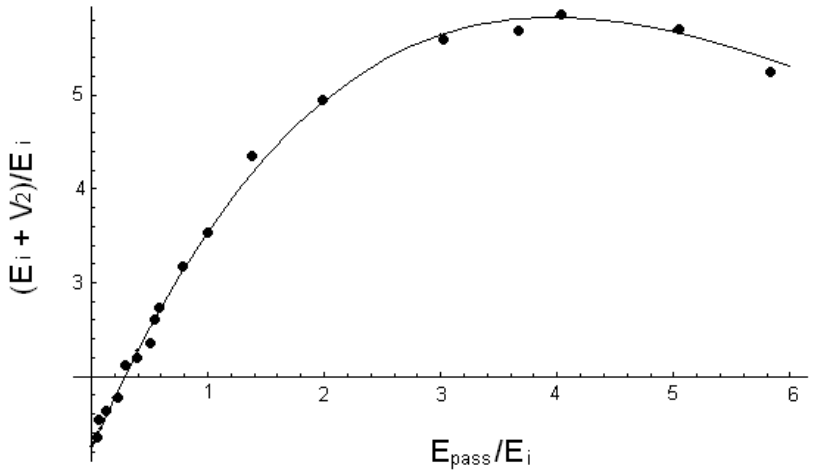

Figure 3.3: Focus curve obtained in this work with a fourth order polynomial fit.

3.1.4 The detector and electronics

The photoelectrons that have passed through the lens system and hemispherical analyser arrive at a single channel electron multiplier, also called a channeltron, to be detected (D on Figure 3.1). The signal from the photoelectrons is converted into voltages pulses and is preamplified and amplified before being passed to a General Purpose I/O National Instrument card, plugged into the computer. LABVIEW software designed for this spectrometer displays the spectrum on the screen. This software is interfaced with the beamline control system at Elettra to allow movement of the monochromator, thus allowing the photon energy in the ionisation chamber to be swept. The voltages applied to the lenses, hemispheres and outer box (for TPES) are determined by this software and sent from digital to analogue converters (DACs) in the computer to be amplified by Kepco power supplies before being delivered to the spectrometer.

3.1.5 The rotation mechanism

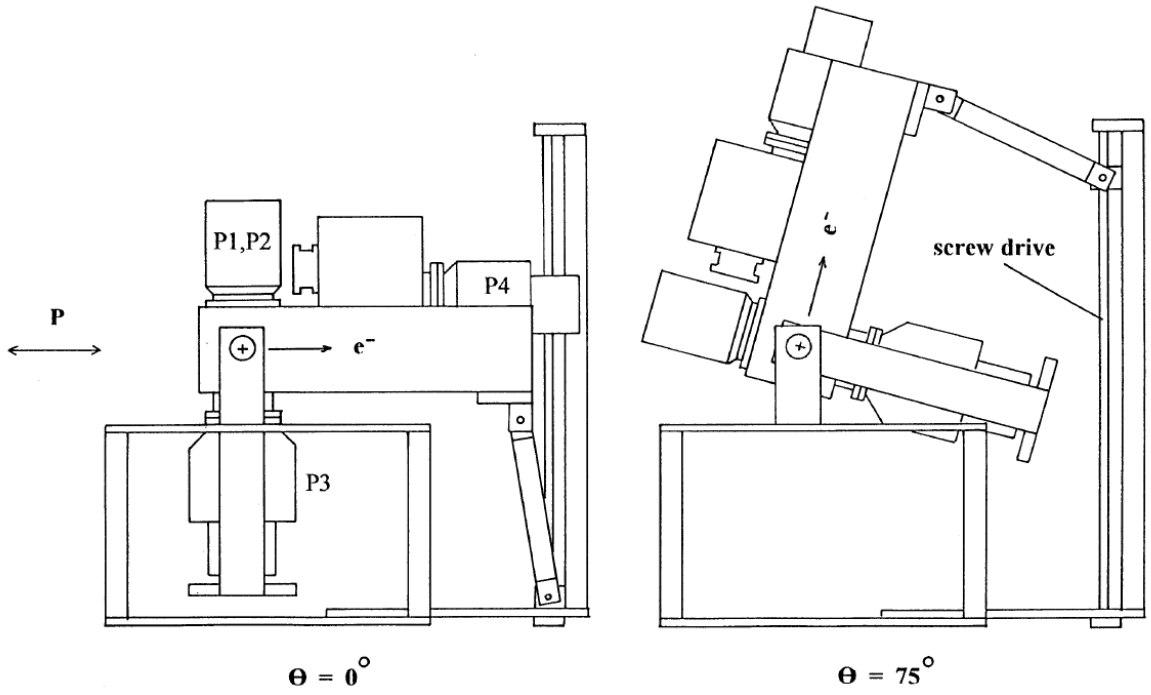

Figure 3.4: Schematic views of the rotation mechanism taken in the direction of the photon beam. The two extreme positions are shown, with angles $\theta = 0°$ and $\theta = 75°$ between the photon beam polarisation direction, P, and the direction of the electron detection (e^-)

With this spectrometer, angular distribution measurements can be performed by measuring PE spectra at two different angles with respect to the direction of the linearly polarised beam, as discussed in Chapter 2. The apparatus was built with a vertical and a horizontal arm attached to P3 and P4 (as seen in Figure 3.4) that are moved with a screw-drive mechanism. This mechanism allows the whole spectrometer to rotate, vacuum system included. There are other ways of performing angular distribution measurements, such as using a magnetic angle changer in the ionisation region [56] or rotating the polarisation of the photon source (in laser experiments) [57]. However, as the plane of polarisation of the photon source could

not be rotated, the spectrometer was built to rotate and Figure 3.4 shows the two extreme rotation positions, with angles $\theta = 0°$ and $\theta = 75°$ between the photon beam polarisation direction, P, and the direction of the electron detection (e^-). When rotating the spectrometer, it is important to make sure that the detection efficiency of the spectrometer stays the same. The main changes in the detection efficiency arise from small misalignments between the axis of rotation and the direction of the photon beam. To account for this, the PE spectrum of helium $(1s)^{-1}$ is recorded at each angle and the angular distribution parameter, β, for photoionisation of helium (which is well established as 2.0) is evaluated (at $h\nu = 28.0eV$). A comparison between the measured β parameter and the known β parameter of helium allows the determination of a correction factor that can be applied to each spectrum recorded while doing angular distribution measurements (see Chapter 6 for a more detailed explanation).

3.1.6 The HeI(α) photon source

Before the use of Synchrotron Radiation Sources in PE measurements, the reaction conditions for production of a selected reactive intermediate need to be optimised in Southampton. This is done by using a laboratory VUV source. The laboratory radiation source used with this spectrometer is the helium discharge photon source. Its principle of operation is as follows. A high-voltage potential is applied across a differentially pumped cell containing flowing helium gas, creating a discharge that excites the atoms to neutral and ionic excited states. The excited atoms then decay emitting radiation in the form of a line spectrum. Two types of radiation are present in a helium discharge; one coming from the decay of excited neutral atoms, with the strongest line at 21.21 eV (known as the HeI(α) line). This originates from the $\mathrm{He}(1s^2)^1S_0 \leftarrow \mathrm{He}\ (1s^12p^1)^1P_1$ emission. The other radiation comes from the decay of singly ionised atoms, the strongest line, known as HeII(α), occurs at 40.81 eV. During

the test experiments in Southampton, the HeI(α) line is used. The photon source operates under low-pressure conditions which are maintained by two backing pumps, a rotary pump and a diffusion pump. The discharge is produced inside a narrow quartz capillary by applying a high voltage between the anode and the cathode. The photons are then directed to the target region by a Pyrex capillary. If the helium pressure is too high, some helium atoms enter the ionisation chamber, reducing the partial pressure of the sample gas that can be added.

3.2 Sample production

Most of the molecules studied during this project have short lifetime at low pressure in the gas phase and so must be produced *in situ* and fed into the ionisation region before they have time to react. In this work, a fast atom-molecule reaction is used to produce the reactive intermediate of interest, where atoms are produced by a microwave discharge at 2.45 GHz in a flowing gas and react with a stable target molecule, introduced via an inner inlet tube [58]. The inlet system used in this project when working with a microwave discharge is shown in Figure 3.5. It consists of two glass tubes, an inner inlet tube and an outer inlet tube. The side of the outer inlet tube has three 90° bends to prevent low energy electrons produced in the discharge from entering the ionisation region. In the Southampton PES group, fluorine atom subtraction is often used to prepare a reactive intermediate for study by PE spectroscopy. This is because fluorine atom abstraction reactions are rapid and often occur at or near collision frequency, and the species F, HF and F_2 all have first ionisation energies above 15 eV and hence do not contribute to the lower ionisation energy region enabling the search for reactive intermediate bands to be made easier [59–61]. When working with a microwave discharge of fluorine with helium (to make F atoms), the inside of the outer inlet tube and the whole inner inlet

tube need to be coated with teflon to avoid attack of the glass by fluorine atoms and the discharge cavity is placed on an alumina section to avoid melting of the teflon due to the heat of the discharge [62]. The distance between the end of the inner inlet tube and the photon beam is called the mixing distance. This is adjusted to give the maximum signal of the reactive species of interest. It is usually determined, along with the optimum reagent partial pressures, during test experiments carried out in Southampton.

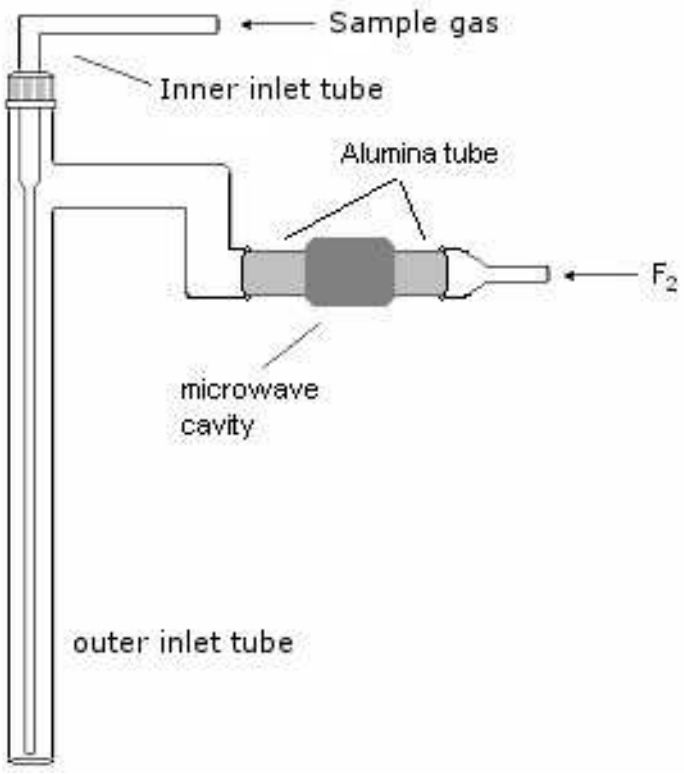

Figure 3.5: Schematic diagram of the inlet system used in this work

During this project, several reactive intermediates were studied. The choice of these intermediates must take into account the feasibility of the reaction. The first requirement is that the ionisation energy of the reactive intermediate must be higher than 10 eV, as the photon intensity decreases rapidly below this at beamline 4.2 at Elettra (see Section 3.4). The second and obvious requirement is that it is necessary

to observe the intermediate with the photoelectron spectrometer. Consider the following consecutive reactions:

$$A + B \rightarrow \mathbf{C} + D \qquad \text{- - reaction (1)}$$

$$\mathbf{C} + E \rightarrow F + G \qquad \text{- - reaction (2)}$$

If the reactive intermediate, C, is of interest then for it to be observed in PES, there are several factors to consider. First, the primary reaction should produce enough intermediate for it to be detected (the detection limit of photoelectron spectroscopy is about 10^{-10} to 10^{-11} molecules.cm^{-3} with the photon source and spectrometer used) [63]. This means that C should be produced rapidly and not be removed too fast. In practice, experiments in the Southampton PES group have shown that with the pumping system used, the rate constant of reaction (1) should be about 10^{-10} to 10^{-11} cm^{-3}.molecules.s^{-1} and the rate constant of reaction (2) should be about 10^{-13} to 10^{-12} cm^{-3}.molecules.s^{-1} [63].

The first experiments of this project were carried out on iodine atoms and IF, which have first ionisation energies of 10.451 eV [60, 61] and 10.62 eV [64] respectively. Iodine atoms and IF were obtained as secondary products of the following reaction:

Primary reaction: $F + CH_2I_2 \rightarrow CH_2I + IF$

Subsequent reactions: $F + CH_2I \rightarrow [CH_2IF]^{\dagger} \rightarrow CH_2F + I$

$\rightarrow CHF + HI$

The rate constant for the first reaction, $k_1 = 1.69 \times 10^{-10}$ cm^3.molecules^{-1}.s^{-1} at $25°C$ [65]. The rate constant of the second reaction is not known but IF can also be obtained from another reaction pathway:

$$F + CH_2I \rightarrow IF + CH_2$$

with $k = 3.50 \times 10^{-10}$ cm^3.molecules^{-1}.s^{-1} at 25°C [65]. This route also contributes to the IF concentration. In this work, which is described in Chapters 5 and 6, F atoms were produced by passing a flowing mixture of 5% F_2 and helium through the microwave discharge. CH_2I_2 was introduced by the inner inlet tube. Several test experiments were performed to find the optimum mixing distance and optimum reagent pressures. It was found that iodine atoms were maximised at a mixing distance of about 4 cm from the photon beam while the IF bands maximised at a mixing distance of about 3 cm. Argon was added to the reaction mixture in order to allow optimisation of the electrode voltages when TPE spectra are recorded. The results obtained from the study of I and IF are presented in Chapters 5 and 6.

SF_2, which was also studied in this work (see Chapter 8), was produced in a similar way by reacting F + OCS:

Primary reaction:	$F + OCS \rightarrow SF + CO$
Subsequent reaction:	$SF + SF \rightarrow SF_2 + S$
Followed by:	$S + S + M \rightarrow S_2 + M$

The rate constant of the primary reaction, F + OCS is $k_1 = 1.8 \times 10^{-11}$ cm^3.molecules^{-1}.s^{-1} at 25°C and the subsequent reaction, SF + SF has a rate constant of $k_2 = 2.5 \times 10^{-11}$ cm^3.molecules^{-1}.s^{-1} at 25°C [66]. In this case, k_2 is faster than k_1 which explains why SF was never seen in PE experiments, even when experiments were carried out to search for it. The optimum mixing distance for the study of SF_2 was found much lower in this case, at 0 cm. Since TPE measurements were also performed on SF_2, argon was added to allow optimisation of the electrode voltages. At this short mixing distance, the contribution of S_2 from the recombination reaction $S + S + M \rightarrow S_2 + M$ is minimised.

Some reactive intermediates can be produced by discharging directly their parent molecules. For example, CF_2 was obtained by a microwave discharge of flowing

hexafluoropropene, C_3F_6, diluted with argon. In this case, the inlet system is modified to a simpler version as both gas and carrier are introduced along the same inlet tube. The inner inlet tube is not necessary and is replaced by a simple blank screw top. The microwave discharge of C_3F_6 also produces C_2F_4 which was also seen in the spectra. The results obtained are shown in Chapter 7.

3.3 Types of spectra

The spectrometer has been designed to allow three different types of spectra, PE, CIS and TPE spectra, to be recorded. They can be described as follows:

3.3.1 Photoelectron Spectroscopy (PES)

In photoelectron (PE) spectroscopy, the energy of the incident radiation is kept fixed and the yield of photoelectrons is measured as a function of their kinetic energy [1]. As previously stated, the spectrometer is operated at fixed pass energy; it is therefore the voltage on the third lens that is scanned to obtain this kind of spectrum. Photoelectron spectra allow ionisation energies to be measured and provide a map of the ionic states that are accessed, as explained in Chapter 2. The overall resolution of a photoelectron band depends on the resolution of the analyser ($\Delta E_{1/2}$ value) and the bandwidth of the radiation and is usually about 40 meV (see section 3.1.2).

3.3.2 Constant Ionic State (CIS) spectroscopy

Unlike photoelectron spectra that can be recorded with a fixed-energy radiation source, Constant Ionic State (CIS) spectra require a photon source that can be

scanned. This is provided by a Synchrotron Radiation Source. In CIS spectra, the kinetic energy of the electrons is scanned simultaneously with the energy of the radiation while maintaining their difference equal to the ionisation energy of the process under investigation, thus keeping the energy separation between the initial molecular state and the final ionic state equal. In this way, a selected ionisation process (for example, a vibrational component of a photoelectron band or an atomic ionisation) can be monitored [67]. CIS spectra show discrete structure when the radiation is resonant with a highly excited neutral state that autoionises to the ionic state under investigation (see Chapter 2). A map of Rydberg states above an ionisation threshold can therefore be obtained. The resolution in CIS spectra only depends on the radiation bandwidth and can be as low as a few meV. Before running a CIS spectrum, a conventional PE spectrum is usually acquired to determine the ionisation energy of the particular band to be monitored. In this work, iodine atoms were studied by CIS and the results obtained are shown in Chapter 6.

Both angle-resolved CIS and PE experiments can be performed with the spectrometer used. Indeed, the angular distribution parameter, β, can be estimated at a selected photon energy by recording PE or CIS spectra at two or more angles with respect to the direction of polarisation of the photon source (see Chapter 2), giving further information about the photoionisation process, mainly concerning the character of the initial orbital and the nature of the free electron wavefunction.

3.3.3 Threshold Photoelectron Spectroscopy (TPES)

Threshold Photoelectron Spectroscopy (TPES) provides information to complement that obtained from conventional PE spectroscopy, where overlapping bands can be a problem, especially when studying reactive molecules (the typical resolution of the spectrometer is about 40 meV ($\Delta E_{1/2}$) when PE spectra are recorded). The

spectrometer used in this work was recently modified to allow TPE spectra to be recorded. In TPE spectra, the yield of near zero kinetic energy photoelectrons is recorded as a function of the photon energy [68–70]. To allow the extraction of low kinetic energy electrons, a small electrostatic field is applied to the interaction region. This penetrating field produces a saddle point in the potential distribution, focussing the low energy electrons toward the lens system [11]. The sensitivity is increased as the photoelectrons are collected over a solid angle of $4\pi sr$. A TPE spectrum is obtained by sweeping the photon energy and detecting low energy (≤ 5 meV) electrons. This results in a significant improvement of the resolution (~ 5 meV) but also means a loss of angular information.

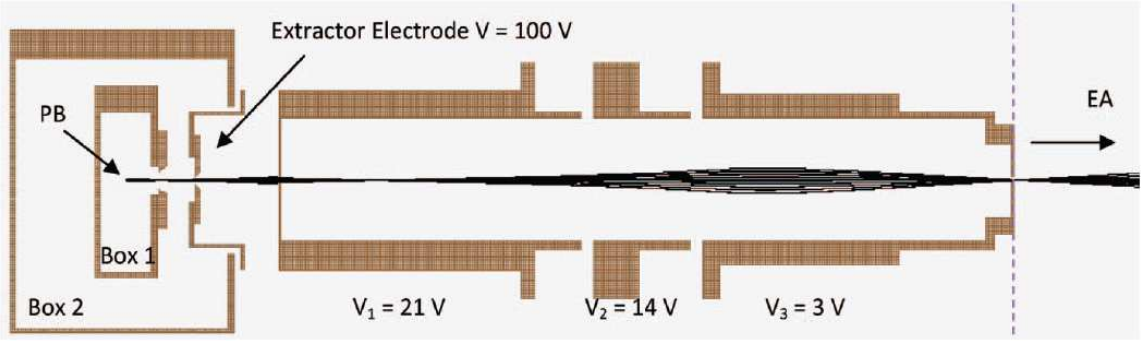

Figure 3.6: Schematic diagram of the interaction region and lens system with voltages typically used in TPES , showing a simulation of trajectories of 1 meV photoelectrons. The photon beam (denoted PB), is at right angles to the plane shown and EA shows the direction of the electron energy analyser [51].

Figure 3.6 shows a schematic diagram of the interaction region and lens system with typical potentials used when recording TPE spectra, with a simulation of trajectories of 1 meV photoelectrons with an extractor potential of 100 V. Higher energy electrons are largely unaffected by the extraction voltage. However, some energetic electrons may pass through the lens system if they have initial trajectories along the axis of the lens system. These would create a high energy tail on a photoelectron band but these

energetic electrons are discriminated against by the hemispherical electron energy analyser. The entrance slit of the lens system also discriminates against more energetic electrons as can be seen in Figure 3.6. A threshold electron will be produced whenever the photon energy is equal to the ionisation energy of an ionic state. TPES therefore maps out the energy levels of the ion. TPE studies of SF_2, CF_2 and I and IF were carried out during this project and the results are shown in Chapters 5, 7 and 8.

3.3.4 Normalisation of the spectra and calibration of the photon energy scale

In order to allow comparison of experimental CIS spectra, these spectra need to be corrected for the change in photon flux with photon energy and the change of transmission function of the spectrometer. Similarly PE spectra need to be corrected for the analyser transmission function and TPE spectra need to be corrected for the change in photon intensity with photon energy. The intensities of the bands are normalised by the photon flux and then corrected for the transmission of the spectrometer. The photon flux as a function of photon energy is estimated from the current measured on the beamline gold mirror placed just before the glass capillary that channelled the radiation into the spectrometer ionisation chamber. From the current measured on the mirror the photon flux can be calculated using the quantum efficiency of gold. The transmission function of the spectrometer, for electrons of different initial electron kinetic energy, is determined by measuring the intensity of the helium $(1s)^{-1}$ photoelectron band (IE = 24.58 eV) at different photon energies [36]. The intensity of the helium $(1s)^{-1}$ band is usually measured in the 26-35 eV photon energy range, from which the efficiency of the analyser can be calculated using the absolute photo-ionisation cross-section of helium in this range [71]. In this way the analyser efficiency can be plotted as a function of the electron kinetic energy and the curve is used to correct the experimental PE and CIS

spectra for the transmission of the spectrometer.

The degree of linear polarisation (P=1) of the synchrotron radiation on the beamline BL4.2 at Elettra (see next section) is well established [72]. For a given sample gas, the asymmetry parameter (β) is measured at selected photon energies and over a photon energy range, by recording PE and CIS spectra at two different angles ($\theta = 0°$ and $\theta = 54°44'$) with respect to the direction of polarisation of the photon source. The angle of $\theta = 54°44'$ corresponds to the angle at which the measurement is independent of β thereby permitting a straightforward determination of the relative partial cross section. The β parameter is then calculated from the expression: $\beta = R - 1$ where $R = I_0/I_{54°44'}$ is the ratio of the experimental intensities at these two angles (see Chapter 2), after applying the above corrections. For the measurements of angular distribution parameter, it is important that the efficiency of the analyser does not change when the spectrometer is rotated. The change of the efficiency of the analyser on rotation arises from small misalignments between the axis of rotation and the direction of the photon beam. In order to quantify this contribution a correction factor was evaluated by measuring the intensity of the He band which has a well established asymmetry parameter ($\beta = 2$) at $\theta = 0°$ and at $\theta = 54°44'$. From the comparisons between the calculated asymmetry parameter and the known asymmetry parameter, the correction factor is determined.

The photon energy is usually calibrated in the 10.5-29.0 eV region using the energies of the Ar $3s^3p^5(^2S_{1/2})np \leftarrow 3s^23p^6(^1S_0)$ resonances [73] and He $1s^1np \leftarrow 1s^2$ absorption lines [74]. The Ar resonances are obtained by recording CIS spectra of the first band (first component) of the $(3p)^{-1}$ ionisation of argon in the photon energy region 26.0-29.0 eV. The absorption spectra of He were recorded by measuring the current on the aluminium plate at the back of the spectrometer in the photon energy ranges 21.0-24.0 eV using first order radiation and in the 11.5-12.3 eV region using second order radiation. These procedures were used to normalise every spectra

recorded during this work.

3.4 The Synchrotron Radiation Source

Photoionisation experiments require a monochromatic source of ultraviolet radiation. A helium discharge photon source is used at Southampton when testing the spectrometer and setting up reaction conditions (as described in Section 3.1). The ELETTRA photon source is used when acquiring PE, CIS and TPE spectra on reactive molecules using synchrotron radiation.

3.4.1 History of Synchrotron Radiation

Synchrotron Radiation was first observed in 1947 at the General Electric 70-MeV synchrotron [75, 76]. However, the production of radiation from moving charges was first predicted in 1898 by Lienard, who obtained a formula for the rate of radiation emitted from the centripetal acceleration of an electron [77]. The classical theory was further developed by Schott [78] who received the Adams Prize in 1908 for his expression of the angular distribution of the radiation. Interest in the radiation as an energy-loss mechanism was lost for a few decades until Blewett published a paper on the effects of radiative energy losses on the operation of electron accelerators [79]. He calculated the effects of the radiative energy losses on the electron orbits and showed that these were observed in the General Electric 100-MeV betatron in 1946; at that time the radiation itself had not yet been seen. Blewett started a search for the radiation which, from the work of Ivanenko and Pomeranchuk, he expected to be significant at the 100 MeV betatron [80]. According to calculations made by Schwinger [81, 82], the radiation spectrum was supposed to appear in the near infrared or visible range. Unfortunately, the tube in which the electrons circulated

was opaque and Blewett searched in the radio and microwave regions. The radiation was not seen from the betatron and a 70-MeV synchrotron was then built in 1946 by Pollock and his team [83] in the same laboratory. On April 24^{th} 1947, intermittent sparking occurred in the synchrotron. The coating of the electron tube was transparent, which allowed a technician to look inside with a mirror. Instead of sparking, he saw an arc in the tube, which was quickly recognised by Langmuir as synchrotron radiation, or Schwinger radiation as he called it [84]. The properties of the radiation were investigated by subsequent measurements at the General Electric synchrotron, as well as at the 250 MeV synchrotron at the Lebedev Institute in Moscow, to establish its spectral and polarisation properties. In the 1950s, these investigations were extended by several groups, like Tomboulian and Hartman [85], who confirmed the spectral and angular distribution of the radiation with a grazing-incidence spectrograph in the ultraviolet region at the 320-MeV electron synchrotron at Cornell. In the 1960s, an experimental programme using synchrotron radiation was started at the National Bureau of Standard (NBS) where its 180-MeV electron synchrotron was modified to allow access to the radiation via a tangent section into the machine's vacuum system. In the late 1960s the first synchrotron program on a storage ring began at the 240-MeV ring, Tantalus I, at the University of Wisconsin [86]. It was used for synchrotron radiation research and had a total of ten beamlines with monochromators.

3.4.2 Evolution of synchrotron radiation sources

Tantalus I started the first generation of storage rings as a source of synchrotron radiation and showed that they offered far more possibilities than synchrotron beams with their stability and constant spectral distribution. Synchrotron beams had repeated injections, accelerations and extractions while storage rings offered a continuous beam, at fixed current, for many hours. Interest in storage rings spread

quickly and more were built in Europe and Japan. In 1971, a 540-MeV ACO storage ring was built at the Orsay laboratory in France. The NBS converted its synchrotron into a 250-MeV storage ring (SURF II) in 1974 and the same year, the 300-MeV storage ring was commissioned by the INS-SOR group in Tokyo. The 2.5-GeV SPEAR ring at the Stanford Linear Accelerator Center (SLAC) was the first multi-GeV storage ring to provide X-rays to a large community of users. It provided a spectral range from 6 eV to 30 keV and had five user stations, each with a monochromator [87].

The first generation of storage rings was also called a parasitic facility as the accelerators were built mainly for high-energy or nuclear physics. They were electron-positron colliding-beam machines operated to provide high collision rates without blowing up the beam, which often meant low beam currents. However, even when used in parasitic mode, the advantage of using synchrotron radiation from a stable storage ring was evident and the demand for storage rings dedicated to the production of synchrotron radiation was quickly growing.

The 2-GeV Synchrotron Radiation Source (SRS) at the Daresbury Laboratory in the UK was the first built especially for this purpose, when the 5-GeV NINA electron synchrotron shut down in 1977. The first experiments began in 1980 and the SRS grew to 40 experimental stations [88]. Other second generation storage rings were built elsewhere and some of the first generation facilities evolved towards second generation status. It was soon acknowledged that a third generation of facilities with lower emittance and long straight sections for undulators would allow even higher brightness.

Third generation sources specialised in either short wavelength (high-energy or hard X-rays) or vacuum-ultraviolet and long wavelength (low energy or soft X-rays regions of the electromagnetic spectrum). The first third generation facility was the 6-GeV European Synchrotron Radiation Facility (ESRF) in Grenoble which was designed for

hard X-rays and opened in 1994. It was followed by the 7-GeV Advanced Photon Source at the Argonne National Laboratory in 1996 and by SPring-8 in Harima Science Garden City in Japan in 1997. Long wavelength sources included the 1.9-GeV Advanced Light Source at Berkeley which opened in 1993, and the 2-GeV Synchrotrone Trieste in Italy which opened in the same year. Long wavelength sources are smaller in circumference (about 200 meters) than short wavelength sources, that can reach 1440 meters in circumference. One of the main improvements over a second generation source, apart from the high brightness, has been the reliability of the source, which is very important in some fields where users only come for a few hours and need to leave with results [89].

Even as third generation sources are still operational, the race for better performance is still on and the best candidate for the fourth generation source is the hard X-ray Free Electron Laser (FEL), which is based on a very long undulator in a high energy electron linear accelerator. The hope is to achieve a peak brightness many orders of magnitude higher than third generation sources, in very short pulses, a few tens of fs wide [89].

3.4.3 Production of Synchrotron Radiation

A charged particle forced to travel along a curved trajectory experiences a centripetal acceleration and so emits radiation. A particle moving at a speed, $v \ll c$, where c is the speed of light, will emit radiation in a dipole pattern as shown schematically in Figure 3.7. However, if the particle moves at a speed close to the speed of light, the radiation pattern is distorted and changes to a narrow cone of radiation with angular spread $\Delta\phi$, as seen in Figure 3.7 [90].

The typical opening angle of the radiation cone in the laboratory system, $\Delta\phi$, shown in Figure 3.7, can be expressed as:

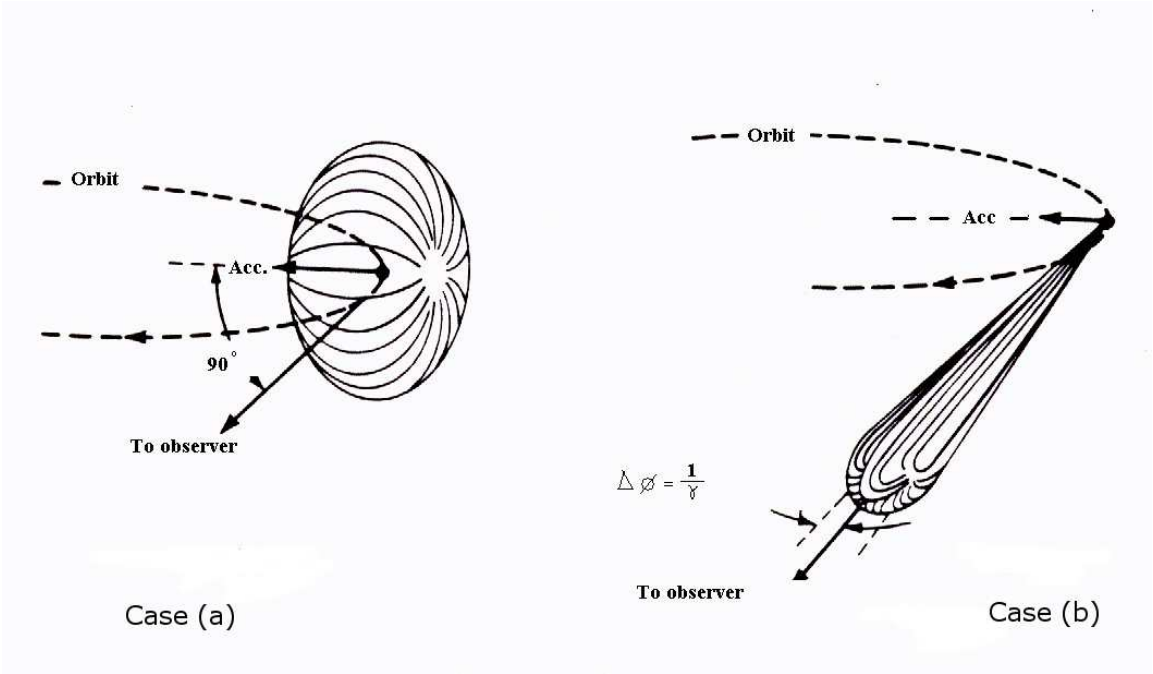

Figure 3.7: Radiation emission pattern of electrons in circular motion. Case (a), $v \ll c$. Case (b), $v \simeq c$.

$$\Delta\phi = \gamma^{-1} \tag{3.4.1}$$

where γ is known as the Lorentz contraction factor and is defined by equation 3.4.3 (see later). According to Einstein, the energy of an electron moving at the speed of light, E, is m_0c^2. However, this corresponds to the electron energy measured in the electron reference frame. In the laboratory frame, this expression changes to [8]:

$$E = \gamma m_0 c^2 \tag{3.4.2}$$

The gamma parameter corresponds to the ratio between the electron energy in the laboratory frame and the rest electron energy. It can also be expressed as:

$$\gamma = \frac{1}{\sqrt{1 - v^2/c^2}} \tag{3.4.3}$$

An observer located in the laboratory frame will see the Synchrotron Radiation emitted by the charged particle as a series of short pulses of light. A Fourier analysis shows that the spectrum produced by the charged particles goes from the frequency of revolution, ω_0 up to a critical frequency ω_c, expressed as [7]:

$$\omega_c = \frac{2c\gamma^3}{R} \tag{3.4.4}$$

where R is the radius of the electron orbit. However, the circulating electron oscillates about its equilibrium orbit so that even the spectrum of a single particle is a continuous distribution. The magnetic structures used to produce synchrotron radiation can be of three different types: bending magnets, undulators or wigglers.

3.4.3.1 Bending magnets

In the first generation of synchrotron, only bending magnets were used as sources of synchrotron radiation. Bending magnets force electrons to move along curved trajectories, as can be seen in Figure 3.8. The radiation is emitted in a narrow angular cone of angle $1/\gamma$ [91], in a forward direction with strong angular collimation, giving a small vertical angular spread (it can be smaller than 0.1 mrad). Since the radiation is emitted in the plane of the electron orbit, it is linearly polarised with the electric vector parallel to the orbital plane. Above and below this plane, the radiation is elliptically polarised [91]. The spectral distribution of the bending magnet in the horizontal plane is a smooth continuum, as can be seen in Figure 3.9.

There are different parameters to characterise the bending magnet emission; one of

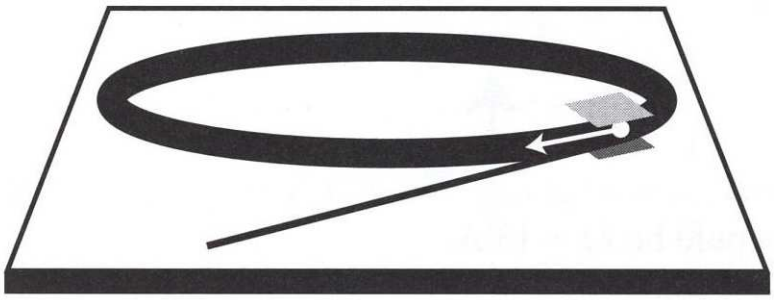

Figure 3.8: Schematic of the emission of synchrotron light by a bending magnet [8].

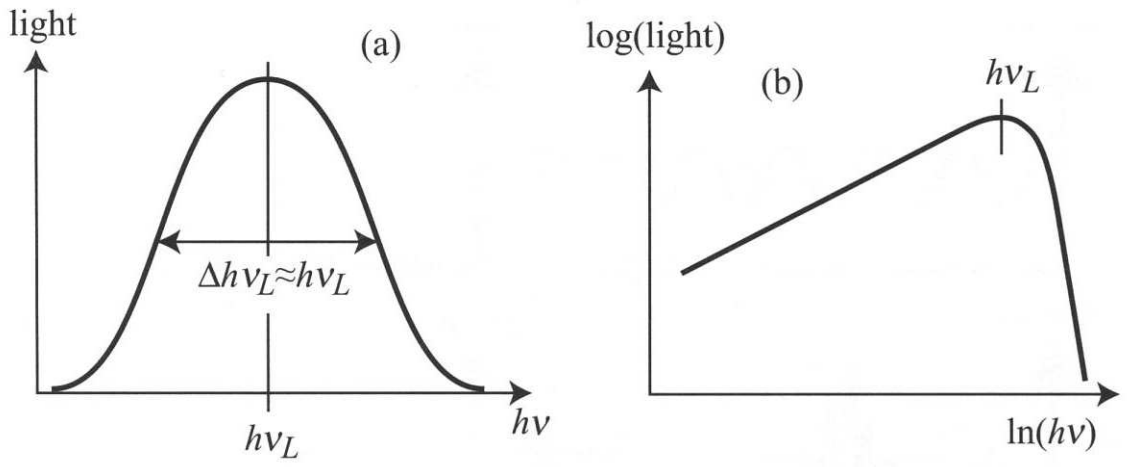

Figure 3.9: (a) Emission spectrum from a bending magnet as a function of the photon energy. (b) is the corresponding log-log plot [8]

them is the critical wavelength, which is the wavelength at which half the synchrotron radiation is emitted above and half below this wavelength. It is given by [8]:

$$\lambda_c = \frac{4}{3}\lambda_L = \frac{4\pi m_0 c}{3\gamma^2 eB} = \frac{7 \times 10^7}{\gamma^2 B(T)} \tag{3.4.5}$$

where B is the strength of the magnetic field in Tesla, e is the charge of an electron and λ_L is the centre of the emission band (see Figure 3.9). The critical energy of the synchrotron radiation produced by the bending magnet is [87]:

$$\varepsilon_c(keV) = \frac{2.218E^3(GeV)}{R(m)} = 0.0665B(kG)E^2(GeV) \tag{3.4.6}$$

where R is the radius of the electron orbit, E is the electron energy in GeV and B is the strength of the magnetic field in kGauss. Bending magnets are good sources of radiation when a "white" synchrotron radiation source is required as emission occurs over a broad range of wavelengths when bending magnets are used. Monochromatic radiation can still be obtained by inserting a filtering device called a monochromator to reject all other wavelengths. The amount of radiation emitted by each magnet depends on the number of electrons circulating in the storage ring.

Each time the electrons emit radiation, they lose energy. Without any correction, the electrons would rapidly lose all their energy and be unable to circulate in the ring. Radio Frequency (RF) cavities are therefore placed around the ring to restore the lost energy. The RF cavity applies a pulsed electric field to each bunch of electrons. The electrons are kicked forward by the cavity as the electric field is positive in front of them and negative behind them. The frequency at which the RF cavity operates controls the length of electron bunches and their separation. The maximum separation between two bunches is obtained in the single bunch mode where only one bunch of electrons circulate in the ring. This bunching of the electrons is an important property of synchrotron radiation, which allow time-resolved experiments to be carried out [92].

3.4.3.2 Undulators

An undulator is a periodic array of magnets inserted along straight sections of the ring. Each magnet applies a force to the electrons that produces transverse acceleration as observed in Figure 3.10. Undulators have small magnetic fields, which cause only a small deviation of the electron trajectories.

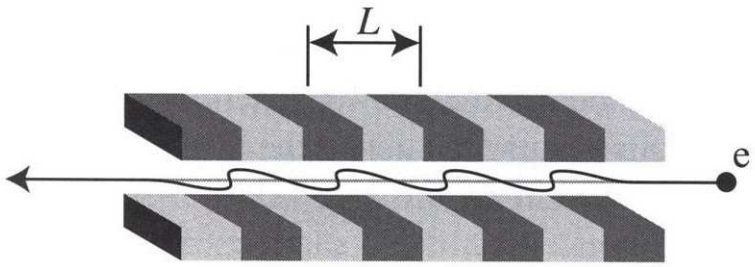

Figure 3.10: Schematic of an undulator; a periodic array of magnets with period L that causes small undulations of the electron (e) [8].

The angular spread, $\Delta\phi$ obtained for the fundamental wavelength is smaller than that of a bending magnet:

$$\Delta\phi = \frac{1}{\gamma\sqrt{N}} \tag{3.4.7}$$

where N is the total number of periods of the undulator and is usually in the order of 100 [92]. The emission from an undulator differs from that of a bending magnet as it has characteristic maxima due to the periodic structure of the magnet. The electrons emit at a frequency related to the period of the magnetic array, L, given by $\nu \simeq c/L$. The emitted wavelength should then be simply related to L by $\lambda \sim L$. However, undulators allow the emission of X-rays by the combination of two relativistic effects, the Lorentz contraction that shortens the period L of the magnetic array and the

Doppler shift that contracts the emitted wavelength. These effects are accounted for by the γ parameter. The emitted wavelength thus becomes [8]:

$$\lambda_L \simeq \frac{L}{2\gamma^2} \tag{3.4.8}$$

A characteristic parameter of periodic magnets is the non-dimensional magnetic strength K. It is proportional to B and relates the maximum deflection angle α of the electron path to the natural opening angle $1/\gamma$ of the radiation cone. It can be expressed as [7]:

$$K = \frac{\alpha}{1/\gamma} \simeq 0.934 \times B \times L \tag{3.4.9}$$

The average transverse speed induced by the undulator is proportional to B and modifies the value of $1/\gamma^2$ from equation 3.4.8 to $(1/\gamma^2)(1 + K^2/2)$. The emitted wavelength therefore changes to:

$$\lambda_L \simeq \frac{L}{2\gamma^2}(1 + \frac{K^2}{2}) \tag{3.4.10}$$

This equation holds for an emission along the axis of the undulator. When observed with an angle θ slightly off axis, λ_L modifies to:

$$\lambda_L \simeq \frac{L}{2\gamma^2}(1 + \frac{K^2}{2} + \gamma^2\theta^2) \tag{3.4.11}$$

where θ is the angle of emission of the radiation with respect to the undulator axis. The undulator will also emit higher harmonics of this wavelength, λ_L/n where $n = 1, 2, 3, ...$ For a small angular deviation, $\theta \to 0$, only odd n are allowed.

Otherwise, even harmonics are also detected [87]. Each harmonic is emitted with a particular bandwidth, $\Delta\lambda_L$, which can be expressed by [8]:

$$\frac{\Delta\lambda_L}{\lambda_L} = \frac{1}{nN} \tag{3.4.12}$$

To modify the value of the emitted wavelength, the magnitude of the magnetic field applied onto the electrons needs to be changed. This is achieved by changing the gap between the magnet poles. The wavelength can thus be tuned to the desired value or continuously scanned throughout an experiment.

Another important characteristic of synchrotron radiation concerns its polarisation properties. There are two main polarisation components, one with the electric field vector parallel to the orbital plane, $I_{\parallel}$, the second with the electric field vector perpendicular to the orbital plane, $I_{\perp}$. The degree of linear polarisation can then be defined by [91]:

$$P_L = \frac{(I_{\parallel} - I_{\perp}}{(I_{\parallel} + I_{\perp})} \tag{3.4.13}$$

The degree of circular polarisation can be obtained with a combination of the same components or with a decomposition of the elliptically polarised wave into right-handed and left-handed waves with intensities I_R and I_L:

$$P_C = \frac{(I_R - I_L)}{(I_R + I_L)} = \frac{2\sqrt{(I_{\parallel} I_{\perp}}}{(I_{\parallel} + I_{\perp})} \tag{3.4.14}$$

The Stokes parameters, S_i (i = 1, 2 and 3), also describe the polarisation properties of the radiation. They vary between +1 and −1. $S_1 = \pm 1$ describes linearly polarised radiation while $S_3 = +1$ describes right circularly polarised radiation. The degree of

polarisation of the radiation is then described by [7]:

$$P = \sqrt{S_1^2 + S_2^2 + S_3^2} \tag{3.4.15}$$

The beam of radiation is completely polarised for the degree of polarisation, $P = 1$. A degree of polarisation, $P = 0$ describes a unpolarised beam and P less than 1 is equivalent to a partially polarised beam.

3.4.3.3 Wigglers

Wigglers are similar to undulators, in that they consist of periodic magnetic arrays inserted into long straight sections of the storage ring. A device with sufficient field range can be operated as an undulator or a wiggler [92]. Wigglers just have a higher magnetic field, B. This gives rise to a larger K value and a larger oscillation amplitude. The critical energy also increases (see equation 3.4.6), thus shifting the spectrum into the hard X-rays region. The radiation cone of a wiggler is broader than that of an undulator which gives less bright radiation. The individual peaks of an undulator merge into a continuum with strong values of B and the radiation pattern is therefore similar to that of a bending magnet with much higher photon flux and a shift to shorter wavelength. The undulator regime is satisfied when the photon cone has an opening smaller than $1/\ \gamma$, which means $K \leq 1$. In contrast, $K \gg 1$ corresponds to a wiggler, equivalent to a series of bending magnets.

A comparison between the different types of emitting devices is shown in Figure 3.11.

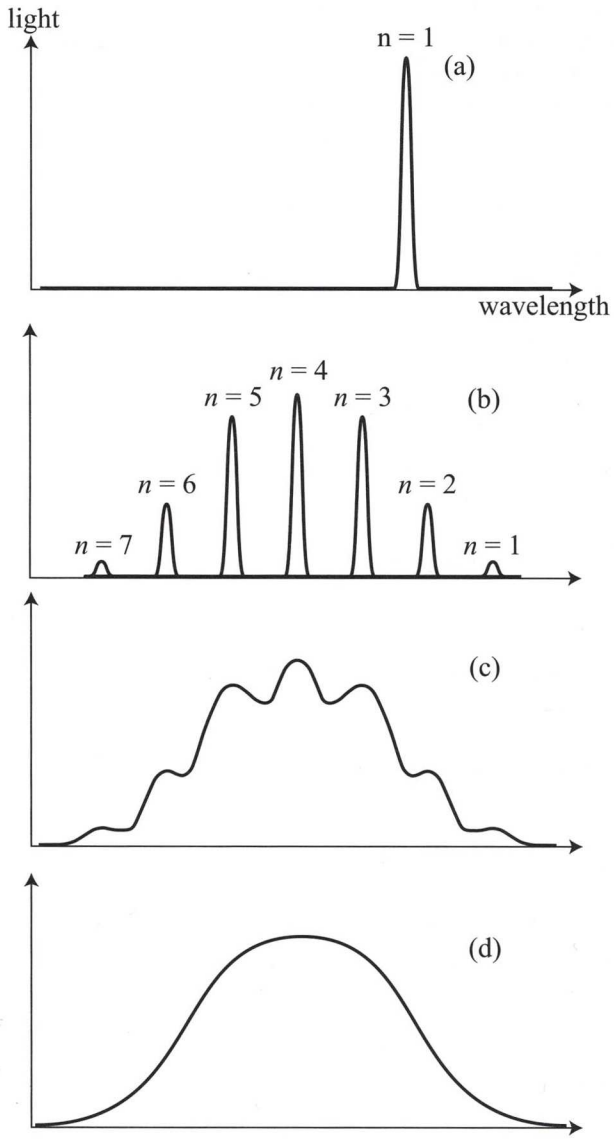

Figure 3.11: Comparison between different types of magnets. (a) Emission from an undulator (weak B field and K parameter) with a narrow band around the fundamental wavelength. (b) Larger K and B values. The fundamental wavelength shifts to higher values but the intensity of the higher harmonics increases as well. (c) Even larger B and K values; in this case the individual bands are broadened. (d) The limiting case of a pure wiggler, with only one broad band; this also corresponds to the emission of a bending magnet. [8]

3.4.4 The ELETTRA Sychrotron Radiation Source

The results obtained during this project were obtained at the Elettra synchrotron radiation source, on the BL 4.2 Circular Polarised Beamline. Elettra is an international multidisciplinary Synchrotron Radiation Laboratory located in Basovizza, on the outskirts of Trieste. It is a third generation synchrotron radiation source. A fourth generation light source based on a Free Electron Laser (FEL) is currently being built on the same site. The Elettra synchrotron source operates since 1993 and is optimised in the VUV and soft X-rays range. The storage rings operates between 2.0 and 2.4 GeV and feeds over 24 beamlines. It is used in many different fields such as chemistry, physics, geology and life sciences and offers photon energies from few eV to tens of keV. It has a spectral brightness of up to 10^{19} photons/s/mm^2/mrad^2/0.1 % bw (the peak brightness of the FEL is expected to go up to 10^{30} photons/s/mm^2/mrad^2/0.1 % bw). Elettra is composed of a storage ring, a linear accelerator and the transfer line. The storage ring is made up of four types of magnets: bending magnets that deflect the circulating beam into a closed circular path (see previous section), quadrupoles that focus the beam, sextupoles that compensate chromatic and non-linear effects and steerer magnets that perform small adjustments to the circular trajectories. The ring is roughly 260 m in circumference and is made up of twelve identical groups of magnets. The electrons are generated in a LINAC (LINear ACcelerator) and then injected in the ring. The LINAC is composed of an electron gun where ceramic discs are heated to very high temperature and therefore produce electrons. The electrons are drawn out off the gun by a high electric field (up to 100 kV). Electron bunches are then accelerated through various radio-frequency structures. The overall length of the LINAC is 66 m, which includes the electron gun, a low energy section and seven high energy sections, each 6 m long. The beam is kept focused by quadrupole magnets placed between the accelerating sections. The LINAC operates at 3 GHz and generates a pulse of electron bunches

that are accelerated to final energies up to 1.2 GeV. The electrons are then transported to the inner side of the ring by the transfer line, which consists of a series of deflection and focussing magnets. Both the LINAC and the transfer line are below ground so that they do not interfere with the beamlines. Pulses of electrons are gradually fed into the ring ten times per second until the desired current is achieved. This can take several tens of minutes. The LINAC, transfer line and the storage ring all operate under ultra high vacuum to minimise the collisions of electrons with residual molecules, therefore avoiding the loss of electrons and increasing the lifetime of the beam. The vacuum in the ring must be of very high quality since the electrons travel at a speed close to the speed of light and so pass a given point more than a million times in one second. The situation is further complicated by the copious emission of synchrotron radiation, around 90 kW of power just from the bending magnets. The unused radiation needs to be absorbed in special places otherwise chamber deformation and photon-electron release of surface gases will occur. Two parameters are important in describing the beam, its brightness and its emittance. The brightness of the beam is proportional to the transverse size and divergence of the beam, while the emittance is the area occupied by the beam in phase space. The smaller the emittance, the better the quality of the beam and the longer its lifetime. To obtain a small emittance, the beam is strongly focused by ring quadrupoles and bending magnets. Radio frequency cavities are used to compensate the energy lost by the electrons when emitting synchrotron radiation as described in the previous section. Four single cell cavities, operating at 500 MHz are used. The maximum electron bunches, separated by 2 ns, that can fit in the circumference of the beam is 432. Usually, about 95% of the ring circumference is filled with electron bunches.

3.4.4.1 The BL 4.2 Circular Polarised Beamline

The BL 4.2, also called the circular polarised beamline, provides radiation in the photon energy range from 5 to 1000 eV. The radiation is produced by an electromagnetic elliptical wiggler (EEW) which forces the electrons to follow an helical orbit around the EEW axis. This is achieved by the combination of a vertical magnetic field generated by permanent magnet poles and a horizontal field due to a horizontal array of electromagnets. The intensity of the vertical magnetic field can be changed by moving the permanent magnets, thus modifying the vertical displacement of the electrons while the horizontal displacement of the electrons is changed by varying the current intensity passing through the coils. This allows the insertion device to be operated as an elliptical wiggler or an elliptical undulator, thus maintaining optimum characteristics of polarisation and photon flux over a wide spectral range. The polarisation of the radiation can be switched from left-handed to right-handed by reversing the horizontal field. To cover the broad photon energy range efficiently, two independent monochromators are used, one working at normal incidence, giving radiation from 5 to 35 eV, and one working at grazing incidence, giving radiation from 30 to 1200 eV [72]. During this work, only the monochromator operating at normal incidence was used. A schematic layout of the normal incidence configuration (NIM) is shown in Figure 3.12.

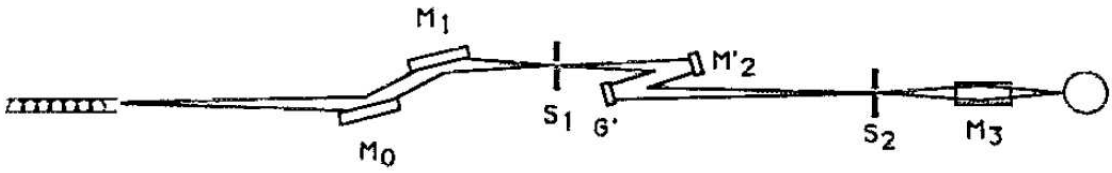

Figure 3.12: Schematic layout of the BL 4.2 in Normal Incidence Configuration [22]

The first mirror, M_0, is flat and diverts the radiation vertically. It protects the later optical components from the hard portion of the radiation spectrum. The second

mirror, M_1, has a toroidal shape and returns the radiation parallel to the orbit plane. It focusses the radiation onto the entrance slit, S_1, of the monochromator along the tangential direction and into the exit slit, S_2, of the monochromator along the radial direction. The monochromator is composed of a cylindrical mirror, M_2, that deflects the radiation vertically and a set of gratings, G, (gold or aluminium) that diffracts the radiation and focuses it onto the exit slit. The radiation is then refocussed on the sample by the toroidal mirror M_3 which diverts the radiation in the horizontal plane. The position of these mirrors can be manually adjusted to maximise the photon flux, which is measured at the back of the spectrometer by a photodiode. A set of valves are present along the beamline to protect the vacuum in the beamline and in the storage ring; they shut automatically if the pressure rises above preset limits. To allow the alignment of the spectrometer with the photon beam, the last valve is a window valve, transparent to visible radiation.

3.5 Conclusions

In this chapter a detailed description of the spectrometer used during this project has been made. The preparative methods of the reactive intermediates studied during this project have been described as well as the different modes of spectral acquisition allowed by the spectrometer. The photon sources used, a helium discharge source and synchrotron radiation source, have also been described. A brief history of synchrotron radiation source has been given and its properties presented. All the results presented in the later chapters of this thesis have been obtained at the BL 4.2 Circular Polarised Beamline at Elettra.

Chapter 4

Electronic structure and related theoretical methods

During the course of this project, reactive intermediates have been studied using different spectroscopic methods such as PE, TPE and CIS spectroscopy. Each method provides different types of information about the electronic structure of the reactive intermediate under investigation. Conventional PE spectra give information on the ionisation energies from the different atomic or molecular orbitals as well as on the nature of the orbital from which the electron was ejected. TPE spectroscopy is a threshold method where zero kinetic energy electrons are collected, thus providing a significant improvement of the resolution compared to conventional PES. TPE spectra may also show modified vibrational structure as they are influenced by autoionisation. CIS spectroscopy gives information on the resonant structure of the atomic or molecular system under investigation. The basics principles of these methods have been described in Chapter 2 while the experimental apparatus used in this work was described in Chapter 3, along with the basic principles of Synchrotron Radiation Sources. In some later chapters, the results obtained from the experimental

work are compared with results of electronic structure calculations, of the reactive molecules investigated, carried out by Dr E. Lee of the Southampton PES group. The electronic structure calculations performed in this work are based on first principles, without any considerations of the chemical characteristics of the system under investigation. This type of method is called *ab-initio* and is mostly based on Hartree-Fock theory [93, 94]. This chapter thus presents the basic principles of *ab-initio* molecular orbital calculations.

4.1 The Schrödinger equation and the Born Oppenheimer approximation

In quantum mechanics, the state of a system at a given time is described by a wavefunction Ψ. The probability of finding an electron in a volume element dV is given by the product of the wavefunction with its complex conjugate Ψ^* multiplied by the volume element dV. When integrating the probability of finding the electron over all space, the result must be unity as the particle must be somewhere. The wavefunctions which satisfy this condition are said to be normalised. In theory, the wavefunction Ψ and the energy E of a system can be obtained from the time independent Schrödinger equation [95]:

$$H\Psi = E\Psi \tag{4.1.1}$$

Ψ is also called an eigenfunction with associated eigenvalue E. H is the Hamiltonian operator and it can be expressed as [96]:

$$H = -\sum_i \frac{1}{2}\nabla_i^2 - \sum_\mu \frac{1}{2m_\mu}\nabla_\mu^2 - \sum_i \sum_\mu \frac{Z_\mu}{r_{i\mu}} + \sum_{i<j} \frac{1}{r_{ij}} + \sum_{\mu<\nu} \frac{Z_\mu Z_\nu}{R\mu\nu} \tag{4.1.2}$$

In this equation i is an electron while μ is a nuclei. j represents the other electrons with which i interacts and ν represents the other nuclei. Z_μ is the charge on nucleus μ, R is the internuclear distance, e.g. $R_{\mu\nu} = |r_\mu - r_\nu|$ and ∇_i^2 is the Laplacian operator for the i^{th} electron [96]:

$$\nabla_i^2 = \frac{\partial^2}{\partial x_i^2} + \frac{\partial^2}{\partial y_i^2} + \frac{\partial^2}{\partial z_i^2} \tag{4.1.3}$$

In equation 4.1.2, the first and second terms are operators for the kinetic energy of the electrons and nuclei respectively, the third term is the Coulomb attraction between the electrons and nuclei, the fourth term represents the interaction between electrons and the fifth term represents the nuclear repulsion. However, the Schrödinger equation can only be solved exactly for two particle systems, such as hydrogen atom-like systems: H, He^+, Li^{2+}, etc. [95].

In order to solve the Schrödinger equation for other systems, approximations must be introduced. The fundamental approximation of molecular orbital theory is the Born-Oppenheimer approximation (already seen in Chapter 2). Since nuclei are much heavier than electrons, the motion of nuclei takes place on a much longer time scale than the electronic motion [97]. The Born-Oppenheimer approximation therefore assumes that nuclear and electronic motions are separable. This results in a partitioning of the total wavefunction:

$$\Psi_{total}(r, R) = \Psi_{nucl}(R).\Psi_{elec}(r, R) \tag{4.1.4}$$

where r and R are the electron and nuclear coordinates respectively for each state of

the molecule. Within the Born Oppenheimer approximation, on an electronic time scale, the nuclear kinetic energy term of the Hamiltonian in equation 4.1.2 can be neglected and the repulsion between the nuclei can be considered to be a constant. The electronic Hamiltonian is then [98]:

$$H_{elec} = \left(-\sum_i \frac{1}{2}\nabla_i^2 - \sum_i \sum_\mu \frac{Z_\mu}{r_{i\mu}} \right) + \left(\sum_{i<j} \frac{1}{r_{ij}} \right) \tag{4.1.5}$$

$$= \sum_i h_i + \sum_{i<j} g_{ij} \tag{4.1.6}$$

where h_i is the one electron Hamiltonian that consists of the electron kinetic energy and the nuclear attraction terms and g_{ij} is the two electron operator describing the interaction between two electrons. It is possible to obtain approximate solutions to the electronic Schrödinger equation for a particular electronic state at fixed nuclei positions. By determining the total electronic energy, E_{elec}, at different nuclear coordinates, the potential energy surface can be computed . This potential energy function can then be substituted into the vibrational Schrödinger equation, and solved, thus obtaining the vibrational energies and wavefunctions. As the rest of the chapter mainly deals with the solution of the electronic Schrödinger equation, the electronic wavefunction and Hamiltonian, Ψ_{elec} and H_{elec}, will therefore be noted Ψ and H for convenience.

4.2 The Hartree-Fock method

4.2.1 Space and spin orbitals

In order to obtain solutions of the Schrödinger equation for a many electron system, another approximation must be made, known as the one-electron approximation. It assumes that each electron in the system can be considered separately and moves in an average field of all the other electrons and nuclei. With this approximation, the wavefunction Ψ of a system can be written as a product of one-electron wavefunctions, the molecular orbitals (MO) [99]:

$$\Psi(r_1, r_2, ..., r_n) = \phi_1(r_1)\phi_2(r_2)...\phi_n(r_n) \tag{4.2.1}$$

where the functions ϕ_i are called space orbitals which are functions of $r_i = \{x, y, z\}$, the position vectors of the electrons i. Spatial molecular orbitals are assumed to be orthonormal:

$$\int \phi_i^*(r)\phi_j(r)dr = \langle\phi_i|\phi_j\rangle = \delta_{ij} \tag{4.2.2}$$

In order to have a complete description of the electrons, their spin must also be specified. A function that describes both the electron's spatial distribution and its spin is a spin orbital, $\psi(i)$. It is defined as:

$$\psi(i) = \begin{cases} \phi(r_i)|\alpha\rangle \\ \phi(r_i)|\beta\rangle \end{cases} \tag{4.2.3}$$

where $|\alpha\rangle$ and $|\beta\rangle$ correspond to spin up ($\uparrow$) and spin down ($\downarrow$) respectively, with

values, $+1/2$ and $-1/2$. Two electrons can occupy the same space orbital provided that they have different spin. It follows that given a set of K spatial orbitals $\{\phi_1, ..., \phi_K\}$, one can form a set of 2K restricted spin orbitals $\{\psi_1, ..., \psi_{2K}\}$. An unrestricted spin orbital, on the other hand, will have different spatial functions for α and β spins [99, 100].

4.2.2 Slater determinant

The Pauli exclusion principle states that two electrons cannot have the same set of quantum numbers [101]. In order to satisfy this condition, the total electronic wavefunction must be antisymmetric (change sign) on interchange of two electrons. This antisymmetric condition of the wavefunction can be satisfied using Slater determinants, as interchange of any two rows leads to a change of sign of the determinant [96, 102]:

$$\Psi = \frac{1}{\sqrt{n!}} \begin{vmatrix} \psi_1(1) & \psi_2(1) & \cdots & \psi_n(1) \\ \psi_1(2) & \psi_2(2) & \cdots & \psi_n(2) \\ \vdots & \vdots & \ddots & \vdots \\ \psi_1(n) & \psi_2(n) & \cdots & \psi_n(n) \end{vmatrix} \tag{4.2.4}$$

The resulting wavefunction is antisymmetric with respect to the exchange of two electrons. The normalised single Slater determinant wavefunction can be expressed in short-hand notation using the $bra - ket$ notation:

$$|\Psi\rangle = |\psi_1 \psi_2 \dots \psi_n\rangle \tag{4.2.5}$$

4.2.3 The variational theorem

In this theorem, the energy of an approximate wavefunction can be obtained from the following expression [96]:

$$E = \frac{\langle \Psi | H | \Psi \rangle}{\langle \Psi | \Psi \rangle} \tag{4.2.6}$$

If the true wavefunction of the system is represented by Ψ_0, with associated energy E_0, the variational principle states that any trial wavefunction (Ψ_{trial}) used to define the system, will give an energy, E_{trial}, which is higher or equal to the exact energy of the ground state, E_0. In other words:

$$E_{trial} \geq E_0 \tag{4.2.7}$$

The best trial wavefunction of a system is thus the one that will give the lowest possible total energy [96]. This is found by varying the parameters that are used to construct the trial wavefunction in an attempt to minimise the total energy of the system. The choice of the initial wavefunction is therefore very important to the success of the method and must be made carefully. This theorem is crucial as it provides a measure of the quality of the trial wavefunctions. However, it must be kept in mind that this theorem is valid only for the total energy of the system and not for other properties.

4.2.4 The Hartree-Fock equations

The denominator of equation 4.2.6 is 1 for a normalised wavefunction. The electronic energy of a normalised wavefunction is therefore expressed as $E = \langle \Psi | H | \Psi \rangle$. With

the expression of the electronic Hamiltonian as seen in equation 4.1.5 and the wavefunction expressed as a Slater determinant, the Hartree-Fock energy for a closed–shell molecule is given by [103]:

$$E = 2\sum_{i} h_i + \sum_{ij}[2J_{ij} - K_{ij}] \tag{4.2.8}$$

where h_i is the one electron Hamiltonian operator as seen in equation 4.1.6, which includes the electron kinetic energy and the electron-nuclei attraction terms. J_{ij} is a Coulomb integral and K_{ij} is an exchange integral, defined as [103]:

$$J_{ij} = \int \frac{\psi_i^*(1)\psi_j^*(2)\psi_i(1)\psi_j(2)}{r_{12}} d\tau \tag{4.2.9}$$

$$K_{ij} = \int \frac{\psi_i^*(1)\psi_j^*(2)\psi_j(1)\psi_i(2)}{r_{12}} d\tau \tag{4.2.10}$$

where $d\tau$ includes both spin and space coordinates. The Coulomb and exchange operators, J_i and K_i respectively can be defined by:

$$J_i(2)\psi_j(2) = \left[\int \frac{\psi_i^*(1)\psi_i(1)}{r_{12}} dr_2\right] \psi_j(2) \tag{4.2.11}$$

$$K_i(2)\psi_j(2) = \left[\int \frac{\psi_i^*(1)\psi_j(1)}{r_{12}} dr_2\right] \psi_i(2) \tag{4.2.12}$$

where the Coulomb potential term represents the interaction of each electron with an average of all the other electrons and the exchange potential term represents the interaction of an electron with other electrons of the same spin. The exchange term has no classical analogue.

The general Hartree-Fock equation, may then be written as:

$$f(i)\psi_i = \varepsilon_i\psi_i \tag{4.2.13}$$

where f is the Fock operator, expressed as:

$$f(i) = h_i + \sum_j (J_j - K_j) \tag{4.2.14}$$

Equation 4.2.13 is called the canonical Hartree-Fock equation with Hartree-Fock molecular orbitals ψ_i and eigenvalues ε_i.

4.2.5 Koopmans' theorem and ΔSCF method

An ionisation energy is the first piece of information obtained from an experimental PE spectrum. In order to compare theory and experiment, it is crucial to also be able to calculate ionisation energies. If the ionisation process leaves the molecular geometry identical (the vertical ionisation, see section 2.1), the ionisation energy for a closed shell molecular system can be calculated using Koopmans' theorem. This theorem states that in a Hartree-Fock calculation for a closed shell system, the energy required to remove an electron from an orbital k, is equal and opposite to the energy of the orbital k [104]:

$$IE = -\varepsilon_k \tag{4.2.15}$$

where IE is the vertical ionisation energy. The negative of the eigenvalues ε_i of the canonical HF equation (equation 4.2.13) thus directly correspond to the vertical ionisation energies. This theorem, however, does not take into account the reorganisation energy (the orbital relaxation when passing from the neutral to the

cation) and the electron correlation energy on ionisation (difference in correlation energy between the molecule and the ion). As a result, the vertical ionisation energies obtained are often too high. To improve the estimation of the vertical ionisation energy, the reorganisation energy R and the electron correlation energy change on ionisation C need to be included. The true vertical ionisation energy (VIE), the Koopmans' vertical ionisation energy and R and C are related by [105]:

$$VIE = IE_{Koopmans} - R + C \tag{4.2.16}$$

Koopmans' theorem often gives a good approximation of the vertical ionisation energy (VIE) as R and C tend to cancel each other. However, this is not guaranteed and as previously mentioned, the VIEs obtained from the theorem are often too high, which implies that $R \geq C$.

It is possible to allow for the reorganisation effect by performing separate Hartree-Fock calculations on the the neutral molecule and on the cation. The VIE is then obtained by subtracting the energy of the neutral molecule from the energy of the cation. This method is called the ΔSCF method [106]. It often gives energies that are too low as it does not allow for the change of electron correlation energy between the molecule and the ion.

4.2.6 Restricted and Unrestricted Hartree-Fock methods

So far, only closed-shell molecules have been considered in the HF equations with each spatial orbitals being doubly occupied, with an α and a β electron. This configuration corresponds to a restricted wavefunction as used in the Restricted Hartree-Fock (RHF) method. However, for open shell systems, at least one spatial orbital is singly occupied. In an open shell system, the α and β electrons do not

experience the same Coulomb and exchange potentials. In this case, a wavefunction where there is no restriction on the spatial orbitals is more appropriate and a different set of spatial orbitals is used for α and β electrons. This is called an unrestricted wavefunction as used in the Unrestricted Hartree-Fock (UHF) method [100]. The total energies obtained following an UHF calculations are lower than those obtained from RHF calculations. However, one disadvantage of the UHF method is that the wavefunction is not an eigenfunction of the S^2 operator. As a result, the UHF wavefunction can contain contributions from a higher lying spin state. The expectation value of S^2 must therefore be checked at the end of the calculation to check for spin contamination. Restricted HF calculations require about 50 % less computer time and are therefore used whenever possible.

4.2.7 Hartree-Fock-Roothaan equations

Solutions of the Hartree-Fock equation are not easy to find. An alternative approach to solve the HF equation is to expand the spatial orbitals ϕ_i as a Linear Combination of Atomic Orbitals (LCAO) [107]:

$$\phi_i = \sum_{\rho=1}^{K} c_{\rho i}\chi_\rho \tag{4.2.17}$$

where χ_ρ are atomic orbitals, also called basis functions and $c_{\rho i}$ are numerical coefficients. Substitution of equation 4.2.17 into the HF equation (equation 4.2.13) gives [103]:

$$f(i)\sum_{\rho=1}^{K} c_{\rho i}\chi_\rho = \varepsilon_i \sum_{\rho=1}^{K} c_{\rho i}\chi_\rho \tag{4.2.18}$$

Multiplying each side by χ_q^* and integrating gives the Roothaan-Hartree-Fock equation:

$$\sum_{\rho} c_{\rho i} F_{\rho q} = \varepsilon_i \sum_{\rho} c_{\rho i} S_{\rho q} \tag{4.2.19}$$

which is equivalent to:

$$\sum_{\rho} c_{\rho i} . (F_{\rho q} - \varepsilon_i S_{\rho q}) = 0 \tag{4.2.20}$$

In these two equations, $F_{\rho q}$ are elements of the Fock matrix, given by:

$$F_{\rho q} = \int \chi_\rho^* f(i) \chi_q dr = \langle \chi_\rho | f(i) | \chi_q \rangle \tag{4.2.21}$$

and $S_{\rho q}$ is the overlap matrix:

$$S_{\rho q} = \int \chi_\rho^* \chi_q dr = \langle \chi_\rho | \chi_q \rangle \tag{4.2.22}$$

In matrix notation, equation 4.2.20 can be expressed as [103]:

$$FC = SC\varepsilon \qquad or \qquad C(F - \varepsilon S) \tag{4.2.23}$$

where C is the coefficient matrix and ε is the diagonal matrix of orbital energies. In equations 4.2.19 and 4.2.23, the Fock operator is $F(i) = H(i) + \sum_j (2J_j(i) - K_j(i))$ where H(i) is a one-electron operator, J_j is a Coulomb operator, K_j is an exchange operator (see equation 4.2.11 and 4.2.12) and the sum runs over all occupied spin

orbitals. Both the J and K expressions contain the wavefunctions to be calculated (see earlier). Therefore, the HF equation (equation 4.2.23 is called a pseudo-eigenvalue problem and has to be solved iteratively.

In a typical calculation, a basis set is selected and $S_{\rho q}$ integrals are calculated. A first estimation of the coefficients $c_{\rho i}$ is then made, which are used to calculate the $F_{\rho q}$ integrals. The equation:

$$det|F_{\rho q} - \varepsilon_i S_{\rho q}| = 0 \tag{4.2.24}$$

is solved and orbital energies obtained. A new set of coefficient $c_{\rho i}$ is calculated from equation 4.2.19 and the total energy calculated. The new coefficients are then used to calculate new $F_{\rho q}$ elements and the whole procedure is repeated until the total energy does not change within a pre-set tolerance. This condition of self-consistency has led to the name Hartree-Fock self-consistent field (SCF) method.

4.2.8 Basis sets

The introduction of basis sets in HF theory allows the expansion of a molecular orbital as a set of known functions. The larger the basis set, the better the representation of the MO. On the other hand, the computational time for a HF calculation for a molecule rises as M^4 where M is the number of basis functions. The choice of basis set is therefore crucial and a compromise between accuracy and cost must be made. There are two types of basis functions commonly used to describe atomic orbitals: Slater Type Orbitals (STO) and Gaussian Type Orbitals (GTO). Slater Type Orbitals have the functional form [98]:

$$\chi(r,\theta,\varphi) = NY_{l,m}(\theta,\varphi)r^{n-1}e^{-\zeta r} \tag{4.2.25}$$

where N is a normalisation constant, $Y_{l,m}$ is a spherical harmonic function and ζ is an orbital exponential factor. STOs reproduce well an atomic electronic distribution but two-electrons integrals expressed in terms of STOs can only be evaluated numerically, with great computational effort. The second type of basis function, Gaussian type orbitals (GTOs), are of the form [108]:

$$\chi(x,y,z) = Nx^a y^b z^c e^{-\zeta r^2} \tag{4.2.26}$$

where a, b and c are integers whose sum is equal to the azimuthal quantum number l. GTOs are easier to evaluate but they represent atomic orbitals less well than STOs, both at short and long distances from the nucleus. This problem can be addressed by combining several GTOs together to form functions known as contracted gaussian type orbitals (CGTO). In this way, the number of basis functions used in a calculation can be reduced, with a reasonably good representation of the MOs.

A basis set that uses a single basis function to represent each formally occupied AO in an atom is a minimal basis set. When two basis functions are used to describe each formally occupied AO, the basis set is called a double zeta basis set (DZ). In the same way, triple zeta basis sets (TZ) and so on, can be constructed.

An alternative approach consists in using a split valence basis set, which uses a minimal set of basis functions to describe the core electrons and a basis set of higher quality to describe valence electrons. This method offers a compromise between time economy and flexibility [107]. The notation used for split valence Gaussian basis sets is of the form K-LMG, e.g. 3-21G. In this basis set, three Gaussian functions are used to describe the core orbitals and the valence orbitals are each represented with two

contracted Gaussians and one diffuse Gaussian [109].

This type of basis set, however, does not take into account the anisotropic charge distribution of some molecules (the charge distribution of an atom in a molecule differs from that of an isolated atom). To account for this effect, polarisation functions are sometimes introduced into the basis set. These usually have higher angular momentum than that of the valence orbitals of the atom. The use of these functions is represented with an (*) in the basis set. As an example, the basis set 3-21G* indicates the use of polarisation function on the heavy (non-hydrogen) atoms, whereas 3-21G** indicates the use of polarisation functions on both the heavy atoms and hydrogen atom [107].

For anions or molecules containing lone pairs, the outer part of the wavefunction also needs to be accurately described. In order to provide a better description at longer distances from the nucleus, a diffuse function can be added to the basis set, which has a lower or equal angular momentum to that of the valence functions. Diffuse functions are indicated by a (+) in the basis set, e.g. 3-21+G is a basis set that contains an additional set of diffuse Gaussian functions. Again, a basis set with (++) indicates that the diffuse functions are included for both the hydrogen and the heavier atoms.

Another type of basis set has been introduced by Dunning [110], made of contracted GTOs. This type of basis set has been recommended by Dunning for use in calculations which include electron correlation and have therefore been called correlation consistent (cc) basis sets. They are labelled as cc-VXZ where X reflects the number of basis functions used for each AO, e.g. cc-VDZ, cc-VTZ, etc. Correlation consistent basis sets can also be used with polarisation functions, indicated with a prefix "p", e.g. cc-pVDZ. In a similar way, the use of diffuse functions in these basis sets is written as aug-cc-pVDZ. In the calculations carried out during this work on CF_2, Dunning's basis sets were mainly used, as will be seen in Chapter 7.

4.3 Electron correlation

In HF theory, electrons are assumed to be moving in a mean potential of the other electrons given by the Coulomb and exchange potential terms. In reality, however, each electron interacts instantaneously with all the other electrons. This instantaneous electron-electron interaction is not accounted for in the HF method, and gives rise to an electron correlation error. The electron correlation energy is defined as the difference in energy between the HF energy, obtained with a very large basis set, i.e. at the HF limit, and the exact non-relativistic energy. There are two types of electron correlation, dynamical and non dynamical electron correlation [111]. Dynamical electron correlation arises from an overestimation of short range electron interaction in HF wavefunctions. In contrast, non-dynamical correlation is a long range effect that is particularly important at the dissociation limit and is due to the inadequacy of a single Slater determinant wavefunction to describe an electronic state that is influenced by other electronic configurations. Several methods have been developed to include these correlation effects in *ab-initio* calculations. In the present work, the Multi Reference Configuration Interaction (MRCI) method, the Multi Configuration Self Consistent Field (MCSCF) approach and the Coupled Cluster (CC) method have been used to account for electron correlation (see Chapter 7) and will therefore be presented in the following paragraphs.

4.3.1 Configuration Interaction (CI)

The HF method uses a single Slater determinant to represent a wavefunction. One of the methods used to improve the HF wavefunction, consists in using a linear combination of determinants [107]:

$$\Psi = c_0\Psi_{HF} + c_1\Psi_1 + c_2\Psi_2 + ... \tag{4.3.1}$$

where Ψ_{HF} is the single determinantal wavefunction obtained from HF theory while Ψ_1, Ψ_2, etc. are determinants that represent configurations obtained by replacing one or more of the occupied spin orbitals in Ψ_{HF} by a unoccupied spin orbital (virtual orbital). The coefficients c reflect the weight of each determinant and are determined via the requirement to minimise the energy of the system. For most systems, the HF determinant dominates in the linear combination, i.e. c_0 is usually close to 1. This method is called Configuration Interaction (CI) and is a variational method [112]. A complete basis set (CBS) full CI is the most complete method that accounts for dynamical electron correlation as it considers all the excitations, i.e. all the possible ways to permute the N electrons and K orbitals of a system. However, it is not practical to consider all possibilities as the total number of permutations of electrons and orbitals can become extremely large and hence the number of determinants in the CI expansion is very large. Usually, only a few levels of excitation are considered. For example, in the configuration interaction singles (CIS) method, only wavefunctions that differ from the HF wavefunction by a single spin orbital are considered. Configuration interaction doubles, CID, is the next level of calculation which involves double substitutions. Even at CIS or CID levels, the number of excited states generated can be very large. However, quadruply excited determinants can be important in the determination of the correlation energy. To avoid performing a calculation that includes single, double, triple and quadrupole excitations (CISDTQ), a formula known as the Davidson correction can be used to estimate the contribution of quadruply excited determinants, ΔE_Q, to the correlation energy in CID calculations [113]:

$$\Delta E_Q = (1 - c_0^2)(E_{CID} - E_{SCF}) \tag{4.3.2}$$

where E_{CID} is the ground state energy energy in a CID calculation and E_{SCF} is the ground state energy associated with Ψ_{HF} obtained in a HF-SCF calculation.

4.3.2 Multi Configuration Self Consistent Field (MCSCF) approach

Non dynamical electron correlation can be dealt with using the Multi Configuration Self Consistent Field (MCSCF) approach. This approach differs from the CI method in that the MOs used to construct the determinants of equation 4.3.1 are optimised as well as the coefficients of the determinants. As a result, the number of variables to be optimised is often larger than for the CI method [114]. The MCSCF method is harder to make converge than the HF method and is likely to converge to a solution that is not a minimum. MCSCF calculations are very demanding in computer resources and much harder to carry out than HF calculations. For this reason, slightly different techniques have been developed to enable MCSCF-type calculations to be performed, the most widely used of these methods is the Complete Active Space Self Consistent Field (CASSCF) method. In this method the MOs are divided into active and inactive spaces [115]. The inactive orbitals are either full or empty while the active orbitals are composed of both occupied and unoccupied MOs. The active orbitals are then used to perform a full CI, thus reducing the number of orbitals to be considered in the calculation [98]. The choice of the MOs to be included in the active space is made manually, depending on the accuracy required and the computational cost. However, even for a reasonably small active space, the CASSCF procedure can become extremely demanding in terms of computing resources. A variation of this procedure was therefore developed, called the Restricted Active Space Self Consistent Field (RCASSCF) method, which restricts the excitation number allowed by further dividing the active MOs into three sections. One space consists of doubly occupied MOs, the second space has both occupied and unoccupied MOs while the third space

consists of empty MOs. Configurations are then generated by a full CI in the second space, which has smaller number of MOs than the classical CASSCF method, and single or doubles CI are performed in the other spaces.

4.3.3 Multi Reference Configuration Interaction (MRCI) method

This method is similar to the CI method except that an MCSCF wavefunction is used as a reference wavefunction instead of the HF wavefunction. The MCSCF reference wavefunction is harder to construct than the HF wavefunction but the improvement of the virtual orbitals can make the CI calculation converge more rapidly. As with single reference CI, MRCI can be truncated to include only single and double excitations (MRCISD). MRCISD calculations can give better results than CI calculations of similar size [96].

4.3.4 Coupled Cluster (CC) method

In the Coupled Cluster (CC) method, the full CI wavefunction is given by [98]:

$$\Psi_{CC} = e^{T}\Psi_0 \tag{4.3.3}$$

where T is the cluster operator and is defined as:

$$T = T_1 + T_2 + T_3 + ... + T_n \tag{4.3.4}$$

where n is the total number of electrons and the T_i operators generate all i^{th} excited

Slater determinants:

$$T_i = \sum_{i}^{occ} \sum_{a}^{vir} t_i^a \Psi_i^a \tag{4.3.5}$$

where t are amplitudes. If all levels of excitations are included, a wavefunction computed at the CC level would be exact. However, this is possible only with small systems. In practice, the cluster operator must be truncated at some excitation level. For example, CCSD denotes a CC method with only single and double excitations. It uses $T = T_1 + T_2$. CCSD involves a computational effort proportional to M^6 while the next level of computational, which involves triple excitations (CCSDT), is much more costly (it scales as M^8) [116]. Alternatively, the triple excitation contributions can be evaluated via another method (e.g. perturbation theory) and added to the CCSD amplitudes. This hybrid method is denoted as CCSD(T). It is very robust and widely used [96].

In the CF_2 calculations described in Chapter 6, RCCSD(T) and CASSCF/MRCI methods are used. The RCCSD(T) method is a Restricted Spin Coupled Cluster method which included single and double excitations plus contribution from triple excitations evaluated via perturbation theory, as explained just above. The CASSCF/MRCI method consists in a CASSCF calculation followed by a MRCI calculation. In this way, both non-dynamic and dynamic electron correlation are accounted for.

4.4 Determination of minimum energy geometries and harmonic vibrational frequencies

In order to determine the minimum energy geometry of a molecule and its harmonic vibrational frequencies, one must remember that the total energy of a molecule in a particular electronic state as a function of the internuclear coordinates is a multidimensional potential energy surface. Minima on these potential energy surfaces can be characterised by their first and second derivatives [96]. The first derivatives, with respect to each of the variables, form a vector called the gradient and the negative of these first derivatives represent the forces acting on the molecule. The second derivatives form a matrix called the Hessian and represent the force constants [117]. The minimum energy geometry of a molecule will have a zero first derivative of the energy for all n internal coordinates. When looking at a global minimum, all the second derivatives are positive. However, a saddle point in the multidimensional potential energy function occurs if one of the second derivatives is negative. The minimum energy geometry of a molecule can therefore be found by looking at the derivatives of the energy via the analytic gradient method [118]. In this method an initial guess of the geometry is formulated as a first step, and the HF (or higher level) energy is calculated at this initial geometry. The energy is then calculated at positive and negative displacement for each of the coordinates. The gradient vector, $g = \partial E/\partial r$, is calculated at each geometry, and gives an indication of the direction to follow in the displacement of the coordinates in order to reach the minimum energy. This process is repeated until the energy obtained from the electronic structure calculation converges toward equilibrium. The Hessian matrix can also be evaluated when necessary from numerical differentiation of the gradient vector. The force constants at the minimum energy geometry are thus obtained and are proportional to the square of the vibrational frequencies of the molecule in the harmonic oscillator model.

4.5 The *ab-initio*/anharmonic FC method for triatomics

Ab-initio molecular orbital calculations can be combined with FC simulations to compute simulated PE spectra of non-linear triatomics. However, care must be taken with non linear polyatomic molecules as there may be a change in geometry, force constant and/or symmetry between the two electronic states upon transition. As a result, mode mixing (Duschinsky effect [119]) needs to be considered between the different vibrational modes when evaluating FCFs. A model to simulate vibrationally resolved photoelectron spectra using a harmonic oscillator was first developed and used in the Southampton PES group that included allowance for the Duschinsky effect [120]. However, it was found that the agreement between simulated and observed vibrational intensity patterns deteriorated in the region of higher vibrational quantum numbers due to anharmonicity. For this purpose, a multidimensional anharmonic FCF code has been recently developed that provides better agreement with vibrationally resolved experimental spectra [121].

Anharmonic *ab-initio*/FCF calculations on non-linear triatomics involve three steps, which will be briefly presented here. The first step consists of the determination of the potential energy surfaces of the two electronic states involved in the transition, which is determined by fitting the following polynomial to an appropriate number of *ab-initio* single energy points, around the minimum energy geometry:

$$V = \sum c_{ij}(S_1)^i(S_2)^j \tag{4.5.1}$$

For a C_{2v} molecule, $S_1 = \Delta r = (\Delta r_1 + \Delta r_2)/2$, $S_2 = (\Delta\theta) + \alpha(\Delta\theta)^2 + \beta(\Delta\theta)^3$ and c_{ij} are coefficients [122]. A least square fitting procedure is employed to obtain the c_{ij}, α and β values from the computed single point energies

In the second step, the anharmonic vibrational wavefunctions of the m-th and n-th electronic states involved in the transition are determined. A simple way to account for anharmonicity consists in expressing the anharmonic wavefunctions as linear combinations of the products of harmonic vibrational wavefunctions, $\phi(\nu_i)$. The anharmonic vibrational wavefunctions is thus expressed as [121]:

$$|m\rangle = \sum c_{m,v}\phi(\nu_1)\phi(\nu_2)\phi(\nu_3) \tag{4.5.2}$$

where $c_{m,v}$ are the expansion coefficients. The expansion coefficients, $c_{m,v}$, are obtained by diagonalising the rovibrational Watson's Hamiltonian [123], which includes the fitted electronic PEF, V, using the harmonic basis set $\phi(\nu_i)$.

Finally, the anharmonic FCF between the m and n anharmonic vibrational states in an electronic transition is expressed as

$$FCF(m,n) = \langle m|n\rangle^2 = \left(\sum_{v',v''} c_{m,v'}c_{n,v''}\langle\nu_1',\nu_2',\nu_3'|\nu_1'',\nu_2'',\nu_3''\rangle\right)^2 \tag{4.5.3}$$

where the primed and double-primed quantities correspond to those of the final state and the initial state, respectively. The expansion coefficients $c_{m,v'}$, and $c_{n,v''}$ are determined as described above, and $\langle\nu_1',\nu_2',\nu_3'|\nu_1'',\nu_2'',\nu_3''\rangle$ is the overlap integral of the corresponding harmonic functions, which can be evaluated at the start of the calculation. Since the Duschinsky rotation matrix is included in this model, the anharmonic FCFs obtained in this way have incorporated the effect of anharmonicity and Duschinsky rotation.

FCFs are very sensitive to the relative geometries of the electronic states involved in an electronic transition. Thus, if the equilibrium geometry of one of the two electronic states (usually the ground state) is known from independent experiments (e.g. from a microwave spectroscopic study), the geometry of the other state can be obtained by adjusting its geometrical parameters systematically until the simulated

spectrum matches the experimental spectrum. This method is called iterative FC analysis (IFCA) [121]. In this procedure, the shapes of the *ab-initio* PEFs of the two electronic states are kept unchanged.

The PE spectra simulated from the FC analysis can then be used to assist or confirm assignment of vibrational features of the experimental PE and TPE spectra, as will be seen for the work on CF_2 in Chapter 7. In the case of diatomic molecules, the ionic vibrational constants and bond length change on ionisation can be obtained directly from the experimental spectra, as was presented in Chapter 2 and will be explained in more detail in the work of IF in Chapter 5.

4.6 Conclusion

In this chapter, the basic principles of the HF theory have been presented as well as different ways to account for electron correlation energy. Different types of basis sets were also introduced. From the electronic structure calculations, the minimum energy geometry of a molecule or ion can be obtained, as described in section 4.4 and FCFs can be determined, thus allowing PE spectral simulation. These methods have been used by Dr E. Lee from the Southampton PES group to simulate PE spectra of CF_2, thus allowing comparison with experimental PE and TPE spectra, as will be described in Chapter 7.

Chapter 5

A study of iodine atoms and IF by photoelectron spectroscopy (PES) and threshold photoelectron spectroscopy (TPES)

This chapter reports a study of I and IF by photoelectron spectroscopy (PES) and threshold photoelectron spectroscopy (TPES). Iodine is a reactive open-shell atom. Investigation of its photoionisation behaviour and measurement of its partial photoionisation cross sections should provide valuable information that will allow comparison between theory and experiment. Also, a study of IF with these methods will allow its valence ionisation energies and low-lying ionic state spectroscopic constants to be established. This chapter starts, in Section 5.1, with a brief review of the previous work carried out on IF and of the two methods used in this work (PES and TPES). Section 5.2 presents the experimental methods and conditions used, followed, in Section 5.3, by the results obtained from the PE study of I and IF. The

TPE study is then described and the results obtained from the two methods are finally compared. A summary of the PE and TPE work on I and IF is made in Section 5.4

5.1 Introduction

IF is a short-lived molecule in the gas phase that typically has a lifetime of several milliseconds in a low pressure flowing gas system. It has been shown to be a promising candidate for a visible chemical laser via energy transfer to its vibrationally excited ground state, IF($X^1\Sigma^+$), from $O_2(a^1\Delta_g)$ to produce IF($B^3\Pi$) [124–126]. Although an initial investigation of IF with PES has been made [64], the higher resolution threshold photoelectron spectrum has not yet been obtained. PES and TPES are complementary methods of studying the electronic structure and spectroscopy of molecular ions. The PE and TPE spectra of the stable halogens and interhalogens F_2, Cl_2, Br_2, ICl, and IBr have been recorded previously [127–130]. In these cases, the TPE spectra are notable in that extra vibrational structure is observed in the Franck–Condon gaps between the PE bands. Also, in the TPE spectra the resolution is higher than that in PES. In TPES, the resolution is limited by the resolution of the scanned photon source (typically 1–3 meV for a synchrotron source), combined with the low energy (threshold) electrons selected (typically below 3 meV). On the other hand, the resolution in UV PES (typically 40 meV), is governed by the geometrical characteristics of the energy analyser used, as was seen in Chapter 3. In the initial study of IF by PES, IF was produced from the rapid gas–phase reaction F + ICl → IF + Cl [64]. However, because of the minor reaction channel F + ICl → FCl + I, I atoms were also observed in the spectra and some of the I atom features overlapped with some of the vibrational components in the first two IF PE bands. For these overlapped bands, the relative contributions of I and IF were not established.

The main objective of this work was therefore to determine these contributions. In this way, reliable vibrational envelopes of the PE bands of IF and the relative intensities of I atom bands will be obtained at the photon energy used. The F + CH_2I_2 reaction was studied at different reactant times to obtain PE spectra with different partial pressures of I and IF in the photoionisation region. These spectra were then used to obtain "pure" PE spectra of both I and IF. Once the PE spectra had been obtained, TPE spectra were then recorded.

5.2 Experimental section

The experiments reported here were undertaken on the Circularly Polarised Beamline (4.2R, Polar) at the Elettra synchrotron radiation source using a photoelectron spectrometer that was specifically designed to study reactive intermediates as was seen in Chapter 3 and in references [16, 17, 49]. PE spectra were recorded as described in Chapter 3, and the same procedures were used to normalise the spectra for the photon flux and the transmission function of the spectrometer [50]. Most spectra were recorded at the angle of $54°44'$ with respect to the direction of polarisation of the photon beam. The rotation mechanism of the spectrometer is as explained in Chapter 3. At the angle of $54°44'$, the measured PE intensity is proportional to the photoionisation cross section and is independent of the angular distribution parameter β, as explained in Chapter 2. The resolution of the PE spectra is $\sim$35 meV. This is determined mainly by the slit widths and the mean radius of the hemispherical analyser used. Because of the DAC card used to supply the voltages to the lenses of the spectrometer, excellent linearity and reproducibility of the ionisation energy scale was obtained in PE spectra. This allowed band maxima to be measured to within 1 meV (see later).

TPES differs from PES in that the energy of the detected electrons is kept low

(typically ≤2 meV) while the photon energy is scanned. A threshold photoelectron signal will be obtained each time the photon energy is equal to the ionisation energy to an ionic state. While the observed intensities of vibrational components in a conventional PE spectrum are almost always governed by Franck–Condon factors (FCFs) between the initial neutral and final ionic state (see Chapter 2), those observed by TPES are often dominated by autoionisation [131, 132]. This is primarily due to the high density of Rydberg states which are parts of series that converge on higher rovibronic ionic levels, some of which can lie just above a selected ionisation threshold. These can autoionise and produce electrons of low kinetic energy that are detected in TPES. As described in Chapter 2, the autoionisation process can enable the observation of ionic states that cannot be observed by direct ionisation from the ground state in conventional PES or can allow extra vibrational components of an ionic state to be observed. In this work, I atoms and IF were produced by the rapid reaction of F atoms with CH_2I_2 [65]:

Primary reaction: $$F + CH_2I_2 \rightarrow CH_2I + IF$$

Subsequent reactions: $$F + CH_2I \rightarrow [CH_2IF]^{\dagger} \rightarrow CH_2F + I$$
$$\rightarrow CHF + HI$$

$$CH_2I + CH_2I \rightarrow [CH_2ICH_2I]^{\dagger} \rightarrow HI + CH_2CHI$$

In an earlier PES study of the F + CH_2I_2 reaction by the Southampton group [18], the first band of CH_2I was observed at low mixing distances (∼0.3 cm), with vertical ionisation energy (VIE) at 8.52 eV. At longer mixing distances (∼3–4 cm) (which corresponds to the conditions used in the present work), only bands from I, IF, HI, HF, CH_2CHI (vinyl iodide), and CF (weakly) were observed. It is clear that the reactive intermediates CH_2F and CHF in the above reaction sequence are converted to CF + HF at the relatively long reaction times used in this work.

A high yield of fluorine atoms was produced by flowing 5 % F_2 in helium through a

microwave discharge at 2.45 GHz in the side arm of a glass inlet system, as described previously [16, 17, 49] and in Chapter 3. This system also has an inner inlet system that is used to transport the target reaction molecule (in this case CH_2I_2) to the reaction region.

Preliminary experiments were carried out in Southampton to determine the optimum pressures and reactant mixing distances above the photon beam that maximise the intensities of the I and IF features in the PE spectra. The optimum partial pressures were: $\Delta p(CH_2I_2) = 1 \times 10^{-6}$, $\Delta p(F_2/He) = 5 \times 10^{-6}$, and $\Delta p(Ar) = 3 \times 10^{-7}$ mbar. These partial pressures were determined using an ionisation gauge connected to the main vacuum chamber and were measured with respect to the background pressure in the vacuum chamber (1×10^{-7} mbar), as seen in Chapter 3. The argon gas was introduced to allow optimisation of the electrode voltages when TPE spectra were recorded. The most intense spectra of the I bands were obtained at a mixing distance of about 4 cm from the photon beam, while the IF bands were optimised at a shorter mixing distance of about 3 cm.

5.3 Results and discussion

The interhalogen IF has the electronic configuration $-12\sigma^2 6\pi^4 13\sigma^2 7\pi^4$. In the initial study of this reactive intermediate with PES using He $I(\alpha)$ radiation, where IF was prepared using the F + ICl reaction, the first two bands were vibrationally resolved [64]. They correspond to ionisation to the $^2\Pi_{3/2}$ and $^2\Pi_{1/2}$ ionic states at VIEs of 10.62 and 11.32 eV, respectively, arising from the $(7\pi)^{-1}$ ionisation. The $(13\sigma)^{-1}$ and $(6\pi)^{-1}$ ionisations gave rise to broad bands at VIEs of 15.22 and 15.94 eV, respectively, which showed no vibrational structure.

The ground-state electronic configuration of atomic iodine is $- - -5s^2 5p^5$. This gives

rise to two states, $^2P_{3/2}$ and $^2P_{1/2}$, separated by 0.94 eV with the $^2P_{3/2}$ state lower [133]. The $^2P_{1/2}$ state is effectively not populated under equilibrium conditions at room temperature. I atoms were first observed by PES by de Leeuw and co-workers, where a partial photoelectron spectrum was obtained [133]. The $(5p)^{-1}$ ionisation from the $^2P_{3/2}$ ground state is expected to give $^3P_2$, $^3P_1$, $^3P_0$, $^1D_2$, and $^1S_0$ ionic states, with the following ionisation energies determined from photoabsorption measurements [60, 61, 74]:

$$\begin{aligned} I^+(^3P_2) &\leftarrow I(^2P_{3/2}) \qquad 10.451eV \\ I^+(^3P_0) &\leftarrow I(^2P_{3/2}) \qquad 11.251eV \\ I^+(^3P_1) &\leftarrow I(^2P_{3/2}) \qquad 11.330eV \\ I^+(^3D_2) &\leftarrow I(^2P_{3/2}) \qquad 12.153eV \\ I^+(^1S_0) &\leftarrow I(^2P_{3/2}) \qquad 14.109eV \end{aligned} \tag{5.3.1}$$

The $(5s)^{-1}$ ionisations, which were not studied in details in this work, give $^3P_{2,1,0}$ and $^1P_1$ ionic states, respectively, with ionisation energies 20.61, 20.89, 21.66, and 23.35 eV, respectively [74].

5.3.1 Photoelectron spectra

Figures 5.1 and 5.2 show PE spectra recorded for the F + CH_2I_2 reaction, in the region from 10.3 to 12.3 eV with mixing distances of 4 and 3 cm, respectively. The selected photon energy, using the synchrotron source, was 21.22 eV, and the spectra were recorded at the angle of $\theta = 54°44'$. In the spectrum recorded at 4 cm mixing distance (Figure 5.1), the intensities of the atomic I spectral features compared to those of the IF features are higher than in the spectrum recorded at 3 cm mixing

distance (Figure 5.2).

As shown in these spectra, two groups of bands were observed in the regions 10.35–10.80 and 11.25–11.55 eV, plus a single band at 12.15 eV. To assist the analysis and discussion, these were labeled (a'-e'), (a-d), and a", as shown in the Figures.

The assignment of the bands shown in Figures 5.1 and 5.2 is as reported in the initial study of IF using He I photoelectron spectroscopy, where the IF was produced from the reaction F + ICl [64]. In brief, bands (b') to (e') are vibrational components of the first IF band, bands (a) to (d) are vibrational components of the second IF band, and I atom ionisations are as labelled in Figure 5.1. However, for some of the observed features, such as features (a) and (b), the relative contribution from I and IF is not known. It is also not known whether IF contributes to band (a').

The spectra shown in Figures 5.1 and 5.2 were normalised in intensity to the pure IF vibrational feature (c'). Gaussian fitting was used to obtain the relative areas of all the bands. This approach was also used to analyse the many PE spectra recorded ($\sim$20) with different I-to-IF ratios. Spectra with different I/IF ratios were obtained by recording PE spectra at different mixing distances and at selected atomic iodine resonance photon energies. The resonance positions to excited atomic Rydberg states were obtained by recording constant ionic state (CIS) spectra on the first and fourth PE bands of I atoms (see Chapter 6). It was also possible to obtain different I/IF ratios at the same mixing distance by recording PE spectra at different times (e.g. when the reaction had just been started and after the reaction had been running for some time). This was possible since the I atom intensity decreased with respect to IF over the time scale of several hours, probably because of the change in efficiency in wall recombination of I atoms with time. Many spectra with different I–to–IF ratios were recorded during the several days that the reaction was running on the beamline.

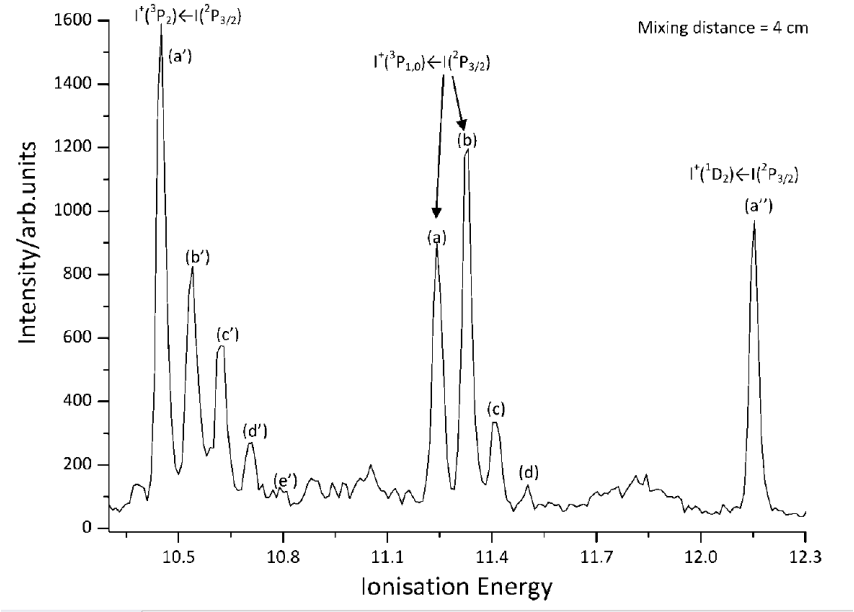

Figure 5.1: PE spectrum recorded at $h\nu = 21.22$ eV at $54°44'$ and 4 cm mixing distance from the photon beam showing a "high" I to IF ratio

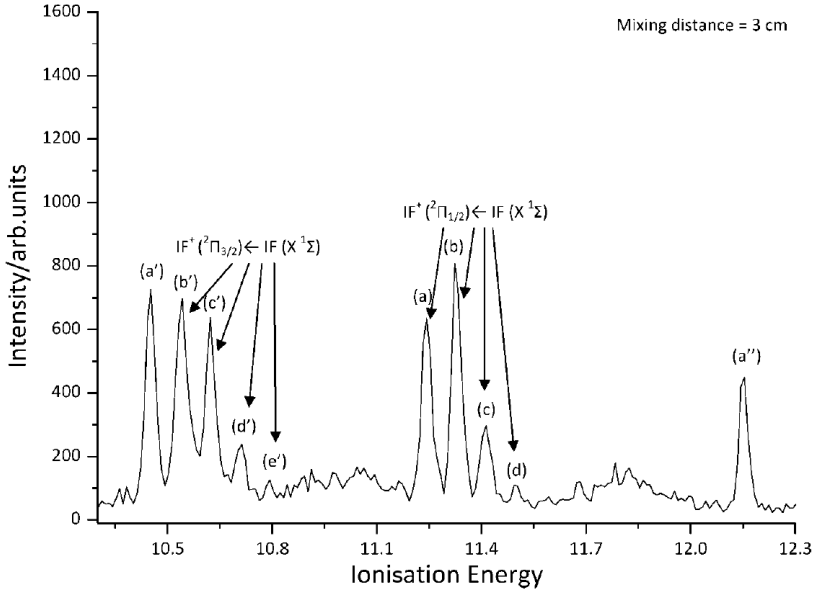

Figure 5.2: PE spectrum recorded at $h\nu = 21.22$ eV at $54°44'$ and 3 cm mixing distance from the photon beam showing a "low" I to IF ratio

Once each PE spectrum had been normalised in intensity to band (c') (an IF vibrational component), spectra were selected in pairs for analysis: one spectrum with "high" I atom intensity and another spectrum with "low" I atom intensity. The procedure used can be illustrated by considering Figures 5.1 and 5.2. The band intensity ratio was calculated for each band by dividing the area of each band in Figure 5.1 by the area of the corresponding band in Figure 5.2. This is expected to be equal to 1.0 for a pure IF band. Since band (a") corresponds to the pure $I^+(^1D_2) \leftarrow I(^2P_{3/2})$ ionisation, the ratio calculated for this band gives the increase (or decrease) of the I atoms between the two spectra. Figure 5.3 shows the ratio for the observed bands calculated by dividing the areas obtained in the spectrum in Figure 5.1 with respect to the areas obtained in the spectrum in Figure 5.2 after the intensity of band (c') was made the same in both spectra. The error associated with each ratio is also reported. All the ratios obtained from analysis of all the PE spectra recorded give a pattern similar to that shown in Figure 5.3. First, it can be seen that, as expected, bands (b'), (c'), (d'), and (c) are pure IF bands since their ratio is equal to 1.0 within the error associated with the measurement. Band (a') has the same ratio as the $I^+(^1D_2) \leftarrow I(^2P_{3/2})$ band, band (a"), indicating that (a') is a pure I band or that the contribution of IF to band (a') is so small that it cannot be determined with this procedure. The ratios for bands (a) and (b) are bigger than 1.0 (when the experimental errors for the ratios of bands (a) and (b) are considered) but smaller than that obtained for a pure I band, band (a"). Therefore, bands (a) and (b) have contributions from both I and IF, as expected because of known I atom ionisations in these positions. It can be seen that band (b) has a bigger contribution of I with respect to band (a).

Taking band (a) as an example, which contains contributions from I and IF, and assuming the I atom ratio in Figure 5.3 for band (a) is the same as that of the pure I atom band (a") (or band (a')), it is possible to separate the contribution of I and IF in band (a). The same procedure can be used for band (b). It is assumed that $Area_1$

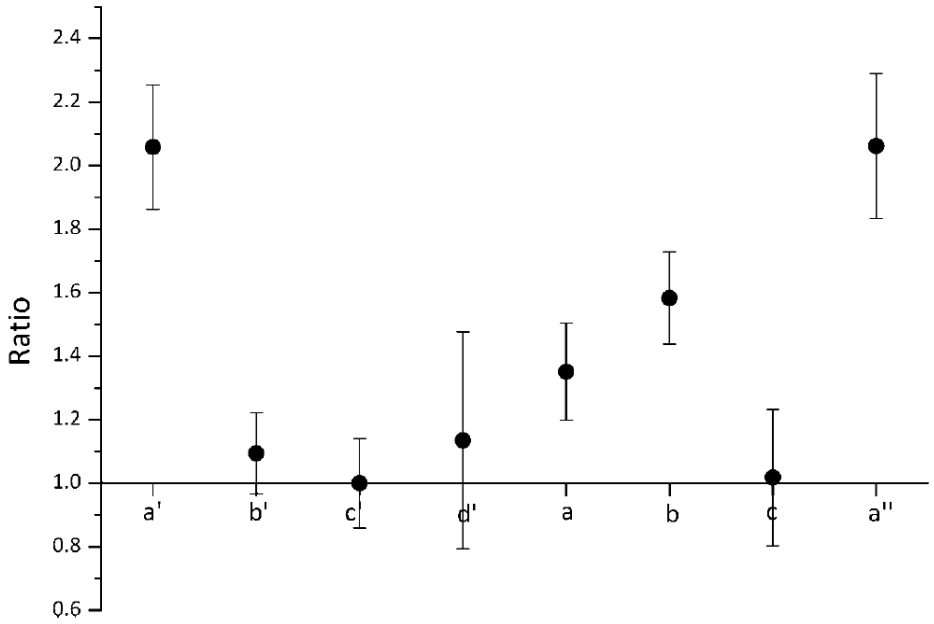

Figure 5.3: Band intensity ratio calculated by dividing the area of the more intense ionic bands in Figure 5.1 by the area of the same bands in Figure 5.2 after the intensity of band (c') was made the same in both spectra (see text).

and $Area_2$ are the areas of band (a) in Figures 5.1 and 5.2 (after normalising the two spectra to ensure areas of band (c) are the same), $Area_{IF}$ is the area of the IF contribution, and I_1 and I_2 are the I contributions to band (a) in the two spectra. The ratio I_1/I_2 is then set equal to the ratio of band (a") or alternatively of band (a') as both are pure I atom bands. Then, using

$$\begin{aligned} Area_1 &= I_1 + Area_{IF} \\ Area_2 &= I_2 + Area_{IF} \\ Ratio = I_1/I_2 &= Ratio(a') \\ I_2 &= \frac{Area_1 - Area_2}{(Ratio - 1)} \\ I_1 &= I_2 \times Ratio \end{aligned} \tag{5.3.2}$$

knowing Ratio, $Area_1$ and $Area_2$, I_1 and I_2 can be calculated, and hence $Area_{IF}$ can be calculated. The same calculation can be applied to band (b), allowing the determination in each spectrum of the relative intensities of the four I atom bands (at positions of bands a', a, b, and a") as well as the relative intensities of the IF vibrational bands. The same procedure was used for any two PE spectra with different I–to–IF ratios from all the PE spectra recorded. All the relative intensities so obtained were averaged, and the results are shown in Figures 5.4, 5.5, and 5.6.

The relative intensities of iodine atom bands obtained in this work, including that measured for the $I^+(^1S_0) \leftarrow I(^2P_{3/2})(5p)^{-1}$ ionisation at 14.109 eV not shown in Figures 5.1 and 5.2, can be compared with those obtained in refs [134] and [135] by PES with a He $I\alpha$ (21.217 eV) photon source, as reported in Table 5.1. The results are quite similar within experimental error to the results obtained in refs [134] and [135] with the exception of the $I^+(^1D_2) \leftarrow I(^2P_{3/2})$ ionisation. This has a much lower relative intensity in this work (0.58 ± 0.03 compared to the He $I(\alpha)$ value in ref [134] of 0.80 ± 0.04) but is closer to the calculated value of refs [134] and [135] (0.57) using an intermediate coupling model. This difference can be partly explained by considering the asymmetry parameter β for each ionisation. The experimental work in refs [134] and [135] was carried out with unpolarised He $I(\alpha)$ radiation, while the present results were obtained with linearly polarised synchrotron radiation (P $>$ 0.99), at the detection angle (54° 44") where the measured intensity is proportional

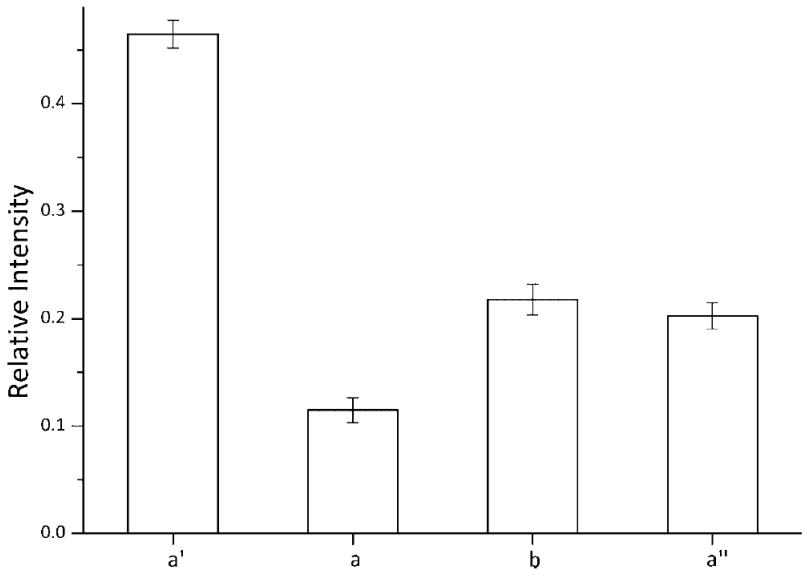

Figure 5.4: Relative intensities of the four iodine atom components, derived using the procedure described in the text.

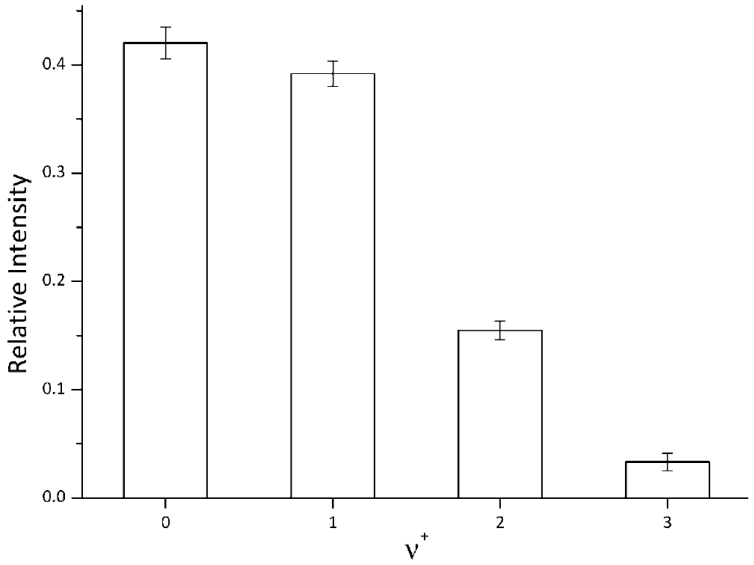

Figure 5.5: Relative intensities obtained for the IF components in the $IF^{+}(X^{2}\Pi_{3/2}) \leftarrow IF(X^{1}\Sigma)$ band.

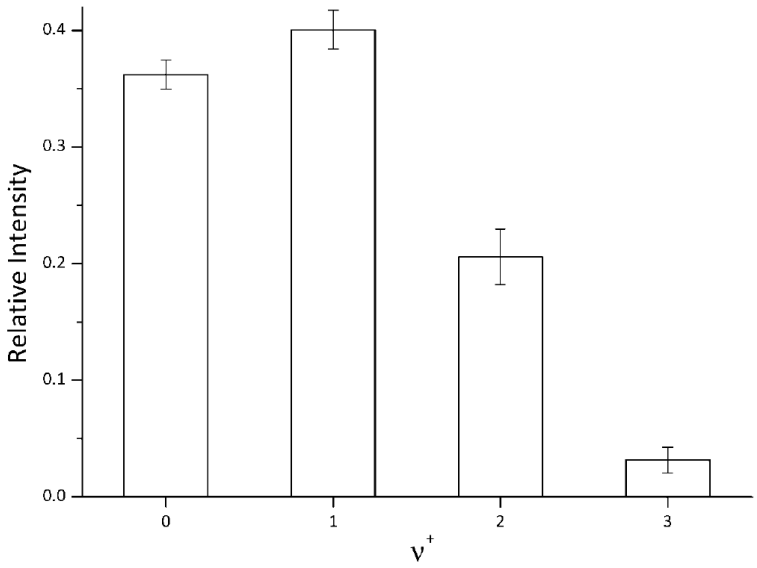

Figure 5.6: Relative intensities obtained for the IF components in the $IF^+(X^2\Pi_{1/2}) \leftarrow IF(X^1\Sigma)$ band.

to the total photoionisation cross section and independent of β. Figure 5.7 shows the asymmetry parameter for the bands measured in the present work, and it can be clearly seen that the value of β is higher for the $I^+(^1D_2) \leftarrow I(^2P_{3/2})$ band (a") than for the $I^+(^3P_2) \leftarrow I(^2P_{3/2})$ band (a'). Relative cross section measurements depending on β would therefore give a higher relative intensity for $I^+(^1D_2) \leftarrow I(^2P_{3/2})$ ionisation with respect to the present work. Indeed, the intensity of a band in a spectrum recorded with an unpolarised photon source and at an angle between the direction of the photoelectrons and the unpolarised radiation of 90°, as used in refs [134] and [135], is proportional to the total photoionisation cross section multiplied by a factor equal to $(1 + \beta/4)$ [1]. Assuming $\beta = 1.01$ for band (a') (the $I^+(^3P_2) \leftarrow I(^2P_{3/2})$ ionisation) and 1.63 for band (a") (the $I^+(^1D_2) \leftarrow I(^2P_{3/2})$ ionisation), then correcting for angular distribution, the relative intensity of bands (a') to (a") changes from 0.80 (value from ref [134]) to 0.71. This value compares with 0.58 ± 0.03 derived in this work and 0.57 obtained using an intermediate coupling model.

$I^+ \leftarrow I(^3P_{3/2})$ bands ionic state	ref [135][a]	ref [134][b]	this work at $h\nu = 21.22$eV
$^3P_2$	1.00 (1.00)	1.00 (1.00)	1.00 ± 0.03
$^3P_1$	0.34 (0.31)	0.39 ± 0.05 (0.31)	0.47 ± 0.03
$^3P_0$	0.17 (0.15)	0.18 ± 0.03 (0.15)	0.25 ± 0.02
$^1D_2$	0.79 (0.57)	0.80 ± 0.04 (0.57)	0.58 ± 0.03
$^1S_0$	0.06 (0.058)	0.04 ± 0.01 (0.05)	0.047 ± 0.005

Table 5.1: Relative intensities of iodine atoms obtained in this work compared with those in references [135] and ref [134]. The values in parentheses are relative intensities computed with an intermediate coupling model. [a] In ref [135], I atoms were generated by heating solid silver iodide and relative intensities were obtained from a He $I(\alpha)$ PE spectrum. [b] In ref [134], I atoms were generated from the F + HI reaction and relative intensities were obtained from a He $I(\alpha)$ PE spectrum.

PE spectral envelopes obtained at 21.22 eV for the two IF bands (Figures 5.5 and 5.6) were simulated by computing the FCFs between the ground state and the ionic state vibrational wave functions. To do this, the spectroscopic constants ω_e, $\omega_e\chi_e$, and r_e for each electronic state were used to generate a Morse potential for the IF and IF^+ states. Then the vibrational wave functions for each electronic state were obtained from numerical solutions of the vibrational Schrödinger equation with the appropriate potential. The vibrational constants used for the $IF(X^1\Sigma^+)$ state for the simulations were taken from a rotational and vibrational analysis of an electronic emission spectrum and from a microwave spectroscopic study [136–138]. The values used were: $\omega_e = 610.24cm^{-1}$, $\omega_e\chi_e = 3.123cm^{-1}$, and $r_e = 1.90975$ Å. The vibrational constants ω_e and $\omega_e\chi_e$ used for the ionic states were obtained by measuring the spacing (ΔE) between the IF vibrational components of each IF band (as was explained in Chapter 2). Since the equilibrium bond length of each ionic state is not known, a trial value must be used in the calculation of the FCFs. This trial value is chosen to be close to,

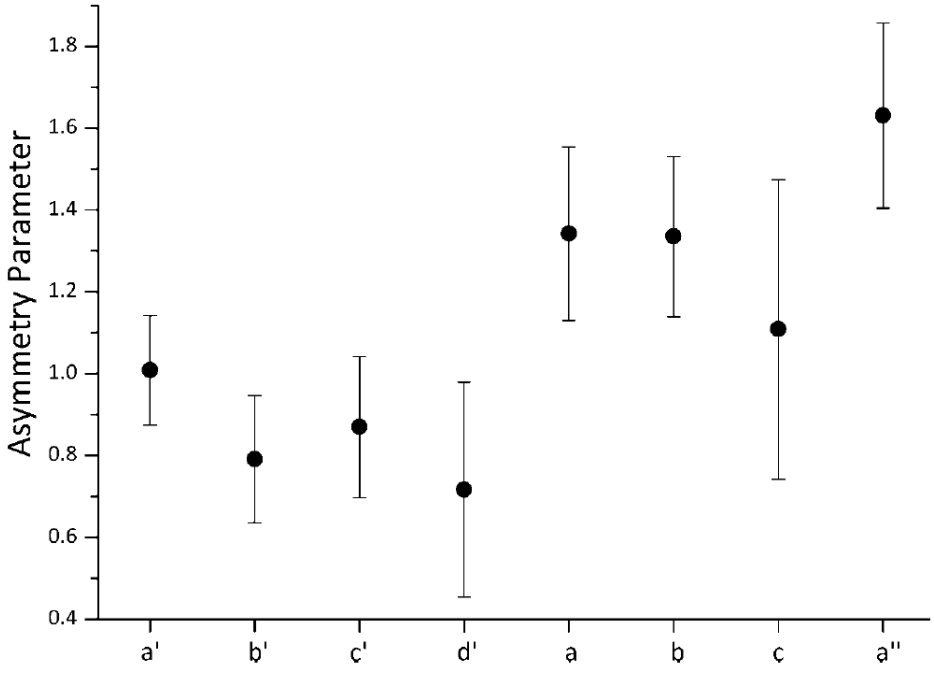

Figure 5.7: Asymmetry parameter β of the more intense bands shown in Figure 5.1 at a photon energy of 21.22 eV.

although shorter than, the value of the neutral state. This is because in both IF bands, an electron has been removed from an antibonding orbital; the equilibrium bond length of the ionic state is therefore expected to be shorter while the vibrational constant ω_e is expected to be larger than that for the IF ($X^1\Sigma^+$) state, as was observed. The actual equilibrium bond length of the ionic state is found by choosing a range of trial values and calculating the quantity $\Sigma[FCFv'(calcd) - FCFv'(expt)]^2$ for each trial bond length [139]. A curve of this quantity plotted as a function of trial ionic bond length was then obtained. The lowest point of the curve represents the recommended value of the equilibrium bond length for the ionic state. During these FCF calculations, it was assumed that the electronic transition moment is constant over the photoelectron band. This assumption gives an error in the equilibrium bond length of the ionic state of 0.005 Å [139]. An example of a least squares plot of this

type is shown in Figure 5.8 for the $IF^+(X^2\Pi_{1/2}) \leftarrow IF(X^1\Sigma^+)$ band.

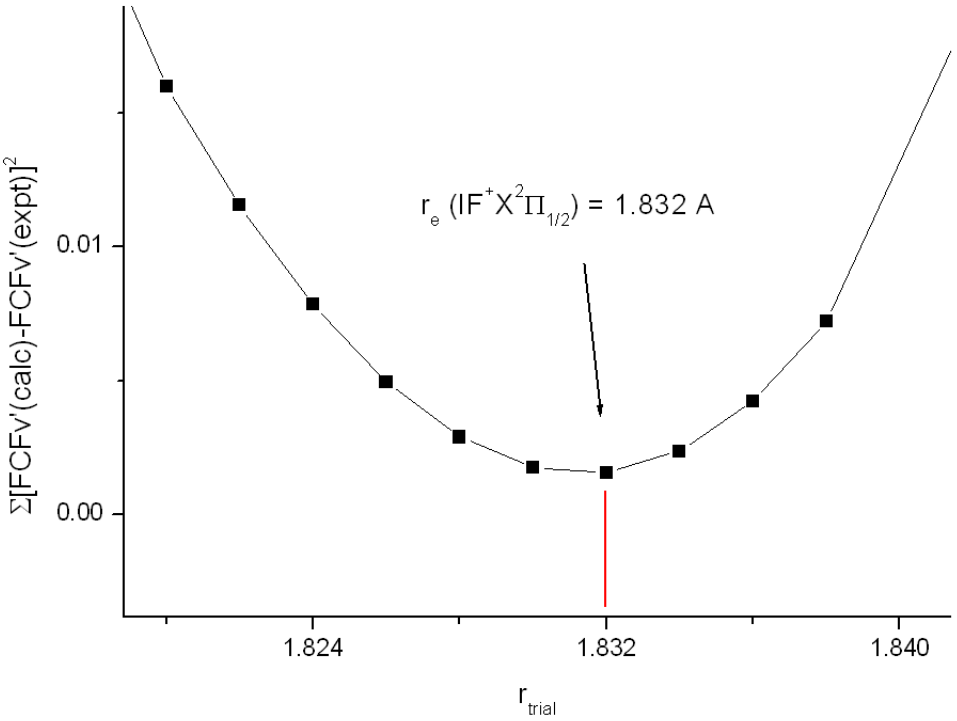

Figure 5.8: Least squares fit for the vibrational components of the $IF^+(X^2\Pi_{1/2}) \leftarrow IF(X^1\Sigma^+)$ band of IF showing the value of the equilibrium bond length, r_e.

The results obtained for both IF bands are shown in Table 5.2, where they are compared with the results obtained in the previous HeI PES work in which IF was produced from the F + ICl reaction [64]. The present results have a much higher precision than the previous ones. This is because the ionisation energies of the IF vibrational bands were determined here to within 1 meV. The ionisation energy scales for all the PE spectra were calibrated using the known values for the $Ar^+(^2P_{3/2},^2P_{1/2}) \leftarrow Ar(^1S_0)(3p)^{-1}$ and $I^+(^1D_2,^3P_2) \leftarrow I(^2P_{3/2})(5p)^{-1}$ ionisations. Excellent linearity of the ionisation energy scale was ensured by the use of a DAC card with 0.1 mV precision to supply the voltage to the lenses of the spectrometer. Also averaging of the results over many PE spectra allowed determination of the

ionisation energies of the IF vibrational bands with high precision.

	$IF^+(X^2\Pi_{3/2})$	$IF^+(X^2\Pi_{1/2})$	$IF^+(X^2\Pi_{3/2})$ (ref [64])	$IF^+(X^2\Pi_{1/2})$ (ref [64])
ω_e (cm^{-1})	696 ± 2	687 ± 2	700 ± 30	710 ± 30
$\omega_e\chi_e$ (cm^{-1})	3.0 ± 0.5	1.2 ± 0.5	10 ± 5	10 ± 5
$r_e(\mathring{A})$	1.836 ± 0.005	1.832 ± 0.005	1.82 ± 0.01	1.82 ± 0.01
AIE (eV)	10.538 ± 0.001	11.244 ± 0.001	10.54 ± 0.01	11.24 ± 0.01
VIE (eV)	10.538 ± 0.001	11.329 ± 0.001	10.62 ± 0.01	11.32 ± 0.01
spin-orbit splitting (cm^{-1})		(5690 ± 8)	(5560 ± 40)	

Table 5.2: Ionic vibrational constants and adiabatic and vertical ionisation energies for the two IF bands observed in this work, compared with reference [64]

It is notable that the Franck–Condon envelopes for the first two bands of IF are slightly different (Figures 5.5 and 5.6) and the derived equilibrium bond lengths for the $X^2\Pi_{3/2}$ and $^2\Pi_{1/2}$ ionic states are also slightly different (Table 5.2). As these ionic states both arise from the IF $(7\pi)^{-1}$ ionisation, their potential curves might be expected to be the same shape and their equilibrium bond lengths and harmonic vibrational constants might be expected to be the same. However, interaction between ionic states (notably spin–orbit interaction between the $^2\Pi_{1/2}$ ionic state and the $^2\Sigma_{1/2}$ ionic state arising from the $(13\sigma)^{-1}$ ionisation) would lead to the $X^2\Pi_{3/2}$ and $^2\Pi_{1/2}$ ionic states having slightly different equilibrium constants and potential curves with slightly different shapes. This would explain why slightly different Franck–Condon envelopes are observed for the first two IF bands (Figures 5.5 and 5.6).

5.3.2 Threshold Photoelectron (TPE) Spectra

To record TPE spectra, the penetrating field analyser system was tuned to detect near–zero energy (threshold) photoelectrons. The detection of threshold electrons was optimized using the $Ar^+(^2P_{3/2},^2P_{1/2}) \leftarrow Ar(^1S_0)(3p)^{-1}$ doublet lines as a guide [140, 141]. Figure 5.9 shows the TPE spectrum of Ar recorded with the optimized values of 100 V for the extractor voltage, V_1 = 27.7 V, V_2 = 13.3 V, and V_3 = 3.0 V (see Chapter 3). The spectral resolution obtained is about 5 meV as estimated from the full width at half-maximum of the main $Ar^+(^2P_{3/2}) \leftarrow Ar(^1S_0)(3p)^{-1}$ band. Argon is a convenient atom to use to test the performance of the spectrometer since there are highlying neutral Rydberg states (11s', 12s', 13s', 14s', etc.) that converge to the $(3p)^{-1}\ ^2P_{1/2}$ ionisation limit. These excited neutral states can autoionise to the lower–lying $^2P_{3/2}$ ionic state leading to the production of electrons with energies of 3, 38, 62, 81 meV, etc., respectively. At photon energies well away from the threshold, the ratio of the intensities of the argon $Ar^+(^2P_{3/2}) \leftarrow Ar(^1S_0)$ and $Ar^+(^2P_{1/2}) \leftarrow Ar(^1S_0)$ bands is the statistical ratio of 2:1. However, at photon energies slightly above threshold, this ratio increases because of the contribution of the 11s' autoionising states which give electrons of 3 meV that enhance the $Ar^+(^2P_{3/2}) \leftarrow Ar(^1S_0)$ channel. The ratio shown in Figure 5.9 is $\sim 5:1$ and indicates that autoionising states are accessed within about 5 meV above the ionisation threshold. Some finite energy electrons will be emitted in the direction of the spectrometer and will also be detected if their energy is within the band-pass of the analyser. This gives rise to a high energy tail in the transmission function of the analyser. As can be seen in Figure 5.9, there is a small peak at 15.798 eV due to the 12s' autoionising state which gives rise to electrons of 38 meV kinetic energy. TPE spectra may therefore contain additional features due to autoionising states, and this must be taken into account in the interpretation of the spectra. In molecules, this effect may lead to the observation of ionic state vibrational levels outside the normal

Franck-Condon region which are enhanced in intensity by autoionisation from close-lying Rydberg states.

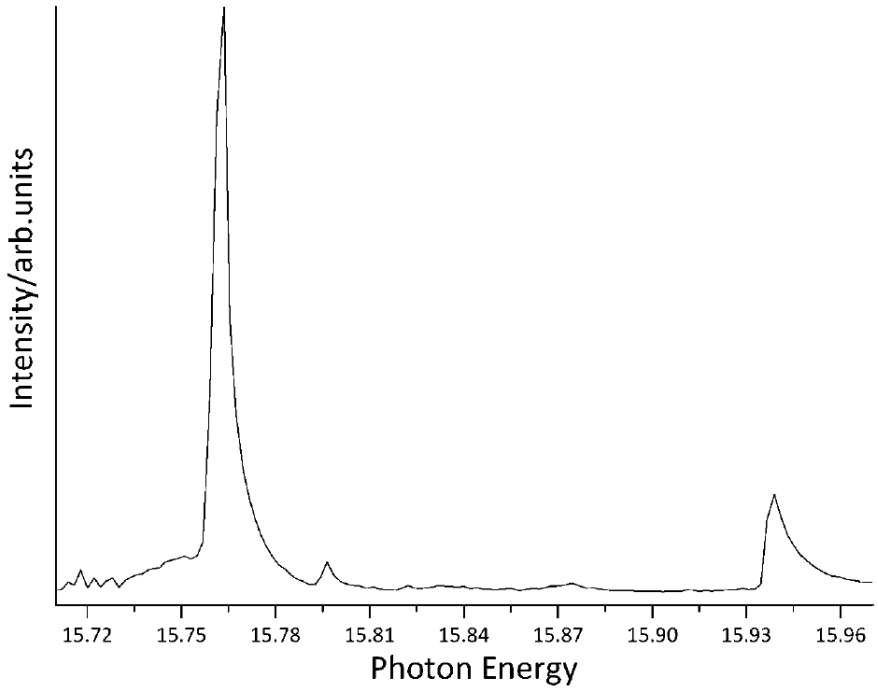

Figure 5.9: TPE spectrum recorded for argon in the region of the $Ar^+(^2P_{3/2}) \leftarrow Ar(^1S_0)$ and $Ar^+(^2P_{1/2}) \leftarrow Ar(^1S_0)(3p)^{-1}$ ionisations.

Figure 5.10 shows the TPE spectrum recorded for the F + CH_2I_2 reaction in the 10.3–12.3 eV photon energy region at a 3 cm mixing distance. The photon energy scale was calibrated using the known values for $Ar^+(^2P_{3/2},^2P_{1/2}) \leftarrow Ar(^1S_0)$ and $I^+(^1D_2,^3P_2) \leftarrow I(^2P_{3/2})$ ionisations. Comparing Figure 5.10 with the PE spectrum shown in Figure 5.2, it can be seen that better resolution is obtained for the TPE spectra, and as expected, different relative intensities of the bands are observed. All the atomic I features have increased in intensity with respect to the IF bands compared to that of the PE spectra. This is particularly the case for band (a'), corresponding to the first iodine atom ionisation, $I^+(^3P_2) \leftarrow I(^2P_{3/2})$. This is probably due to an autoionisation resonance as for the case of the $Ar^+(^2P_{3/2}) \leftarrow$

$Ar(^1S_0)$ ionisation. In the photoionisation work of Berkowitz et al. [142], the ns Rydberg series converging to the $I^+(^3P_0)$ limit of atomic I has an $n = 8$ component at an excitation energy equal to 10.4535 eV. This Rydberg level is only 2.5 meV above the $I^+(^3P_2) \leftarrow I(^2P_{3/2})$ limit, and therefore it can autoionise, giving electrons of 2.5 meV that enhance the $I^+(^3P_2) \leftarrow I(^2P_{3/2})$ channel. In a photoabsorption study, Sarma and Joshi [143] observed a different ns series converging to the $^3P_1$ limit assigned as $(^3P_1)ns[1]_{3/2}$ in the $J_c l$ coupling scheme. The $n = 8$ state of this series has an excitation energy of 10.4596 eV, 8.6 meV above the $I^+(^3P_2) \leftarrow I(^2P_{3/2})$ ionisation energy at 10.451 eV. It can also autoionise to the $I^+(^3P_2)$ state enhancing the $I^+(^3P_2) \leftarrow I(^2P_{3/2})$ TPE intensity.

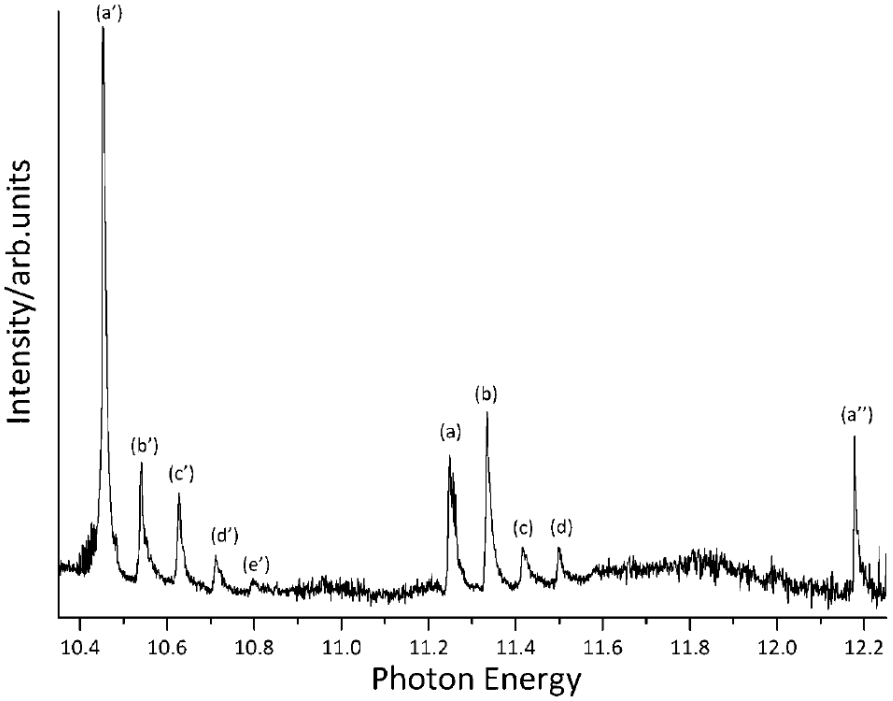

Figure 5.10: TPE spectrum recorded for the F + CH_2I_2 reaction in the 10.3-12.3 eV photon energy region at a mixing distance of 3 cm.

Comparison of Figures 5.2 and 5.10 also shows that the relative intensities of the $IF^+ \leftarrow IF$ bands are similar in both the TPE and PE spectra. In particular, higher

vibrational members of the first IF photoelectron band are not observed in the TPE spectrum in the "non–Franck–Condon region" between the $IF^+(X^2\Pi_{3/2}) \leftarrow IF(X^1\Sigma)$ and $IF^+(^2\Pi_{1/2}) \leftarrow IF(X^1\Sigma)$ bands, indicating an absence of significant autoionisation to these vibrational states.

An expanded scan in the energy region of the $I^+(^3P_2) \leftarrow I(^2P_{3/2})$ and the $IF^+(X^2\Pi_{3/2}) \leftarrow IF(X^1\Sigma)$ bands, 10.40–10.85 eV, is shown in Figure 5.11. A small band can be observed of about 5% the intensity of the $I^+(^3P_2) \leftarrow I(^2P_{3/2})$ band and 31 meV higher in photon energy (it is denoted by an "*" in Figure 5.11). This could be associated with a high–lying neutral Rydberg state that autoionises to the lower-lying $I^+(^3P_2)$ state. Berkowitz et al. [142] assigned the $n = 8$ state of an ns series converging to the $^3P_1$ limit at a photon energy of 10.4827 eV. Sarma and Joshi [143] reported three ns series converging to the $^3P_2$ limit assigned as $(^3P_2)ns[2]_{5/2}$, $(^3P_2)ns[2]_{3/2}$ and $(^3P_2)ns[1]_{1/2}$. The $(^3P_2)8s[1]_{1/2}$ Rydberg state has an excitation energy of 10.4830 meV, which is comparable with the result obtained by Berkowitz et al [142]. Autoionisation of this state to the lower–lying $I^+(^3P_2)$ ionic state would give photoelectrons of 31 meV.

Figure 5.12 shows an expanded scan of the energy region 11.22–11.52 eV containing the $I^+(^3P_{1,0}) \leftarrow I(^2P_{3/2})$ and the $IF^+(X^2\Pi_{1/2}) \leftarrow IF(X^1\Sigma)$ bands. Associated with band (a), two intense sharp peaks (a_1 and a_2) and four smaller peaks (a_3, a_4, a_5, and a_6) can be seen. As noted above, band (a) has contributions from both I and IF. It is possible that the two contributions are resolved, but the fact that band (a_1) is sharp (2-3 meV) may indicate that it is associated with an autoionising I atom Rydberg state. Moreover, its photon energy (∼11.255 eV) is too high to be assigned as the $I^+(^3P_0) \leftarrow I(^2P_{3/2})$ band at 11.251 eV. This may suggest that the wide band (a) (width 5-6 meV) has contributions from overlapping I and IF bands, while the first sharp peak (a_1) could be associated with 4 meV electrons arising from autoionisation of an I atom Rydberg state. CIS spectra on the $I^+(^3P_2) \leftarrow I(^2P_{3/2})$ ionisation band

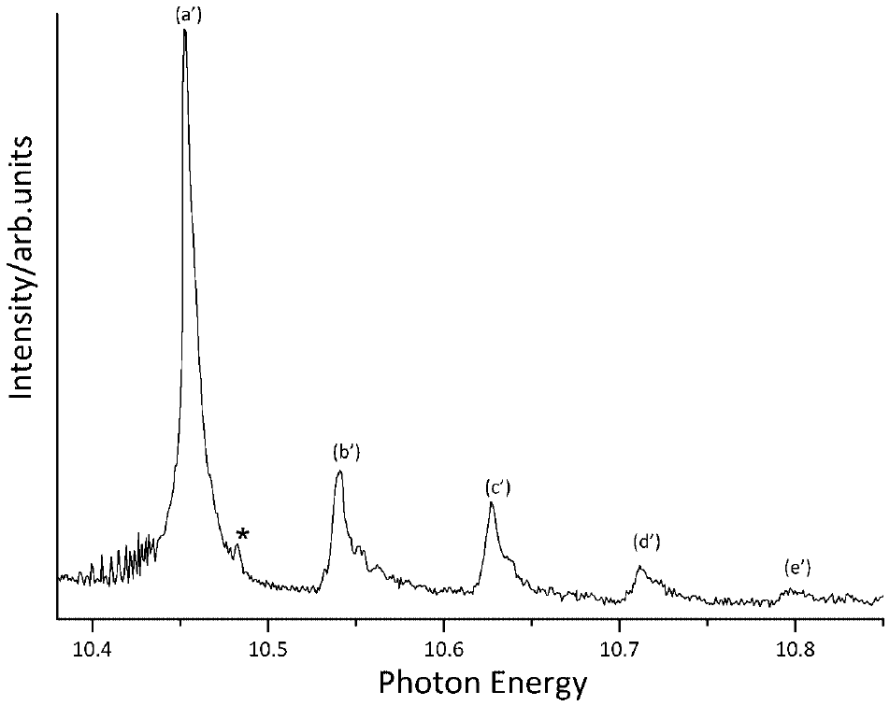

Figure 5.11: TPE spectrum showing the $I^+(^3P_2) \leftarrow I(^2P_{3/2})$ and the IF $(X^2\Pi_{3/2}) \leftarrow$ IF$(X^1\Sigma)$ bands.

have been recorded, and they will be reported in Chapter 6. An analysis of these spectra shows several Rydberg states converging to the $I^+(^3P_1) \leftarrow I(^2P_{3/2})$ limit at 11.330 eV [144, 145] in the 11.0–11.3 eV photon energy region. This again suggests that the band (a) is an overlap of I and IF bands, while the other sharp features, (a_1) to (a_6), are associated with I atom Rydberg autoionising resonances. Berkowitz et al. [142] found one ns and one nd series converging to the $(^3P_1)$ limit with several resonances in the 11.255–11.285 eV photon energy region. The same Rydberg series but with slightly different photon energies were reported by Gu et al. [146] and assigned as $(^3P_1)ns[1]_{3/2}$ and $(^3P_1)nd[2]_{5/2}$ resonances from the $I(^2P_{3/2})$ ground state. Autoionisation of $(^3P_1)16d[2]_{5/2}$ and $(^3P_1)18s[1]_{3/2}$ I atom Rydberg states to the $I^+(^3P_0)$ ionic state can be associated with bands (a_1) and (a_2) at 11.2565 and 11.2606 eV, respectively. Features (a_3, a_4, a_5 and a_6) may also be assigned as overlapping

autoionisation features from higher n Rydberg states of both ns and nd series [142, 146].

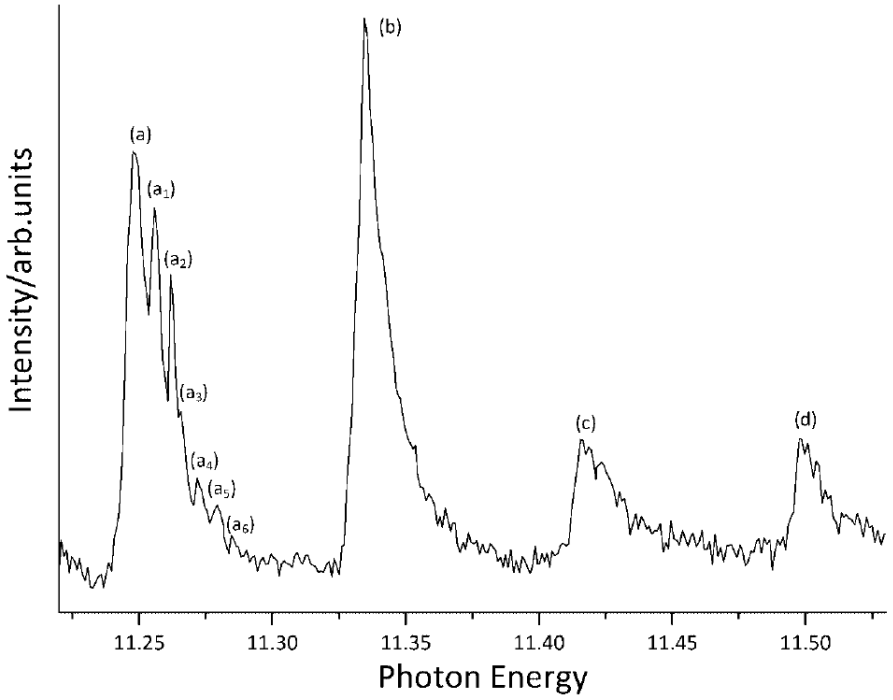

Figure 5.12: TPE spectrum showing the $I^+(^3P_{0,1}) \leftarrow I(^2P_{3/2})$ and $IF^+(^2\Pi_{1/2}) \leftarrow IF(X^1\Sigma)$ bands. Bands (a) and (b) are overlapped I and IF features, whereas bands (c) and (d) are IF vibrational components (see text).

Table 8.5 compares the ionisation energies obtained from PE and TPE spectra for the $IF^+(X^2\Pi_{3/2}) \leftarrow IF(X^1\Sigma)$ and $IF^+(X^2\Pi_{1/2}) \leftarrow IF(X^1\Sigma)$ bands. The agreement between the two sets of measurements is in general excellent. This is significant since their respective uncertainties arise from different sources. In the case of the PE spectra, the linearity and precision of the energy calibration depends upon the voltages applied to the spectrometer, notably the voltage applied to the third lens element. This voltage has a precision of about 0.2 mV. The peak position of each photoelectron band is determined from a Gaussian fit with a precision of about 0.5–1.0 meV for an intense band. Furthermore, in this work the ionisation energy

position for each band was averaged over the results obtained from many PE spectra. Therefore, the error associated with the ionisation energy of any of the intense bands is estimated to be 1 meV. On the other hand, for the case of the TPE spectra the voltages applied to the spectrometer are held constant and the photon energy is swept linearly. The photon energy calibration of the monochromator is obtained with a precision of about 1 meV, while the TPE peak position is obtained with a precision of about 0.5 meV. The error associated with the photon energy position of a TPE band is thus estimated to be between 1 and 2 meV.

	$IF^+(X^2\Pi_{3/2})$	$IF^+(X^2\Pi_{3/2})$	$IF^+(X^2\Pi_{1/2})$	$IF^+(X^2\Pi_{1/2})$
ν^+	PES	TPES	PES	TPES
0	10.539 ± 0.001	10.539 ± 0.001	11.244 ± 0.001	11.245 ± 0.001
1	10.625 ± 0.001	10.625 ± 0.002	11.329 ± 0.001	11.333 ± 0.001
2	10.709 ± 0.001	10.709 ± 0.002	11.413 ± 0.001	11.413 ± 0.001
3	10.792 ± 0.003	10.793 ± 0.002	11.497 ± 0.002	11.496 ± 0.002

Table 5.3: Comparison between the measured positions of the vibrational components of the two IF bands as obtained in PE and TPE spectra

The same ionisation energy values are obtained for three of the four $IF^+(X^2\Pi_{3/2}, v^+) \leftarrow IF(X^1\Sigma, v'' = 0)$ vibrational components ($v^+ = 0, 1, 2$). For the fourth ($v^+ = 3$), there is a difference of 1 meV, which is within experimental error (Table 8.5). Also, for the four $IF^+(X^2\Pi_{1/2}, v^+) \leftarrow IF(X^1\Sigma, v'' = 0)$ vibrational components, similar ionisation energy values are obtained, except for the $v^+ = 1$ state, which has a difference of 4 meV (this contributes to band (b) in Figure 5.12). The value of 11.333 eV obtained in the TPE measurement is too high to be associated with either IF or I. A possible explanation is a contribution from autoionising I atom Rydberg states. Berkowitz et al. [142] reported two ns series converging to the $^1D_2$ limit with excitation energies to the $n = 8$ Rydberg states close to 11.333 meV. The lower photon energy side of a TPE band has normally a sharp

increase corresponding to the energy width of the incident photon beam, in this work about 3–4 meV from the bottom to the top of the peak. This value is 10 meV for band (b). This can be explained if band (b) in the TPE spectrum arises from the overlap of IF and I contributions at lower photon energy and contributions from one or two autoionising I atom Rydberg states at higher photon energy.

5.4 Conclusion

In this chapter, an investigation of the IF and I bands in the ionisation energy region 10.0–15.0 eV by PES was presented. Their relative intensities were measured and, where IF and I bands overlapped, their relative contributions were established. This was not done in the initial study [64]. This work has led to improved adiabatic ionisation energies (AIEs) and VIEs of the $IF^+(X^2\Pi_{3/2}) \leftarrow IF(X^1\Sigma^+)$ and $IF^+(^2\Pi_{1/2}) \leftarrow IF(X^1\Sigma^+)$ ionisations and improved spectroscopic constants ω_e, $\omega_e\chi_e$, and r_e for the two IF ionic states $X^2\Pi_{3/2}$ and $^2\Pi_{1/2}$.

Comparison of the TPE and PE spectra for IF and I shows that no difference can be seen between the vibrational envelopes of the two observed IF bands. Unlike TPE spectra recorded for other diatomic halogens [127–130], no extra vibrational structure is observed in the TPE spectrum of IF, particularly in the "Franck–Condon gap" between the two observed bands. The extra structure seen in the TPE spectra, notably associated with bands (a) and (a'), and the position of band (b), which is higher in the TPE spectrum compared to its position in the PE spectrum by 4 meV, can be attributed to autoionisation contributions from known I atom Rydberg states.

Chapter 6

Angle-resolved Constant Ionic State (CIS) spectroscopy of atomic iodine

This chapter reports the results obtained by CIS spectroscopy on iodine atoms. Rydberg series converging to three thresholds of iodine were observed and analysed. The angular distribution parameter for the first and fourth band was also determined as a function of photon energy and is presented in this chapter. An introduction to the iodine atom work, and more generally on atomic halogens is presented in Section 6.1, followed by a description of the experimental procedures in Section 6.2. Some theoretical considerations are given in Section 6.3 before presenting the results in Section 6.4. Section 6.5 finally presents a summary of the angular distribution plots for the observed ionisations.

6.1 Introduction

In this work, atomic iodine was studied by angle resolved Constant Ionic State (CIS) spectroscopy using synchrotron radiation. This follows an initial investigation of atomic iodine, I, and IF by photoelectron spectroscopy (PES) and threshold photoelectron spectroscopy (TPES) in which PE and TPE spectra were recorded with different I to IF ratios to determine improved spectroscopic constants for the two lowest ionic states of IF and the relative intensities of I atom PE bands at 21.22 eV photon energy. This work is presented in Chapter 5 and in reference [51]. Atomic iodine is a halogen with ground state electronic configuration I...$5s^2 5p^5(^2P)$. The spin-orbit splitting between the two components of the ground state $^2P_{1/2}$ and $^2P_{3/2}$ is 0.94 eV, with the $^2P_{3/2}$ state lying lower. The $I^+...5s^2 5p^4$ ionic states obtained on $(5p)^{-1}$ photoionisation are $^3P_{2,1,0}$, $^1D_2$ and $^1S_0$. The halogen atoms have been thoroughly studied by a number of spectroscopic methods as they represent a transition from their closed shell neighbours in the Periodic Table, the rare gases, to the more complex open shell atoms. In this chapter, an angle-resolved PE study of autoionisation from the $I^*...5s^2 5p^5\ ^3P_1$, $^1D_2$ and $^1S_0$ ns, nd resonances arising from $5p$ photoexcitation from the ground state is reported.

Early work on atomic iodine was performed in 1962 by Minnhagen [144] who revised the analysis of the photographic electronic absorption work of Kiess and Corliss [147] by recalculating the entire energy level system. He also determined accurate values for the five $I^+..5s^2 5p^4$ terms and demonstrated that the neutral iodine excited states are best descibed by $J_c l$ (or JK) coupling. In the following years, Huffman et al. [60, 61] recorded the absorption spectra of all atomic halogens, produced in a microwave discharge through a He-molecular halogen mixture for Cl, Br and I and through a He-SF_6 mixture for F, and confirmed Minnhagen's ionisation limits for iodine atoms. Berkowitz et al. [135, 142] then observed Rydberg series converging to the four higher ion core limits, above the first ionisation limit, by mass analysed

photoionisation spectra of iodine atoms, produced by vaporising AgI. Berkowitz and co-workers also studied the photoionisation of the other halogens atoms, i.e. fluorine [148], chlorine [149] and bromine [150]. Sarma and Joshi later assigned Rydberg series converging to the $I^+ \ ^3P_{2,1,0}$ thresholds with principal quantum number up to n = 20 [151]. They produced iodine atoms with a flash pyrolysis technique and photographed the VUV absorption spectrum obtained. Following this, Pratt [152, 153] studied Rydberg states of atomic iodine produced by laser photodissociation of methyl iodide. He used resonant enhanced multiphoton ionisation (REMPI) combined with time of flight (TOF) mass spectrometry and electron energy analysis. As two photons were used to prepare the excited state, he was able to study single-photon forbidden np and nf series. In related work, Pratt et al. [154] studied the two-color multiphoton excitation spectra of autoionising $I^* \ ^1D_2$ ns and nd Rydberg series in atomic iodine. In this work, Rydberg states were resolved up to principal quantum numbers as high as n = 35. This technique uses a total of three photons and therefore accesses excited states of the same parity as those in single photon excitation. More recently, Gu et al. [146] observed two Rydberg series (one ns and one nd series) built on the $I^+ \ ^3P_1$ ion core and resolved states with principal quantum number up to n = 47. They combined multiphoton ionisation with time of flight photoelectron spectroscopy and mass spectrometry. Iodine atoms were produced in this work from laser dissociation of molecular iodine.

Caldwell, Krause and co-workers have carried out extensive angle resolved photoelectron studies on oxygen atoms and the halogen atoms, except iodine atoms. They measured partial cross sections and partial differential cross sections following ionisation of both inner and outer shell electrons. Atoms were produced by microwave discharge and the experiments were carried out with monochromatised synchrotron radiation. The photoelectrons were energy- and angle- selected before being detecting and counted. A summary of their work is presented in a paper published in 2004 [155]. Atomic bromine is the closest halogen to iodine in the Periodic Table. Its

He(I) PE spectrum was recorded during several studies [133, 134, 156, 157] and shows the same PE bands as iodine atoms, $Br^+ \, ^3P_{2,1,0}, ^1D_2, ^1S_0 \leftarrow Br \, ^2P_{3/2}$. Rydberg series converging to the $Br^+ \, ^3P_{2,1,0}$ and $^1D_2$ limits have been observed and assigned in the absorption spectra of atomic bromine, obtained from the flash pyrolysis technique, by Sarma and Joshi [151]. The more recent work of Caldwell and co-workers [158] measured CIS spectra for all PE bands except the $Br^+(^3P_2) \leftarrow Br \, (^2P_{3/2})$ band. Rydberg series converging to each available threshold were observed and analysed. The angular distribution of the ejected photoelectron was also studied for the first and fourth band as a function of photon energy. The asymmetry parameter, β, was determined by recording each CIS spectrum at two different angles. Atomic chlorine and fluorine were also thoroughly studied [155]. The same PE bands appear in their He(I) PE spectra as in atomic bromine and iodine. CIS spectra were recorded and analysed for Cl and F; they also show Rydberg series converging to each threshold. The angular distribution parameter of the ejected photoelectrons was also determined as a function of the photon energy for chlorine atoms [155]. Unfortunately, the microwave discharge source used by Caldwell and co-workers does not allow the generation of iodine atoms for electron spectroscopy studies. As a result, iodine atoms is the halogen that has been the least studied and in particular, no angle resolved CIS measurements have been made on this atom.

The aim of the present work was therefore to study atomic iodine by CIS spectroscopy, recording spectra at two angles with respect to the direction of polarisation of the photon source, in order to allow the beta parameter, β, to be determined. CIS spectra were recorded in the photon energy range 11 to 23 eV and with smaller step size and better statistics between 11 and 14.5 eV where structure is expected. Rydberg series converging to the three higher ion core limits, $I^+ \, ^3P_1$, $^1D_2$ and $^1S_0$, are reported in this chapter. Ionisation energies and quantum defects were determined for each Rydberg series from Fano fitting of the resonances. This chapter presents the results obtained from this work on iodine atoms.

6.2 Experimental

As previsously mentioned, the experiments carried out during this project were undertaken at the Elettra synchrotron light source on the BL 4.2R Polar beamline. The monochromator used on this beamline covers the photon energy range 5 to 35 eV. The photoelectron spectrometer was specifically designed to study reactive intermediates with photoelectron spectroscopy using synchrotron radiation and has been described in details in Chapter 3 and in reference [17]. In this work, measurements were carried out either by recording conventional photoelectron (PE) spectra, in which the photon energy is fixed, or by recording constant ionic state (CIS) spectra, where the intensity of a particular photoelectron feature (such as a particular atomic ionisation) is monitored as a function of photon energy (see Chapter 3). The study of the PE and TPE spectra of atomic iodine was presented in Chapter 5 and the present work builds on this initial study. Both CIS and PE spectra were recorded in constant pass energy mode, by scanning the voltage on a lens which accelerates (or decelerates) the photoelectrons before they enter the analyser. This ensures constant resolution over the spectrum. CIS spectra were recorded in this work in the photon energy range 11 to 23 eV for the first band of iodine atoms and between 12.5 and 23 eV for the fourth band of iodine atoms. Smaller step size (2 meV rather than 5 meV) and better statistics were used between 11 and 14.5 eV where structure is expected. Iodine atoms were produced from the following consecutive reactions:

Primary reaction: $F + CH_2I_2 \rightarrow CH_2I + IF$

Subsequent reactions: $F + CH_2I \rightarrow [CH_2IF]^{\dagger} \rightarrow CH_2F + I$

$\rightarrow CHF + HI$

A high yield of F atoms was produced by flowing 5% F_2 in helium through a microwave discharge at 2.45 GHz in the sidearm of a glass inlet system [62]. This inlet system also has an inner inlet which is used to transport the target reaction

molecules (in this case, CH_2I_2) to the reaction region. The intensities of the bands in the experimental PE and CIS spectra were normalised by the photon flux and the transmission correction of the spectrometer as explained in Chapter 3 and in reference [50].

Test experiments were carried out in Southampton in order to determine the optimum pressures and mixing distance above the photon beam which maximise the intensity of the I atom features. The optimum partial pressures were: Δp (CH_2I_2) = 1 $\times 10^{-6}$ mbar, Δp (F_2/He) = 5 $\times 10^{-6}$ mbar, and Δp (Ar) = 3 $\times 10^{-7}$ mbar. These partial pressures were determined using an ionisation gauge connected to the main vacuum chamber and were measured with respect to the background pressure in the vacuum chamber (1×10^{-7} mbar). Spectra which showed the most intense I atom bands were obtained at a mixing distance of about 4 cm from the photon beam.

6.3 Theoretical considerations

Atomic iodine is an open shell atom and its ground state electronic configuration is ...$5s^2$ $5p^5$. This gives rise to two states, $^2P_{3/2}$ and $^2P_{1/2}$, separated by 0.94 eV, with the $^2P_{3/2}$ state lower [133]. The $^2P_{1/2}$ state is effectively not populated under equilibrium conditions at room temperature. The $(5p)^{-1}$ photoionisation from the $^2P_{3/2}$ state gives rise to the final ionic states of I^+...$5s^2 5p^4$ ($^3P_{2,1,0}$, $^1D_2$ and $^1S_0$). The energies of these ionisations are 10.451, 11.330, 11.251, 12.153 and 14.109 eV, respectively [60, 61, 134, 135]. PE spectra recorded during this work show bands for all five iodine atom ionisations. CIS spectra recorded for a selected PE band show resonances converging to different thresholds. The resonances correspond to excitation to Rydberg states that are part of a series, which converges to each threshold, followed by autoionisation to the ionic state selected. To assign the series, it is helpful to draw up tables (Tables 6.1 and 6.2) of the excited states to which

transitions are allowed from the ground state I...$5s^2 5p^5(^2P_{3/2})$ and which autoionise to the ionic states $I^+...5s^2 5p^4(^3P_2)$ and $I^+...5s^2 5p^4(^1D_2)$ respectively, in the $J_c l$ coupling scheme (also known as JK coupling). In this coupling scheme, the total angular momentum of the ion core, J_c, couples with the orbital angular momentum of the electron, l, to give K. The spin of the Rydberg electron, s, is then coupled to K to give the total angular momentum, J. The selection rule on J is $\Delta J = 0, \pm 1$ from the $^2P_{3/2}$ neutral ground state, and the selection rule on parity is odd $\leftrightarrow$ even.

The resonances seen in experimental CIS spectra often show an asymmetric profile. This is due to interference between the direct and indirect processes and results in a characteristic Fano profile [10, 37], where the cross section can be expressed as:

$$\sigma(E) = \sigma_a \times \frac{(q+\varepsilon)^2}{1+\varepsilon^2} + \sigma_b \tag{6.3.1}$$

In this equation, σ_a and σ_b represent two portions of the cross section which correspond, respectively, to transitions to states of the continuum that do and do not interact with the discrete autoionising state, as was seen in Chapter 2. ε is the reduced energy and can be expressed as follow:

$$\varepsilon = \frac{E - E_n}{\frac{1}{2}\Gamma} \tag{6.3.2}$$

where E_n is the resonance energy and Γ is the natural width of the autoionising state which represents the bound-continuum mixing of the resonance state. The q parameter characterises the line profile. The Fano fitting of the resonances allows the resonance positions (E_n) to be established. The effective quantum number ($n^* = n - \delta$) and principal quantum number, n, of each Rydberg state can then be determined from [40]:

Excited states	$[J_c l]_{Jfinal}$	ionic state after autoionisation
$5s^2 5p^4(^1D_2)ns\ ^2D_{5/2}$	$[2]_{5/2}$	$5s^2 5p^4(^3P_2) + \varepsilon s/\varepsilon d$
$5s^2 5p^4(^1D_2)ns\ ^2D_{3/2}$	$[2]_{3/2}$	$5s^2 5p^4(^3P_2) + \varepsilon s/\varepsilon d$
$5s^2 5p^4(^1D_2)nd\ ^2D_{5/2}$	$[3,2]_{5/2}$	$5s^2 5p^4(^3P_2) + \varepsilon s/\varepsilon d$
$5s^2 5p^4(^1D_2)nd\ ^2D_{3/2}$	$[2,1]_{3/2}$	$5s^2 5p^4(^3P_2) + \varepsilon s/\varepsilon d$
$5s^2 5p^4(^1D_2)nd\ ^2P_{3/2}$	$[2,1]_{3/2}$	$5s^2 5p^4(^3P_2) + \varepsilon s/\varepsilon d$
$5s^2 5p^4(^1D_2)nd\ ^2P_{1/2}$	$[1,0]_{1/2}$	$5s^2 5p^4(^3P_2) + \varepsilon d$
$5s^2 5p^4(^1D_2)nd\ ^2S_{1/2}$	$[1,0]_{1/2}$	$5s^2 5p^4(^3P_2) + \varepsilon d$
$5s^2 5p^4(^3P_0)ns\ ^2P_{1/2}$	$[0]_{1/2}$	$5s^2 5p^4(^3P_2) + \varepsilon d$
$5s^2 5p^4(^3P_0)nd\ ^2D_{5/2}$	$[2]_{5/2}$	$5s^2 5p^4(^3P_2) + \varepsilon s/\varepsilon d$
$5s^2 5p^4(^3P_0)nd\ ^2D_{3/2}$	$[2]_{3/2}$	$5s^2 5p^4(^3P_2) + \varepsilon s/\varepsilon d$
$5s^2 5p^4(^3P_0)nd\ ^2P_{3/2}$	$[2]_{3/2}$	$5s^2 5p^4(^3P_2) + \varepsilon s/\varepsilon d$
$5s^2 5p^4(^3P_1)ns\ ^2P_{3/2}$	$[1]_{3/2}$	$5s^2 5p^4(^3P_2) + \varepsilon s/\varepsilon d$
$5s^2 5p^4(^3P_1)ns\ ^2P_{1/2}$	$[1]_{1/2}$	$5s^2 5p^4(^3P_2) + \varepsilon d$
$5s^2 5p^4(^3P_1)nd\ ^2D_{5/2}$	$[3,2]_{5/2}$	$5s^2 5p^4(^3P_2) + \varepsilon s/\varepsilon d$
$5s^2 5p^4(^3P_1)nd\ ^2D_{3/2}$	$[2,1]_{3/2}$	$5s^2 5p^4(^3P_2) + \varepsilon s/\varepsilon d$
$5s^2 5p^4(^3P_1)nd\ ^2P_{3/2}$	$[2,1]_{3/2}$	$5s^2 5p^4(^3P_2) + \varepsilon s/\varepsilon d$
$5s^2 5p^4(^3P_1)nd\ ^2P_{1/2}$	$[1]_{1/2}$	$5s^2 5p^4(^3P_2) + \varepsilon d$
$5s^2 5p^4(^1S_0)ns\ ^2S_{1/2}$	$[0]_{1/2}$	$5s^2 5p^4(^3P_2) + \varepsilon d$
$5s^2 5p^4(^1S_0)nd\ ^2D_{5/2}$	$[2]_{5/2}$	$5s^2 5p^4(^3P_2) + \varepsilon s/\varepsilon d$
$5s^2 5p^4(^1S_0)nd\ ^2D_{3/2}$	$[2]_{3/2}$	$5s^2 5p^4(^3P_2) + \varepsilon s/\varepsilon d$

Table 6.1: States to which transitions are allowed from the ground state I...$5s^2 5p^5(^2P_{3/2})$ and which autoionise to the ionic state $I^+...5s^2 5p^4(^3P_2)$, in the $J_c l$ coupling scheme

$$E_n = E_\infty - \frac{R}{(n-\delta_n)^2} \tag{6.3.3}$$

Excited states	$[J_c l]_{J final}$	ionic state after autoionisation
$5s^2 5p^4(^1S_0)ns\ ^2S_{1/2}$	$[0]_{1/2}$	$5s^2 5p^4(^1D_2) + \varepsilon d$
$5s^2 5p^4(^1S_0)nd\ ^2D_{5/2}$	$[2]_{5/2}$	$5s^2 5p^4(^1D_2) + \varepsilon s/\varepsilon d$
$5s^2 5p^4(^1S_0)nd\ ^2D_{3/2}$	$[2]_{3/2}$	$5s^2 5p^4(^1D_2) + \varepsilon s/\varepsilon d$

Table 6.2: States to which transitions are allowed from the ground state I...$5s^2 5p^5(^2P_{3/2})$ and which autoionise to the ionic state I^+...$5s^2 5p^4(^1D_2)$, in the $J_c l$ coupling scheme

where R is the Rydberg constant for iodine atoms (109736.84 cm^{-1}) and E_∞ is the series limit. This equation can then be used, with known E_n and n values, to obtain the true ionisation energy, E_∞ and the quantum defect, δ_n of the series. The parameters q, Γ, σ and δ are regarded as energy independent [43]. However, a slow variation of these parameters with energy was observed in this work.
During this work, all CIS spectra were recorded at two different angles with respect to the photon polarisation axis, $\theta = 0°$ and $\theta = 54°44'$. At $\theta = 54°44'$ the measured intensity is proportional to the total photoionisation cross section, independent of β [1, 12]. The angular distribution parameter, β, can be determined from the following equation (see Chapter 2):

$$\beta = R - 1 \tag{6.3.4}$$

where $R = I_0/I_{54°44'}$ is the ratio of the experimental intensities at $\theta = 0°$ and $\theta = 54°44'$. For the measurement of the β parameter, it is also important to evaluate a correction factor to account for the changes in the efficiency of the analyser at the two different angles of measurement. These changes arise from small misalignments which may occur on rotation of the analyser between the axis of rotation and the direction of the photon beam (see Chapter 3). Each time the spectrometer was

rotated, the intensity of the helium $(1s)^{-1}$ ionisation was measured (at $h\nu = 28.0$ eV). This allowed the β parameter for helium (which is well established) [71] to be measured. A comparison between the measured β parameter and the known β parameter of helium allowed the determination of the correction factor that was then applied to each β plot. Plots of β as a function of photon energy thus obtained are presented with the results, in the next section.

6.4 Results and Discussion

6.4.1 Overview

A PE spectrum recorded for the F + CH_2I_2 reaction, at an angle $\theta = 54°44'$ with respect to the polarisation axis of the radiation is shown in Figure 6.1. This spectrum was recorded with a photon energy of 21.22 eV, in the ionisation energy region from 10.3 to 12.3 eV and at a reagent mixing distance of 4 cm. The assignment of the bands was made as in an earlier study of I and IF by PES [64]. The PE spectrum shows four of the iodine atom bands, overlapped with vibrational components of the $IF^+(X^2\Pi_{3/2}) \leftarrow IF(X^1\Sigma)$ and $IF^+(^2\Pi_{1/2}) \leftarrow IF(X^1\Sigma)$ bands.

CIS spectra were recorded for the first and fourth PE bands of iodine atoms, i.e., the $I^+(^3P_2) \leftarrow I(^2P_{3/2})$ and the $I^+(^1D_2) \leftarrow I(^2P_{3/2})$ bands, as they are the most intense and are not overlapped with IF features. CIS spectra were recorded for the first band, the $I^+(^3P_2) \leftarrow I(^2P_{3/2})$ band, in the photon energy range 11.0 to 23.0 eV. This photon energy range covers the third ($I^+(^3P_1) \leftarrow I(^2P_{3/2})$), fourth ($I^+(^1D_2) \leftarrow I(^2P_{3/2})$) and fifth ($I^+(^1S_0) \leftarrow I(^2P_{3/2})$) thresholds of iodine atoms as well as the $(5s)^{-1}$ thresholds. The second threshold of iodine atoms ($I^+(^3P_0)$) is also within the CIS spectral region recorded for the first band (at 11.251 eV). However, there is only 5 meV between the beginning of the CIS spectra and the threshold, which is not enough to allow a study

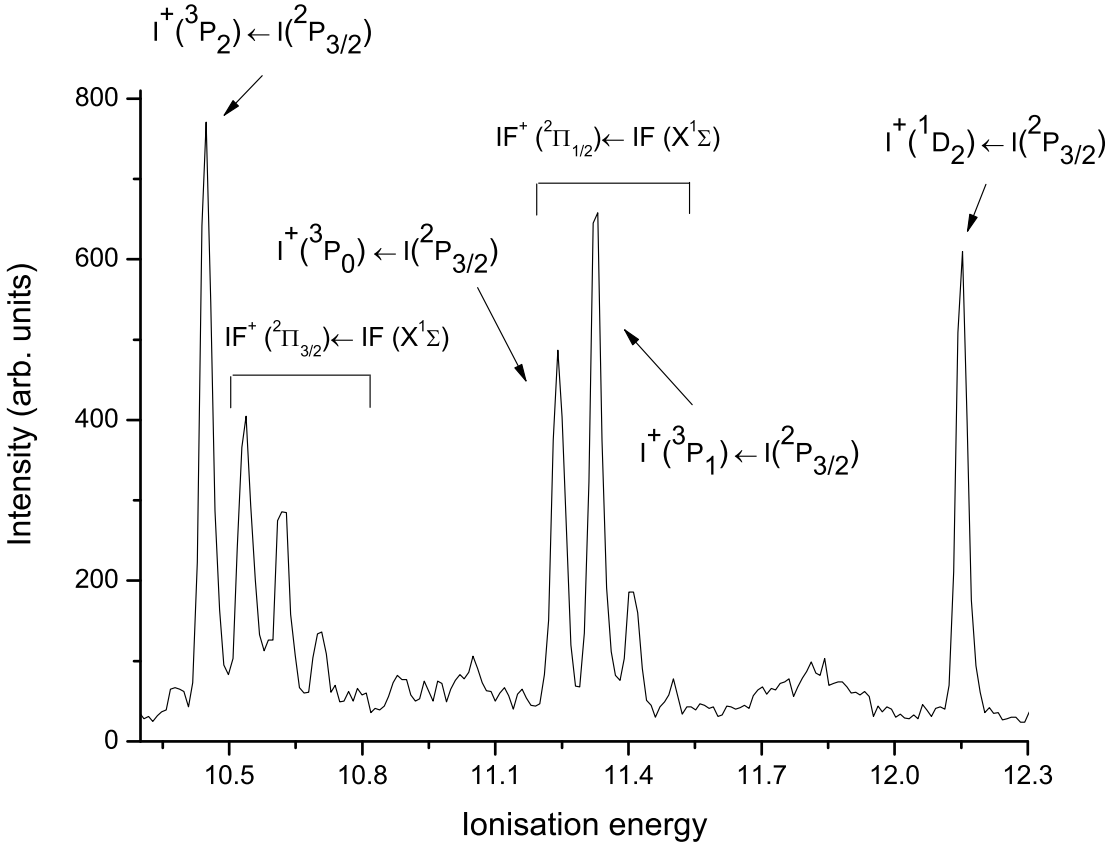

Figure 6.1: PE spectrum of the reaction F + CH_2I_2, recorded at $h\nu = 21.22$ eV, over the ionisation energy range 10.3 to 12.3 eV, and at an angle $\theta = 54°44'$ showing atomic I and IF features

of Rydberg states converging to this threshold. As a result, series converging to the $I^+(^3P_0)$ have not been observed in the present work. CIS spectra were also recorded for the fourth band of iodine atoms, the $I^+(^1D_2) \leftarrow I(^2P_{3/2})$ band, over the photon energy range 13 to 23 eV. This photon energy range only covers the fifth $(5p)^{-1}$ threshold ($I^+(^1S_0) \leftarrow I\ ^2P_{3/2}$) and the $(5s)^{-1}$ thresholds. CIS spectra recorded in the photon energy region of the $(5s)^{-1}$ photoionisations, from 20.0 to 23.0 eV, were not analysed as the spectra were not of sufficient quality. The CIS spectra obtained during this work are in good agreement with the spectra obtained by Berkowitz et

al. [142], which were obtained from mass-analysed photoionisation of atomic iodine. The assignments given by Berkowitz et al. are based on those given by Huffman et al [60, 61] in a gas-phase optical absorption study. However, in the present work, higher resolution was achieved and β parameter plots as a function of photon energy are obtained.

6.4.2 Series converging to the $I^+(^1S_0)$ threshold

CIS spectra recorded in the photon energy range 12.9 to 14.1 eV show two Rydberg series converging to the $I^+(^1S_0)$ threshold at 14.109 eV. The spectra were recorded for two of the iodine atom PE bands, the first one, $I^+(^3P_2) \leftarrow I(^2P_{3/2})$ and the fourth one, $I^+(^1D_2) \leftarrow I(^2P_{3/2})$. These spectra were also recorded at two different angles with respect to the polarisation axis of the radiation, $\theta = 0°$ and $\theta = 54°44'$ and are shown in Figures 6.2 and 6.3. Figure 6.2(a) shows the relative cross sections of the $I^+(^3P_2) \leftarrow I(^2P_{3/2})$ band at an angle of $\theta = 0°$ while Figure 6.2(b) was recorded at an angle of $\theta = 54°44'$. Figure 6.3 shows the spectra obtained for the fourth band of iodine atoms, the $I^+(^1D_2) \leftarrow I(^2P_{3/2})$ band. Figure 6.3(a) was recorded at an angle $\theta = 0°$ while Figure 6.3(b) was recorded at an angle $\theta = 54°44'$. All the spectra show a similar trend with two clearly distinguishable Rydberg series converging to the $I^+(^1S_0)$ threshold, one of which is much broader than the other. It is worth noting that the shapes of the resonances vary between the first and fourth PE bands of iodine atoms while resonances are very similar for CIS spectra recorded for the same PE band at the two different angles. According to Tables 6.1 and 6.2, the same transitions are allowed from the ground state $I...5s^25p^5(^2P_{3/2})$ to the excited states $I^*...5s^25p^4(^1S_0)$ ns or nd whether the ionic state after autoionisation is the $I^+...5s^25p^4(^3P_2)$ or the $I^+...5s^25p^4(^1D_2)$ state. From these Tables, one can see that three series are allowed to converge to the $I^+(^1S_0)$ threshold, one ns and two nd series. Since only two series are observed and the quantum defects obtained for them

correspond to the assignment of one ns and and one nd series [159], it is assumed that the splitting between the $nd[2]_{5/2,3/2}$ state is too small to be resolved in this work. This would explain why only two series are observed experimentally, the $ns[0]_{1/2}$ and the $nd[2]_{5/2,3/2}$ series. The nd series is expected to be broad as nd series are usually broader than ns series, with a pronounced tail towards the high energy side, as is common in other halogens, rare gases and other elements except for the atoms of the first row [160]. In contrast, ns series are sharp and symmetric. The series observed in the present work closely resemble those obtained by Benzaid et. al. [158] for bromine atoms and those obtained by Wu et. al. [161] for xenon. Fano fitting was used to find the position and fitting parameters of each resonance separately. The fitting parameters include the shape parameter, q, the natural width, Γ and the correlation index, ρ^2. From equation 6.3.3, the effective quantum number, n^* and principal quantum number, n were derived for each Rydberg state. The results thus obtained are shown in Tables 6.3 and 6.4. Also included in these tables is the value of the product Γn^{*3}, which is called the reduced linewidth and should be constant throughout a series [37]. However, a slow increase of this parameter throughout the series is observed, as can be seen in the tables. Table 6.3 presents the values obtained for resonances seen in the first band CIS , $I^+(^3P_2) \leftarrow I(^2P_{3/2})$, while Table 6.4 presents the values obtained for the fourth band CIS, $I^+(^1D_2) \leftarrow I(^2P_{3/2})$. Shown as examples, are the fits obtained for series converging to the $I^+(^1S_0)$ threshold at an angle $\theta = 0°$. The fit of each resonance was carried out independently and then the individual fits were put together to show the full progression. Figure 6.4 shows the separate fits for the two series obtained for resonances in the CIS spectra recorded for the first PE band of iodine atoms in the photon energy region 13.0 to 14.0 eV, the $I^+(^3P_2) \leftarrow I(^2P_{3/2})$ band. Figure 6.4(a) shows fitting of the nd resonances while Figure 6.4(b) shows ns resonances. Similarly, Figure 6.5(a) shows the fitting of the nd resonances recorded in the CIS spectra for the fourth PE band of iodine atoms in the photon energy region 13.0 to 14.0 eV, the $I^+(^1D_2) \leftarrow I(^2P_{3/2})$ band, while Figure 6.5(b) shows the ns resonances.

The position of the resonances at the two angles and for the two different bands are in good agreement, within experimental error (see Tables 6.3 and 6.4). The fitting parameters show a regular pattern, as well as the n^* values, which indicates a good reliability of the fits. From these values, the $I^+(^1S_0) \leftarrow I(^2P_{3/2})$ threshold and the quantum defect can be obtained for each observed series (equation 6.3.3). The results are shown in Table 6.5. The derived $I^+(^1S_0) \leftarrow I(^2P_{3/2})$ ionisation energies are in good agreement with the value obtained by Berkowitz [142] of 14.109 eV within experimental error. Radler et al. [159] showed that the quantum defect of Xe was ~ 4 for ns series and ~ 2.3 for nd series and investigations of resonances in atomic chlorine and bromine have shown to give in general the same quantum defects as their rare gas neighbours [162]. Berkowitz also found [142] quantum defects for iodine atoms of about 0 (modulo 1) for ns series and of about 0.3 (modulo 1) for nd series. (In some cases, the quantum defect, δ, is written modulo 1, in which case δ is given by the non-integral part of $(n - n^*)$ [154]). This is consistent with the previous assignment for the $ns[0]_{1/2}$ and $nd[2]_{5/2,3/2}$ series, as quantum defects found for this threshold are approximately 2.30 for the broad $nd[2]_{5/2,3/2}$ series and approximately 3.75 for the sharper $ns[0]_{1/2}$ series. The agreement of the results obtained for the two different bands and angles is in general excellent.

More information on the series can be obtained by looking at the asymmetry parameter, β, plotted as a function of photon energy. Beta plots were obtained from the ratio of the experimental intensities in CIS spectra at the two different angles, $\theta = 0°$ and $\theta = 54°44'$. They were determined in this photon energy range from CIS spectra recorded for both the first and the fourth iodine bands, and are presented in Figure 6.6. Figure 6.6(a) shows the beta plot of the first, $I^+(^3P_2) \leftarrow I(^2P_{3/2})$, band of iodine atoms whereas Figure 6.6(b) shows the beta plot of the fourth, $I^+(^1D_2) \leftarrow I(^2P_{3/2})$ band of iodine atoms. They are different from CIS spectra as the resonances have similar shapes for the two bands and are symmetric. However, the values of the beta parameter are different in Figure 6.6(a) and 6.6(b); the beta parameter for the

first band of iodine atoms has a mean value of approximately -0.3. It shows broad resonances with values changing from -0.4 to -0.1 and sharp resonances going to -0.5 (see Figure 6.6(a)). The beta parameter for the fourth band of iodine atoms has a mean value of -0.6 across the photon energy range with dips at the resonances going to -0.85. The position of the resonances obtained from the Fano fits are marked on the spectra. Only the $nd[2]_{5/2,3/2}$ series is seen in the beta plots.

(a)

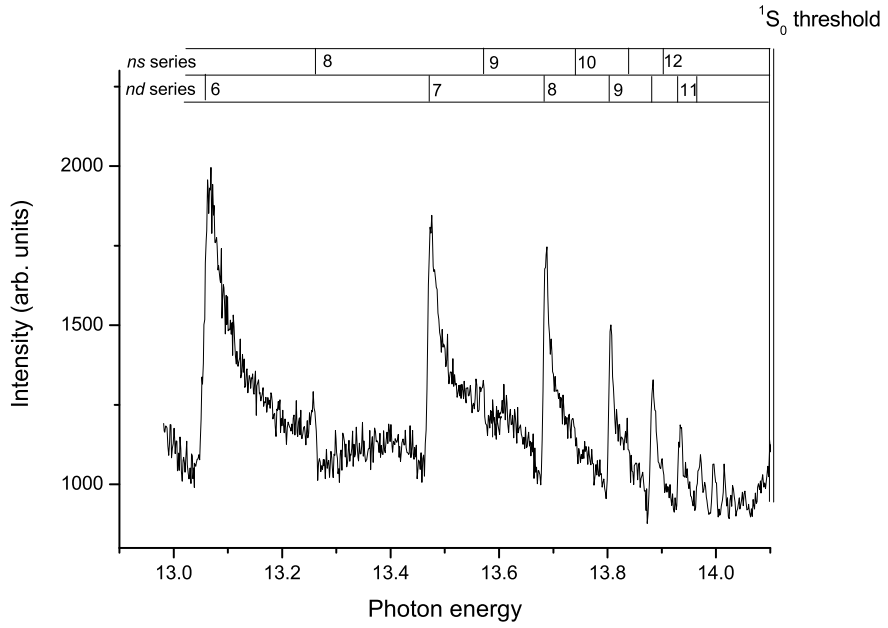

(b)

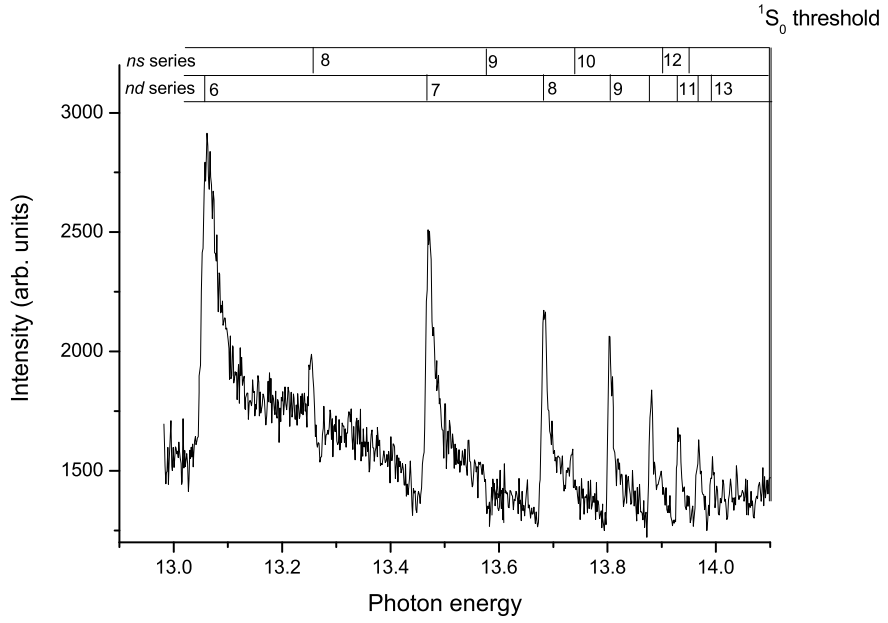

Figure 6.2: CIS spectra recorded over the photon energy region 12.9 to 14.1 eV, showing autoionising resonances converging to the $I^+(^1S_0)$ threshold at 14.109 eV, recorded for the $I^+(^3P_2) \leftarrow I(^2P_{3/2})$ band of iodine atoms. Figure 6.2(a) was recorded at an angle $\theta = 0°$ whereas Figure 6.2(b) was recorded at an angle $\theta = 54°44'$.

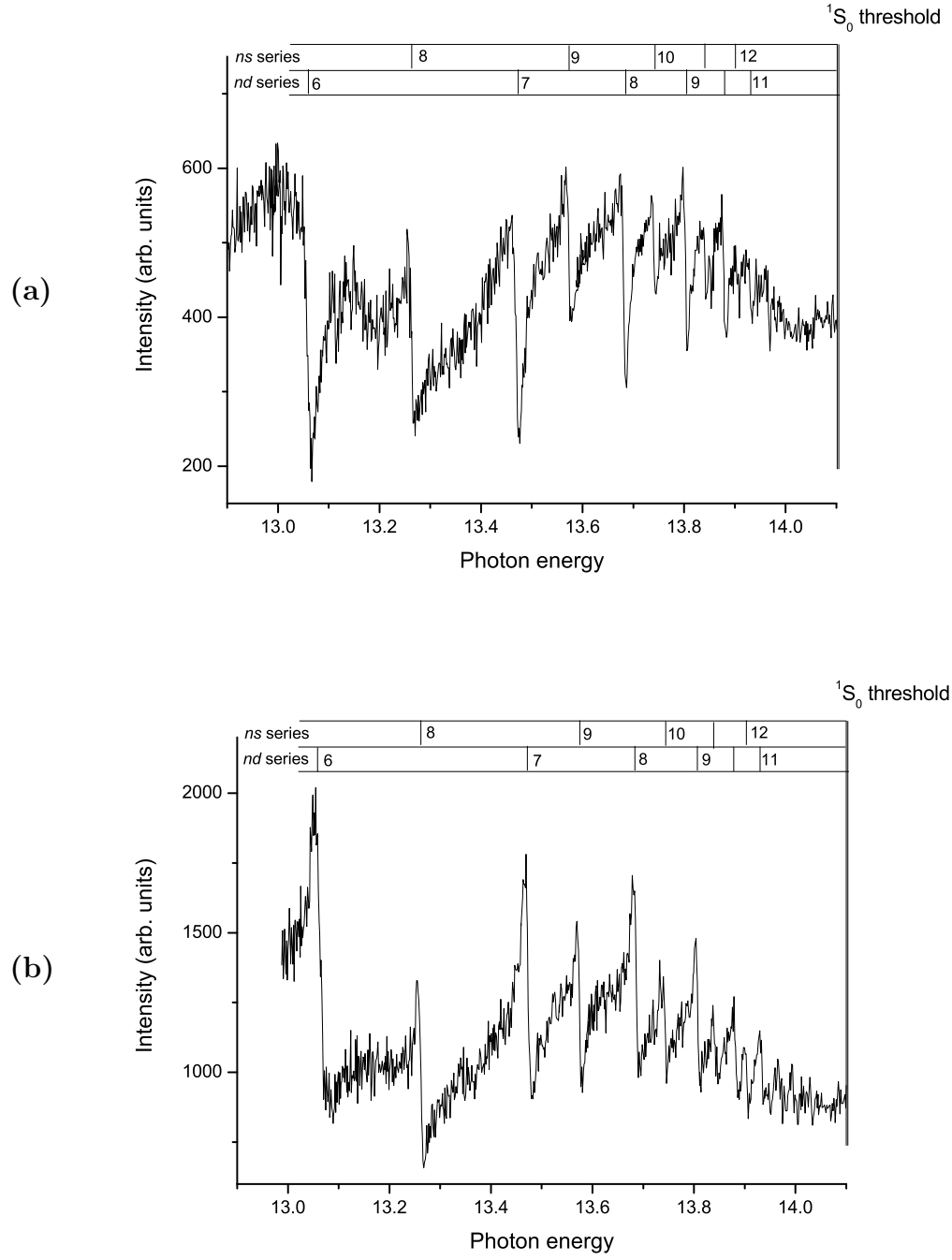

Figure 6.3: CIS spectra recorded over the photon energy region 12.9 to 14.1 eV, showing autoionising resonances converging to the $I^+(^1S_0)$ threshold at 14.109 eV, recorded for the $I^+(^1D_2) \leftarrow I(^2P_{3/2})$ band of iodine atoms. Figure 6.3(a) was recorded at an angle $\theta = 0°$ whereas Figure 6.3(b) was recorded at an angle $\theta = 54°44'$.

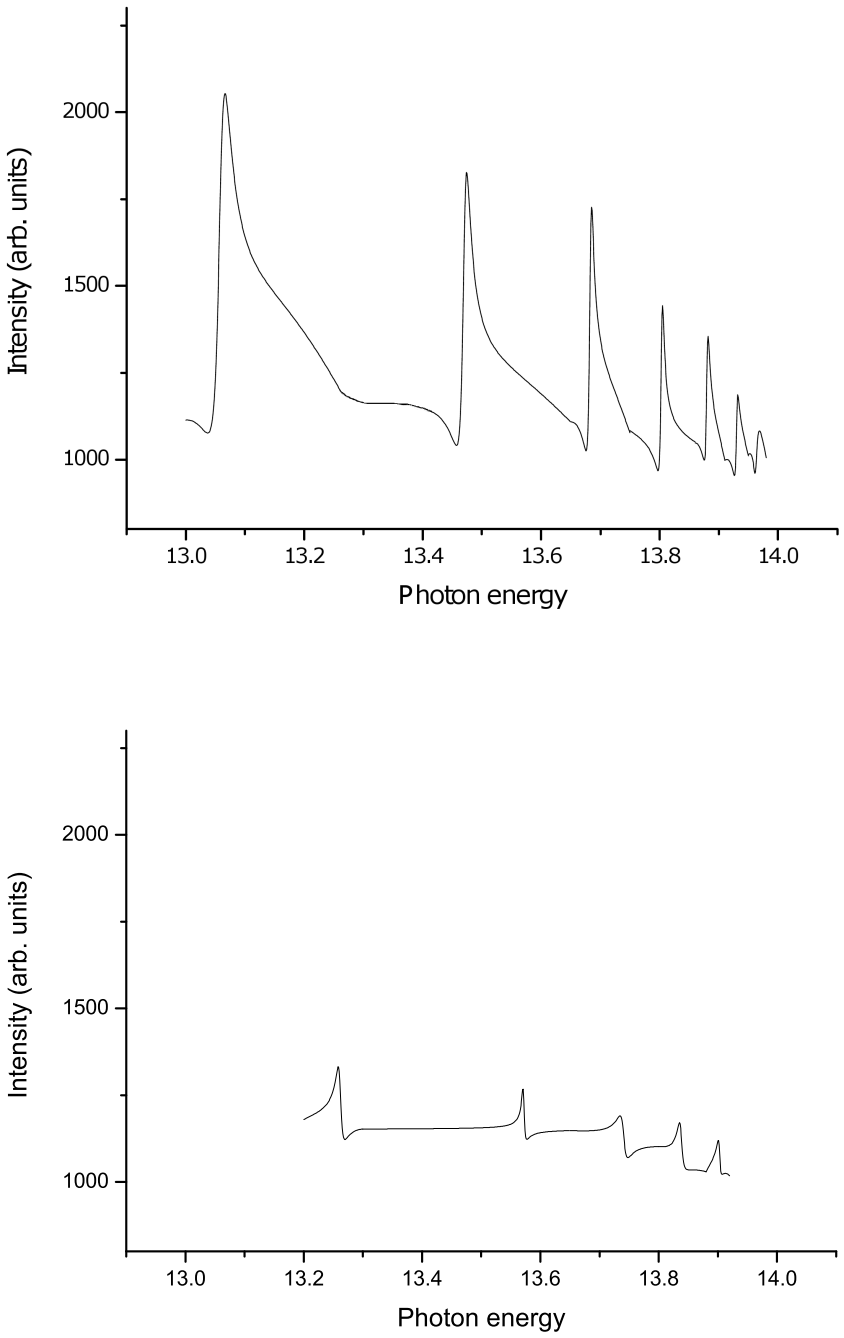

Figure 6.4: Fano fits of the resonances converging to the $I^+(^1S_0)$ threshold at 14.109 eV, recorded for the $I^+(^3P_2) \leftarrow I(^2P_{3/2})$ band of iodine atoms at an angle $\theta = 0°$. Figure 6.4(a) shows *nd* resonances while Figure 6.4(b) shows *ns* resonances. The experimental spectrum is shown in Figure 6.2(a).

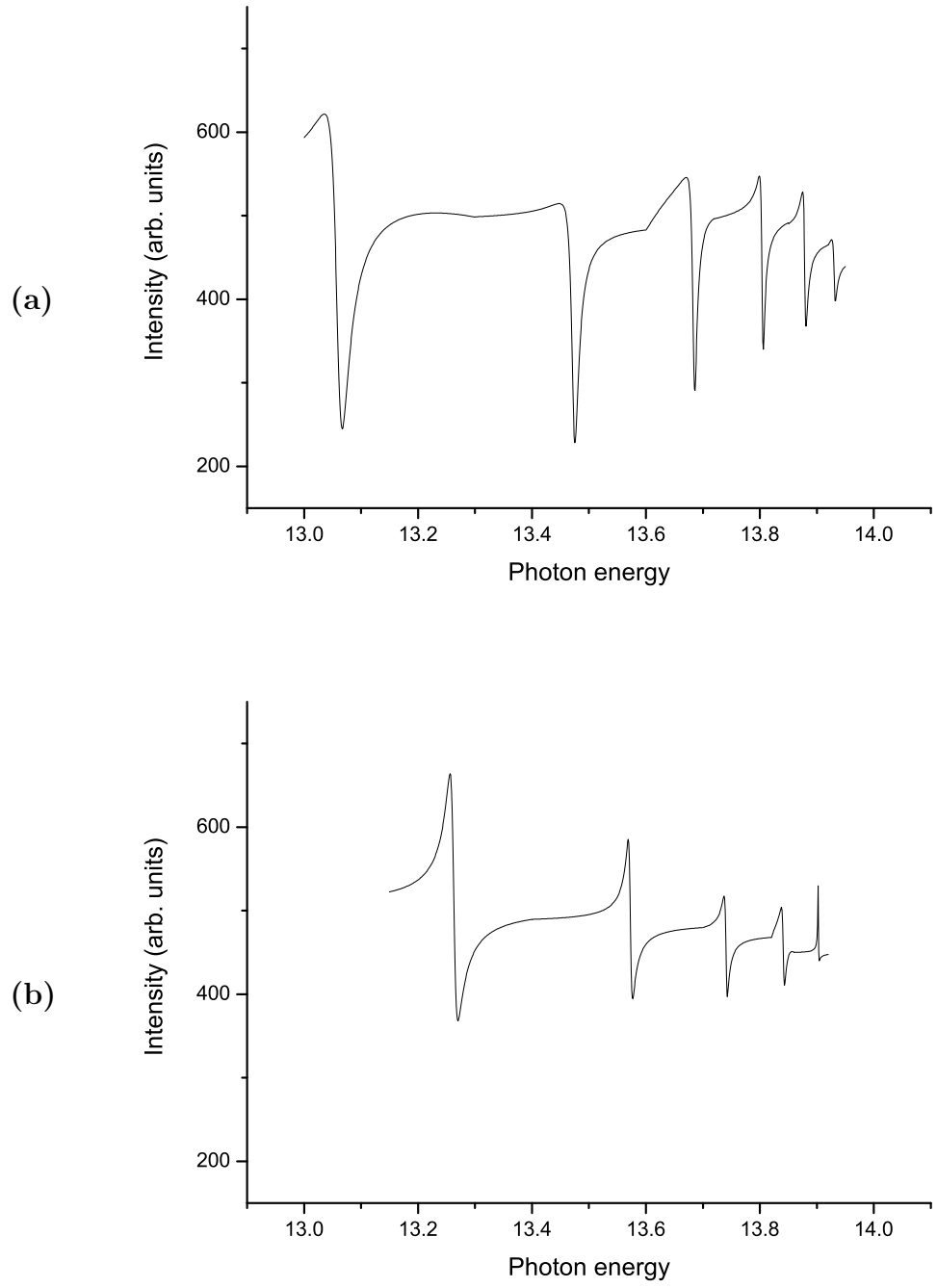

Figure 6.5: Fano fits of the resonances converging to the $I^+(^1S_0)$ threshold at 14.109 eV, recorded for the $I^+(^1D_2) \leftarrow I(^2P_{3/2})$ band of iodine atoms at an angle $\theta = 0°$. Figure 6.5(a) shows *nd* resonances while Figure 6.5(b) shows *ns* resonances. The experimental spectrum is shown in Figure 6.3(a).

E_r (eV)	n^*	n	q	Γ (meV)	ρ^2 ($\times 10^2$)	$\Gamma \times n^{*3}$
1. $ns[0]_{1/2}$ series						
	$\theta = 0°$					
13.262 ± 0.0010	4.01 ± 0.01	8	-1.58 ± 0.41	10.0 ± 1.4	5.4 ± 0.1	0.64 ± 0.09
13.572 ± 0.0008	5.03 ± 0.01	9	-2.01 ± 0.80	5.1 ± 1.5	2.4 ± 0.1	0.66 ± 0.19
13.741 ± 0.0031	6.08 ± 0.04	10	-1.11 ± 0.90	13.0 ± 5.3	4.7 ± 1.0	2.92 ± 1.18
13.837 ± 0.0028	7.08 ± 0.06	11	-2.10 ± 1.98	9.9 ± 4.2	2.2 ± 1.1	3.53 ± 1.49
13.902 ± 0.0014	8.11 ± 0.07	12	-1.56 ± 1.23	5.8 ± 1.9	2.7 ± 0.7	3.11 ± 1.03
	$\theta = 54°44'$					
13.258 ± 0.0008	4.00 ± 0.01	8	-1.75 ± 0.35	8.5 ± 1.4	5.0 ± 0.1	0.54 ± 0.09
13.576 ± 0.0023	5.05 ± 0.02	9	-0.64 ± 0.55	8.6 ± 3.2	9.1 ± 0.8	1.12 ± 0.41
13.736 ± 0.0013	6.04 ± 0.03	10	-1.78 ± 0.72	7.0 ± 1.3	2.8 ± 0.3	1.55 ± 0.58
not seen						
13.900 ± 0.0010	8.06 ± 0.06	12	-2.21 ± 1.41	4.5 ± 2.3	1.2 ± 0.3	2.37 ± 1.20
13.951 ± 0.0013	9.29 ± 0.10	13	-0.89 ± 0.72	1.5 ± 3.1	5.3 ± 4.9	1.18 ± 2.52
2. $nd[2]_{5/2,3/2}$ series						
	$\theta = 0°$					
13.059 ± 0.0005	3.60 ± 0.01	6	1.67 ± 0.09	24.2 ± 0.8	18.4 ± 0.2	1.13 ± 0.04
13.470 ± 0.0003	4.61 ± 0.01	7	1.76 ± 0.07	14.6 ± 0.5	15.5 ± 0.1	1.44 ± 0.05
13.683 ± 0.0003	5.65 ± 0.02	8	1.69 ± 0.12	8.1 ± 0.4	15.1 ± 0.3	1.46 ± 0.08
13.803 ± 0.0003	6.67 ± 0.03	9	1.89 ± 0.15	6.3 ± 0.5	9.8 ± 0.4	1.86 ± 0.15
13.880 ± 0.0005	7.71 ± 0.05	10	1.59 ± 0.27	6.0 ± 0.9	9.4 ± 0.1	2.75 ± 0.43
13.930 ± 0.0007	8.71 ± 0.08	11	1.22 ± 0.27	5.8 ± 1.1	9.2 ± 0.2	3.82 ± 0.77
13.963 ± 0.0009	9.65 ± 0.11	12	0.44 ± 0.16	7.4 ± 2.1	10.9 ± 0.1	6.66 ± 1.93
	$\theta = 54°44'$					
13.056 ± 0.0005	3.59 ± 0.01	6	2.30 ± 0.14	24.4 ± 0.9	12.0 ± 0.02	1.13 ± 0.04
13.468 ± 0.0003	4.61 ± 0.01	7	2.82 ± 0.18	12.2 ± 0.7	8.2 ± 0.02	1.19 ± 0.07
13.681 ± 0.0003	5.64 ± 0.02	8	2.69 ± 0.17	10.0 ± 0.5	7.6 ± 0.02	1.79 ± 0.09
13.803 ± 0.0003	6.66 ± 0.03	9	3.00 ± 0.42	6.9 ± 0.7	5.8 ± 0.08	2.04 ± 0.20
13.878 ± 0.0005	7.67 ± 0.05	10	2.09 ± 0.34	6.2 ± 0.9	6.4 ± 0.11	2.82 ± 0.42
13.929 ± 0.0008	8.70 ± 0.08	11	2.75 ± 0.82	6.3 ± 1.8	3.5 ± 0.3	4.13 ± 1.21
13.966 ± 0.0016	9.74 ± 0.12	12	2.84 ± 1.52	7.4 ± 1.5	2.3 ± 0.6	6.83 ± 3.48
13.990 ± 0.0015	10.70 ± 0.16	13	1.81 ± 1.01	6.5 ± 2.8	3.4 ± 0.6	7.98 ± 3.48

Table 6.3: Energy of resonances converging to the $I^+(^1S_0)$ threshold at 14.109 eV, recorded for the first, $I^+(^3P_2) \leftarrow I(^2P_{3/2})$, band of iodine atoms. Also shown, are the effective and principal quantum numbers, n^* and n, the fitting parameters, q, Γ, ρ and the ratio Γn^{*3} for each Rydberg state.

E_r (eV)	n^*	n	q	Γ (meV)	ρ^2 ($\times 10^2$)	$\Gamma \times n^{*3}$
1. $ns[0]_{1/2}$ series						
	$\theta = 0°$					
13.262 ± 0.0009	4.01 ± 0.01	8	-1.08 ± 0.17	13.8 ± 1.3	27.0 ± 0.1	0.89 ± 0.09
13.573 ± 0.0006	5.04 ± 0.03	9	-1.05 ± 0.17	7.6 ± 1.0	18.8 ± 0.1	0.97 ± 0.13
13.741 ± 0.0005	6.08 ± 0.05	10	-0.77 ± 0.13	5.5 ± 1.0	14.9 ± 0.09	1.23 ± 0.23
13.841 ± 0.0010	7.13 ± 0.09	11	-0.69 ± 0.35	5.1 ± 1.7	13.0 ± 0.4	1.84 ± 0.62
13.902 ± 0.0005	8.11 ± 0.13	12	-2.98 ± 4.62	1.1 ± 4.4	2.0 ± 3.9	0.61 ± 2.34
	$\theta = 54°44'$					
13.261 ± 0.0004	4.00 ± 0.01	8	-1.19 ± 0.09	10.2 ± 0.4	26.3 ± 0.05	0.66 ± 0.05
13.575 ± 0.0005	5.05 ± 0.01	9	-0.92 ± 0.12	6.8 ± 0.7	23.2 ± 0.04	0.88 ± 0.09
13.744 ± 0.0008	6.10 ± 0.03	10	-0.77 ± 0.23	5.4 ± 1.3	16.4 ± 0.3	1.24 ± 0.29
13.839 ± 0.0012	7.10 ± 0.04	11	-2.99 ± 1.62	7.6 ± 2.4	2.1 ± 0.4	2.71 ± 0.87
13.905 ± 0.0008	8.17 ± 0.07	12	-0.68 ± 0.22	5.3 ± 1.4	13.8 ± 0.2	2.89 ± 0.79
2. $nd[2]_{5/2,3/2}$ series						
	$\theta = 0°$					
13.060 ± 0.0009	3.60 ± 0.01	6	-0.52 ± 0.05	26.1 ± 1.8	54.7 ± 0.02	1.22 ± 0.09
13.473 ± 0.0005	4.63 ± 0.01	7	-0.29 ± 0.03	14.8 ± 1.1	53.8 ± 0.02	1.46 ± 0.11
13.684 ± 0.0003	5.66 ± 0.02	8	-0.32 ± 0.03	9.3 ± 0.8	44.8 ± 0.02	1.69 ± 0.15
13.804 ± 0.0004	6.68 ± 0.03	9	-0.56 ± 0.09	5.6 ± 0.8	32.0 ± 0.08	1.68 ± 0.25
13.879 ± 0.0006	7.69 ± 0.05	10	-0.70 ± 0.17	5.8 ± 1.3	22.7 ± 0.3	2.63 ± 0.61
13.931 ± 0.0013	8.73 ± 0.08	11	-0.64 ± 0.34	5.9 ± 2.2	11.6 ± 0.4	3.96 ± 1.47
	$\theta = 54°44'$					
13.060 ± 0.0009	3.60 ± 0.01	6	-1.93 ± 0.19	24.9 ± 1.4	20.0 ± 0.07	1.16 ± 0.07
13.472 ± 0.0004	4.62 ± 0.01	7	-1.42 ± 0.12	8.9 ± 0.8	21.2 ± 0.07	0.88 ± 0.08
13.685 ± 0.0004	5.66 ± 0.02	8	-1.43 ± 0.12	8.9 ± 0.8	17.7 ± 0.06	1.61 ± 0.14
13.806 ± 0.0004	6.70 ± 0.04	9	-1.56 ± 0.17	6.8 ± 0.7	12.3 ± 0.07	2.05 ± 0.23
13.880 ± 0.0014	7.71 ± 0.06	10	-1.70 ± 0.71	8.4 ± 2.3	7.0 ± 0.6	3.85 ± 1.08
13.930 ± 0.0011	8.72 ± 0.08	11	-4.09 ± 1.97	10.5 ± 2.9	1.5 ± 0.2	6.97 ± 1.96

Table 6.4: Energy of resonances converging to the $I^+(^1S_0)$ threshold at 14.109 eV, recorded for the fourth, $I^+(^1D_2) \leftarrow I(^2P_{3/2})$, band of iodine atoms. Also shown, are the effective and principal quantum numbers, n^* and n, the fitting parameters, q, Γ, ρ and the ratio Γn^{*3} for each Rydberg state.

			E_∞ (eV)	$\Delta(E)$ to ref [142](meV)	δ
$ns[0]_{1/2}$ series	$\theta = 0°$	1^{st} band	14.1114 ± 0.0027	2.4	3.79 ± 0.10
		4^{th} band	14.1121 ± 0.0039	3.1	3.77 ± 0.15
	$\theta = 54°44$	1^{st} band	14.1122 ± 0.0086	3.2	3.77 ± 0.36
		4^{th} band	14.1111 ± 0.0042	2.1	3.65 ± 0.15
$nd[2]_{5/2,3/2}$ series	$\theta = 0°$	1^{st} band	14.1116 ± 0.0021	2.6	2.35 ± 0.06
		4^{th} band	14.1116 ± 0.0013	2.6	2.24 ± 0.03
	$\theta = 54°44$	1^{st} band	14.1128 ± 0.0010	3.8	2.34 ± 0.30
		4^{th} band	14.1137 ± 0.0029	4.7	2.27 ± 0.07

Table 6.5: Ionisation energies and quantum defects obtained from the fit of series converging to the $I^+(^1S_0)$ threshold at 14.109 eV. Also shown, is the difference in meV from the value given in ref [142] (14.109 eV).

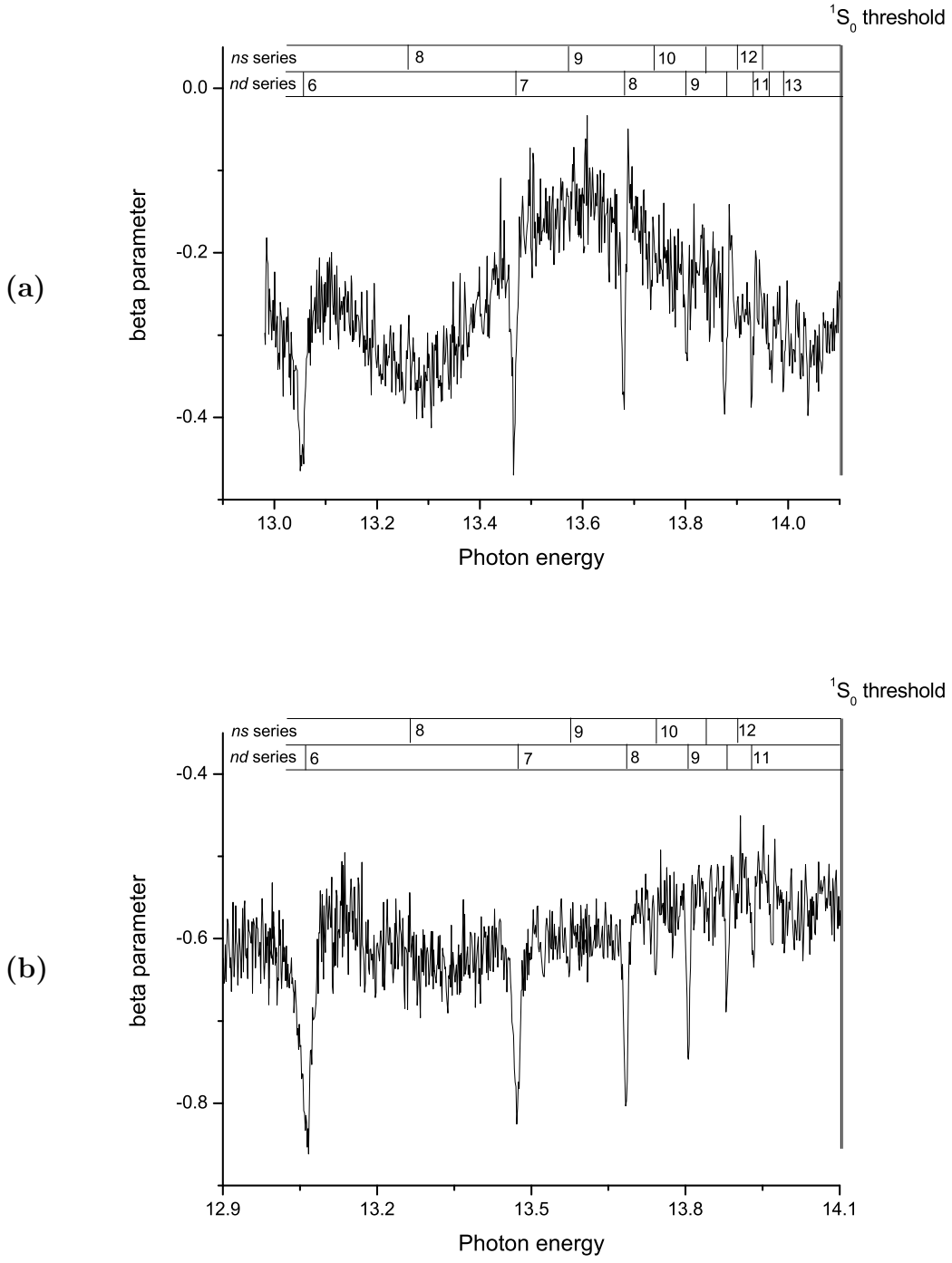

Figure 6.6: Beta plots recorded over the photon energy region 12.9 to 14.1 eV. Spectrum 6.6(a) was recorded for the $I^+(^3P_2) \leftarrow I(^2P_{3/2})$ band of iodine atoms whereas 6.6(b) was recorded for the $I^+(^1D_2) \leftarrow I(^2P_{3/2})$ band of iodine atoms. The resonance positions in the CIS spectra have been marked on for reference

6.4.3 Series converging to the $I^+(^3P_1)$ threshold

Autoionising series converging to the $I^+(^3P_1) \leftarrow I(^2P_{3/2})$ threshold at 11.3298 eV were only recorded for the first PE band, $I^+(^3P_2) \leftarrow I(^2P_{3/2})$, of iodine atoms and are presented in Figure 6.7. Figure 6.7(a) corresponds to spectra recorded at an angle $\theta = 0°$ with respect to the polarisation axis of the radiation and Figure 6.7(b) corresponds to spectra recorded at an angle $\theta = 54°44'$. The resonances are similar in shape at the two angles, even though the relative intensities of the features are different. Of the nine series allowed to converge to the $I^+(^3P_1)$ threshold (Table 6.1), only three appear in the experimental spectra, one ns and two nd series. Two of them were assigned from the work of Berkowitz et al. [142] from mass-analysed photoionisation spectra obtained from atomic iodine (one ns and one nd series), while the third one was assigned from the work of Sarma et. al., in an absorption study of atomic iodine [143] and from the more recent work of Gu et al. [146] where autoionisation in I and I_2 were observed by two photon ionisation, time of flight spectroscopy and mass spectrometry. Unlike series converging to the $I^+(^1S_0) \leftarrow I(^2P_{3/2})$ threshold, the observed series converging to the $I^+(^3P_1) \leftarrow I(^2P_{3/2})$ threshold overlap. Also, the intensity of the members of the series do not have regular patterns. This can be the result of interchannel coupling or coupling with other members of the series. This irregular intensity pattern was previously observed by Benzaid et. al. [158] on their study of bromine atoms and similar series were observed in their work, converging to the $Br^+(^3P_{1,0})$. The fitting of the resonances was much harder for series converging to the $I^+(^3P_1)$ threshold than to the $I^+(^1S_0)$ threshold. Even though the fitting was still made separately for each resonance, it was necessary to look at the series as a whole while fitting individual resonances, and thus fitting of each resonance was carried out several times with slightly different parameters in order to make sure the whole series could be fitted. The results obtained are presented in Table 6.6 with the derived effective and principal quantum number, n^* and n and fitting parameters,

q, Γ, ρ and Γn^{*3}. The trends in the fitting parameters throughout a series are less obvious than for series converging to the $I^+(^1S_0)$ threshold and some of the errors are much bigger. However, it was still possible to obtain reliable results for the $ns[1]_{3/2}$ series and the $nd[1]_{3/2,1/2}$ series. No trends were found in the fitting parameters of the $nd[2]_{5/2,3/2}$ series and only the resonance positions are given in Table 6.6 for this series. The results in Table 6.6 were then used to find the ionisation energy and quantum defect for each series converging to the $I^+(^3P_1) \leftarrow I(^2P_{3/2})$ threshold and these are presented in Table 6.7. The ionisation energies obtained are in good agreement with the value in reference [60, 61] of 11.3298 eV, within experimental error. The quantum defects are greater than the ones obtained for the $I^+(^1S_0) \leftarrow I(^2P_{3/2})$ threshold; ~ 4 instead of 3.7 for the $ns[1]_{3/2}$ series and ~ 2.6 instead of 2.3 for the nd series. The agreement between the series for the ionisation energy and quantum defects is also very good, which shows the reliability of the results. The asymmetry parameter plot in this energy region has no clear structure, as shown in Figure 6.8. It has a mean value of -0.3. The resonance positions from the CIS spectra are marked on the beta plot but none of them can be clearly seen in Figure 6.8.

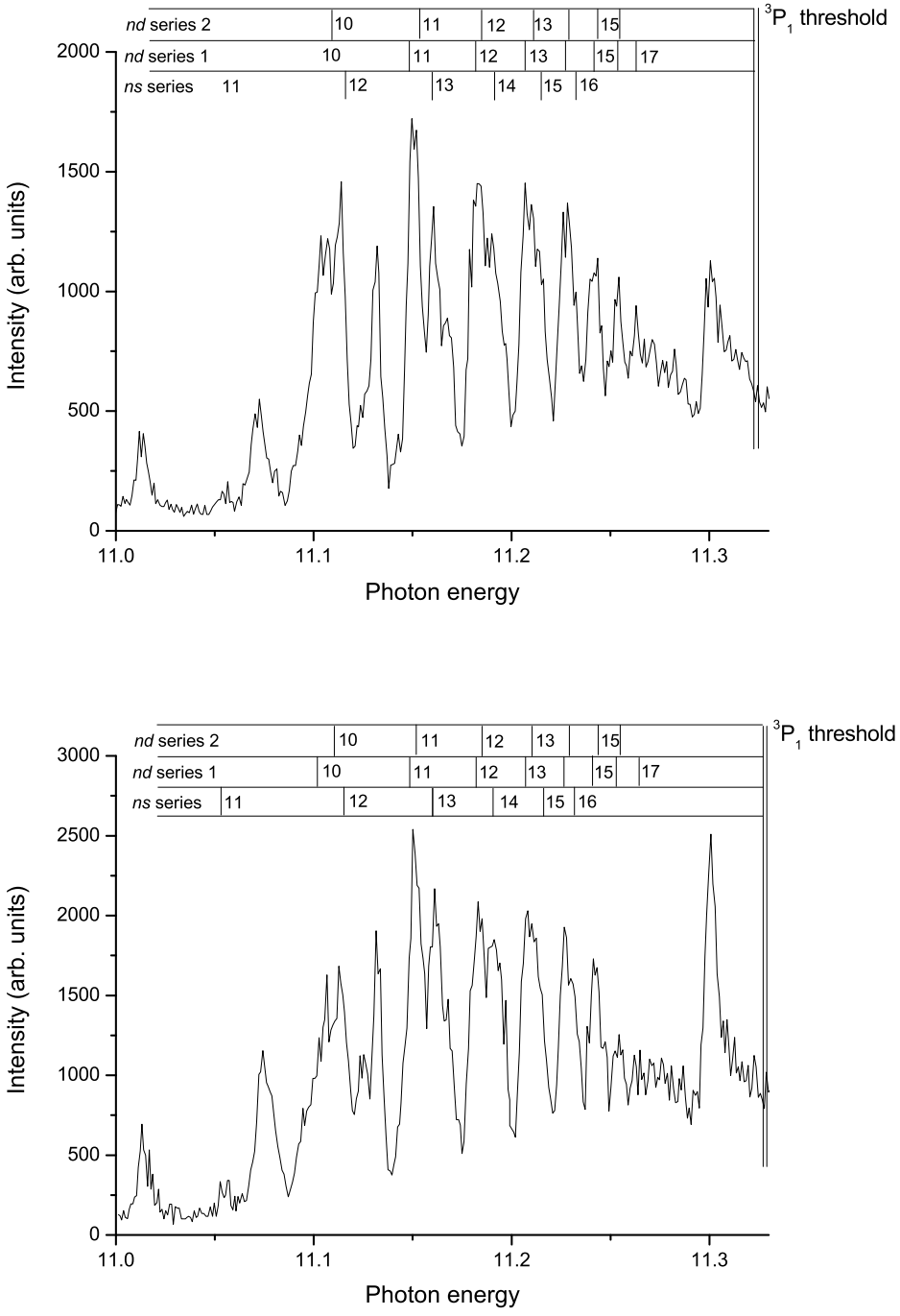

Figure 6.7: CIS spectra recorded over the photon energy region 11.0 to 11.35 eV, for the $I^+(^3P_2) \leftarrow I(^2P_{3/2})$ band of iodine atoms, showing autoionising resonances converging to the $I^+(^3P_1)$ threshold at 11.3298 eV. Spectrum 6.7(a) was recorded at an angle $\theta = 0°$ whereas spectrum 6.7(b) was recorded at an angle $\theta = 54°44'$

E_r (eV)	n^*	n	q	Γ (meV)	ρ^2 ($\times 10^2$)	$\Gamma \times n^{*3}$
1. $ns[1]_{3/2}$ series						
	$\theta = 0°$					
11.052 ± 0.0019	6.99 ± 0.03	11	-2.49 ± 1.86	8.2 ± 4.4	12.0 ± 3.0	2.82 ± 1.51
11.116 ± 0.0003	7.97 ± 0.06	12	-1.60 ± 0.26	5.6 ± 0.5	39.6 ± 20.2	2.86 ± 0.27
11.159 ± 0.0006	8.93 ± 0.08	13	-2.83 ± 1.54	4.9 ± 2.5	11.4 ± 2.0	3.53 ± 1.79
11.192 ± 0.0034	9.93 ± 0.17	14	-2.75 ± 22.18	11.9 ± 5.4	9.4 ± 9.5	11.68 ± 5.33
11.215 ± 0.0036	10.89 ± 0.23	15	-3.24 ± 8.63	9.4 ± 3.5	13.3 ± 29.7	12.11 ± 4.60
11.233 ± 0.0006	11.87 ± 0.19	16	-1.65 ± 1.32	2.2 ± 1.2	12.3 ± 3.4	3.70 ± 2.04
	$\theta = 54°44'$					
11.052 ± 0.0006	7.00 ± 0.04	11	-1.66 ± 0.66	3.0 ± 1.2	28.9 ± 2.0	1.01 ± 0.41
11.115 ± 0.0006	7.96 ± 0.06	12	-2.37 ± 0.70	7.0 ± 1.3	13.7 ± 0.4	3.53 ± 0.64
11.159 ± 0.0024	8.93 ± 0.10	13	-3.47 ± 3.57	11.0 ± 3.5	36.6 ± 144	7.88 ± 2.55
11.190 ± 0.0026	9.87 ± 0.14	14	-7.71 ± 36.43	4.8 ± 8.1	0.3 ± 5.7	4.60 ± 7.76
11.216 ± 0.0049	10.93 ± 0.28	15	-1.67 ± 5.18	7.8 ± 3.5	20.70 ± 46.6	10.22 ± 4.61
11.232 ± 0.0167	11.77 ± 1.17	16	-4.49 ± 50.4	16.3 ± 29.9	5.80 ± 38.9	26.57 ± 49.39
2. $nd[1]_{3/2,1/2}$ series						
	$\theta = 0°$					
11.101 ± 0.0016	7.72 ± 0.06	10	2.31 ± 0.96	18.5 ± 1.6	49.7 ± 8.0	8.54 ± 1.07
11.148 ± 0.0008	8.64 ± 0.07	11	1.41 ± 0.42	8.3 ± 1.6	63.3 ± 7.5	5.35 ± 1.08
11.182 ± 0.0008	9.61 ± 0.10	12	4.07 ± 0.85	15.3 ± 2.7	42.7 ± 7.3	13.56 ± 2.42
11.207 ± 0.0008	10.54 ± 0.14	13	4.17 ± 1.10	13.4 ± 2.7	46.8 ± 22.0	15.76 ± 3.26
11.227 ± 0.0028	11.51 ± 0.24	14	7.65 ± 33.02	11.3 ± 2.8	13.7 ± 0.87	17.28 ± 5.93
11.241 ± 0.0018	12.40 ± 0.25	15	11.39 ± 39.24	8.2 ± 4.7	1.0 ± 9.1	15.61 ± 9.05
11.254 ± 0.0005	13.36 ± 0.27	16	13.74 ± 19.65	3.9 ± 1.4	0.3 ± 15.5	9.31 ± 3.33
11.263 ± 0.0004	14.27 ± 0.33	17	7.19 ± 7.82	1.8 ± 0.8	0.7 ± 20.2	5.65 ± 2.16
	$\theta = 54°44'$					
11.102 ± 0.0203	7.73 ± 0.37	10	3.19 ± 72.08	6.5 ± 20.9	10.9 ± 78	3.01 ± 9.67
11.149 ± 0.0008	8.68 ± 0.07	11	2.74 ± 0.81	10.2 ± 1.2	33.4 ± 0.6	6.67 ± 0.80
11.181 ± 0.0020	9.58 ± 0.12	12	2.88 ± 3.04	9.7 ± 1.0	12.6 ± 11.2	8.52 ± 8.53
11.207 ± 0.0007	10.55 ± 0.14	13	3.73 ± 1.19	9.7 ± 2.0	17.5 ± 0.8	11.35 ± 0.26
11.226 ± 0.0008	11.45 ± 0.17	14	3.68 ± 1.21	9.0 ± 2.6	18.0 ± 3.4	13.49 ± 3.93
11.241 ± 0.0010	12.38 ± 0.23	15	4.64 ± 3.69	7.2 ± 3.3	7.1 ± 2.6	13.69 ± 6.31
11.253 ± 0.0030	13.32 ± 0.39	16	8.09 ± 27.93	9.6 ± 7.8	1.8 ± 32.5	22.72 ± 18.57
11.265 ± 0.0231	14.48 ± 3.61	17	1.29 ± 8.67	2.5 ± 27.1	10.8 ± 49	7.58 ± 82.48

E_r (eV)	n^*	n	
3. $nd[2]_{5/2,3/2}$ series			
	$\theta = 0°$		
11.109 ± 0.0003	7.85 ± 0.05	10	
11.153 ± 0.0011	8.77 ± 0.08	11	line shape fit carried
11.185 ± 0.0009	9.70 ± 0.11	12	out but the data are
11.211 ± 0.0102	10.68 ± 0.51	13	too poor to give
11.227 ± 0.0019	11.53 ± 0.20	14	reasonable parameters
11.244 ± 0.0026	12.57 ± 0.30	15	(q, Γ, ρ^2) for this series
11.254 ± 0.0004	13.40 ± 0.27	16	
	$\theta = 54°44'$		
11.110 ± 0.0006	7.86 ± 0.05	10	
11.153 ± 0.0109	8.78 ± 0.30	11	line shape fit carried
11.186 ± 0.0004	9.74 ± 0.10	12	out but the data are
11.210 ± 0.210	10.66 ± 1.09	13	too poor to give
11.230 ± 0.0082	11.69 ± 0.55	14	reasonable parameters
11.244 ± 0.0008	12.59 ± 0.23	15	(q, Γ, ρ^2) for this series
11.254 ± 0.0039	13.39 ± 0.46	16	

Table 6.6: Energy of resonances converging to the $I^+(^3P_1)$ threshold at 11.3298 eV, recorded for the first, $I^+(^3P_2) \leftarrow I(^2P_{3/2})$, band of iodine atoms. Also shown, are the effective and principal quantum numbers, n^* and n, the fitting parameters, q, Γ, ρ and the ratio Γn^{*3} for each Rydberg state.

		E_∞ (eV)	$\Delta(E)$ to ref [60,61](meV)	δ
$ns[1]_{3/2}$	$\theta = 0°$	11.3293 ± 0.0007	0.5	4.34 ± 0.10
series	$\theta = 54°44$	11.3287 ± 0.0030	1.1	4.35 ± 0.37
$nd[1]_{3/2,1/2}$	$\theta = 0°$	11.3271 ± 0.0010	2.7	2.64 ± 0.18
series	$\theta = 54°44$	11.3271 ± 0.0020	2.7	2.76 ± 0.36
$nd[2]_{5/2,3/2}$	$\theta = 0°$	11.3274 ± 0.0014	2.4	2.79 ± 0.24
series	$\theta = 54°44$	11.3270 ± 0.0017	2.8	2.51 ± 0.28

Table 6.7: Ionisation energies and quantum defects obtained from the fit of series converging to the $I^+(^3P_1)$ threshold at 11.3298 eV. Also shown, is the difference in meV from the value in references [60, 61] of 11.3298 eV.

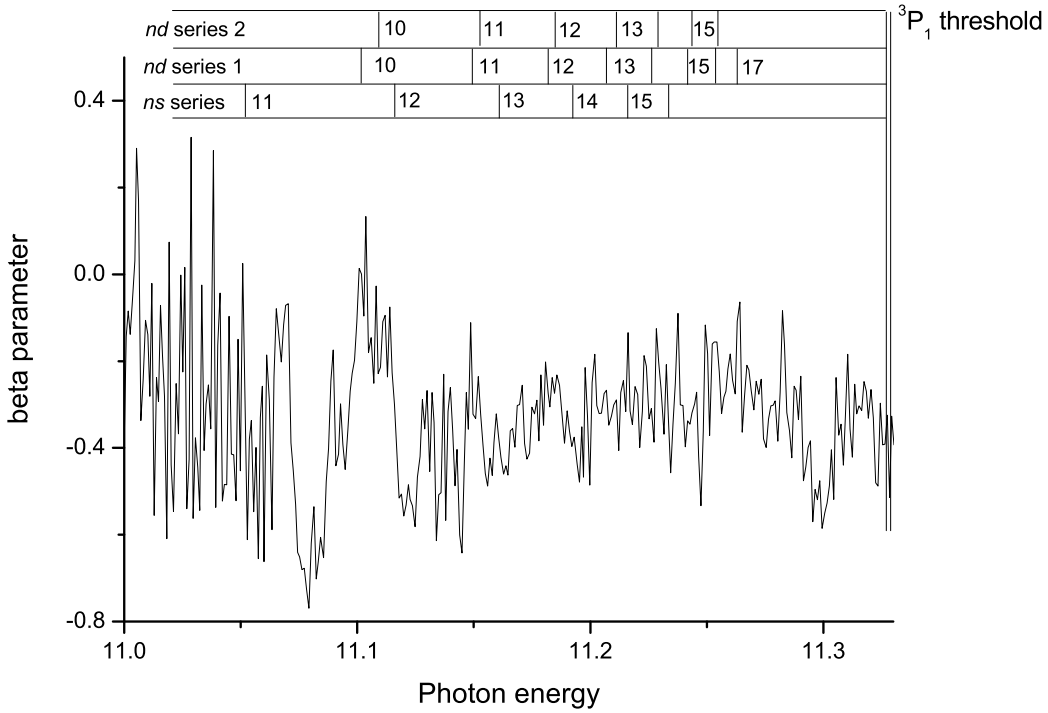

Figure 6.8: Beta plot recorded over the photon energy region 11.00 to 11.33 eV, for the $I^+(^3P_2) \leftarrow I(^2P_{3/2})$ PE band. The resonance positions from CIS spectra have been marked on for reference.

6.4.4 Series converging to the $I^+(^1D_2)$ threshold

As with the series converging to the $I^+(^3P_1)$ threshold, series converging to the $I^+(^1D_2)$ threshold at 12.1532 eV were recorded for only one PE band, the $I^+(^3P_2) \leftarrow I(^2P_{3/2})$ band of iodine atoms. The spectra obtained are shown in Figure 6.9. Figure 6.9(a) was recorded at an angle $\theta = 0°$ with respect to the polarisation axis of the radiation while Figure 6.9(b) was recorded at an angle $\theta = 54°44'$. Again, the shape of the resonances is similar at the two angles but the relative intensities are different. Four series are observed experimentally, out of the twelve that are allowed to converge to this threshold (Table 6.1), two ns and two nd series. Table 6.1 shows that there are only two accessible ns series for this threshold, the $ns[2]_{5/2,3/2}$ series. According to Minnhagen's work [144], the spin-orbit splitting between these two ns series is only 38.12 cm^{-1} (about 5 meV) at $n = 6$. In this work, the splitting between the two ns series is 20 meV at $n = 9$, which is much higher than expected. The $(^1D_2)6s[2]_{3/2}$ resonance observed by Minnhagen is at an energy of 68587.87 cm^{-1} (8.50 eV), which is below the first ionisation energy of atomic iodine. As a result, the value of the splitting for n = 6 could not be verified in this work. In an unperturbed system, the splitting between the two components of a series is expected to go down as n gets higher. However, as iodine is an heavy atom, perturbations via spin-orbit interactions are expected to occur. This can change the splitting between the two components of the series and make it greater for $n = 9$ than for $n = 6$. The initial assignment of Berkowitz [142] of these two series is therefore retained as two distinct ns series, $ns[2]_{5/2}$ and $ns[2]_{3/2}$. According to Minnhagen's work, the $ns[2]_{3/2}$ series is lower in energy. Regarding the nd series, calculations showed that the broad series observed in the single photon ionisation spectrum of atomic chlorine is in fact a superposition of the $I^+(^1D_2)\ nd\ ^2P$ and ^2D series [163, 164]. The narrow series was identified as $I^+(^1D_2)\ nd\ ^2S$. These studies [163, 164] also confirmed the assignment of the ns series as $I^+(^1D_2)\ ns\ ^2D$, which is consistent with the assignment previously made (see Table

6.1). If the same behaviour is observed in atomic iodine, one expects the broad nd series to be a superposition of the $(^1D_2)\ nd\ ^2P$ and $(^1D_2)\ nd\ ^2D$ series. The sharp nd series would then correspond to $(^1D_2)\ nd\ ^2S_{1/2}$ series, which corresponds to the nd $[1,0]_{1/2}$ series (see Table 6.1). Once again, the series observed in the present work closely resemble those observed for bromine atoms in reference [158].

The resonances were fitted with Fano profiles to obtain the resonance positions and fitting parameteres. The results thus obtained are shown in Table 6.8. The fitting of the Rydberg series converging to the $I^+(^1D_2)$ threshold was complicated due to overlapping of the resonances. As can be seen in Table 6.8, the errors in some parameters are large and it was not possible to fit the second nd series. The resonance positions given for this series were obtained by taking the peak maxima. Care was taken to do so in a consistent manner.

The ionisation energies obtained from the resonance energies for each Rydberg series converging to the $I^+(^1D_2)$ threshold are presented in Table 6.9 with the derived quantum defects of the series. The results are in good agreement with previous results of Berkowitz [142]. The ionisation energies obtained agree with the reference value of 12.1532 eV [142] within experimental errors. The quantum defects are similar to the ones obtained for series converging to the $^3P_1$ threshold, i.e, ~ 4.1 for ns series and ~ 2.6 for nd series. Once again, the results are consistent with the four series converging to the $^3P_1$ threshold. This shows that the fitting results are reliable, even though the errors are bigger than for the previous thresholds. The beta plot obtained for this photon energy region is shown in Figure 6.10. It has a mean value of -0.2 with dips going to -0.75. One series is strongly visible on the beta plot, the first nd series. Some components of the second nd series and of the first ns series are also visible, although much weaker.

E_r (eV)	n^*	n	q	Γ (meV)	ρ^2 ($\times 10^2$)	$\Gamma \times n^{*3}$
1. $ns[2]_{5/2}$ series						
	$\theta = 0°$					
11.636 ± 0.0012	5.13 ± 0.02	9	-3.27 ± 0.76	17.6 ± 3.3	5.4 ± 2.1	2.37 ± 0.44
11.787 ± 0.0007	6.10 ± 0.03	10	-8.75 ± 3.46	13.8 ± 2.0	1.3 ± 1.8	3.12 ± 0.45
11.883 ± 0.0018	7.10 ± 0.05	11	-5.73 ± 3.35	27.4 ± 2.6	68.7 ± 24.3	9.83 ± 0.94
11.943 ± 0.0014	8.04 ± 0.06	12	-4.46 ± 2.61	18.8 ± 3.1	31.2 ± 3.4	9.75 ± 1.64
11.988 ± 0.0012	9.07 ± 0.09	13	-1.02 ± 0.34	11.3 ± 1.6	55.9 ± 2.9	8.43 ± 1.20
12.018 ± 0.0016	10.04 ± 0.12	14	-0.68 ± 0.57	9.5 ± 3.5	56.0 ± 3.8	9.63 ± 3.57
12.040 ± 0.0020	10.97 ± 0.17	15	-0.39 ± 0.55	8.0 ± 1.8	46.4 ± 1.4	10.62 ± 2.51
12.056 ± 0.0034	11.86 ± 0.27	16	-0.21 ± 0.69	10.6 ± 2.5	36.5 ± 1.9	17.68 ± 4.37
	$\theta = 54°44'$					
11.635 ± 0.0015	5.12 ± 0.07	9	-1.53 ± 4.31	28.7 ± 19.3	25.8 ± 50.5	3.87 ± 2.60
11.789 ± 0.0006	6.11 ± 0.02	10	-3.81 ± 1.02	9.8 ± 1.5	5.9 ± 0.3	2.25 ± 0.35
11.883 ± 0.0002	7.10 ± 0.04	11	-3.61 ± 0.41	9.6 ± 0.8	9.2 ± 0.7	3.44 ± 0.28
11.944 ± 0.0025	8.07 ± 0.08	12	-1.92 ± 3.57	5.3 ± 4.1	11.3 ± 12.3	2.82 ± 2.18
11.987 ± 0.005	9.05 ± 0.08	13	-2.43 ± 0.74	6.8 ± 1.6	20.8 ± 0.5	5.09 ± 1.23
12.018 ± 0.0005	10.05 ± 0.11	14	-0.92 ± 0.22	5.7 ± 0.8	41.9 ± 0.2	5.78 ± 0.87
12.040 ± 0.0018	10.97 ± 0.17	15	-1.12 ± 1.11	5.3 ± 2.9	14.2 ± 2.8	7.05 ± 3.83
2. $ns[2]_{3/2}$ series						
	$\theta = 0°$					
11.616 ± 0.0020	5.03 ± 0.17	9	-0.39 ± 0.36	10.2 ± 3.6	15.6 ± 0.6	1.30 ± 0.46
11.778 ± 0.0058	6.02 ± 0.05	10	-6.95 ± 52.48	7.7 ± 7.9	1.1 ± 78.2	1.69 ± 1.75
11.873 ± 0.0006	6.97 ± 0.04	11	-1.22 ± 0.98	1.5 ± 0.9	12.6 ± 1.2	0.50 ± 0.31
11.939 ± 0.0006	7.97 ± 0.06	12	-2.15 ± 0.93	4.9 ± 1.0	4.6 ± 0.4	2.49 ± 0.49
11.985 ± 0.0009	9.00 ± 0.08	13	-1.66 ± 0.74	6.0 ± 3.4	18.6 ± 1.4	4.40 ± 2.48
12.017 ± 0.0019	10.00 ± 0.13	14	-1.16 ± 0.92	10.5 ± 3.6	48.1 ± 0.8	10.47 ± 3.62
12.039 ± 0.004	10.91 ± 0.14	15	-0.92 ± 0.23	5.9 ± 0.5	29.7 ± 0.2	7.72 ± 0.69
	$\theta = 54°44'$					
11.612 ± 0.0005	5.01 ± 0.01	9	-0.53 ± 0.12	6.3 ± 1.6	33.3 ± 0.1	0.80 ± 0.21
11.774 ± 0.0004	5.99 ± 0.02	10	-1.24 ± 0.27	6.3 ± 1.4	17.3 ± 0.1	1.35 ± 0.31
11.876 ± 0.0038	7.00 ± 0.06	11	-1.33 ± 39.9	1.3 ± 3.5	18.6 ± 20.3	0.45 ± 12.08
11.939 ± 0.0011	7.97 ± 0.06	12	-0.81 ± 0.46	6.2 ± 4.5	20.6 ± 2.0	3.13 ± 2.27
11.983 ± 0.0006	8.94 ± 0.08	13	-0.86 ± 0.44	2.5 ± 1.5	15.2 ± 0.9	1.81 ± 1.09

E_r (eV)	n^*	n	q	Γ (meV)	ρ^2 ($\times 10^2$)	$\Gamma \times n^{*3}$
3. $nd\ ^2S_{1/2}$ series						
	$\theta = 0°$					
11.500 ± 0.0008	4.56 ± 0.01	7	3.76 ± 0.75	19.5 ± 2.2	101.6 ± 35.1	1.85 ± 0.24
11.713 ± 0.0008	5.56 ± 0.02	8	2.57 ± 0.56	10.7 ± 2.8	39.3 ± 5.9	1.84 ± 0.48
11.834 ± 0.0004	6.53 ± 0.03	9	1.75 ± 0.27	8.9 ± 0.7	70.5 ± 0.8	2.47 ± 0.20
11.908 ± 0.0007	7.44 ± 0.05	10	0.78 ± 0.27	9.8 ± 1.9	89.7 ± 0.1	4.05 ± 0.79
11.962 ± 0.0004	8.43 ± 0.07	11	2.16 ± 0.62	7.6 ± 0.4	41.5 ± 0.4	4.59 ± 0.27
11.999 ± 0.0008	9.38 ± 0.09	12	2.14 ± 1.04	9.3 ± 0.9	67.9 ± 1.2	7.70 ± 0.78
12.029 ± 0.0012	10.47 ± 0.14	13	6.26 ± 3.70	12.2 ± 3.5	6.2 ± 1.6	14.01 ± 4.09
12.047 ± 0.0350	11.34 ± 2.53	14	6.21 ± 147	16.8 ± 35.0	10.6 ± 154	24.49 ± 46.80
12.068 ± 0.0006	12.63 ± 0.23	15	0.91 ± 0.38	3.1 ± 1.1	10.6 ± 0.4	6.27 ± 2.23
	$\theta = 54°44'$					
11.509 ± 0.0013	4.59 ± 0.01	7	2.83 ± 1.56	10.1 ± 2.4	7.2 ± 1.1	0.98 ± 0.23
11.714 ± 0.0011	5.56 ± 0.02	8	2.07 ± 0.66	13.9 ± 4.9	93.7 ± 54.1	2.40 ± 0.84
11.836 ± 0.0006	6.55 ± 0.03	9	1.86 ± 0.39	10.8 ± 0.8	73.3 ± 8.4	3.04 ± 0.24
11.908 ± 0.0017	7.45 ± 0.05	10	0.57 ± 0.58	7.5 ± 2.2	79.8 ± 2.7	3.12 ± 0.91
11.965 ± 0.0018	8.50 ± 0.08	11	1.06 ± 1.29	5.3 ± 7.0	7.9 ± 1.6	3.25 ± 4.33
12.002 ± 0.0025	9.49 ± 0.12	12	3.04 ± 2.39	11.6 ± 7.8	6.1 ± 8.0	9.95 ± 6.73
12.029 ± 0.0023	10.48 ± 0.16	13	7.49 ± 14.92	14.5 ± 4.4	22.8 ± 39.3	16.76 ± 5.16
4. $nd\ ^2P + {}^2D$						
	$\theta = 0°$					
11.559 ± 0.0012	4.78 ± 0.01	7				
11.744 ± 0.0010	5.77 ± 0.02	8	the data are too poor to give			
11.854 ± 0.0010	6.74 ± 0.03	9	reasonable parameters (q, Γ, ρ^2)			
11.925 ± 0.0011	7.72 ± 0.05	10	for this series, resonance			
11.973 ± 0.0006	8.69 ± 0.07	11	positions taken as band maxima			
12.009 ± 0.0006	9.71 ± 0.10	12				
	$\theta = 54°44'$					
11.565 ± 0.0010	4.81 ± 0.01	7				
11.748 ± 0.0010	5.79 ± 0.02	8	the data are too poor to give			
11.859 ± 0.0008	6.68 ± 0.04	9	reasonable parameters (q, Γ, ρ^2)			
11.928 ± 0.0008	7.77 ± 0.05	10	for this series, resonance			
11.976 ± 0.0006	8.76 ± 0.08	11	positions taken as band maxima			
12.011 ± 0.0006	9.78 ± 0.11	12				

Table 6.8: Energies of Rydberg states which are parts of series converging to the $I^+(^1D_2)$ threshold at 12.153 eV, recorded for the first, $I^+(^3P_2) \leftarrow I(^2P_{3/2})$, band of iodine atom. Also shown, are n^*, n and q.

		E_∞ (eV)	$\Delta(E)$ to ref [142](meV)	δ
$ns[2]_{5/2}$	$\theta = 0°$	12.1514 ± 0.0016	1.8	4.03 ± 0.13
series	$\theta = 54°44$	12.1507 ± 0.0007	2.5	3.90 ± 0.06
$ns[2]_{3/2}$	$\theta = 0°$	12.1539 ± 0.0022	0.7	4.24 ± 0.16
series	$\theta = 54°44$	12.1522 ± 0.0028	1.0	4.13 ± 0.17
$nd\ ^2S_{1/2}$	$\theta = 0°$	12.1520 ± 0.0028	1.2	2.62 ± 0.15
series	$\theta = 54°44$	12.1523 ± 0.0030	0.9	2.63 ± 0.14
$nd\ ^2P + {}^2D$	$\theta = 0°$	12.1521 ± 0.0013	1.2	2.36 ± 0.07
series	$\theta = 54°44$	12.1528 ± 0.0011	0.4	2.25 ± 0.06

Table 6.9: Ionisation energies obtained from the fits with their errors, as well as the difference from the reference value [142] and the quantum defect of the series converging to the $I^+(^1D_2)$ threshold at 12.1532 eV

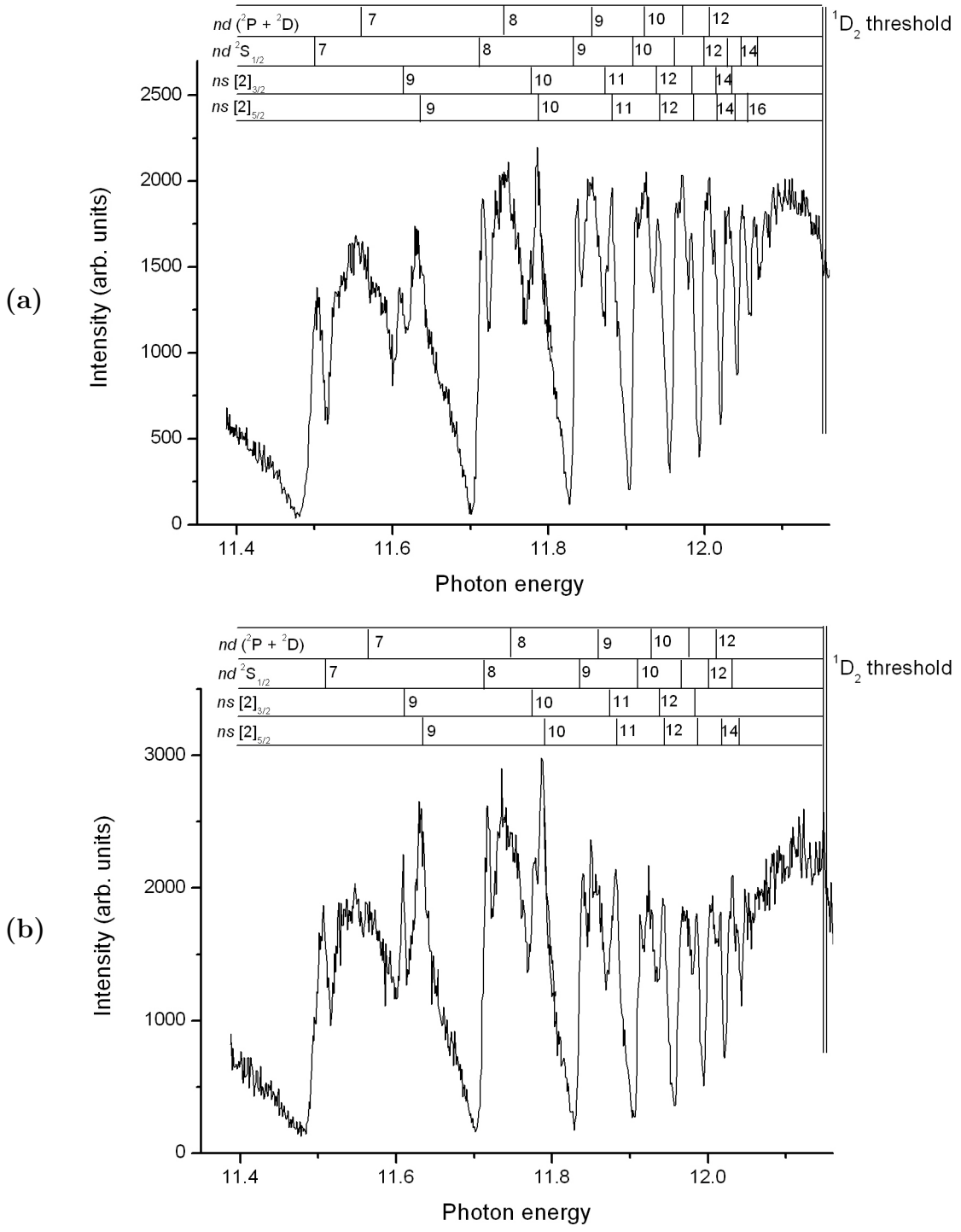

Figure 6.9: CIS spectra recorded over the photon energy region 11.4 to 12.2 eV, for the $I^+(^3P_2) \leftarrow I(^2P_{3/2})$ band of iodine atoms, showing autoionising resonances converging to the $I^+(^1D_2)$ threshold at 12.153 eV. Spectrum 6.9(a) was recorded at an angle $\theta = 0°$ whereas spectrum 6.9(b) was recorded at an angle $\theta = 54°44'$

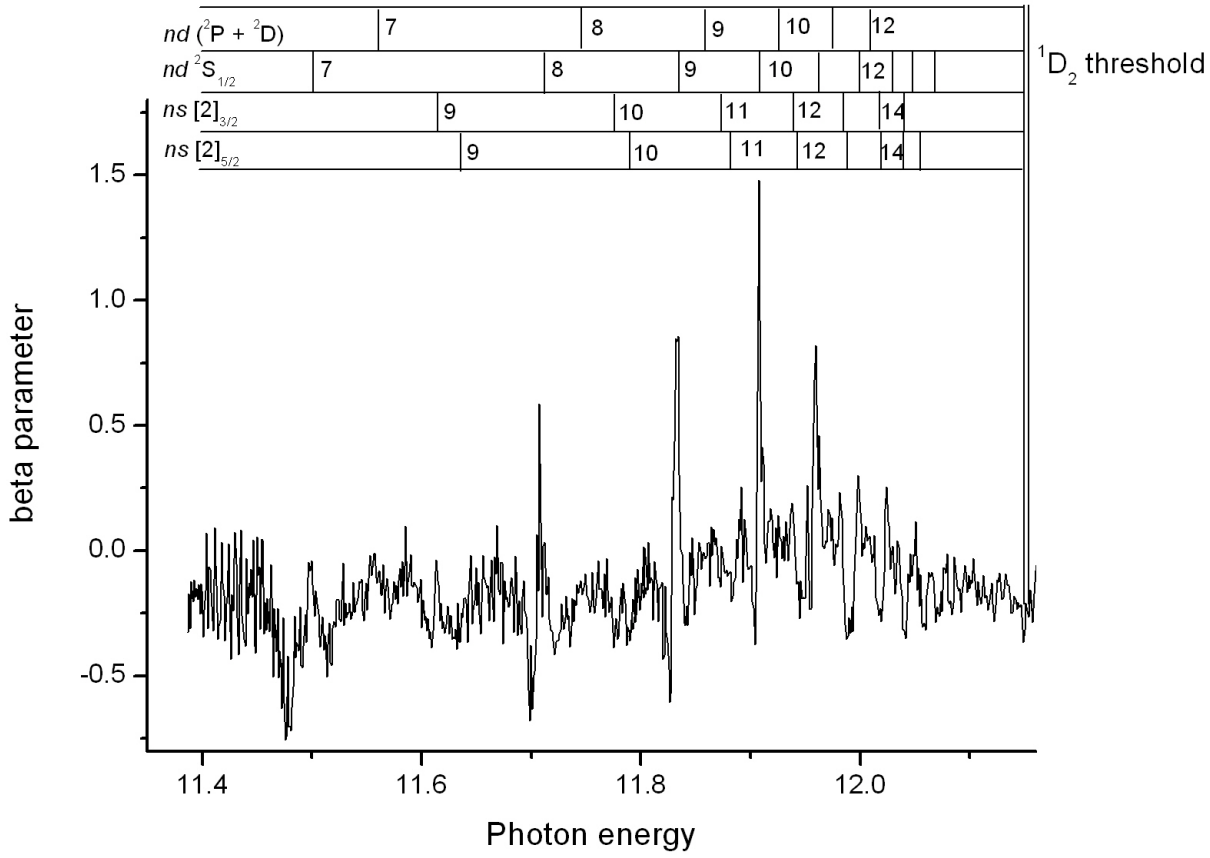

Figure 6.10: Beta plot recorded over the photon energy region 11.4 to 12.3 eV, for the $I^+(^3P_2) \leftarrow I(^2P_{3/2})$ PE band. The resonance positions from the CIS spectra have been marked on for reference.

6.4.5 $(5s)^{-1}$ ionisations

CIS spectra were also recorded in the photon energy region of the $(5s)^{-1}$ thresholds ($^3P_{2,1,0}$, $^1P_1$), for both PE bands of iodine atoms, the $I^+(^3P_2) \leftarrow I(^2P_{3/2})$ band and the $I^+(^1D_2) \leftarrow I(^2P_{3/2})$ band. The values of the $(5s)^{-1}$ thresholds, $I^+..5s^15p^5\ ^3P_{2,1,0}$ and $^1P_1$, have been obtained experimentally by resonant $I^*..4d^95s^25p^6\ ^2D_{5/2}$ excitation in atomic iodine, produced by laser-induced dissociation of molecular iodine, by Nahon et. al. [165]. The PE spectrum recorded on this resonance show few lines corresponding to the $5s^15p^5$ configuration, associated with the $^3P_{2,1,0}$ and $^1P_1$ ionic states. They are shown in Table 6.10 and compared with values obtained from electronic absorption results by Minnhagen [144]. The CIS spectra obtained in this work in the $(5s)^{-1}$ threshold region (17.5 to 22.5 eV) are not good enough for analysis with Fano fitting as the signal to noise ratio is quite poor. However, Meyer et. at. [166] studied the autoionisation of the $5s - np$ resonances of atomic iodine by photoelectron spectroscopy in the same photon energy region. The results he obtained by monitoring CIS spectra of the $I^+..5s^25p^4\ ^3P_2$, $^3P_{0,1}$ and $^1D_2 \leftarrow I^2P_{3/2}$ bands are shown in Figure 6.11. Figure 6.12 shows CIS spectra recorded for the $I^+..5s^25p^4\ ^3P_2$ and $^1D_2 \leftarrow I^2P_{3/2}$ bands, in the present work, in the same energy range. Even though it is not explicitly stated in ref [166], the first ^3P threshold seen in Figures 6.11 and 6.12 corresponds to the $I^+5s^15p^5\ ^3P_2$ threshold while the second one corresponds to the $I^+5s^15p^5\ ^3P_{1,0}$ threshold. Meyer et al. [166] assigned some of the resonances converging to the $I^+..5s^15p^5\ ^3P$ and ^1P thresholds by comparison with Xe. However, Xe has a much simpler structure as it has only one main $(5s)^{-1}$ threshold at 23.4 eV [166]. Meyer et al. also made a theoretical study of the $(5s)^{-1}$ ionisations of atomic iodine but the complexity of the experimental spectra only allowed few resonances to be assigned. The $I^*..5s^15p^5(^3P_2)$ 6p and 7p components were assigned to resonances at 18.25 eV and 19.43 eV and are also seen in the present work. The $I^*..5s^15p^5(^3P_{1,0})$ 6p component was tentatively assigned to the resonance

at 18.63 eV. Higher members of the series are situated in regions where many lines are found so only tentative assignments were made. Most of the lines converging to the $^1P_1$ threshold are thought to be satellites for which the core configuration is I*..$5s^2 5p^3 5d\ nd$. Assignment of the lines converging to the $^1P_1$ threshold are only tentative. The agreement between Meyer's work and the present work in this photon energy range is in general very good. The positions of the resonances, marked on the spectrum according to Meyer's work, are shown in Figure 6.12. In order to pursue this work further on the $(5s)^{-1}$ ionisations of atomic iodine, the spectra should be recorded again with better statistics, in order to improve the signal to noise ratio and allow a more definite assignment of the features.

Electron configuration	Energy from Minnhagen [144] (eV)	Energy from Nahon [165] (eV)
$I^+\ 5s^1 5p^5\ ^3P_2$	20.61	20.80
$I^+\ 5s^1 5p^5\ ^3P_1$	20.89	
$I^+\ 5s^1 5p^5\ ^3P_0$	21.04	21.30
$I^+\ 5s^1 5p^5\ ^1P_1$	22.35	22.29

Table 6.10: Energy levels of the $(5s)^{-1}$ ionisations in atomic iodine

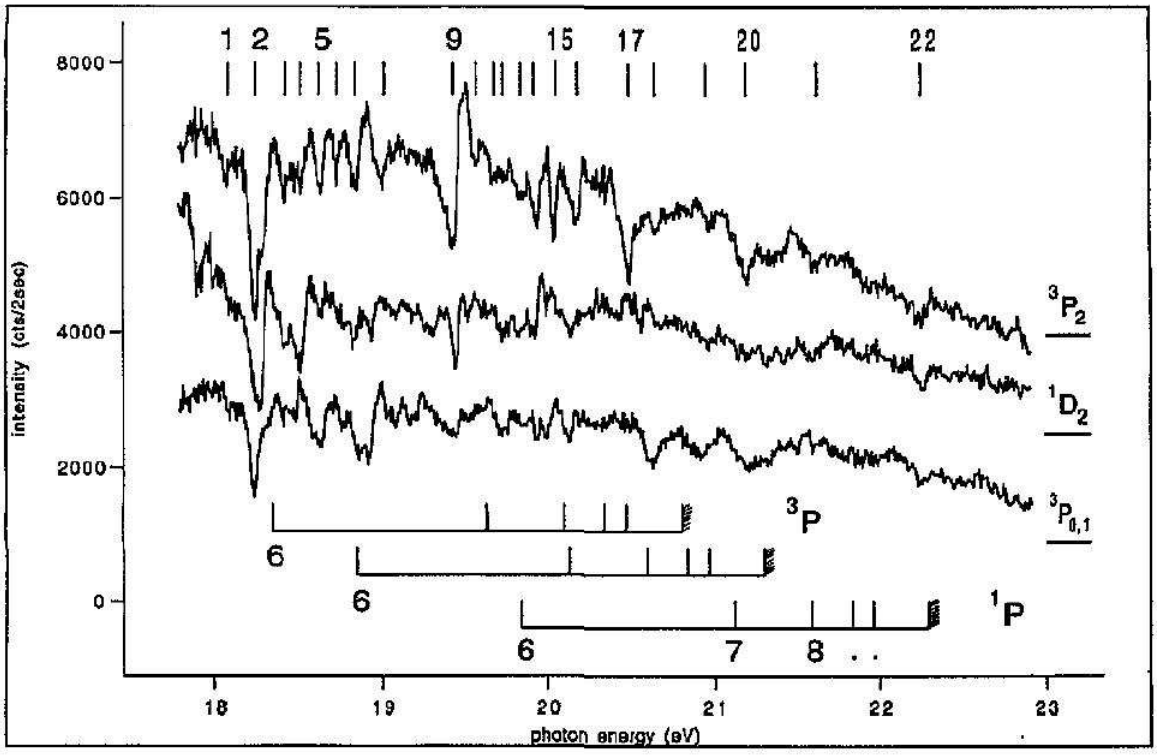

Figure 6.11: CIS spectra of $I^+5s^25p^4\ {}^3P_2, {}^3P_{0,1}$ and $^1D_2 \leftarrow I^2P_{3/2}$ bands of atomic iodine in the region $5s - np$ resonances and $5s^{-1}$ thresholds, as obtained by Meyer et. al. [166].

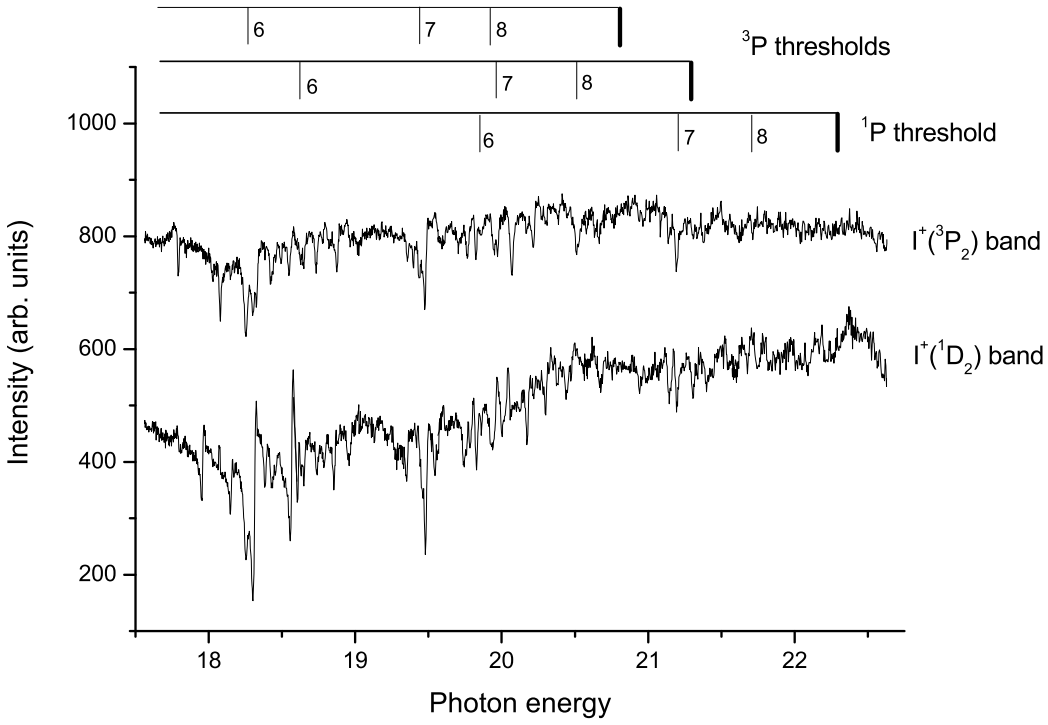

Figure 6.12: CIS spectra obtained in the present work of the $I^+5s^25p^4\ ^3P_2$ and $^1D_2 \leftarrow I^2P_{3/2}$ bands of atomic iodine in the region of the $5s - np$ resonances and $(5s)^{-1}$ thresholds (17.5 to 22.5 eV). Even though no analysis of these spectra were carried out, the main series identified in the work of Meyer et al. [166] have been marked on for comparison.

6.5 Angular distribution

6.5.1 Overview

An overview of the beta parameter plot determined over the whole photon energy range is presented in Figure 6.13. Figure 6.13(a) shows the beta plot determined for the first, $I^+(^3P_2) \leftarrow I(^2P_{3/2})$, PE band of iodine atoms in the photon energy range 11 to 23 eV while Figure 6.13(b) shows the beta plots determined for the fourth, $I^+(^1D_2) \leftarrow I(^2P_{3/2})$, PE band of iodine atoms in the photon energy range 12.5 to 23 eV. As can be seen from the spectra, the beta parameter plots are very different for each PE band. In the first band, the asymmetry parameter has a constant mean value of about -0.3 and shows some oscillations between 11 and 18 eV. The oscillations are not regular in intensity nor frequency but the mean value of the beta parameter is constant throughout the PE band. On the other hand, the asymmetry parameter for the fourth band of iodine atoms has very few oscillations but increases regularly. It rises from -0.6 at 12.5 eV to 1.6 at 23 eV. The fact that the beta plots for the two bands are different can be explained with the Cooper Zare formula (see Chapter 2):

$$\beta = \frac{l(l-1)R_{l-1}^2 + (l+1)(l+2)R_{l+1}^2 - 6(l+1)R_{l+1}R_{l-1}cos(\delta_{l+1} - \delta_{l-1})}{(2l+1)[lR_{l-1}^2 + (l+1)R_{l+1}^2]} \qquad (6.5.1)$$

The first term in this equation is zero since $(l-1) = 0$ for an electron initially in a p orbital. The remaining two terms are the contribution from the d wave and the cosine interference term. The Xe $5p \rightarrow \epsilon d$ partial photoionisation cross section varies smoothly with the photon energy as can be seen in reference [167]. On increasing the photoelectron energy from zero, the Xe $5p \rightarrow \epsilon d$ cross-section goes down. If a similar behaviour is observed in atomic iodine, the interference term in the first PE band of iodine atoms should just balance the d wave contribution since the mean beta value is

constant throughout the PE band. The interference term of the fourth band should be stronger than for the first band since the beta parameter goes up throughout the PE band. However, the Cooper Zare model does not consider the exchange between the ion core and the escaping electron and is thus most accurate for a closed shell system (see Chapter 2). The halogens atoms are a stepping stone between closed shell and open shell systems and a departure from the Cooper Zare model is thus expected.

Also, since the JK coupling scheme is more appropriate for atomic iodine, an investigation of the parity favoured/unfavoured ionisation channels might provide more information on the value of the beta parameter. Photoionisation can be accompanied by a transfer of angular momentum between the neutral atom and the atomic ion including the spin of the photoelectron. The photoelectron ejection can thus be schematically represented as [46]:

$$X(J_0\pi_0) + h\nu(j_{h\nu} = 1, \pi_{h\nu} = -1) \rightarrow X^+(J_c\pi_c) + e^{-1}[lsj, \pi_e = (-1)^l] \tag{6.5.2}$$

where $X(J_0\pi_0)$ and $X^+(J_c\pi_c)$ represent the atom and resultant ion, with total angular momentum J and parity π. The angular momentum transferred between the molecule and the ion and photoelectron, j_t, is defined by:

$$\vec{j_t} = \vec{j_{h\nu}} - \vec{l} = \vec{J_c} + \vec{s} - \vec{J_0} \tag{6.5.3}$$

where $\vec{J_0} + \vec{j_{h\nu}} = \vec{J_c} + \vec{s} + \vec{l}$. The conservation of parity π also implies:

$$\pi_{h\nu}\pi_0 = \pi_c\pi_e \tag{6.5.4}$$

which, in the electric dipole approximation reduces to

j_t	l odd	β	l even	β
0	1	2		
1	1	-1	0	0
			2	1
2	1	1/5	2	-1
	3	4/5		
3	3	-1	2	2/7
			4	5/7
4	3	3/9	4	-1
	5	6/9		

Table 6.11: The asymmetry parameter β for different values of the angular momentum transfer j_t [168]

$$\pi_c \pi_0 = (-1)^{l+1} \tag{6.5.5}$$

The parity transfer, π_t is defined as the difference in parities between the neutral and ionic states. If π_t matches j_t (both odd or both even), then the partial cross section is parity favoured. When π_t and j_t are mismatched (one odd, the other even) then the partial cross section is parity unfavoured and the asymmetry parameter, β_{unf} is -1; hence the angular distribution is energy independent. Table 6.11 shows values of the asymmetry parameter β at different values of the angular momentum transfer j_t obtained from the work of Dill and Fano [47] by Chang [168].

In general, the asymmetry parameter is given as a weighted average of the various $\beta(j_t)$:

$$\beta = \Sigma_{Jcs}\left(\frac{\Sigma_{j_t}^{fav}\sigma(j_t)_{fav}\beta(j_t)_{fav} - \Sigma_{j_t}^{unf}\sigma(j_t)_{unf}}{\sigma}\right) \tag{6.5.6}$$

The results shown in Table 6.11 can be used to obtain values of $\beta(j_t)$ for specific ionisation channels and thus help the understanding of the experimental spectra. As an example, the case of xenon is considered:

$$h\nu + Xe(5s^25p^6)^1S \rightarrow Xe^+(5s^25p^5)^2P_{1/2,3/2} + e^{-1} \tag{6.5.7}$$

For the $^2P_{1/2}$ ion, $\vec{j_t} = \vec{J_c} + \vec{s}$ - $\vec{J_0} = 1\vec{/}2 + 1\vec{/}2$ - $\vec{0} = 0$, 1 and $\pi_c\pi_0$ = odd. From equation 6.5.5, l must be even. For l even, it is not possible to have a value of $j_t = 0$; j_t is restricted to $|l-1|$ (see Table 6.11). Table 6.11 also shows that for $j_t = 1$, l can have two values, 0 or 2 with values of $\beta(j_t)$ of 0 or 1 respectively. π_t is odd, which matches j_t and hence, the partial cross section is parity favoured.

For the $^2P_{3/2}$ ion, $\vec{j_t} = 3\vec{/}2 + 1\vec{/}2$ - $\vec{0} = 0$, 1, 2. $\pi_c\pi_0$ = odd and l must be even (j_t = 0 is not possible). Table 6.11 shows that for $j_t = 1$, l can have two values, 0 or 2 with values of $\beta(j_t)$ of 0 or 1 respectively. Since π_t is odd, the partial cross section is parity favoured for $j_t = 1$. However, for $j_t = 2$, $l = 2$, $\beta(j_t)$ = -1; the partial cross section is parity unfavoured. The beta parameter for transition to the Xe^+ $^2P_{3/2}$ ion, will therefore contain both parity favoured and parity unfavoured partial cross sections.

Now, looking at the case of iodine atoms for direct ionisation from the ground state $I(5s^25p^5)$ $^2P_{3/2}$ to the ground ionic state $I^+(5s^25p^4)$ $^3P_2$:

$$h\nu + I(5s^25p^5)^2P_{3/2} \rightarrow I^+(5s^25p^4)^3P_2 + e^{-1} \tag{6.5.8}$$

In this transition, $\vec{j_t} = \vec{2} + 1\vec{/}2$ - $3\vec{/}2 = 0$, 1, 2, 3, 4. $\pi_c\pi_0$ = odd, l must be even. π_t is

also odd ($j_t = 0$ is not possible).

$$For\ \ j_t = 1, l = 0\ \ or\ \ 2, \beta(j_t) = 0\ \ or\ \ 1\ \ respectively \tag{6.5.9}$$

$$For\ \ j_t = 2, l = 2, \beta(j_t) = -1,\ \ parity\ \ unfavoured \tag{6.5.10}$$

$$For\ \ j_t = 3, l = 2\ \ or\ \ 4, \beta(j_t) = 2/7\ \ or\ \ 5/7\ \ respectively \tag{6.5.11}$$

$$For\ \ j_t = 4, l = 4, \beta(j_t) = -1,\ \ parity\ \ unfavoured \tag{6.5.12}$$

$$\tag{6.5.13}$$

When j_t is odd, it matches with the parity transfer π_t and the partial cross section is parity favoured. In contrast, when j_t is even, the partial cross section is parity unfavoured and beta becomes -1. In the present work, the beta parameter was determined for the first and fourth PE band of iodine atoms, i.e. the $I^+(^3P_2) \leftarrow I(^2P_{3/2})$ and $I^+(^1D_2) \leftarrow I(^2P_{3/2})$ bands of iodine atoms. However, in this method of analysis, only the J quantum number is of importance so that the same results apply for transitions to the first PE band and to the fourth PE band. The beta parameter for iodine atoms for these two PE bands will therefore be a weighted average of parity favoured and parity unfavoured partial cross sections. This can be seen in Figure 6.13. In Figure 6.13 (a), recorded for the first PE band of iodine atoms, the general background of the beta parameter is approximately - 0.25, so both the parity favoured and unfavoured j_t terms are clearly playing a part. In Figure 6.13 (b), recorded for the fourth band of iodine atoms, the beta parameter starts at -0.6 at 13 eV but slowly increases to 1.5 at 23 eV. This shows that the weight of the different $\beta(j_t)$ terms vary with photon energy. The parity unfavoured $\beta(j_t)$ contributions are stronger near threshold and are slowly giving way to the parity favoured $\beta(j_t)$. In both figures, the beta parameter shows sharp excursions at resonances.

One must therefore look at the autoionisation process, i.e. the decay from the

resonance state to the ionic state:

$$I^*(5s^2 5p^4, nd) \rightarrow I^+(5s^2 5p^4)^3P_2 + e^{-1} \tag{6.5.14}$$

This process does not involve a photon, as a result, equation 6.5.5 modifies to:

$$\pi_c \pi_0 = (-1)^l \tag{6.5.15}$$

From the excited neutral state $I^*(5s^2 5p^4, nd)$, i.e. $I^*(^1D_2, nd)$, it is possible to obtain the following states: $^2S_{1/2}$, $^2P_{1/2,3/2}$, $^2D_{3/2,5/2}$, $^2F_{5/2,7/2}$ and $^2G_{7/2,9/2}$.

Taking as example a decay from a state with J = 3/2; $\vec{j_t} = \vec{2} + 1\vec{/}2 - 3\vec{/}2 = 1, 2, 3, 4$. $\pi_c \pi_0$ = even, l must be even and π_t is even. These j_t values are the same to those of direct ionisation. Autoionisation from one of those states will therefore enhance the role of a channel that was already present in direct ionisation.

However, decay from a state with J = 5/2 will have $\vec{j_t} = \vec{2} + 1\vec{/}2 - 5\vec{/}2 = 0, 1, 2, 3, 4, 5$. $\pi_c \pi_0$ = even, l even and π_t even. This gives rise to one new channel with $j_t = 5$. Similarly, decay from states with J = 7/2 or 9/2 will have access to channels that were not available in direct ionisation.

This illustrates that autoionisation may enhance the role of weak channels in direct ionisation, i.e. weak terms in equation 6.5.6 but can also give rise to extra angular angular momentum transfer, j_t, which are not present in direct ionisation [46]. Inspection of the resonances in the beta parameter plots in the following section will thus take into account these considerations.

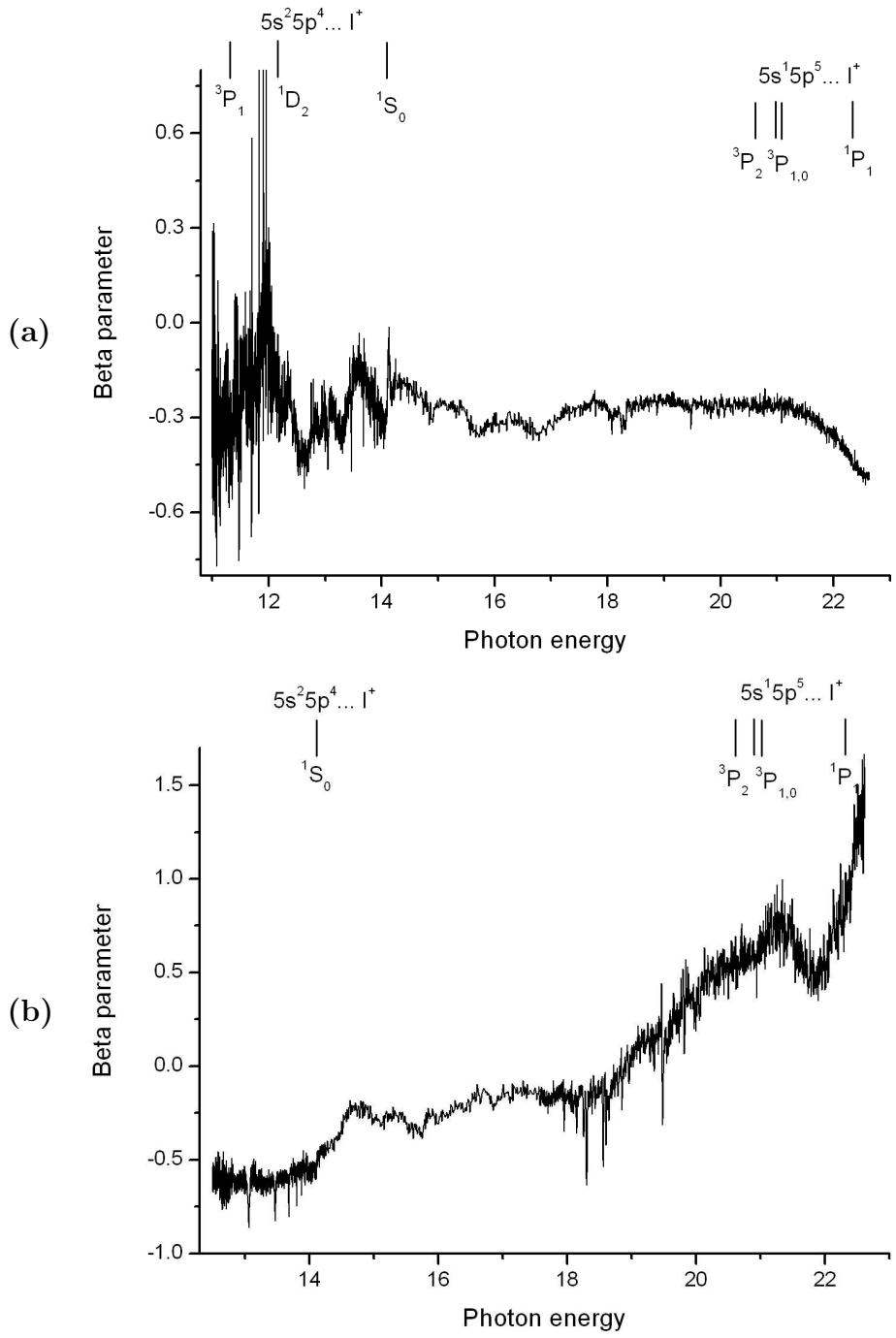

Figure 6.13: Overview of the beta parameter plots determined over the whole photon energy range. Spectrum 6.13(a) shows the beta parameter plot for the $I^+(^3P_2) \leftarrow I(^2P_{3/2})$ PE band of iodine atoms, in the photon energy range 11 to 23 eV. Spectrum 6.13(b) shows the beta parameter plot for the $I^+(^1D_2) \leftarrow I(^2P_{3/2})$ PE band of iodine atoms, in the photon energy range 12.5 to 23 eV.

6.5.2 Scans to the I^+ $^1S_0$ threshold

The beta plots obtained in the photon energy region of series converging to the I^+ $^1S_0$ threshold are shown in Figure 6.6. Figure 6.6(a) shows the beta parameter plot determined for the first, $I^+(^3P_2) \leftarrow I(^2P_{3/2})$, PE band of iodine atoms whereas Figure 6.6(b) shows the beta parameter plot determined for the fourth, $I^+(^1D_2) \leftarrow I(^2P_{3/2})$, PE band of iodine atoms. The beta plot of the first PE band (Figure 6.6(a)) shows two different structures, a large oscillation and sharp symmetric resonances. Only one cycle of the large oscillation is observed on the portion of the beta plot shown in Figure 6.6(a), going from -0.1 to -0.4. The second structure seen on the plot corresponds to the symmetric resonances that appear at energies corresponding to the $nd[2]_{5/2,3/2}$ resonances in the CIS spectra. The position of the resonances obtained from the Fano fits in this photon energy region are marked on the spectrum. Resonance positions from CIS spectra of the fourth band are also marked on Figure 6.6(b), which also shows symmetric resonances in positions corresponding to the $nd[2]_{5/2,3/2}$ resonances. However, the beta parameter for the fourth band does not oscillate and has a mean value of about -0.6. It is worth noting that the resonances on both beta plots have similar shape, which was not the case in the CIS spectra. The first resonance in Figure 6.6(a) has a minimum at -0.47 and a width of 22 meV. The second one has very similar characteristics with a minimum at -0.48 and a width of 21 meV. The following resonances have a minimum around -0.4 with width decreasing from 15 meV to 7 meV. The resonances in Figure 6.6(b) decrease regularly in intensity, with a minimum of -0.9 and a width of 33 meV for the first resonance and a minimum of -0.65 with a width of 8 meV for the last observed resonance. The fact that the resonances are more negative than the general background level shows that the parity unfavoured terms are enhanced on resonances (see previous section). This seems to be the case even more strongly for the beta parameter shown in Figure 6.6 (b) where the resonances have minima close to -1.

Extensive angular distribution studies have been carried out on the noble gases, including Xe [46, 161, 167, 169] in which the variation in β was compared with the variation in σ. They showed that, in general, resonances are expected in the β plots when autoionisation occurs. The shape of the resonances can vary from one resonance to another, being symmetric or asymmetric. In most cases, the β parameter is mostly positive, except at resonances, which usually have a minimum below 0. Similar behaviour was observed by Caldwell and co-workers [155] who determined beta plots for most halogen atoms and oxygen atoms. The asymmetry parameter was mostly positive, except for wide resonances which can have a minimum below 0. Surprisingly, the beta plot for iodine atom does not look like the one of bromine atom, even though the cross sections are very similar between the two atoms. Also, the dips in β in the present work are damped in comparison with those of Xe, where the minima are close to -1. This is due to an increase of the exit channels accessible and of the coupling possibilities in open shell atoms with respect to the noble gases. Also, the fact that the beta parameter is always negative in the present work indicates that the interference terms in atomic iodine are strong and that the parity unfavoured terms play a significant role. This was not unexpected as iodine is a heavy atom, which departs from the Russell-Saunders coupling and is best described in the JK coupling. It is also the first halogen atom which has an inversion of the $I^+\ ^3P_{0,1} \leftarrow I\ ^2P_{3/2}$ PE bands, the $I^+\ ^3P_1$ ionic state being higher in energy than the $I^+\ ^3P_0$ ionic state.

6.5.3 Scans to the $I^+\ ^3P_1$ threshold

The beta plot obtained in the photon energy region of series converging to the $I^+\ ^3P_1$ threshold is shown in Figure 6.8. As can be seen on the spectrum, no structure is observed in this photon energy region. The resonance positions have been marked on the spectrum for reference but do not seem to be reproduced at all. This can either mean that the autoionisation process does not affect the asymmetry parameter in this

energy region or that the experimental resolution is not good enough to see any structure. However, the beta parameter is negative as expected from the overview of the beta plots, with a mean value of -0.3 and seems to oscillate gradually between 0 and -0.5. Similarly to the beta plot obtained for the energy region of series converging to $I^+ \ ^1S_0$ threshold, the beta plot in this energy region does not resemble the one of bromine atom [158] in the same energy region, even though their cross section plots are very similar.

6.5.4 Scans to the $I^+ \ ^1D_2$ threshold

The beta plot obtained in the photon energy region of series converging to the $I^+ \ ^1D_2$ threshold is shown in Figure 6.10. The asymmetry parameter in this photon energy region does not oscillate and it has a mean value of -0.2. The observed resonances are asymmetric, unlike the symmetric resonances observed in the photon energy region of the $I^+ \ ^1S_0$ threshold. Also, the resonances are going towards positive values, which shows that in this case, it is the parity favoured terms that enhance the resonances, unlike those converging to the $I^+ \ ^1S_0$ threshold. The main series of resonances seen on this plot correspond to the $nd[3]_{5/2}$ series. The intensities of the resonances are not regular, they increase from the first observed resonance, with principal quantum number $n = 8$, which has a maximum at 0.7, to the third resonance ($n = 10$), which has a maximum at 1.5 and regularly decrease for the following resonances. The width of the resonances is also very irregular and difficult to determine. Some structure seems to be seen in positions corresponding to one of the ns series. Unfortunately, the signal-to-noise ratio is too poor to confirm this. Similarly, the broad second nd series might be present as well but its features are too weak to be confirmed. The beta parameter is still mostly negative, except at the maxima of the resonances. Once again, the beta parameter plot does not resemble the one of bromine atom in the same energy region. In light atoms, excitations that appear in the partial cross

section can have stronger effects on the beta parameter [46, 161, 167, 169]. Resonances in the β parameter of iodine atoms were thus expected for both ns and nd series. However, resonances were only observed for nd series and with attenuated amplitude. Another striking feature of the asymmetry parameter of atomic iodine is that β is nearly always negative in these plots. This clearly indicates that atomic iodine has strong interference terms and that the parity unfavoured partial cross section play a significant part in equation 6.5.6.

Since the beta parameter plot of iodine is clearly different from published beta plots of bromine atoms or xenon, comparison with theoretical studies of iodine atoms are needed. There have been two main theoretical studies of atomic iodine by Hartree-Fock calculations. One was performed by Manson et. al. [170] and one by Combet Farnoux et. al. [171]. The study by Manson et. al [170] was based on a Hartree-Fock model with no correlation or relativistic effects included. The method of Combet Farnoux et. al. [171] was similar but it improved the continuum wavefunctions by allowing some final state interaction. Both studies obtain a very similar plot for the beta parameter. Figure 6.14 shows the beta plot obtained by Manson et. al. [170] for comparison with the beta parameter plots obtained in the present work (see Figure 6.13). In this figure, the calculated asymmetry parameter plots for the outer np^5 subshells of iodine are shown. The solid lines correspond to the beta parameter for the ^3P, ^1D and ^1S ionic term levels calculated in the Hartree–Fock approximation while the dashed line corresponds to β values calculated in the Herman–Skillman central potential approximation. The energy region studied in the present work is between 1 and 2 Rydbergs photoelectron energy (13.6 to 27.2 eV), which corresponds to a very small region on the plot shown in Figure 6.14. Nevertheless, in the studies by Manson et. al. [170] and Combet Farnoux et. al. [171], the beta parameter is always positive. The fact that the beta parameter in the present work in very different from these studies shows again that correlation and relativistic terms cannot be left out in β parameter calculations of iodine atoms and

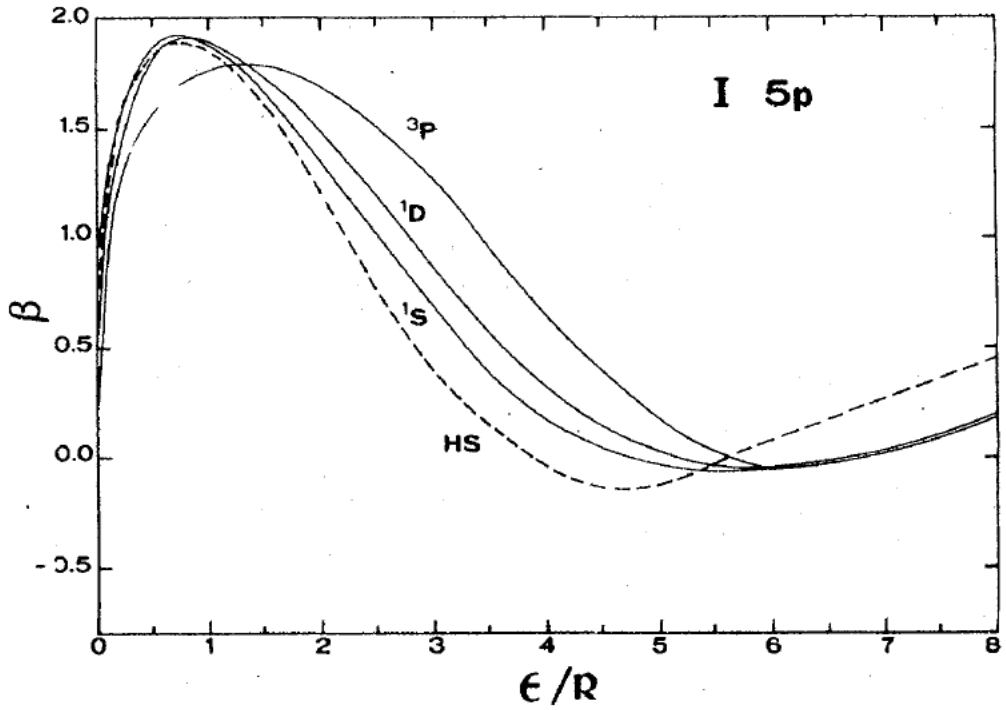

Figure 6.14: Calculated asymmetry parameter plots for the outer np^5 subshells of iodine by Manson et. al. [170]. Solid lines correspond to the beta parameters for the ^3P, ^1D and ^1S ionic terms levels calculated in the Hartree–Fock approximation; dashed line correspond to Herman–Skillman central potential approximation for β. The horizontal axis is the free electron energy in Rydbergs.

that other electronic structure calculations with improved models are needed.

6.6 Conclusion

In this chapter, the results obtained by Constant Ionic State (CIS) spectroscopy on iodine atoms were presented. PE spectra recorded during this work showed bands for the five iodine atom ionisations. CIS spectra were recorded for the first and fourth band of iodine atoms, the $I^+(^3P_2) \leftarrow I(^2P_{3/2})$ and the $I^+(^1D_2) \leftarrow I(^2P_{3/2})$ bands, from

11.0 to 23.0 eV photon energy. This photon energy range covered the third, fourth and fifth thresholds of the $(5p)^{-1}$ ionisations as well as the $(5s)^{-1}$ thresholds. CIS spectra recorded in the photon energy region of the $(5s)^{-1}$ ionisations were not analysed as the spectra were not of sufficient quality. CIS spectra recorded for the $(5p)^{-1}$ ionisations showed resonances converging to different thresholds, which correspond to Rydberg states that are part of a series converging to each threshold, followed by autoionisation to the selected ionic state. Two Rydberg series (one ns and one nd) were assigned converging to the $I^+\ ^1S_0$ threshold. Three Rydberg series (one ns and two nd) were assigned converging to the $I^+\ ^3P_1$ threshold while four series (two ns and two nd) were assigned converging to the $I^+\ ^1D_2$ threshold. Each Rydberg resonance was fitted using a Fano profile in order to find the position of the resonance and fitting parameters, such as the linewidth and the shape parameter. Each series was then fitted using the Rydberg formula to obtain the ionisation energy and quantum defect of the series. The results obtained agree well with previous work [60, 61, 142, 143] and are consistent for different series converging to the same threshold. This supported the reliability of the fitting procedure. Beta parameter plots of iodine atom were also derived for the first time and show very unexpected behaviour. In contrast to the cross section plots, which are very similar between iodine atoms and bromine atoms, the beta parameter plot of iodine does not resemble that of bromine atoms. Also, the beta parameter plot of iodine atoms shows little structure. Only a few nd resonances are seen in the beta parameter plot, and with damped amplitudes. In these plots, β is almost always negative, in contrast to the β plots of other halogens, Xe and the previous theoretical studies of iodine. This difference is almost certainly due to neglect of correlation and relativistic effects in the calculations. Indeed, iodine is a heavy halogen atom, its spectrum is thus expected to be complicated. Detailed calculations of cross sections and beta parameters as a function of photon energy, that include correlation and relativistic effects, are thus needed for comparison with the experimental plots of the cross sections and asymmetry parameter.

Chapter 7

Difluorocarbene studied by TPES

This chapter presents a study of difluorocarbene, CF_2, by Threshold Photoelectron Spectroscopy (TPES). In this work, the experimental spectra have been compared with results of *ab-initio*/Franck-Condon calculations on the first PE band of CF_2. The previous related work carried out on CF_2 is presented in Section 7.1 while Section 7.2 presents the experimental and computational details of the study. The results are presented in Section 7.3: the experimental spectra are presented first, followed by results of the *ab–initio* calculations carried out on CF_2 and CF_2^+, the computed Franck-Condon factors (FCF) and the simulated spectra of the first PE band of CF_2. Comparison is made between the experimental and simulated first PE band of CF_2, thus allowing assignment of the vibrational features, as is shown in the last section of this chapter.

7.1 Previous work on CF_2

Difluorocarbene, CF_2, is important in plasma processing and is produced in the stratosphere by photodissociation of chlorofluorocarbons by radiation from the sun. It has been studied in some detail spectroscopically in the ultraviolet [172–175], microwave, [176, 177] and infrared regions [178–181]. Structural parameters of the ground state, X^1A_1, and a number of excited states have been derived from electronic emission [175], absorption spectroscopy [173, 174], and single vibronic level (SVL) fluorescence [172]. Several microwave studies have been reported which provide precise rotational constants for the X^1A_1 state [176, 177].

Small reactive intermediates, such as CF_2, play important roles in determining the etching rate, selectivity and anisotropy of plasma-etching processes. The mechanisms of CF_2 production and destruction in fluorocarbon reactive ion-etching processes have been investigated using techniques such as laser induced fluorescence [182], broad-band UV absorption spectroscopy [183, 184] and infrared diode laser spectroscopy [185]. It has been found that the primary mechanism for CF_x production (where $x = 1$, 2 and 3) is neutralisation and fragmentation of CF_x^+ ($x = 1$, 2, 3 and 4) ions incident on the powered electrode and not direct electron-impact induced fragmentation of the feedstock gas [186]. In order to understand, model and ultimately control plasmas, spectroscopic methods such as those listed above are needed to monitor reactive intermediates in plasmas. Rate-constant measurements and reaction enthalpy determinations are required for relevant reactions involving CF_2 and CF_2^+.

The first adiabatic ionisation energy (AIE) of CF_2 is important in contributing to the determination of the enthalpy of ion - molecule reactions involving CF_2^+ in plasmas. Previous determinations of the first AIE of CF_2 have included a study by vacuum ultraviolet photoelectron spectroscopy (PES), which gave the first AIE as

(11.42 ± 0.01) eV [14]. CF_2 has also been studied by photoionisation mass spectrometry (PIMS) [187], using radiation derived from a synchrotron source. This study gave the first AIE as (11.445 ± 0.025) eV, while a study by electron impact mass spectrometry, gave a value of (11.5 ± 0.4) eV [188]. The PES study [14] shows the first band of CF_2 to consist of regular structure, with at least fifteen components. It was interpreted as a regular series in the deformation mode in the ionic state. The vertical ionisation energy (VIE) was measured as (12.240 ± 0.005) eV. In the present work, this band has been re-investigated at higher resolution using threshold photoelectron spectroscopy (TPES). The objective is to obtain a higher resolution spectrum of the first band of CF_2. The spectrum obtained, supported by appropriate *ab-initio*/Franck - Condon factor calculations, should allow the first AIE to be determined more reliably than previously and to enable the vibrational structure in the first band to be analysed more thoroughly.

7.2 Experimental and computational details

7.2.1 Experimental section

As all experiments carried out during this project, the experiments reported here were undertaken on the Circularly Polarised Beamline (4.2R, Polar) at the Elettra synchrotron radiation source (Trieste). The photoelectron spectrometer described in Chapter 3 was used, which has been specifically designed to study reactive intermediates with PE and CIS spectroscopy [16, 17, 49]. This spectrometer was recently modified to allow TPE spectra to be obtained, as was explained in Chapter 3 and in reference [51]. In order to record TPE spectra, the photoelectron spectrometer was tuned to detect near-zero energy (threshold) photoelectrons. The detection of threshold electrons was optimised using the $Ar^+(^2P_{3/2},^2P_{1/2}) \leftarrow Ar(^1S_0)(3p^{-1})$ TPE

spectrum [51, 140, 141]. The spectral resolution obtained was typically about 5 meV as estimated from the full-width at half maximum of the main $(3p)^{-1}\mathrm{Ar}^{+}(^{2}P_{3/2}) \leftarrow \mathrm{Ar}(^{1}S_{0})$ line. Conventional photoelectron (PE) spectra were also recorded as described in earlier chapters. The procedures described in Chapter 3 were used to normalise the spectra for the photon flux, the transmission function of the spectrometer and to calibrate the photon energy scale of the TPE spectra. CF_2 was produced by a microwave discharge of flowing hexafluoropropene, C_3F_6, diluted with argon. Preliminary experiments were carried out in Southampton in order to determine the optimum pressures which maximise the intensity of the first CF_2 band in the PE spectra, as was explained in Chapter 3. The optimum partial pressures were: $\Delta p(C_3F_6)=5\times10^{-6}$ mbar and $\Delta p(Ar)=1\times10^{-7}$ mbar. These partial pressures were measured using an ionisation gauge connected to the main vacuum chamber and are with respect to the background pressure in the vacuum chamber (3×10^{-7} mbar).

7.2.2 Computational details

In order to compute potential energy functions for the ground neutral and ionic states so that Franck-Condon factors could be calculated for the first PE band of CF_2, *ab-initio* calculations were performed by Dr E. Lee from the Southampton PES group. These can be described as follows:

***Ab initio* calculations**: For the X^2A_1 state of CF_2^+, geometry optimisation and vibrational frequency calculations were carried out using the restricted spin CCSD(T) method (RCCSD(T)) with augmented correlation-consistent polarised valence (aug-cc-pVXZ or AVXZ) and core-valence (aug-cc-pCVXZ or ACVXZ) basis sets of up to the quintuple-zeta (X= Q or 5) quality. The basic principles of these methods have been described in Chapter 4. With the core-valence basis sets, all electrons were correlated. For the X^1A_1 state of CF_2, *ab-initio* total energies at different bond

lengths and angles, the RCCSD(T)/aug-cc-pV5Z potential energy function (PEF), and anharmonic vibrational wavefunctions, have been taken from a previous study on CF_2 [189], except for RCCSD(T)/aug-cc-pCV5Z results, which have been obtained in the present study. The largest aug-cc-pCV5Z calculations have 543 contracted basis functions. For the evaluation of the best theoretical geometrical parameters (r_e and θ_e) and adiabatic ionisation energy (AIE), the $1/X^3$ formula was used to extrapolate the computed RCCSD(T)/ACVQZ and RCCSD(T)/ ACV5Z values to the complete basis set (CBS) limit [190]. Since the RCCSD(T)/ACVXZ (X=Q or 5) values were used in the extrapolation, core correlation contributions have already been accounted for. For the correction for zero-point vibrational energies (ΔZPE) in order to give AIE_0, available experimental fundamental vibrational frequencies for the X^1A_1 state of CF_2 were used [191–193]. For the X^2A_1 state of CF_2^+, the best theoretical zero point energy (ZPE) was used, and it was estimated using the CBS value extrapolation employing the $1/X^3$ formula, with the ZPEs evaluated using the computed RCCSD(T)/AVQZ and RCCSD(T)/AV5Z harmonic vibrational frequencies plus core correlation correction (the difference between the RCCSD(T)/ACVQZ and RCCSD(T)/AVQZ values).

Potential energy functions, anharmonic vibrational wavefunctions and Franck-Condon factor calculations: The PEF of the X^2A_1 state of CF_2^+ was fitted to 106 computed CASSCF/MRCI+D/AV5Z energies in the ranges of $0.9 \leq r(CF) \leq 1.95$ Å and $70.0 \leq \theta(FCF) \leq 160.08$ Å. The multi-reference CASSCF/MRCI method (including the Davidson correction, with a full valence active space) has been used in energy scans for the fitting of the PEF of the X^2A_1 state of CF_2^+ because multi-reference character becomes non-negligible in the region with $r \geq 1.6$ Å. Nevertheless, computed CI coefficients of the major electronic configuration obtained from the MRCI calculation of the X^2A_1 state of CF_2^+ in this region have values larger than 0.778, and the sums of the squares of the computed CI coefficients of all reference configurations, $\Sigma(C_{ref})^2$, have values larger than 0.959,

indicating that the computed MRCI wavefunctions describe the electronic state studied adequately. The root-mean-square (r.m.s) deviations of the fitted PEFs of the X^2A_1 state of CF_2^+ from computed *ab-initio* energies is 12.9 cm^{-1}. Details of the coordinates and polynomial employed for the PEFs, the rovibrational Hamiltonian [123] and anharmonic vibrational wavefunctions used in the variational calculations, and the Franck-Condon (FC) factor calculations which include Duschinsky rotation and anharmonicity have been given in Chapter 4 and in references [189, 194]. Nevertheless, some details of the harmonic basis functions used in the calculation of the anharmonic vibrational wavefunctions of the X^2A_1 state of CF_2^+ are given here. The vibrational quantum numbers of the harmonic basis functions of the symmetric stretching and bending modes employed in the calculation of anharmonic wavefunctions have values of up to $v_1 = 12$, $v_2 = 25$ with the restriction of $(v_1 + v_2) \leq 25$.

For the FC factor calculations, the best computed geometry of the X^2A_1 state of CF_2^+ obtained at the CBS limit in the present study, the experimental geometry of the X^1A_1 state of CF_2 (r_e=1.2975 Å and $\theta_e = 104.81°$, derived from experimentally derived A_e and B_e values) [195] and the experimental AIE_0 value of 11.362 eV (see later) obtained from the TPES spectrum in the present study were used. In addition, FC factors were calculated at Boltzmann vibrational temperatures of 0 K and 600 K. The $CF_2^+(X^2A_1) + e^- \leftarrow CF_2(X^1A_1)$ photoelectron band has been simulated with these computed FC factors. The method includes allowance for Duschinsky rotation and anharmonicity. A Gaussian linewidth of 0.005 eV full-width-at-half-maximum (FWHM) was used for each vibrational component in the spectral simulation, as the experimental threshold photoelectron spectrum (TPES) has a resolution of ca. 0.005 eV FWHM. The MOLPRO suite of programs was employed for all *ab initio* calculations carried out in the present investigation [196].

7.3 Results and Discussion

7.3.1 Experimental spectra

The UV photoelectron spectrum of C_3F_6 shows a structured band in the region 10.4-11.9 eV and five broad bands in the ionisation energy region 14.0-17.0 eV [197, 198]. Microwave discharge of flowing C_3F_6/Ar mixtures gives rise to complete destruction of C_3F_6 with production of CF_2 and C_2F_4. It is also known from separate experiments that microwave discharge of flowing C_2F_4/Ar mixtures gives CF_2. In this work, the discharge conditions and partial pressures of C_3F_6 and Ar were optimised to give the maximum yield of CF_2. A photoelectron spectrum obtained at $h\nu = 21.0$ eV from discharged C_3F_6/Ar in the ionisation region 10.0-13.2 eV showing the first bands of C_2F_4 [199] and CF_2 [14] is shown in Figure 7.1.

Figure 7.2 shows the TPE spectrum of CF_2 recorded in the photon region from 11.3 to 13.2 eV together with a PE spectrum recorded at $h\nu$=21.0 eV. Whilst the observed relative intensities of vibrational components in a PE band in a conventional PE spectrum are almost always governed by Franck-Condon factors between the initial neutral and final ionic state, those observed by TPES are often dominated by autoionisation [131, 132]. This is primarily due to the high density of Rydberg states, which are parts of series that converge on higher rovibronic ionic levels. These can autoionise and produce electrons of low kinetic energy that are detected in TPES. As a result, autoionisation processes can lead to non–Franck-Condon distributions as well as the observation of ionic vibrational levels which are not observed in the normal Franck-Condon distribution. Also, these autoionisation processes may lead to observation of ionic states that cannot be observed by direct ionisation from the ground state in conventional PES, as was explained in Chapter 2. The TPE spectrum in Figure 7.2 shows a better resolution and a very different vibrational profile with

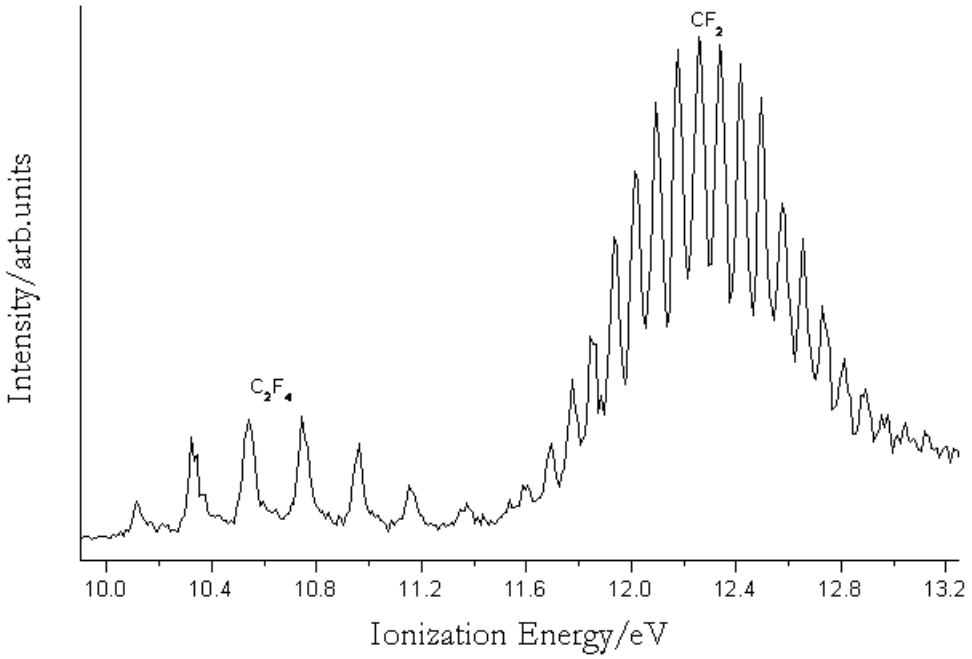

Figure 7.1: UV photoelectron spectrum recorded at a photon energy of 21.0 eV of a microwave discharge of a flowing mixture of hexafluoropropene, C_3F_6, in Ar. Spectra obtained under these conditions show that all the C_3F_6 is destroyed and converted into CF_2 and C_2F_4.

respect to the Franck-Condon distribution of the PE spectrum.

In the TPE spectrum the lower vibrational bands are more intense and more clearly resolved than in the PE spectrum where the lowest vibrational component that is clearly observed is at about 11.6 eV (two additional lower-energy components were observed in the original PES study [14]). In the earlier PES study of CF_2, the adiabatic and vertical ionisation energies were determined as 11.42 ± 0.01 eV and 12.240 ± 0.005 eV respectively. In the present study it is possible to measure the VIE from the PE spectrum as 12.258 ± 0.002 eV and the lowest vibrational band observed in the TPE spectrum is at 11.438 ± 0.004 eV. In both cases the shift with respect to the previous study is up by 18 meV. From the experimental TPE spectrum, it is not

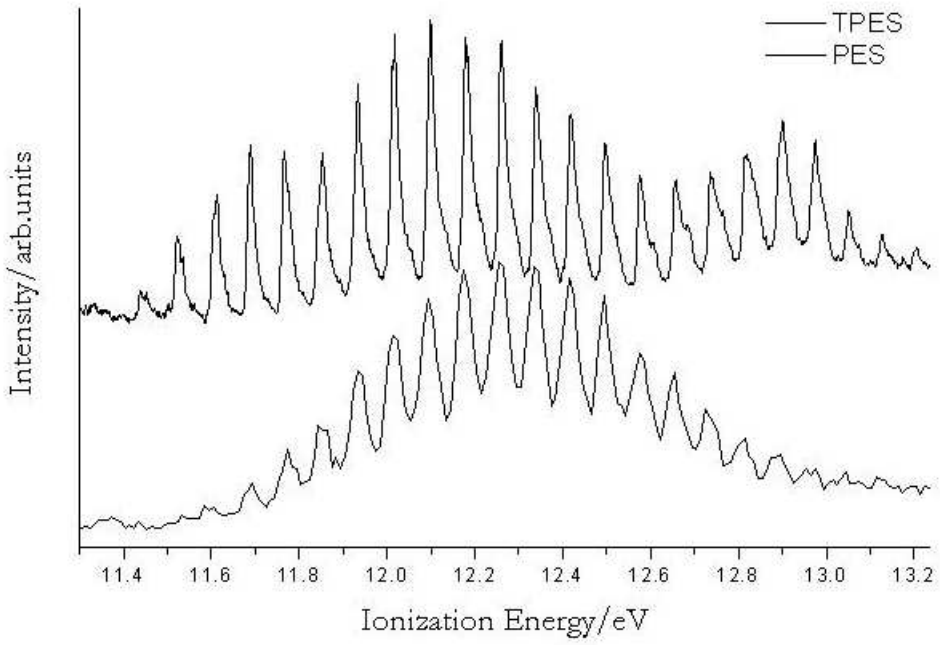

Figure 7.2: TPE (upper) and PE (lower) spectra recorded for a flowing CF_2 and Ar mixture in the 11.3-13.2 eV photon energy region.

possible to establish if the component observed at 11.438 eV is really the lowest vibrational component in the PE spectrum of CF_2. This is because below 11.4 eV, there is a contribution from the highest observed vibrational component of the first PE band of C_2F_4, as can be seen in Figure 7.2. Also, the intensity of a lower vibrational band of CF_2, if present, would be very small compared to the noise level. Indeed, in the TPE spectrum in Figure 7.2, it is possible to observe some structure below 11.4 eV but the signal-to-noise is not sufficient to allow unambiguous identification of weak C_2F_4 contributions and possible weak vibrational components of CF_2. For this reason the experimental TPE spectrum was compared with an *ab-initio*/Franck-Condon computed vibrational envelope to see if the AIE of CF_2 could be established.

Figure 7.3 shows the experimental TPE spectrum compared with the simulated $CF_2^+(X^2A_1) \leftarrow CF_2(X^1A_1)$ photoelectron spectrum at 0 K. The spectral simulation used a Gaussian function of width 5 meV for each vibrational component, which is comparable with the experimental resolution. The calculated adiabatic component is placed at 11.367 eV. This was done by positioning the computed envelope so that the structure in the higher components in the TPE spectrum matches well with the computed structure, notably in the third, fourth, sixth and ninth components. The 11.36 eV component has a very small relative intensity and it is below the noise level of the experimental TPE spectrum. The positions of all the observed vibrational components are in excellent agreement with the computed components although the TPE vibrational envelope is different from the computed envelope. This is because of the non-Franck-Condon behaviour of threshold photoionisation. The shape of each experimental vibrational component closely matches the shape of the corresponding calculated vibrational component as can be seen from the comparison of the lowest vibrational components shown in Figure 7.4. In the third, sixth and eleventh experimental vibrational components (counting the 11.36 eV component, not shown in Figure 7.4, as the first), it is possible to observe two features with the one at lower ionisation energy more intense; the same pattern is observed in the calculated vibrational components. The fourth, seventh and ninth experimental vibrational components each show two features with the one at higher ionisation energy more intense; the same pattern is observed in the calculated fourth and seventh vibrational components while in the ninth component the two contributing features are comparable in intensity. In the other calculated vibrational components in Figure 7.4, the 5 meV band-width used is not good enough to allow separation of different components and the same is true for the corresponding experimental vibrational components which appear to be a single feature. The exception is the vibrational component at ∼11.45 eV in Figure 7.4 which is a single vibrational component in the calculated spectrum while it appears to have two components in the experimental spectrum.

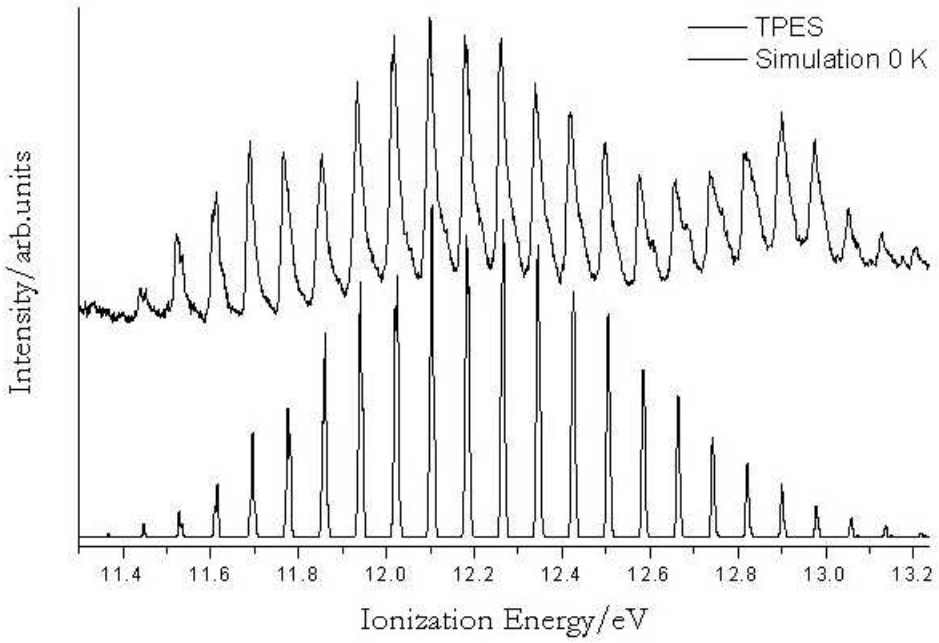

Figure 7.3: TPE spectrum recorded for a flowing CF_2 and Ar mixture in the 11.3-13.2 eV photon energy region (upper). Simulated $CF_2^+(X^2A_1) \leftarrow CF_2(X^1A_1)$ photoelectron spectrum for 0 K Boltzmann vibrational temperature (lower).

The simulated spectrum in Figure 7.4 was computed with a Boltzmann vibrational temperature of 0 K. The calculation has been repeated using a Boltzmann distribution at a temperature of 600 K and the result is shown in Figures 7.5 and 7.6. The main differences with respect to the simulation at 0 K are at ionisation energies above 12.8 eV and for the vibrational component in Figure 7.4 at $\sim$ 11.45 eV. This band, in the calculation at 600 K, has a "hot" band on the higher ionisation energy side as can be seen in Figure 7.6. The shape of the 11.45 eV vibrational component in the experimental TPE spectrum in Figure 7.4 is therefore explained considering the contribution from the "hot" band. The simulated spectrum at 600 K offers an even better match with the experimental spectrum with respect to the simulated spectrum

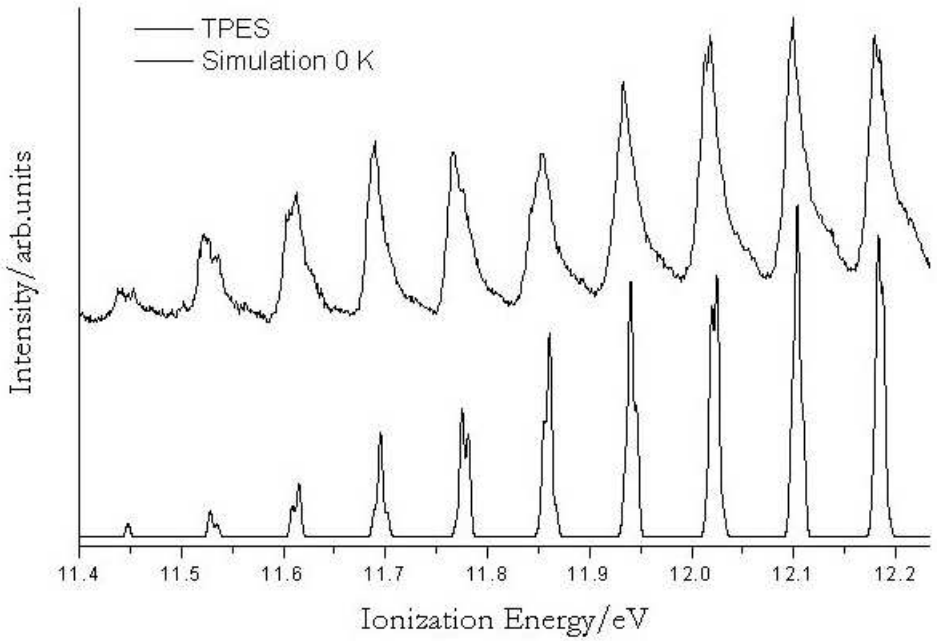

Figure 7.4: Expanded TPE spectrum of CF_2 in the 11.4-12.2 eV photon energy region (upper). Simulated $CF_2^+(X^2A_1) \leftarrow CF_2(X^1A_1)$ photoelectron spectrum for 0 K Boltzmann vibrational temperature (lower).

at 0 K. Indeed, on comparing Figure 7.4 with Figure 7.6 it is possible to notice an improvement of the agreement with the calculated spectrum at 600 K in particular for the fourth, sixth and ninth vibrational components (counting the component at 11.36 eV as the first).

The vibrational components above 12.8 eV in the TPE experimental spectrum show considerable intensity and a clear deviation from the computed Franck-Condon relative intensities. This is probably due to strongly autoionising Rydberg states converging to higher ionic limits of CF_2. The simulation at 600 K shows some weak extra structure above 12.8 eV, due to the contributions from "hot" bands, with respect to the simulation at 0 K (compare Figure 7.3 with Figure 7.5).

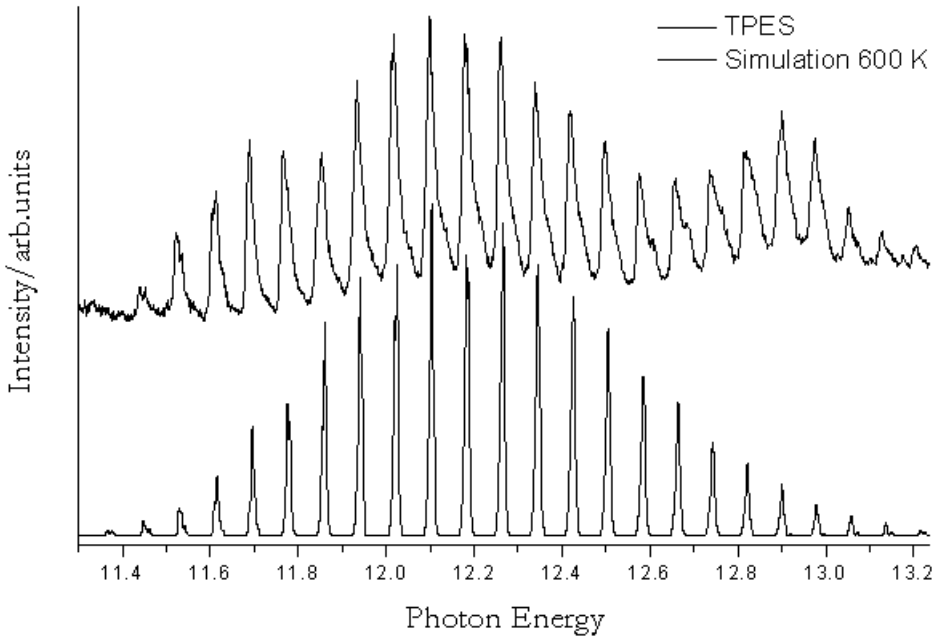

Figure 7.5: TPE spectrum recorded for a flowing CF_2 and Ar mixture in the 11.3-13.2 eV photon energy region (upper). Simulated $CF_2^+(X^2A_1) \leftarrow CF_2(X^1A_1)$ photoelectron spectrum for 600 K Boltzmann vibrational temperature (lower).

The ionisation energies of the calculated vibrational components from the *ab-initio*/Franck-Condon factor calculations are on average 5 meV higher than the more intense experimental vibrational components in the 11.6-12.6 eV region. Hence, by moving the computed bands in Figure 7.3 by 5 meV to match the more intense experimental TPE vibrational component positions in the photon energy region 11.6-12.6 eV, the AIE is moved by 5 meV compared to the value obtained from the simulation. This gives a value of 11.362 ± 0.005 eV for the AIE.

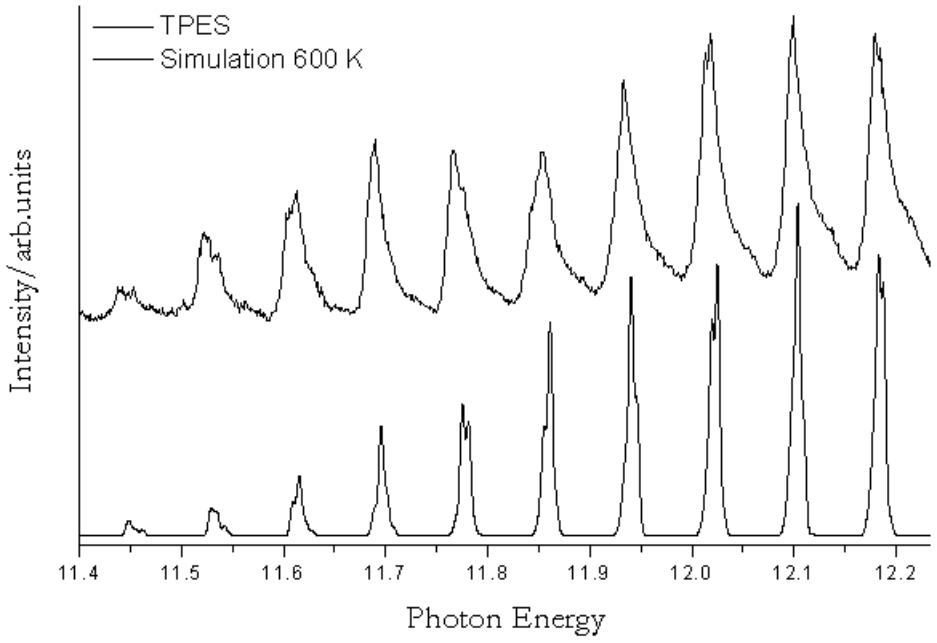

Figure 7.6: Expanded TPE spectrum of CF_2 in the 11.4 - 12.2 eV photon energy region (upper). Simulated $CF_2^+(X^2A_1) \leftarrow CF_2(X^1A_1)$ photoelectron spectrum for 600 K Boltzmann vibrational temperature (lower).

7.3.2 *Ab-initio* results

The computed *ab-initio* results obtained in the present study for the X^2A_1 state of CF_2^+ are summarised in Table 7.1, and the corresponding results obtained for CF_2 X^1A_1 are shown in Table 7.2. Previous MRSDCI/DZP results of Cai [200] (see references therein for earlier, lower level, *ab-initio* results) on the X^2A_1 state of CF_2^+ are also included in Table 7.1. Nevertheless, since the *ab-initio* calculations carried out in the present work are of significantly higher level and also are more systematic than previous work, the following discussion will be focussed on the results obtained in the present work. From Table 7.1, the best computed geometrical parameters of the X^2A_1 state of CF_2^+ obtained at the CBS limit (including core correlation as mentioned above) are r_e(CF)=1.2131 $\pm$ 0.0006 Å and θ_e(FCF)=124.59 $\pm$ 0.04°. The

associated uncertainties have been estimated by the differences between the CBS and RCCSD(T)/ACV5Z values. These geometrical parameters are currently the most reliable values, as no experimentally derived values are available at present.

Regarding computed harmonic vibrational frequencies of the X^2A_1 state of CF_2^+ obtained in the present study from RCCSD(T) calculations, the largest difference between values obtained using different basis sets is less than 6 cm^{-1}. The difference between the computed symmetric stretching harmonic frequencies obtained from RCCSD(T)/AV5Z calculations and the CASSCF/MRCI/AV5Z PEF is about 9 cm^{-1}, which may be considered as the largest theoretical uncertainty associated with the computed vibrational frequencies reported in this chapter. Before the vibrational assignment of the TPES spectrum is considered, it should be noted that the only available experimental vibrational frequency of the X^2A_1 state of CF_2^+ is that of the bending mode, 650 ± 40 cm^{-1}, measured in the previously recorded UV photoelectron spectrum [14]. This experimental ν_2' value agrees very well with the corresponding computed value of 651.7 cm^{-1} obtained from the MRCI PEF of the present study. However, as will be shown below in the comparison between the simulated PE spectrum and the experimental TPE spectrum, the observed vibrational structure in the UV PE spectrum is not due to a single ν_2' progression, but a number of combination bands [14]. Nevertheless, the excellent agreement between the simulated PE spectrum and the observed TPE spectrum, in terms of position and shape of the individual vibrational components, indicates that the computed vibrational frequencies reported here are very close to the true values.

Method	r_e	θ_e	ω	IE
RCCSD(T)/aug-cc-pVQZ	1.2168	124.63	1374.6, 648.6, 1698.9	11.3865
RCCSD(T)/aug-cc-pV5Z	1.2160	124.58	1379.1, 649.7, 1701.7	11.4010
RCCSD(T)-aug-cc-CVQZ[a]	1.2143	124.67	1379.1, 651.2, 1704.6	11.3807
RCCSD(T)/aug-cc-CV5Z[a]	1.2137	124.63		11.3937
CAS/MRCI/aug-cc-pV5Z	1.2185	124.63		
(as above)PEF	1.2185	124.52	1370.0, 653.2, -	
(as above)PEF$\nu's$			1356.3, 651.7, -	
CBS (ACVQZ, ACV5Z)[b]	1.2131	124.59		11.412 ± 0.018
Δ ZPE[c]				+0.046
best theoretical IE_0[d]				11.458 ± 0.020
MRSDCI/DZP[e]	1.222	124.5	1259, 656, 1599	
photoion.MS[f]				11.445 ± 0.025
HeI photoelectron spectrum[g]			-, 650 ± 40, -	11.42 ± 0.01
TPES				11.362 ± 0.005

Table 7.1: Optimized geometrical parameter (r_e in Å and θ_e in degrees) and computed vibrational frequencies $\omega_1(a_1)$, $\omega_2(a_1)$ and $\omega_3(b_2)$ in cm^{-1} of, and computed adiabatic ionisation energies (IE in eV), to the X^2A_1 state of CF_2^+, obtained at different levels of calculations.

[a] All electrons correlated; see text. [b] Extrapolation to the CBS, employing the $1/X^3$ formula and the RCCSD(T) values calculated using the aug-cc-pCVQZ (ACVQZ) and aug-cc-pCV5Z (ACV5Z) basis sets. The estimated uncertainty for IE is the difference between the best theoretical value and the ACV5Z value. [c] Contribution of zero-point energies (ZPE) of the two states involved. For CF_2, the experimental fundamental vibrational frequencies, 1225.08, 666.25 and 1114.44 cm^{-1} (gas phase values from NIST WebBook, [174, 191, 193]), were used, giving a ZPE value of 0.1863 eV. For CF_2^+, the CBS($1/X^3$; AVQZ, AV5Z) ZPE value of 0.2315 eV and core(AVQZ, ACVQZ) correction of +0.0008 eV give the best theoretical ZPE value of 0.2323 eV and a best estimated Δ(ZPE) value of 0.045 eV. [d] CBS+ΔZPE. [e] From ref. [200]. [f] Photoionisation mass spectrometry, from ref. [187]. [g] Ref. [14].

RCCSD(T)	R_e[Å]	θ_e[°]	ω_1	ω_2	ω_3
Aug-cc-pVQZ	1.3008	104.786	1242 [1231]	670 [668]	
Aug-cc-pV5Z	1.2953	104.907	1247 [1234]	675 [672]	
Aug-cc-pCVQZ	1.2981	104.846			
exptl. [201]	1.2975	104.81	[1225.0793]	666.24922]	[1114.4435]

Table 7.2: Computed geometrical parameters and harmonic vibrational frequencies (fundamental values in cm^{-1}) of the X^1A_1 of CF_2 obtained at the RCCSD(T) level of calculation using different basis sets. The RCCSD(T)/aug-cc-pV5Z potential energy function (PEF) and anharmonic vibrational wavefunctions used have been taken from the previous study on CF_2 [189].

The best computed AIE obtained at the CBS limit in the present study is 11.412 ± 0.018 eV. Correction of zero point energies of the two states involved yields the best computed AIE_0 value of 11.46 ± 0.02 eV. This value agrees very well with the earlier experimental values of 11.445 ± 0.025 eV and 11.42 ± 0.01 eV obtained from photoionisation mass spectrometry [187] and UV photoelectron spectroscopy [14], respectively but less well with the AIE derived in this work of 11.362 eV.

7.3.3 Computed Franck-Condon factors and simulated photoelectron spectrum

The computed FC factors (FCFs) of the $CF_2^+(X^2A_1) + e^- \leftarrow CF_2(X^1A_1)$ photoionisation process obtained with Boltzmann vibrational temperatures of 0 and 600 K are shown in Figure 7.7 (upper and lower spectra in this Figure, respectively; the computed FCF of the strongest vibrational component is set to 100 arbitrary units in all parts of this figure). The computed FCFs of vibrational "hot" bands

arising from ionisations from the (0,1,0), (1,0,0), (0,2,0) and (1,1,0) levels of the X^1A_1 state of CF_2 obtained at 600 K are also shown in Figure 7.7 (middle spectrum). It can be seen from this Figure that "hot" band contributions to the whole simulated spectrum are small. The most noticeable contributions of "hot" bands are probably in the low IE region, relative to ionisations from the (0,0,0) level of the X^1A_1 state, as has already been discussed in the comparison between the simulated PE spectrum and the experimental TPE spectrum.

Although the vibrational structure of the previously reported UV PE spectrum [14] appears to consist of only one vibrational series, the FCFs computed in this work show that a large number of combination bands are involved. The computed FCFs of eight major vibrational series obtained at a Boltzmann vibrational temperature of 0 K, which contribute to the $CF_2^+(X^2A_1) + e^- \leftarrow CF_2(X^1A_1)$ ionisation process, are shown in Figure 7.8. In practice, vibrational components with v_1' and/or v_2' having values of up to at least 8 for both vibrational quantum numbers have non-negligible contributions. It should be noted, however, that computed anharmonic wavefunctions of vibrational levels of the X^2A_1 state of CF_2^+ with relatively high quantum numbers show contributions from several different basis functions. Consequently, vibrational assignments of levels with v_1' and/or v_2', having values larger than 7, are tentative. Nevertheless, it is clear that the (3,v_2',0) $\leftarrow$ (0,0,0) series is the strongest vibrational progression and the (3,3,0) $\leftarrow$(0,0,0) vibrational component has the largest computed FC factor (see Figure 7.8).

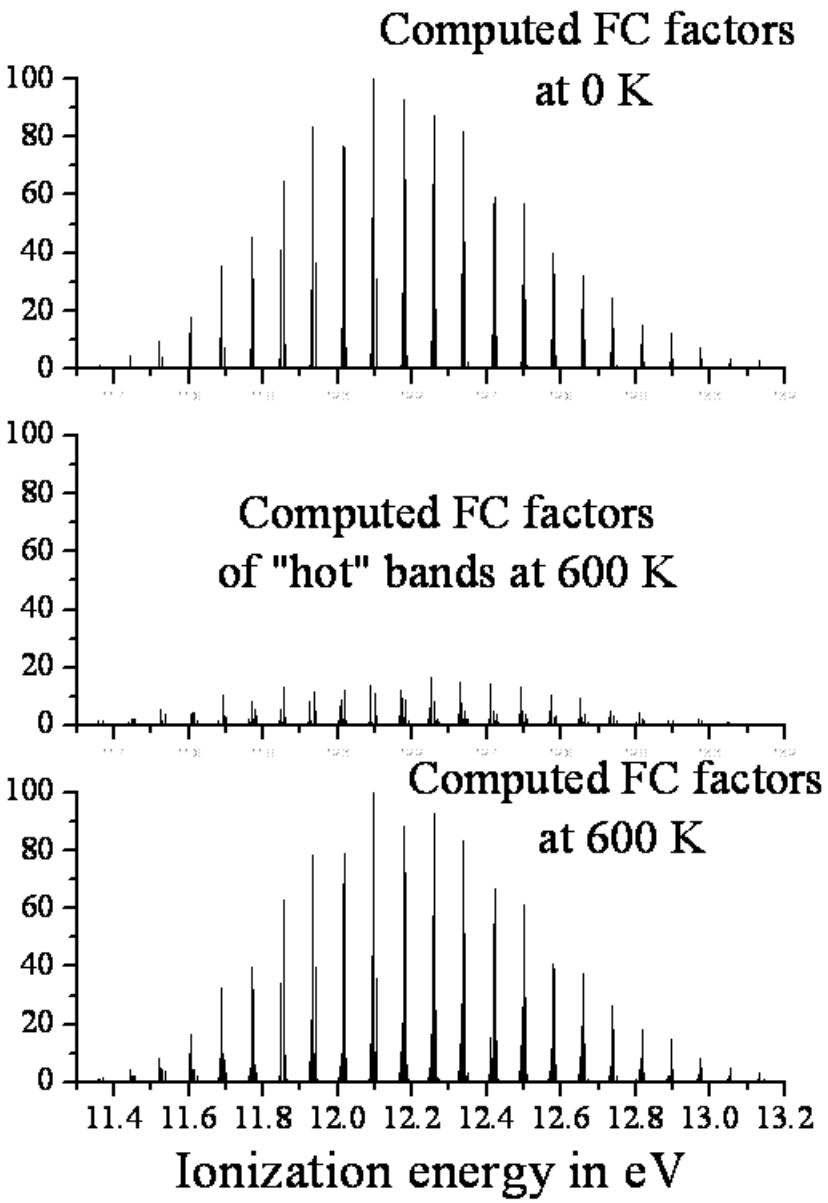

Figure 7.7: Computed Franck-Condon factors of the $CF_2^+(X^2A_1) + e^- \leftarrow CF_2(X^1A_1)$ photoionisation process obtained with Boltzmann vibrational temperatures of 0 K (top trace) and 600 K (bottom trace), and those of "hot" bands arising from ionisations from the (0,1,0), (1,0,0), (0,2,0) and (1,1,0) levels of the X^1A_1 state of CF_2 (middle trace).

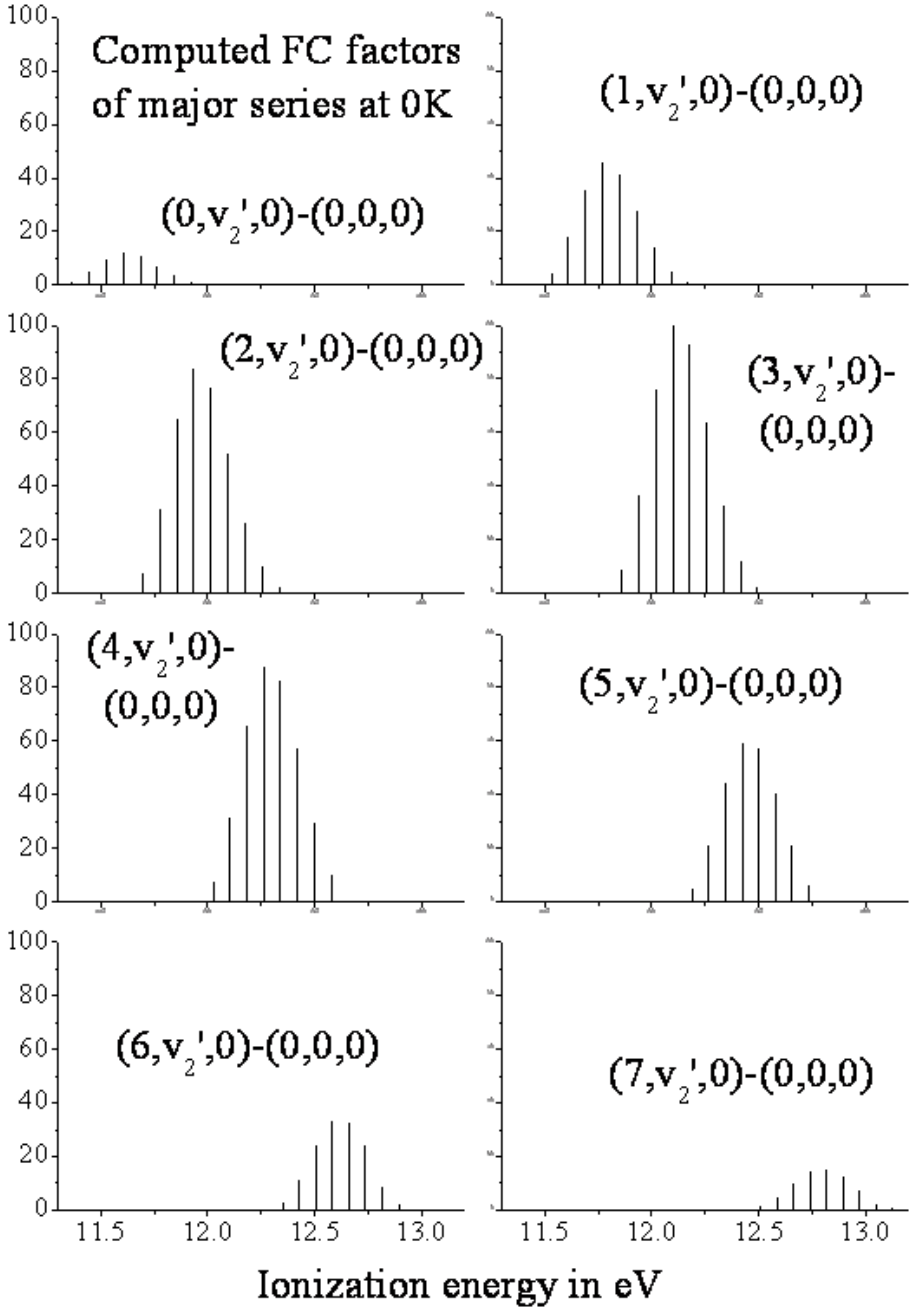

Figure 7.8: Computed Franck-Condon factors of eight major vibrational progressions at 0 K of the $CF_2^+(X^2A_1)+e^- \leftarrow CF_2(X^1A_1)$ photoionisation process and their vibrational assignments.

In Figure 7.9, computed FCFs in the 11.5-12.9 eV IE region at a Boltzmann vibrational temperature of 600 K and vibrational assignments of some of the relatively strong vibrational components arising from the (0,0,0) level of the X^1A_1 state of CF_2 are shown. In this IE region, some partially resolved components with a doublet structure were observed in the TPE spectrum. Computed FCFs in this region show that these doublet structures are due to $(v_1', v_2' + 2, 0) \leftarrow (0, 0, 0)$ and $(v_1' + 1, v_2', 0) \leftarrow (0, 0, 0)$ ionisations, because $2\nu_2'$ has a magnitude close to ν_1'.

In Figure 7.10, computed FC factors and assignments of some vibrational components in the adiabatic ionisation region are shown. It can be seen from the Figure that there are a number of "hot" band components, namely the $(0, 1, 0) \leftarrow (0, 1, 0)$, $(1, 0, 0) \leftarrow (0, 2, 0)$ and $(0, 2, 0) \leftarrow (1, 0, 0)$ components at computed ionisation energies of 11.359, 11.363 and 11.370 eV, respectively, which are very close to the $(0, 0, 0) \leftarrow (0, 0, 0)$ component at 11.362 eV. However, in order to resolve the vibrational structure in this congested region, a better experimental resolution than 5 meV FWHM is required.

An overview of the assignment of the main structure in the experimental TPE spectrum in the photon energy region 11.3-12.2 eV is shown in Figure 7.11. As can be seen, the main structure shown corresponds to $(v_1', v_2', 0) \leftarrow (0, 0, 0)$ combination bands with $v' = 0, 1, 2$ and 3. The doublet structure observed in some of these bands arises because $2\nu_2'$ is approximately equal to ν_1'. On comparing Figure 7.11 with the experimental TPE spectrum in the photon energy region 11.4-12.2 eV (Figure 7.6), and using the information provided in the simulations in Figures 7.9 and 7.10, the doublet structure observed in the experimental vibrational components can be assigned. For example, in the first two observed components at 11.45 and 11.52 eV the doublet structure can be assigned to the $(0, 1, 0) \leftarrow (0, 0, 0)$ and $(1, 0, 0) \leftarrow (0, 1, 0)$ ionisations, and the $(0, 2, 0) \leftarrow (0, 0, 0)$ and $(1, 2, 0) \leftarrow (1, 0, 0)$, respectively. Also, the doublet structure in the band at 11.77 eV can be assigned to

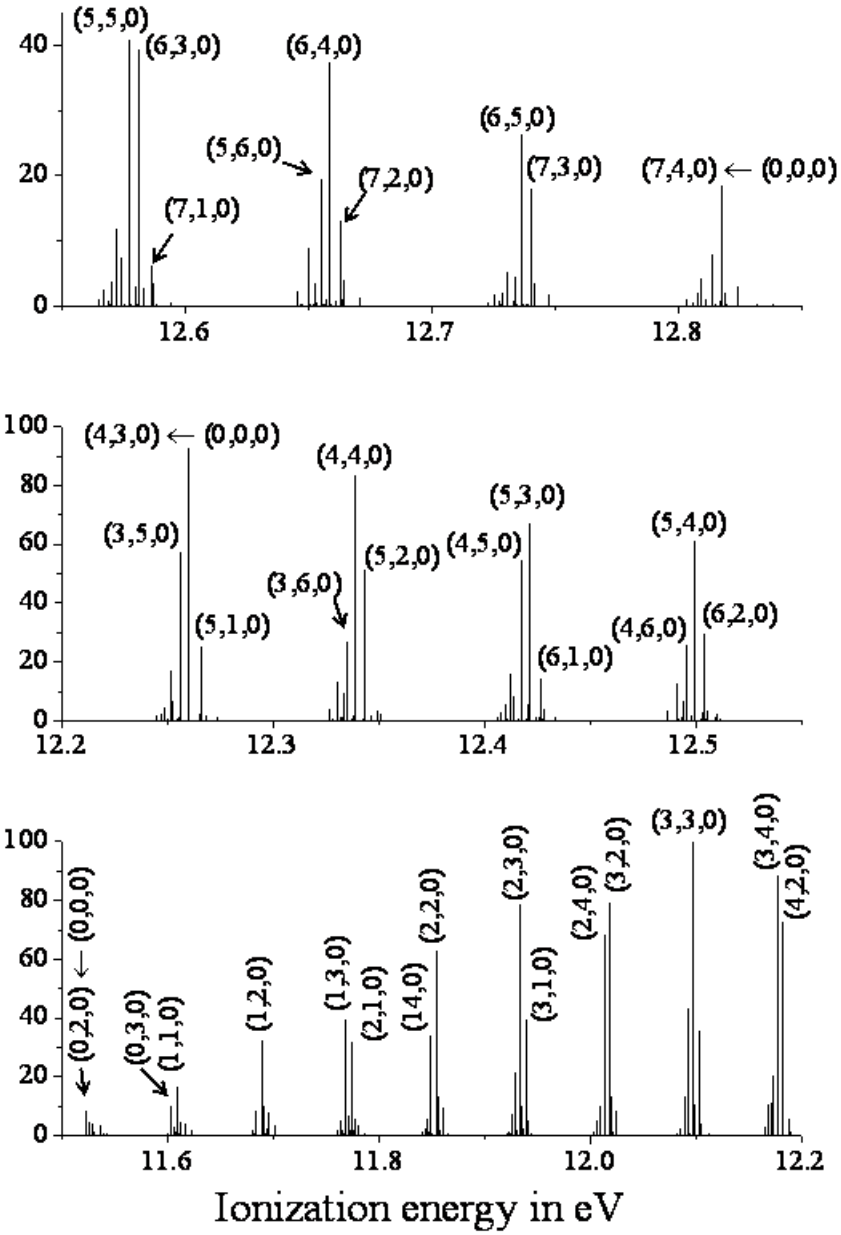

Figure 7.9: Computed Franck-Condon factors of the $CF_2^+(X^2A_1) + e^- \leftarrow CF_2(X^1A_1)$ photoionisation process in the 11.5-12.9 eV IE region, and vibrational assignments of some vibrational components, which contribute to some of the doublet structures in the observed threshold photoelectron spectrum (see text).

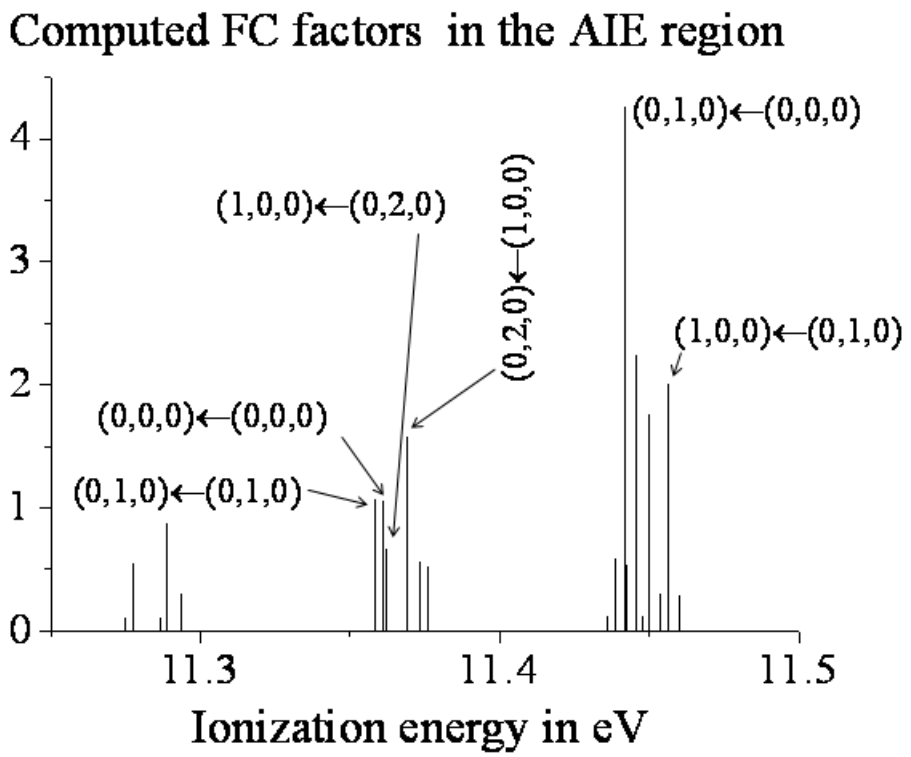

Figure 7.10: Computed Franck-Condon factors of the $CF_2^+(X^2A_1) + e^- \leftarrow CF_2(X^1A_1)$ photoionisation process and assignments of some vibrational components in the AIE region.

the ionisations $(1, 3, 0) \leftarrow (0, 0, 0)$ and $(2, 1, 0) \leftarrow (0, 0, 0)$.

Once the main assignments of the structure in the experimental TPE spectrum have been established, values of the vibrational constants ν_1' (sym. stretching mode) and ν_2' (sym. bending mode) in the ionic state can be derived. For ν_1', ω_e and $\omega_e\chi_e$ were obtained as (1370 ± 20) and (7 ± 10) cm^{-1}. The value for ω_e, compares very well with the value of 1370.0 cm^{-1} obtained from the CAS/MRCI/aug-cc-pV5Z PEF while the fundamental separation (1356 ± 20) cm^{-1} also compares very well with the value of 1356.3 cm^{-1} derived from the CAS/MRCI/aug-cc-pV5Z PEF (see values listed in Table 7.1). The agreement is not so good for ν_2'. The harmonic and fundamental

values expected from the CAS/MRCI/aug-cc-pV5Z PEF are 653.2 and 651.7 cm^{-1} respectively. The corresponding ω_e and $\omega_e\chi_e$ values obtained from the experimental TPE spectrum are (635 ± 10) cm^{-1} and (0 ± 5) cm^{-1}, giving the harmonic and fundamental values as (635 ± 10) cm^{-1}.

This work indicates that studies with TPE spectroscopy, supported by *ab-initio*/Franck-Condon calculations, of other tri– and tetra–atomic reactive intermediates, in which vibrational structure in more than one vibrational mode in the first and higher PE bands is expected, is possible and this is planned for future work. The results should lead to a more reliable determination of the AIE, assignment of the observed vibrational structure and hence determination of vibrational frequencies in the ionic state.

7.4 Conclusion

In this work, the first photoelectron band of difluorocarbene, CF_2, has been recorded with threshold photoelectron (TPE) spectroscopy. Extensive vibrational structure was obtained for this band but the adiabatic component was not observed. Even though the TPE vibrational envelope is non–Franck-Condon in nature, comparison of the structure seen in the vibrational components with that expected from an *ab-initio*/Franck-Condon simulation has allowed the upper state vibrational quantum numbers associated with each observed vibrational component to be determined. The position of the adiabatic component could then be determined. Also, the harmonic and fundamental vibrational frequencies for ν_1' and ν_2' for the ionic state, $CF_2^+(X^2A_1)$, have been derived from the experimental TPE spectrum. These compare well with those determined from the potential energy function for $CF_2^+(X^2A_1)$ computed in this work with high level electronic structure calculations. The adiabatic ionisation energy of CF_2 is recommended as 11.362 ± 0.005 eV.

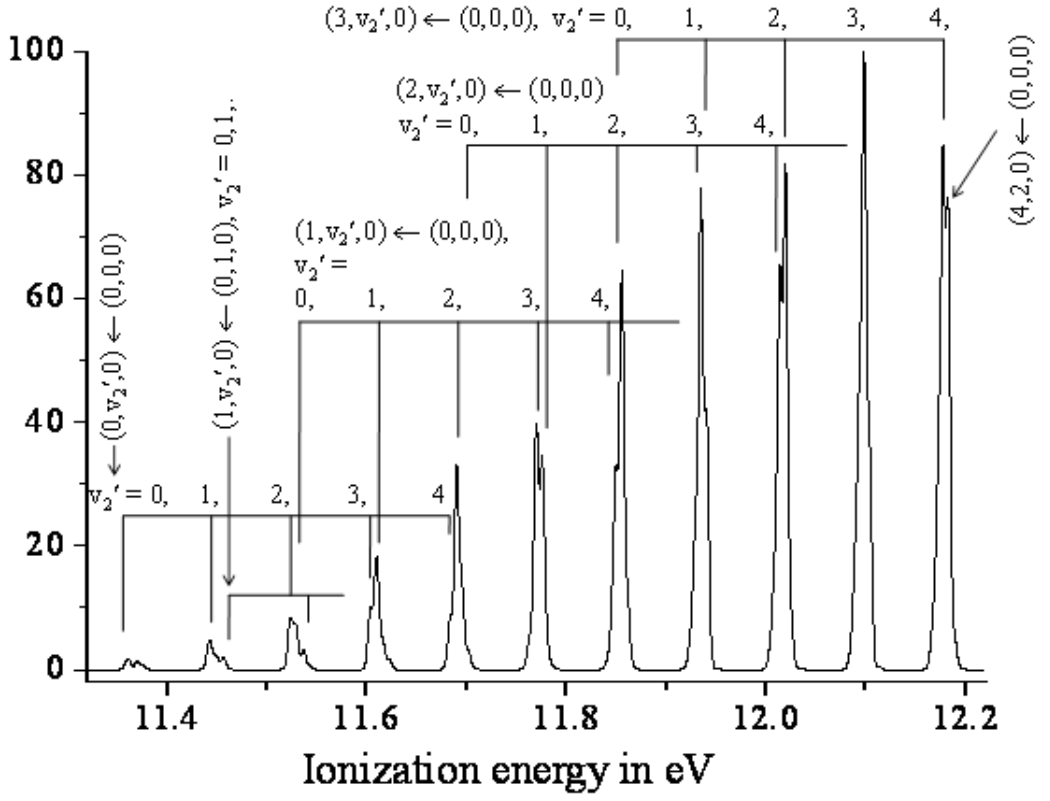

Figure 7.11: A simulated spectrum showing assignment of the main structure in the low energy region (11.3-12.2 eV) in the first photoelectron band of CF_2. The doublet structure observed in some of the bands arises because $2\nu_2'$ is approximately equal to ν_1'. More detail of the structure in the band at 11.36 eV is shown in Figure 7.10. The main structure shown corresponds to $(v_1', v_2', 0) \leftarrow (0, 0, 0)$ combination bands with $v' = 0, 1, 2$ and 3.

Chapter 8

Study of SF_2 and HO_2 by TPES

SF_2 and HO_2 are both non linear triatomics that have received much attention because of their respective roles in the semiconductor industry, and in the chemistry of the atmosphere and combustion. Their first PE bands were investigated in the present work using threshold photoelectron spectroscopy and the results are presented in this chapter. The work carried out on SF_2 is presented in sections 8.1 to 8.3. Previous experimental and theoretical work on SF_2 is reviewed in section 8.1, section 8.2 presents the experimental conditions used while the results are shown in section 8.3. The preliminary work carried out on HO_2 is presented in section 8.4 and a conclusion for both experiments is presented in section 8.5.

8.1 Previous work on SF_2

SF_x reactive intermediates have received considerable attention both experimentally and theoretically, motivated partly because of their importance in the semiconductor industry [202], where they play a major role in plasma etching in SF_6/O_2 plasmas.

The existence of SF_2 was confirmed in 1969 by microwave spectroscopy [203] and by mass spectrometry [204]. In a microwave study, Kirchhoff et al [205], determined the force field for SF_2 from the centrifugal distortion constants and derived the following vibrational frequencies, $\nu_1 = 840 \pm 20$ cm^{-1}, $\nu_2 = 357 \pm 2$ cm^{-1} and $\nu_3 = 809 \pm 10$ cm^{-1}. Endo et al. [206] obtained anharmonic potential constants from the microwave spectrum of SF_2 in the first excited vibrational states of the three normal modes and determined the equilibrium geometry of its ground state ($r_e = 1.58745 \pm 0.00012$ Å, θ_e(F–S–F) $= 98.048 \pm 0.013°$). Deroche et. al. [207] performed an infrared spectroscopy study in the gas phase and obtained the following vibrational frequencies: $\nu_1 = 838.5299 \pm 0.0015$ cm^{-1} and $\nu_3 = 813.0413 \pm 0.0005$ cm^{-1}. In these studies, SF_2 was obtained from the reaction of OCS with discharged SF_6 [203], CF_4 [206] or F_2 [207]. Glinsky et al. [208, 209] studied SF_2 from the emission spectrum recorded for the reaction of F_2 with CS_2 and found ground state vibrational frequencies that compare well with those previously obtained, $\nu_1 = 838 \pm 2$ cm^{-1}, $\nu_2 = 355 \pm 2$ cm^{-1} and $\nu_3 = 817 \pm 6$ cm^{-1}. The He(I) photoelectron (PE) spectrum of SF_2 was recorded in 1978 by de Leeuw et al. [210]. In this study, SF_2 was produced by the reaction of OCS with discharged SF_6 and CF_4. Five PE bands were observed in the He(I) PE spectrum and vibrational structure was seen only in the first PE band. It has a regular progression in the symmetric stretching mode of the ion, with an average separation of 935 cm^{-1} (116 meV) [210]. In this work [210], the PE spectrum was compared with PE spectra of similar AB_2 molecules and with results of calculations of their vertical ionisation energies. The adiabatic and vertical first ionisation energy, AIE and VIE, experimentally obtained are 10.08 eV and 10.31 eV. In a resonance-enhanced multiphoton ionisation (REMPI) study, two Rydberg series were observed and assigned by Johnson et al. [211]. In each series, structure in both vibrational frequencies ν_1 and ν_2 were observed. In a second REMPI study by Li et al. [212], eight Rydberg series were assigned, also showing structure in both vibrational frequencies, ν_1 and ν_2. The band positions and quantum defects were fitted, which gave a first adiabatic ionisation energy for SF_2 of 10.021 eV.

Electronic structure calculations have also been performed on SF_2. In 1976, Thomson [213] carried out *ab-initio* calculations using a large Gaussian basis set. Geometry optimisation was performed and one-electron properties were calculated. In 1995, Irikura [214] carried out *ab-initio* calculations to determine the molecular structure and the thermochemistry of the sulphur fluorides SF_n (n = 1 - 5) and sulphur fluoride cations SF_n^+ (n = 1 – 5) in the gas phase. An adiabatic ionisation energy of 10.15 ± 0.19 eV and vibrational frequencies of $\nu_1 = 840$ cm^{-1}, $\nu_2 = 339$ cm^{-1} and $\nu_3 = 827$ cm^{-1} for SF_2 and $\nu_1 = 956$ cm^{-1}, $\nu_2 = 389$ cm^{-1} and $\nu_3 = 976$ cm^{-1} for SF_2^+ were obtained in this work [214]. More recently, Lee et al. [215] simulated the He(I) photoelectron spectrum of SF_2 via *ab-initio* calculations on SF_2 and SF_2^+ followed by Franck-Condon factor calculations which allowed for anharmonicity in each state. The agreement with the experimental spectrum obtained for the first PE band by de Leeuw et al. [210] was very good. The computed vibration frequencies thus obtained are $\nu_1 = 846.6$ cm^{-1}, $\nu_2 = 357.0$ cm^{-1} and $\nu_3 = 823.9$ cm^{-1} for SF_2 and of $\nu_1 = 985.6$ cm^{-1}, $\nu_2 = 413.4$ cm^{-1} and $\nu_3 = 1012.5$ cm^{-1} for SF_2^+ with an AIE of 10.075 eV [215]. In the present work, the first PE band of SF_2 has been reinvestigated by Threshold Photoelectron Spectroscopy (TPES). The objective was to obtained a higher resolution spectrum of the first PE band of SF_2, and to determine the first adiabatic ionisation energy (AIE).

8.2 Experimental

The experiments reported here were undertaken on the Circularly Polarised Beamline (4.2R, Polar) at the Elettra synchrotron radiation source using the photoelectron spectrometer described in Chapter 3. PE and TPE spectra were recorded as explained in Chapter 3 and the same procedures were used to normalise the spectra for photon flux and the transmission function of the spectrometer. In the present

work, SF_2 was produced from the rapid reaction of F + OCS:

Primary reaction:	F + OCS→SF + CO
Subsequent reaction:	SF + SF → SF_2 + S
Followed by:	S + S + M → S_2 + M

The rate constants of the primary reaction (k_1) and of the subsequent reaction (k_2) are: $k_1 = 1.8 \times 10^{-11}$ $cm^3.molecule^{-1}.s^{-1}$ at 25° C and $k_2 = 2.5 \times 10^{-11}$ $cm^3.molecule^{-1}.s^{-1}$ at 25° C [66]. Preliminary PE experiments were carried out in Southampton in order to determine the optimum partial pressures and reactant mixing distance above the photon beam which maximise the intensity of the first SF_2 PE band. The optimum partial pressures were: $\Delta p(Ar) = 5.40\times10^{-7}$ mbar, $\Delta p(OCS) = 3.50\times10^{-6}$ mbar and $\Delta p(F_2/He) = 4\times10^{-6}$ mbar. The most intense spectra of the SF_2 features were obtained with a reactant mixing distance of about 8 cm from the photon beam. Argon was introduced with the reagents to optimise the voltages when recording TPE spectra, as was seen in Chapter 3. It should be noted that the X^1A_1 state of SF_2 has the electronic configuration $...(8a_1)^2(3b_1)^2(5b_2)^2(1a_2)^2$ [215].

8.3 Results and discussion

A photoelectron spectrum of the reaction F + OCS, recorded at a photon energy of $h\nu = 21.22$ eV and a mixing distance of 8 cm, is shown in Figure 8.1. It shows a progression in the symmetric stretching mode, ν_1, of SF_2^+ [210, 215] as well as secondary products of the reaction, like S atoms, S_2 and CO. S atom has its first component at 10.36 eV (VIE) [36] while S_2 has four bands in the energy region of interest, at 9.41, 11.82, 12.33 and 13.20 eV (VIE) [216]. All these bands are seen and assigned on the PE spectrum shown in Figure 8.1. There is very little excess OCS and significantly more S_2 than S atoms, which indicates that the S atoms have had

time to recombine. However, the yield of SF_2 is good and the vibrational progression clearly visible, which should allow TPE spectra to be recorded without difficulties.

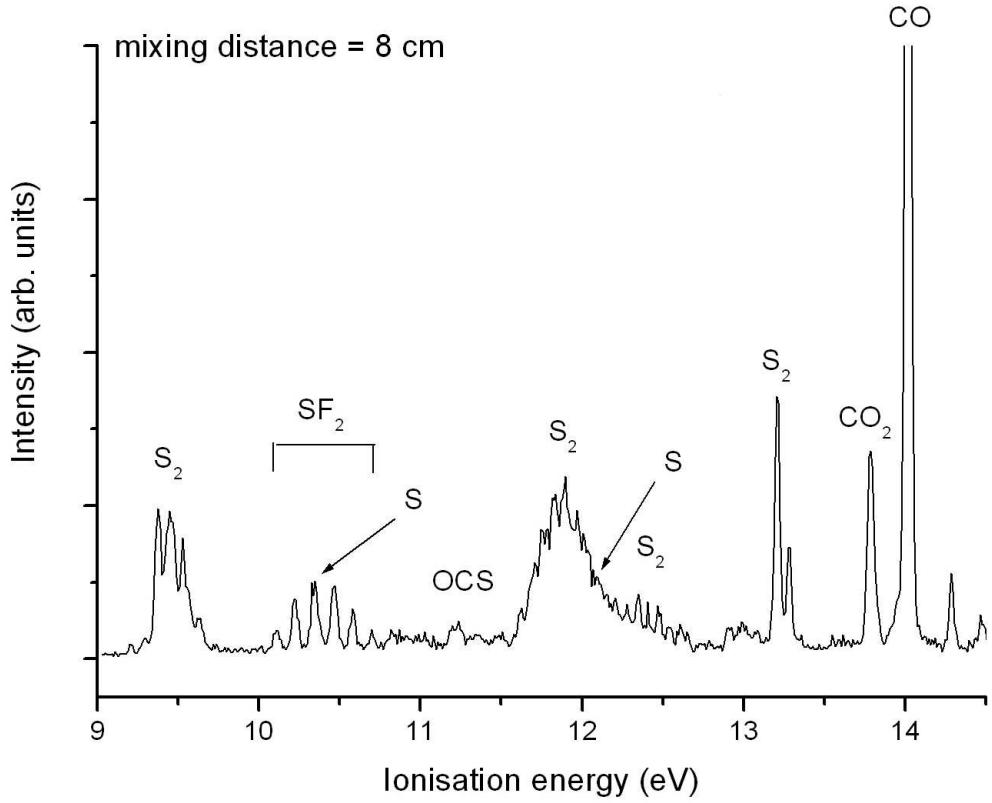

Figure 8.1: PE spectrum of the reaction F + OCS recorded at a photon energy of 21.22 eV and a mixing distance of 8 cm, which gives a low SF_2:S_2 ratio.

To record TPE spectra of the SF_2 vibrational structure with a spectral resolution of about 5 meV (as estimated from the full width at half maximum of the main $(3p)^{-1}$ $Ar^+(^2P_{3/2}) \leftarrow Ar(^1S_0)$ line), the penetrating-field analyser was tuned to detect near-zero energy (threshold) photoelectrons. The detection of threshold electrons was optimised using the $(3p)^{-1}$ $Ar^+(^2P_{3/2,1/2}) \leftarrow Ar(^1S_0)$ TPE spectrum as explained in Chapter 3. A TPE spectrum of the F + OCS reaction, obtained in the photon energy range 9.8 to 11.2 eV, is presented in Figure 8.2.

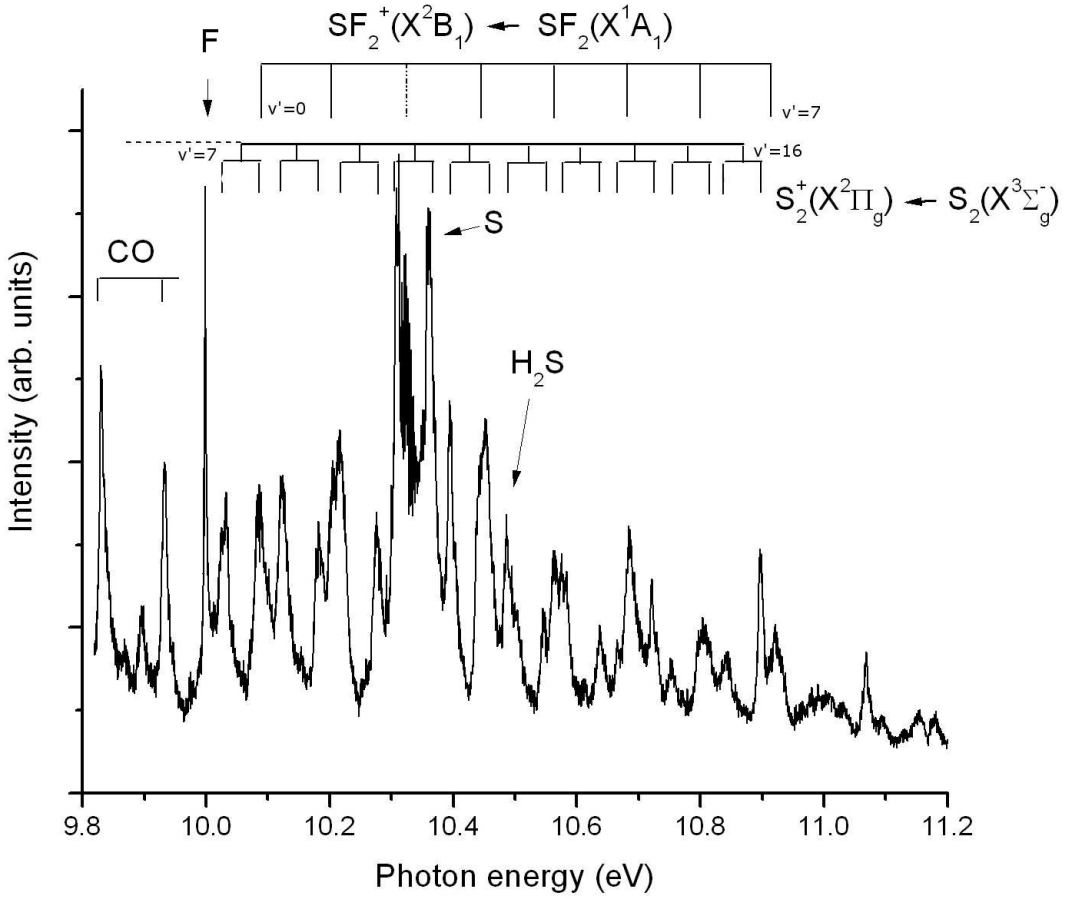

Figure 8.2: TPE spectrum of the reaction F + OCS in the photon energy region 9.8 to 11.2 eV recorded with low a SF_2:S_2 ratio. The SF_2 and S_2 vibrational progressions are shown on the spectrum.

The TPE spectrum shown in Figure 8.2 has a very different structure from the PE spectrum shown in Figure 8.1. This is because TPE spectra are often dominated by autoionisation processes, which can lead to non–Franck-Condon distributions as well as the observation of ionic vibrational levels which are not observed in the normal Franck-Condon distribution, as was explained in Chapter 2. The main SF_2 features in the TPE spectrum in Figure 8.2 have been assigned with the help of the PE spectrum seen in Figure 8.1 and correspond to a progression in the symmetric stretching mode,

ν_1 of SF_2^+. Other features are also visible in the TPE spectra, like H_2S, which arises from the reaction of OCS with residual water absorbed on the inlet system (its VIE is 10.48 eV [217]) and S atoms. From the PE spectrum, it was expected that the energy region of the $SF_2^+ \leftarrow SF_2$ vibrational progression would be clear from any contamination, except S atoms. However, the TPE spectrum shown in Figure 8.2 contains many more features than just the ones associated with the $SF_2^+ \leftarrow SF_2$ vibrational progression. It is known from the PE spectrum that there is a significant amount of S_2 produced in the ionisation region. A TPE study of O_2 by Ellis et al. [218] showed that in TPE experiments, the vibrational structure associated with the first O_2 band extended between the first two bands. S_2 has a very similar spectrum to O_2 as they have the same valence electronic configuration. The vibrational splitting of the first band of S_2 is 790 cm^{-1} (94.2 meV) [216] and the spin orbit splitting is 470 cm^{-1} (58.3 meV). Assuming that the same autoionisation effect occurs in S_2 as in O_2, some of the non-assigned structure in Figure 8.2 could be attributed to S_2. The spacings between the unassigned features have been measured and correspond indeed to the expected vibrational splitting and spin-orbit splitting in S_2. These features were thus assigned to S_2, as shown on the spectrum. The first observed vibrational component of S_2 on the TPE spectrum appears at 10.03 eV (second order peaks prevent the observation of earlier vibrational components of S_2). Extrapolating from the PE spectrum showing the first S_2 PE band, the first vibrational component seen in the TPE spectrum has been assigned to the vibrational quantum number $v' = 7$, in the ionic state of the $S_2^+(X^2\Pi_g, v') \leftarrow S_2(X^3\Sigma_g^-, v'' = 0)$ ionisation. The three sharp bands at 9.83, 9.93 and 10.00 eV observed in the TPE spectrum in Figure 8.2 are second order bands, and were also observed in TPE spectra recorded in the photon energy region 19.6 to 22.4 eV. The band at 10.00 eV in Figure 8.2 corresponds to F atoms ($F^+(^1D) \leftarrow F(^2P)$ at $h\nu = 20.007$ eV) [36] while the other two correspond to the CO ($CO^+(B^2\Sigma^+) \leftarrow CO(X^1\Sigma^+)$ ionisation, with two vibrational components at $h\nu = 19.688$ eV and $h\nu = 19.896$ eV [217]. Both CO and F atoms are clearly seen in PE spectra recorded at $h\nu = 21.22$ eV.

The unexpected contribution of S_2 in the TPE spectrum in the energy region of the first $SF_2^+ \leftarrow SF_2$ band prevented the assignment of the SF_2 vibrational features to be reliably made. For that reason, conditions where the SF_2:S_2 ratio is higher are needed. The F + OCS reaction was therefore studied at different mixing distances (reaction times) as well as at different partial pressures to try and find conditions where no S_2 was seen. It was found that a short reactant mixing distance (0 cm) allowed the observation of the reaction at an early stage where S atoms recombination is low and not much S_2 is produced. The optimum partial pressures at this short mixing distance are: $\Delta p(OCS) = 2.80\times10^{-6}$ mbar and $\Delta p(F_2/He) = 6.00\times10^{-6}$ mbar.

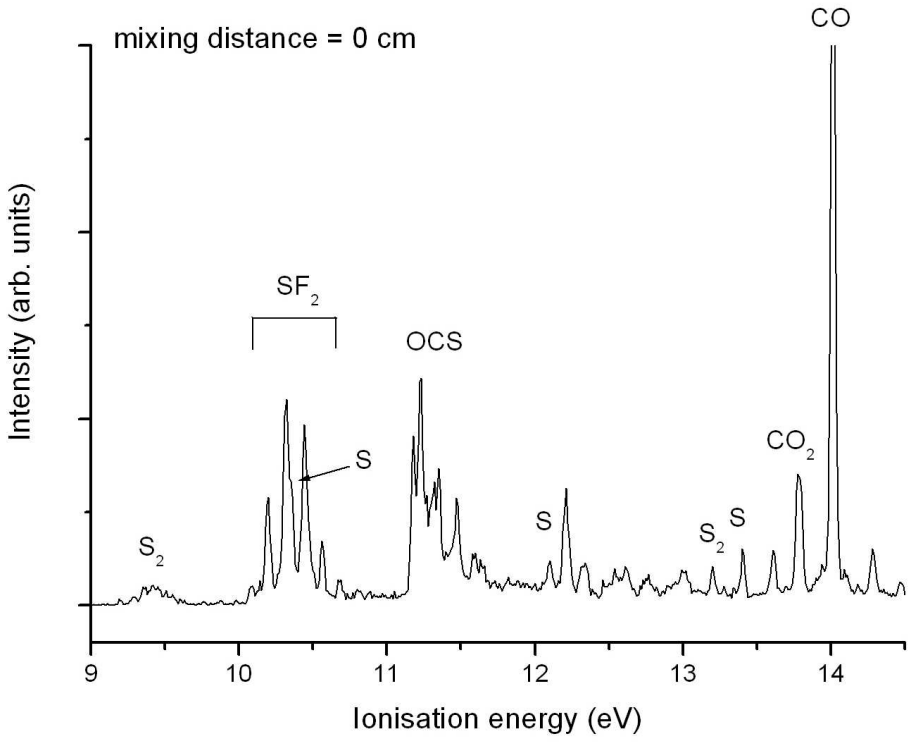

Figure 8.3: PE spectra of the reaction F + OCS obtained at a photon energy of $h\nu$ = 21.22 eV and a mixing distance of 0 cm, which shows a high SF_2:S_2 ratio. The main features are marked on the spectrum

This set of conditions will be called condition 2 (with a high SF_2:S_2 ratio) in

comparison to the first set of conditions, condition 1 (with a low SF_2:S_2 ratio). A PE spectrum obtained with these conditions (condition 2) is shown in Figure 8.3. It was recorded at a photon energy $h\nu$= 21.22 eV and shows a high SF_2:S_2 ratio. The difference in the SF_2:S_2 ratio between Figure 8.1 and Figure 8.3 is clearly visible. By moving the reactant mixing distance forward, the reaction is now observed earlier and significantly less S_2 is formed. There is a some unreacted OCS and the yield of SF_2 is still good. A TPE spectra recorded under these conditions (high SF_2:S_2 ratio) is shown in Figure 8.4, in the ionisation energy region 9.9 to 11.2 eV.

The TPE spectrum shown in Figure 8.4 shows a much clearer $SF_2^+ \leftarrow SF_2$ vibrational progression than the TPE spectrum obtained with the first set of conditions (Figure 8.2), especially above 10.5 eV. Few secondary products of the reaction are still observed, like S and SH; these are marked on the spectrum, as well as some second order features. Unfortunately, it was not possible to fully remove the S_2 contribution and its first band vibrational progression is still seen on the TPE spectrum.

In order to see clearly the difference in the intensity of the SF_2 and S_2 features between the two sets of conditions, a comparison of the TPE spectra is shown in Figure 8.5. The TPE spectrum at the top of the Figure was obtained during the first experiments, in 2007, with low SF_2:S_2 ratio. The TPE spectrum shown in the middle of Figure 8.5 was obtained in 2009 with the second set of conditions (notably shorter mixing distance), to try and minimise the S_2 contribution in the spectra, and it has a much higher SF_2:S_2 ratio. The lowest part of Figure 8.5 shows a second order TPE spectrum recorded in order to estimate the contribution of second order peaks in the TPE spectra recorded for SF_2. The SF_2 and S_2 progressions are indicated at the top of the Figure. The difference between the two sets of spectra is clearly visible. The S_2 contribution in the second set of experiments is much smaller and the SF_2 vibrational progression much clearer, which permitted a more reliable assignment of the features to be made. Unfortunately, the S_2 contribution in this energy region prevented the

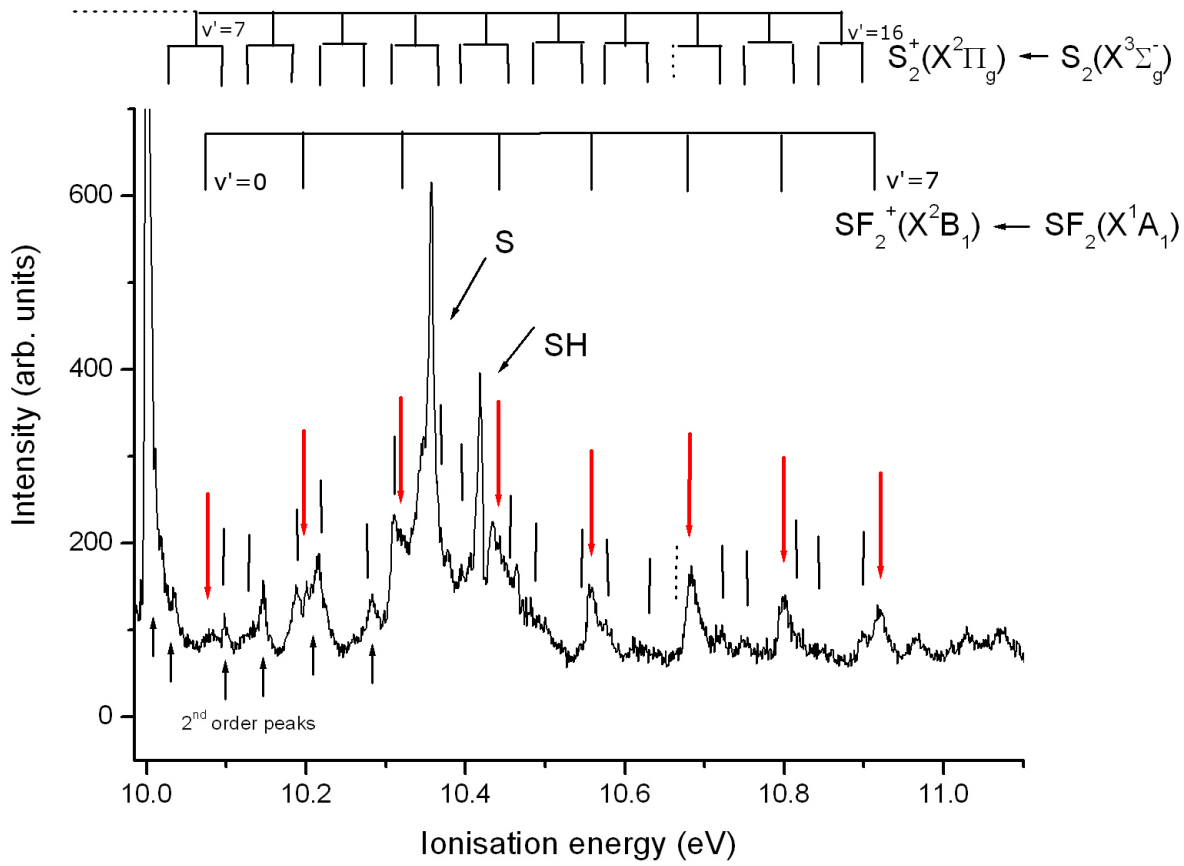

Figure 8.4: TPE spectrum of SF_2 recorded with the second set of conditions (high SF_2:S_2 ratio), in the photon energy region 9.9 to 11.2 eV. The $S_2^+ \leftarrow S_2$ vibrational progression is shown with black vertical lines while the $SF_2^+ \leftarrow SF_2$ vibrational progression is shown with red arrows. Second order peaks are indicated from the bottom with black arrows.

observation of any additional structure in the $SF_2^+ \leftarrow SF_2$ vibrational progression, like contribution from "hot" bands, as seen in the simulated PE spectrum of SF_2 in reference [215], or a progression in a vibrational mode of SF_2^+ other than the symmetric stretching mode, ν_1.

Nevertheless, vibrational components up to v' = 7 have been observed for the symmetric stretching mode of SF_2^+. In order to find the band position of each

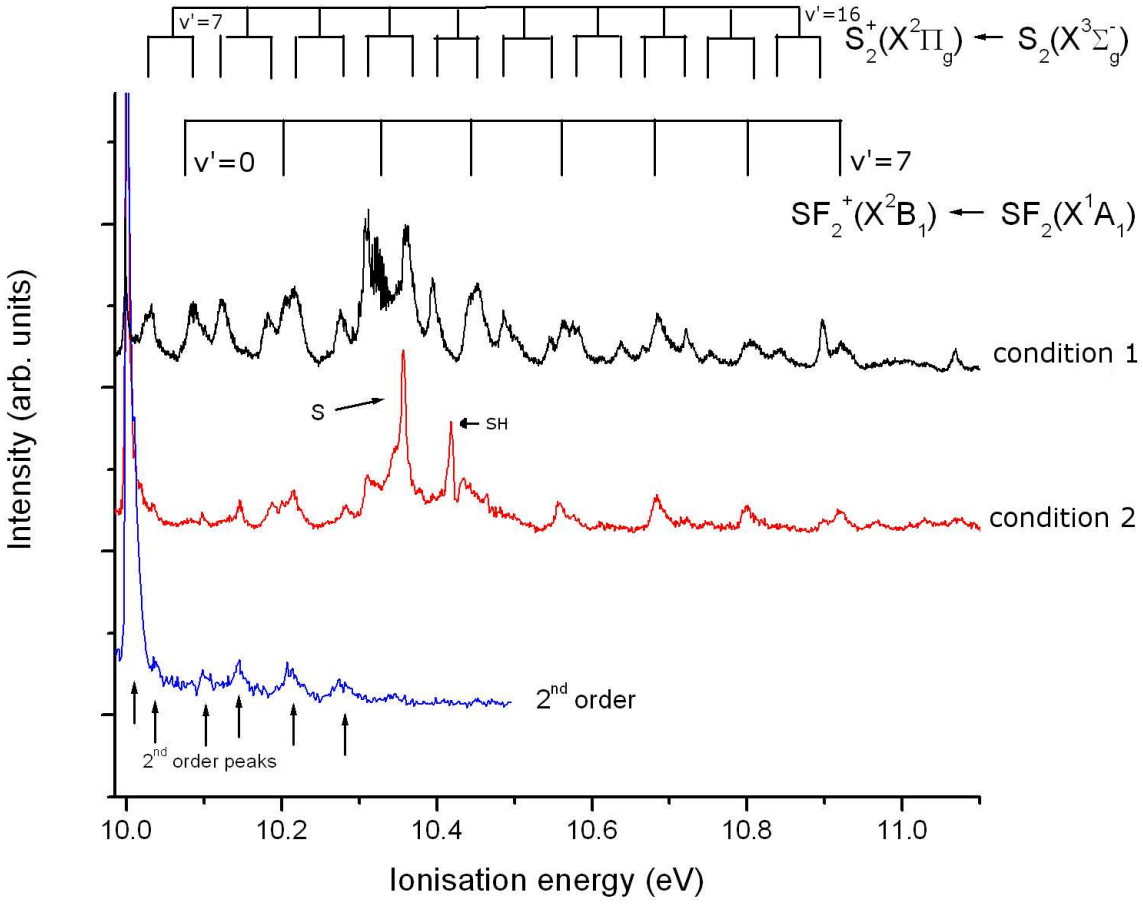

Figure 8.5: Comparison of TPE spectra of SF_2 recorded under different experimental conditions. The top part of the Figure shows the TPE spectrum obtained with the 1st set of conditions (low SF_2:S_2 ratio). The middle TPE spectrum was obtained with the 2nd set of conditions (high SF_2:S_2 ratio). The lower spectrum shows a second order TPE spectrum. $SF_2^+ \leftarrow SF_2$ and $S_2^+ \leftarrow S_2$ vibrational progressions are indicated on top of the spectra.

component, the components were fitted using an asymmetric Gaussian function. This procedure was carried out on all the TPE spectra (about 10) recorded with the second set of conditions and the results were averaged; the results are shown in Table 8.1. The spacing ΔE between bands is also shown in the Table. Vibrational

components with quantum numbers v' = 4, 5, 6 and 7 are clearly observed, as is seen in Figure 8.4, and hence, were easy to fit (the error in the band position is thus small). Vibrational components with quantum numbers v' = 1, 2 and 3 are very close to other features, which made the fitting procedure much harder. Also, the v' = 0 component is very weak in intensity, as can be seen in Figure 8.6, which shows a TPE spectrum of the adiabatic ionisation energy region (10.0 to 10.25 eV) obtained with the second set of conditions (high SF_2:S_2 ratio). This figure shows the two first vibrational components of SF_2^+, four components of the S_2^+ progression and five second order peaks. It can thus be understood that the fitting of the features in this energy region is approximate due to the number of peaks present.

	Band position (eV)	Spacing ΔE (cm^{-1})	Comment
v'=0	10.076 ± 0.002		very weak
v'=1	10.198 ± 0.003	984 ± 10	close to other peaks
v'=2	10.320 ± 0.004	976 ± 10	close to other peaks
v'=3	10.441 ± 0.003	976 ± 10	close to other peaks
v'=4	10.559 ± 0.002	976 ± 9	well defined
v'=5	10.680 ± 0.001	976 ± 8	well defined
v'=6	10.799 ± 0.002	958 ± 8	well defined
v'=7	10.919 ± 0.001	958 ± 8	well defined

Table 8.1: Band position of the SF_2^+ vibrational progression in eV obtained by fitting the experimental features. Also given in the table, are the spacings ΔE between the features.

However, knowing the positions of the last four vibrational components (v' = 4 to v' = 7), and their spacings, allowed an approximate position of the first four vibrational components to be determined by extrapolation. This permitted the fitting of the first four components (v' = 0 to v' = 3) to be performed with reasonable accuracy, as can

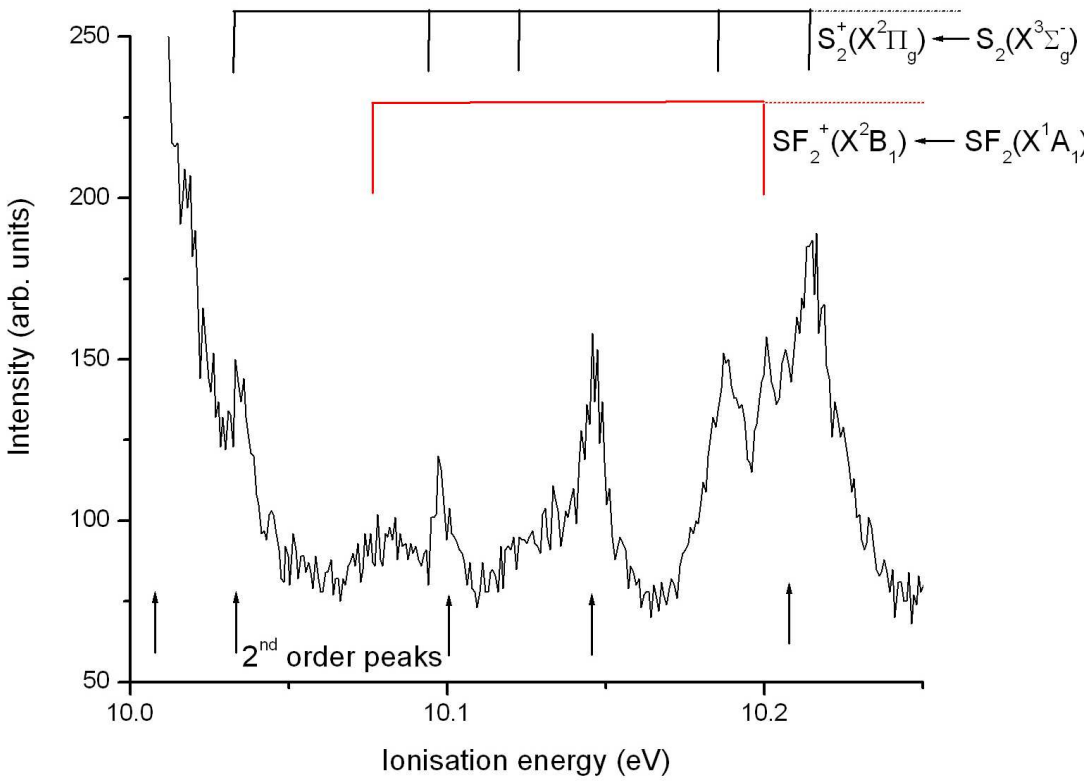

Figure 8.6: TPE spectrum of the adiabatic ionisation energy region of SF_2 recorded with the second set of conditions, showing the first two vibrational components of $SF_2^+ \leftarrow SF_2$ (red) and some $S_2^+ \leftarrow S_2$ vibrational components (black), as well as second order peaks (arrows)

be seen in Table 8.1.

ω_e and $\omega_e\chi_e$ in the symmetric stretching mode of the ionic state of SF_2 could then be obtained from the spacing (ΔE) between the vibrational components plotted against (v'+1). This gives a straight line of slope -2 $\omega_e\chi_e$ and intercept equal to ω_e, as was explained in Chapter 2. The results are shown in Table 8.2, along with the measured adiabatic and vertical ionisation energies (AIE and VIE). The results are also compared in this table with previous experimental and theoretical results obtained by de Leeuw et. al. [210] and Lee et. al. [215] respectively.

	This work	ref [215]	ref [210]
ω_e (cm^{-1})	988 ± 7	985.6	935 ± 40
$\omega_e\chi_e$ (cm^{-1})	2 ± 1		
AIE (eV)	10.076 ± 0.002	10.075 ± 0.011	10.08
VIE (eV)	10.320 ± 0.004	10.319	10.31

Table 8.2: Comparison of the results (AIE, VIE and vibrational constants) obtained in the present work and in previous experimental [210] and theoretical [215] works for the study of SF_2.

The results obtained in the present work compare well with those of previous works, especially with those obtained by Lee et. al. by *ab initio*/Franck–Condon factor calculations [215] (the value of the AIE and VIE between the present work and ref [215] differ only by 1 meV). The value of ω_e obtained experimentally by de Leeuw et. al. [210] is quite far from the values obtained in the present work and in ref [215] but this discrepancy was discussed in reference [215], and it was concluded that the agreement between theory and experiment was just within the combined experimental and theoretical uncertainties. Lee et. al. [215] performed state-of-the-art *ab initio* calculations on SF_2 and SF_2^+. The fact that the results obtained in the present work agree so well with those results [215] shows the improvement in resolution obtained using the threshold photoelectron technique compared to conventional PES. Even though all the TPE spectra were contaminated by S_2, reliable results could be obtained from the TPE study of SF_2.

8.4 Preliminary measurements on HO_2

HO_2 has been widely studied because of its importance in atmospheric and combustion reactions [219–221]. Its He(I) PE spectrum was recorded in 1981 by Dyke et. al. [222] and shows a vibrational progression in the O–O stretching mode (ν_2) of HO_2^+. HO_2 was made in this work from the F + H_2O_2 reaction, where H_2O_2 was prepared in the gas–phase by pumping on a concentrated aqueous H_2O_2 solution. The first AIE derived from this work is 11.35 eV [222] and the vibrational frequency obtained for the O–O stretching mode is 1560 cm^{-1} (0.19 eV). In the present work, HO_2 was studied by PE and TPE spectroscopy. It was also prepared for study from reaction F + H_2O_2 [222]:

Primary reaction: $F + H_2O_2 \rightarrow HO_2 + HF$

Subsequent reaction: $F + HO_2 \rightarrow O_2 + HF$

The rate constants of the primary reaction (k_1) and of the subsequent reaction (k_2) are: $k_1 = 4.98 \times 10^{-11}$ $cm^3.molecule^{-1}.s^{-1}$ at 25° C and $k_2 = 8.30 \times 10^{-11}$ $cm^3.molecule^{-1}.s^{-1}$ at 25° C [223]. H_2O_2 was obtained by warming up a H_2O_2:urea complex (Sigma Aldrich) mixed with sand (Sigma Aldrich) to about 35° C using a heating mantle. H_2O_2 then reacts with F atoms to give HO_2. A PE spectrum obtained from this reaction at a photon energy $h\nu = 21.22$ eV is shown in Figure 8.7. This is in good agreement with that recorded earlier [222].

In the PE spectrum shown in Figure 8.7, the $HO_2^+(X^3A'') \leftarrow HO_2(X^2A'')$ ionisation is observed with a progression in the ν_2 stretching mode of HO_2^+ (the O-O symmetric stretch). Also, the third component of the first band of HO_2 is broader than the other components and, as suggested in earlier work, this could be the start of the second band of HO_2, the $HO_2^+(a^1A') \leftarrow HO_2(X^2A'')$ ionisation [224–226]. Secondary products of the reaction are also seen like a vibrational progression in the

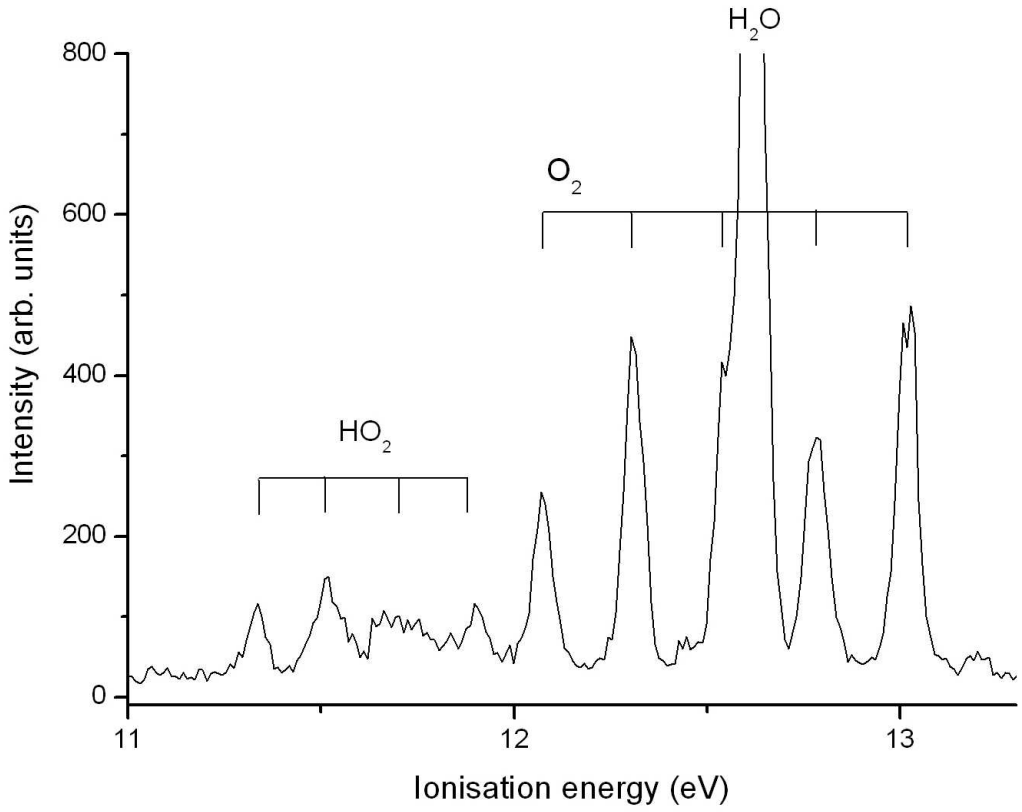

Figure 8.7: PE spectrum of HO_2 obtained from the reaction F + H_2O_2 recorded at a photon energy of 21.22 eV. The HO_2 band labelled is the $HO_2^+(X^3A'') \leftarrow HO_2(X^2A'')$ ionisation.

$O_2^+(X^2\Pi_g, v' = 0) \leftarrow O_2(X^3\Sigma_g^-, v'' = 0)$ ionisation, as was seen in the VUV PES study of HO_2 in reference [222]. Water was also seen. This arises from the heated solid sample. The aim of the measurements performed in the present work was to obtain a spectrum of the HO_2^+ vibrational structure with better resolution than achieve previously. For that reason, TPE measurements were carried out and the spectrum obtained in the photon energy range 11.3 to 12.2 eV is presented in Figure 8.8.

The TPE spectrum of HO_2 shows vibrational components in the stretching mode of HO_2^+ (the O-O symmetric stretch) at 11.35, 11.55 and 11.75 eV. Unfortunately, the

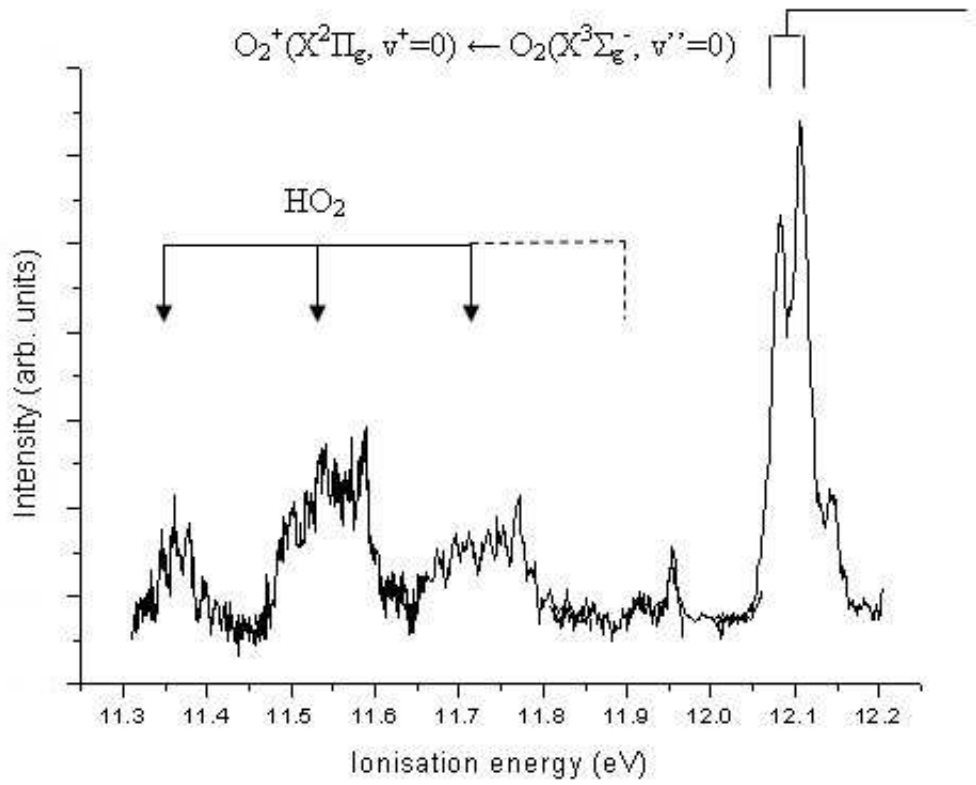

Figure 8.8: TPE spectrum of HO_2 obtained from the reaction F + H_2O_2 in the photon energy region 11.3 to 12.2 eV

improvement in the resolution between the PE and TPE spectra is very small, which prevents the observation of any underlying structure. The fourth component of the HO_2^+ vibrational progression did not have repeatable intensity and can therefore not be assigned with certainty. The first component of O_2 is seen at 12.07 eV and is part of the first band of oxygen, $O_2^+(X^2\Pi_g, v' = 0) \leftarrow O_2(X^3\Sigma_g^-, v'' = 0)$. The doublet structure corresponds to ionisation to the the spin-orbit states $O_2^+(X^2\Pi_{1/2g})$ and $O_2^+(X^2\Pi_{3/2g})$ [227] in $v' = 0$. The reason why the resolution is so poor in the TPE spectrum shown in Figure 8.8, and in all the TPE spectra recorded during this set of experiments, arises from a fluctuation of the temperature in the heated H_2O_2 precursor. Indeed, the heating mantle used during the experiments to warm up the

H_2O_2:urea complex was not able to maintain a constant temperature (to within ± 0.1° C) of the heated complex. As a result, the TPE spectra obtained, all suffered from fluctuations due to the temperature instability, which gave rise to a vapour pressure fluctuation. This experiment thus needs to be carried out again with an accurate temperature control on the heater system used for the H_2O_2:urea complex to achieve a constant vapour pressure of H_2O_2. The aim is to resolve the underlying structure in the HO_2 first band and if possible obtain clear evidence of the second band which is expected to have its first component in the 11.5–12.0 eV region [224–226].

8.5 Conclusion

In this chapter, the results of TPE measurements on SF_2 and HO_2 were presented. In the case of SF_2, the first photoelectron band was recorded using TPE spectroscopy with different experimental conditions (i.e. low and high SF_2:S_2 ratios). Vibrational components from v' = 0 to v' = 7 in the symmetric stretching mode in the ionic state were assigned, which permitted the experimental determination of the vibrational frequency in the symmetric stretching mode, ν_1, in the ground state of SF_2^+. The harmonic frequency obtained compares well with the one obtained computationally from the previous work of Lee et. al. [215]. The adiabatic and vertical ionisation energies of SF_2 determined in this work (11.076 ± 0.002 and 11.320 ± 0.004 eV) also compare well with those obtained from previous works [210, 215]. The agreement between the AIE and VIE values, and ω_e in ν_1, in the ionic state obtained in the present work and with state-of-the-art *ab initio* calculations [215] is within 1 meV, which shows the precision of the TPE technique. Unfortunately, the presence of an S_2 vibrational progression prevented the observation of any additional structure in SF_2^+, and although better resolution was achieved with respect to previous experimental

work [210], it was not possible to obtain more information from the spectra. For this reason, another way to produce SF_2 that does not produce any S_2 is needed. Similarly, an improved experimental protocol is needed to repeat the TPE measurements on HO_2, which would provide stable conditions, in the hope of resolving the underlying structure.

Chapter 9

Conclusions and future work

9.1 Conclusions

The aim of this project, as stated in the Introduction, was to study the photoionisation behaviour of selected reactive species in the gas phase using photoelectron spectroscopy at the Synchrotron Radiation Source of Elettra, Trieste. In this thesis, work carried out on the reactive intermediates I, IF, CF_2, SF_2 and HO_2 was presented. It was shown that successful studies of reactive intermediates could be performed using several spectroscopic techniques, such as angle-resolved photoelectron spectroscopy (PES), angle-resolved constant ionic state (CIS) spectroscopy and threshold photoelectron spectroscopy (TPES). The characteristics of the different techniques used, allowed different types of information to be obtained for the selected reactive intermediates.

I and IF were studied by photoelectron spectroscopy, which led to the determination of improved adiabatic and vertical ionisation energies (AIE) and (VIE) of the $IF^+(X^2\Pi_{3/2}) \leftarrow IF(X^1\Sigma^+)$ and $IF^+(^2\Pi_{1/2}) \leftarrow IF(X^1\Sigma^+)$ ionisations and improved

spectroscopic constants ω_e, $\omega_e\chi_e$, and r_e for the two IF ionic states $X^2\Pi_{3/2}$ and $^2\Pi_{1/2}$ (see Chapter 5). Also, in this chapter, a source of iodine atoms was developed and the relative intensities of I atom PE bands at fixed photon energy (21.22 eV) was established. This source was then used in a study by angle-resolved constant ionic state spectroscopy of iodine atoms (see Chapter 6). In this case, Rydberg series converging to different thresholds of iodine atoms were assigned and analysed. The quantum defect and ionisation energy of each series was obtained by fitting the Rydberg states to the Rydberg series energy expression. The asymmetry parameter, β, was determined as a function of photon energy for the first time for iodine atoms and showed unexpected behaviour. This behaviour was attributed to the fact that iodine is a heavy atom, where perturbations and strong relativistic and correlation effects are expected.

Threshold photoelectron spectroscopy was used in the study of the triatomic reactive intermediates CF_2, SF_2 and HO_2 (Chapters 7 and 8). CF_2 and SF_2 showed extensive vibrational structure in their first PE bands and their study by TPES allowed the determination of vibrational frequencies and ionisation energies. The experimental spectra of CF_2 were compared with results of *ab-initio*/Franck-Condon simulations which allowed a detailed assignment of the vibrational structure in the adiabatic ionisation energy region and an improved determination of the first adiabatic ionisation energy (see Chapter 8).

9.2 Future work

The success of the study of reactive intermediates by threshold photoelectron spectroscopy, followed by comparison with results of *ab-initio*/Franck–Condon simulations, opens new possibilities for the study of reactive intermediates. The support of *ab-initio*/Franck-Condon factor calculations in the analysis of TPE spectra

has proven very useful in the assignment of the vibrational components and in the determination of the adiabatic ionisation energy. In the near future, it is therefore planned to study other triatomics by TPES at the synchrotron radiation source of Elettra, followed by *ab-initio*/Franck-Condon calculations. The main objective, as described in the thesis, is to obtain higher resolution PE spectra of triatomic and tetratomic reactive intermediates via TPES to allow extra vibrational structure to be resolved (e.g. structure in more than one vibrational mode in a PE band) and extra vibrational components to be observed in TPES through autoionisation effects. This will allow extra information to be obtained on the ionic state investigated. In particular, an attempt has already been made to study HOCl by TPES during this project. PE spectra of HOCl were recorded in Southampton and showed vibrational structure in the first two PE bands. Unfortunately, the method of preparation of HOCl [228] proved unreliable and prevented the recording of TPE spectra at the synchrotron radiation source of Elettra. Another way of preparing HOCl is currently under test in the Southampton PES group, in the hope of observing this triatomic at the next visit to Elettra. It is also planned to perform *ab-initio*/Franck-Condon simulations on HOCl to support the experimental TPE spectra.

Similarly, improvements in the preparation of HO_2 are needed (as was described in Chapter 8), that would give improved temperature stability of the heated H_2O_2:urea complex in order to achieve a constant vapour pressure of H_2O_2. In this way, clear evidence of the HO_2 second band, which is expected to have its first component overlapped with the first band should be obtained [226]. Also, the improvement in resolution compared to conventional PES should allow clearer observation of the vibrational structure in the first two PE bands.

Other small reactive intermediates such as HONO [229], ClNO [230] and CH_3O_2 [231] are possibilities for future work. These reactive intermediates play important roles in combustion and tropospheric chemistry [229, 231]. The CH_3O_2 radical is involved in

reactions with nitric oxide to produce ozone in the troposphere while HONO is formed from the reaction of OH and NO, which are abundant in the troposphere [229, 231]. However, despite their importance in the chemistry of the atmosphere, there has been little experimental studies on these reaction intermediates. Their study by TPES could therefore lead to the determination of reliable AIEs as well the observation of vibrational structure in the ionic states. For example, the first three bands of ClNO are very close in energy and unresolved in the PE spectra [230]. A TPE study should allow resolution of the three bands. HONO can be made using a HONO reactor (from the reaction of HCl with $NaNO_2$) [232] and bled into the spectrometer through the needle valve. CH_3O_2 can be prepared on the spectrometer from the reaction of CH_3 with O_2, where CH_3 is made from the F + CH_4 reaction [231], while ClNO can be made on a vacuum line by the direct reaction of NO and Cl_2 [233]. The ClNO produced can be brought to the spectrometer in a bulb.

It is also known that the reaction of alkenes with ozone form aldehydes or ketones via carbonyl oxide intermediates, which are also called Criegee intermediates. Direct observation of the gas phase Criegee intermediate has proven very difficult because of its short lifetime. The first experimental observation of the Criegee intermediate was made by Taatjes et. al. in 2008 [234] from a photoionisation efficiency spectrum of the m/z = 46 signal observed in the Cl-initiated oxidation of dimethyl sulfoxide (DMSO). In this study [234], a photoionisation mass spectrum was obtained of the following reactions, using synchrotron radiation:

Primary reaction: $Cl + (CH_3)_2SO \rightarrow CH_3S(O)CH_2 + HCl$
Subsequent reaction: $CH_3S(O)CH_2 + O_2 \rightarrow CH_2OO + CH_3SO$

The photoionisation efficiency (PIE) spectrum of the m/z = 46 product was recorded and shows thioformaldehyde (CH_2S) and the Criegee intermediate CH_2OO (formaldehyde oxide). This route of preparing the Criegee intermediate is a lot less exothermic than preparing the Criegee intermediate via the ethylene plus ozone

reaction. As a result, the Criegee intermediate prepared by the Cl + $DMSO/O_2$ route is expected to be less excited and hence longer–lived under these reaction conditions than when produced from the ethylene plus ozone reaction. The main problem of this experiment [234] is the overlapping of the Criegee intermediate and thioformaldehyde in the PIE spectrum as they have same mass–to–charge ratio, although separate onsets were observed in the m/z = 46 photoionisation efficiency spectrum at 9.4 and 10.0 eV. This problem would be avoided in a PES study of this reaction as these two compounds have different ionisation energies. The AIE of CH_2OO is 10.0 eV [234] while the AIE of CH_2S is 9.376 ± 0.003 eV [235]. As a result, studying this reaction by UV PES at the synchrotron radiation source of Trieste could lead to the observation of the Criegee intermediate, the determination of an improved adiabatic ionisation energy and an investigation of the vibrational structure in the first PE band.

As described, the spectrometer used in the project was modified to allow Threshold Photoelectron Spectroscopy (TPES) studies to be performed. This modification was inspired by the work of other groups performing similar TPES experiments [70, 236]. Nevertheless, other improvements in the capabilities of the spectrometer are still possible and are currently under consideration. For example, it would be possible to replace the single channel detector that is currently used with a position-sensitive, multichannel device [237]. This would increase the spectral acquisition rate, which would be an important advantage when working at the synchrotron radiation source where time is limited. It would also be an advantage for working with reactive intermediates, that are present in low partial pressures, and/or for working with chemically aggressive species (as was the case during this project) that contaminate the spectrometer, decreasing its performance. For these reasons, faster data acquisition would be a major advantage.

Another improvement of the spectrometer would be the incorporation of an ion

detector, such as a time-of-flight mass analyser. This would permit the identification of all species in the ionisation region and also allow Photoelectron-Photoion-COincidence (PEPICO) measurements to be performed. In this way, the problem of overlapping PE bands produced by different species in the ionisation region would be avoided. Ion-electron coincidence studies of reactive intermediates in the gas phase with synchrotron radiation would then become possible. Since the spectrometer is already equipped for the detection of threshold electrons, Threshold Photoelectron-Photoion-COincidence (TPEPICO) measurements could also be performed [238]. In any case, the existing apparatus can allow further measurements on atmospherically important reactive intermediates to be obtained, and these are planned.

Bibliography

[1] J. H. D. Eland. *Photoelectron Spectroscopy.* Butterworths, London (1984).

[2] H. Hertz. *Annalen der Physics*, **31** (1987), 983.

[3] A. Einstein. *Annalen der Physik*, **17** (1905), 132.

[4] C. R. Brundle and A. D. Baker. *Electron Spectroscopy: Theory, Techniques and Applications.* Academic Press Inc. (London) Ltd (1977).

[5] J. W. Rabalais. *Principles of Ultraviolet Photoelectron Spectroscopy.* John Wiley and Sons, Ltd., USA (1977).

[6] J. E. Pollard, D. J. Trevor, J. E. Reutt, Y. T. Lee, and D. A. Shirley. *J. Chem. Phys.*, **77** (1982), 34.

[7] V. Schmidt. *Electron Spectrometry of Atoms using Synchrotron Radiation.* Cambridge University Press ed. New York (1997).

[8] G. Margaritondo. *Elements of Synchrotron Light.* Oxford University Press Inc., New York (2002).

[9] A. B. F. Duncan. *Rydberg series in Atoms and Molecules.* Academic Press Inc., London (1971).

[10] U. Fano. *Phys. Rev.*, **124** (1961), 1866.

[11] S. Cvejanovic and F. H. Read. *J. Phys. B*, **7** (1974), 1180.

[12] J. B. West. *Vacuum Ultraviolet Photoionisation and Photodissociation of Molecules and Clusters*. C.Y. Ng, New Jersey (1991).

[13] N. Jonathan, D. J. Smith, and K. J. Ross. *J. Chem. Phys.*, **53** (1970), 3758.

[14] J. M. Dyke, L. Golob, N. Jonathan, A. Morris, and M. Okuda. *J.C.S. Faraday II*, **70** (1974), 1828.

[15] A. Morris, N. Jonathan, J. M. Dyke, P. D. Francis, N. Keddar, and J. D. Mills. *Rev. Sci. Instrum.*, **55** (1984), 172.

[16] J. B. West, J. M. Dyke, A. Morris, T. G. Wright, and S. D. Gamblin. *J. Phys. B*, **32** (1999), 2763.

[17] J. M. Dyke, S. D. Gamblin, A. Morris, T. G. Wright, A. E. Wright, and J. B. West. *J. Elec. Spect. Rel. Phenom.*, **97** (1998), 5.

[18] L. Andrews, J. M. Dyke, N. Jonathan, N. Keddar, and A. Morris. *J. Phys. Chem.*, **88** (1984), 1950.

[19] L. Beeching, A. Dias, J. Dyke, A. Morris, S. Stranges, J. West, N. Zema, and L. Zuin. *Mol. Phys.*, **101** (2003), 575.

[20] L. Zuin, F. Innocenti, M. Costa, A. Dias, A. Morris, A. Paiva, S. Stranges, J. West, and J. Dyke. *Chem. Phys.*, **298** (2004), 213.

[21] F. Innocenti, L. Zuin, M. Costa, A. Dias, A. Morris, A. Paiva, S. Stranges, J. West, and J. Dyke. *J. Elect. Spect. Rel. Phen.*, **142** (2005), 241.

[22] www.trieste.elettra.it.

[23] www.srs.co.uk.

[24] G. Herzberg. *Molecular Spectra and Molecular Structure, III. Electronic Spectra and Electronic Structure of Polyatomic Molecules*. D. Van Nostrand Company, Inc. (1967).

[25] J. M. Hollas. *Modern Spectroscopy*. John Wiley and Sons, Ltd., Great Britain (1987).

[26] J. K. Cashion. *J. Chem. Phys.*, **39** (1963), 1872.

[27] R. N. Zare and J. K. Cashion. The IBM Share Program for Solution of the Schrödinger Equation, University of California, Unpublished.

[28] J. W. Cooley. *Math. Computation*, **XV** (1961), 363.

[29] P. M. Guyon and I. Nenner. *Appl. Opt.*, **19** (1980), 4068.

[30] G. Herzberg. *Molecular Spectra and Molecular Structure, I. Spectra of Diatomic Molecules*. D. Van Nostrand Company, Inc. (1950).

[31] K. P. Lawley and R. J. Donovan. *J. Chem. Soc. Faraday Trans.*, **89** (1993), 1885.

[32] J. Berkowitz and W. A. Chupka. *J. Chem. Phys.*, **51** (1969), 2341.

[33] R. S. Berry. *J. Chem. Phys.*, **45** (1966), 1228.

[34] J. Berkowitz. *Photoabsorption, Photoionization and Photoelectron Spectroscopy*. Academic Press Inc., London (1979).

[35] M. B. Robin. *Higher Excited States of Polyatomic Molecules, Vol 1*. Academic Press, Inc., London (1974).

[36] C. E. Moore. *Atomic Energy Levels*. National Bureau of Standards ed. Washington (1949).

[37] U. Fano and J. W. Cooper. *Phys. Rev.*, **137** (1965), pA1364.

[38] M. J. Seaton. *Proc. Phys. Soc.*, **88** (1966), 801.

[39] M. J. Seaton. *Rep. Prog. Phys.*, **46** (1983), 167.

[40] A. Giusti-Suzor and U. Fano. *J. Phys. B*, **17** (1984), 215.

[41] W. E. Cooke and C. L. Cromer. *Phys. Rev. A*, **32** (1985), 2725.

[42] J. P. Connerade. *J. Phys. B*, **16** (1983), 329.

[43] J. Dubau and M. J. Seaton. *J. Phys. B*, **17** (1984), 381.

[44] K. Ueda. *Phys. Rev. A*, **35** (1987), 2484.

[45] D. Cubric, A. Willis, J. Comer, and P. Hammond. *J. Phys. B*, **29** (1996), 4151.

[46] D. Dill. *Phys. Rev. A*, **7** (1973), 1976.

[47] D. Dill and U. Fano. *Phys. Rev. Lett.*, **29** (1972), 1203.

[48] D. Dill, A. F. Starace, and S. T. Manson. *Phys. Rev. A*, **11** (1975), 1596.

[49] F. Innocenti, L. Zuin, M. L. Costa, A. Dias, A. Morris, S. Stranges, J. B. West, and J. M. Dyke. *J. Chem. Phys.*, **126** (2007), 154310.

[50] F. Innocenti, M. L. Costa, A. Dias, M. Goubet, A. Morris, S. Stranges, N. Zema, and J. M. Dyke. *Mol. Phys.*, **105** (2007), 755.

[51] F. Innocenti, M. Eypper, S. Beccaceci, A. Morris, S. Stranges, J. B. West, G. C. King, and J. M. Dyke. *J. Phys. Chem. A*, **112** (2008), 6939.

[52] D. J. Hucknall and A. Morris. *Vacuum technology calculations in chemistry.* RSC ed. Cambridge (2003).

[53] A. Poulin and D. Roy. *J. Phys. E*, **11** (1978), 35.

[54] J. L. Gardner and J. A. R. Samson. *J. Elec. Spect. Rel. Phenom.*, **8** (1976), 123.

[55] E. Harting and F. H. Read. *Electrostatic lenses*. Elsevier ed. Amsterdam (1976).

[56] D. Cubric, D. B. Thompson, D. R. Cooper, G. C. King, and F. H. Read. *J. Phys. B*, **30** (1997), L857.

[57] J. Baker. *Single and Multiphoton Ionisation of Short Lived Molecules in the Gas Phase*. Ph.D. thesis, University of Southampton (1991).

[58] A. Morris and J. M. Dyke. *Vacuum*, **53** (1999), 339.

[59] K. Kimura, S. Katsumata, Y. Achiba, T. Yamazaki, and S. Iwata. *Handbook of HeI Photoelectron Spectra of Fundamental Organic Molecules*. Japan Scientific Societies Press, Tokyo (1981).

[60] R. E. Huffman, J. C. Larrabee, and Y. Tanaka. *J. Chem. Phys.*, **47** (1967), 856.

[61] R. E. Huffman, J. C. Larrabee, and Y. Tanaka. *J. Chem. Phys.*, **48** (1968), 3835.

[62] M. C. R. Cockett, J. M. Dyke, and H. Zamanpour. *Vacuum Ultraviolet Photoionization and Photodissociation of Molecules and Clusters*. C.Y. Ng. World Scientific ed. London (1991).

[63] M. J. Winter. *Studies of some small transient species by ultraviolet photoelectron spectroscopy*. Ph.D. thesis, University of Southampton (1981).

[64] E. A. Colbourn, J. M. Dyke, N. K. Fayad, and A. Morris. *J. Elec. Spect. Rel. Phenom.*, **14** (1978), 443.

[65] U. Worsdorfer and H. Heydtmann. *Ber. Bunsenges. Phys. Chem.*, **93** (1989), 1132.

[66] J. Brunning and M. A. A. Clyne. *J.C.S. Faraday II*, **80** (1984), 1001.

[67] A. Haworth, D. G. Wilden, and J. Comer. *J. Elec. Spect. Rel. Phenom.*, **37** (1985), 291.

[68] G. C. King, A. J. Yencha, M. Cristina, and A. Lopes. *J. Elec. Spect. Rel. Phenom.*, **114** (2001), 33.

[69] G. C. King. *Rad. Phys. Chem.*, **68** (2003), 15.

[70] S. Y. Truong, A. J. Yencha, A. M. Juarez, S. J. Cavanagh, P. Bolognesi, and G. C. King. *Chem. Phys.*, **355** (2009), 183.

[71] J. West and G. Marr. *Atom. Data Nucl. Data Tables*, **18** (1976), 497.

[72] A. Derossi, F. Lama, M. Piacentini, T. Prosperi, and N. Zema. *Rev. Sci. Instrum.*, **66** (1995), 1718.

[73] W. F. Chan, G. Cooper, X. Guo, G. R. Burton, and C. E. Brion. *Phys. Rev. A*, **46** (1992), 149.

[74] http://physics.nist.gov.PhysRefData.

[75] F. R. Elder, A. M. Gurewitsch, R. V. Langmuir, and H. C. Pollock. *Phys. Rev.*, **71** (1947), 829.

[76] F. R. Elder, R. V. Langmuir, and H. C. Pollock. *Phys. Rev.*, **74** (1948), 52.

[77] A. Lienard. *L'eclairage Elec.*, **16** (1898), 1.

[78] G. A. Schott. *Electromagnetic Radiation.* Cambridge University Press ed. Cambridge (1912).

[79] J. P. Blewett. *Phys. Rev.*, **69** (1946), 87.

[80] D. Iwanenko and I. Pomeranchuk. *Phys. Rev.*, **65** (1944), 343.

[81] J. Schwinger. *Phys. Rev.*, **70** (1946), 798.

[82] J. Schwinger. *Phys. Rev.*, **75** (1949), 1912.

[83] F. R. Elder, A. M. Gurewitsch, R. V. Langmuir, and H. C. Pollock. *J. Appl. Phys.*, **18** (1947), 810.

[84] H. C. Pollock. *Am. J. Phys.*, **51** (1983), 278.

[85] D. H. Tomboulian and P. L. Hartman. *Phys. Rev.*, **102** (1956), 1423.

[86] E. M. Rowe and F. E. Mills. *Part. Accel.*, **4** (1973), 211.

[87] S. Doniach, K. Hodgson, I. Lindau, P. Pianetta, and H. Winick. *J. Synchrotron Rad.*, **4** (1997), 380.

[88] I. H. Munro. *J. Synchrotron Rad.*, **4** (1997), 344.

[89] Y. Petroff. *J. Elec. Spect. Rel. Phenom.*, **156** (2007), 10.

[90] H. Winick and S. Doniach. *Synchrotron Radiation Research.* Plenum Press, New York (1980).

[91] S. Krinsky, M. L. Perlmann, and R. E. Watson. *Handbook on Synchrotron Radiation, Vol 1A, Chapter 2.* E.E. Koch ed. Amsterdam (1983).

[92] C. Kunz and E. M. Rowe. *Synchrotron Radiation.* C. Kunz, ed. New York (1979).

[93] D. R. Hartree. *Proc. Camb. Phil. Soc.*, **24** (1928), 89.

[94] V. Fock. *Z. Physik*, **61** (1930), 126.

[95] J. Simons. *J. Phys. Chem.*, **95** (1991), 1017.

[96] C. J. Cramer. *Essentials Computational Chemistry, Second Edition.* John Wiley and Sons, Ltd (2007).

[97] M. Born and R. Oppenheimer. *Ann. Phys.*, **84** (1927), 457.

[98] F. Jensen. *Introduction to Computational Chemistry.* John Wiley and Sons, Ltd (1999).

[99] A. Szabo and N. S. Ostlund. *Modern Quantum Chemistry, Introduction to Advanced Electronic Structure Theory.* Dover Publications, Inc., New York (1989).

[100] J. A. Pople and R. K. Nesbet. *J. Chem. Phys.*, **22** (1954), 571.

[101] W. Pauli. *Z. Phys. A-Hadron. Nucl.*, **31** (1925), 765.

[102] J. C. Slater. *Phys. Rev.*, **34** (1929), 1293.

[103] C. C. J. Roothaan. *Rev. Mod. Phys.*, **23** (1951), 69.

[104] T. Koopmans. *Physica*, **1** (1934), 104.

[105] W. G. Richards. *Int. J. Mass Spec. Ion. Phys.*, **2** (1969), 419.

[106] M. F. Guest and V. R. Saunders. *Mol. Phys.*, **29** (1975), 873.

[107] A. E. Leach. *Molecular Modelling, Principles and Applications, Second edition.* Henry Ling Ltd, Dorchester (2001).

[108] S. F. Boys. *Proc. Roy. Soc. Lond. A Math.*, **200** (1950), 542.

[109] W. J. Hehre, R. Ditchfield, and J. A. Pople. *J. Chem. Phys.*, **56** (1972), 2257.

[110] T. H. Dunning. *J. Chem. Phys.*, **90** (1989), 1007.

[111] O. Sinanoglu and D. F. Tuan. *J. Chem. Phys.*, **38** (1963), 1740.

[112] W. J. Hehre, L. Radom, P. V. R. Schleyer, and J. A. Pople. *Ab initio molecular orbital theory.* Wiley Interscience, New York (1986).

[113] P. Atkins and R. Friedman. *Molecular Quantum Mechanics, fourth edition.* Oxford University Press (2005).

[114] M. Frisch, I. N. Ragazos, M. A. Robb, and H. B. Schlegel. *Chem. Phys. Lett.*, **189** (1992), 524.

[115] B. O. Roos, P. R. Taylor, and P. E. M. Siegbahn. *Chem. Phys.*, **48** (1980), 157.

[116] R. J. Bartlett. *J. Chem. Phys.*, **93** (1989), 1697.

[117] H. B. Schlegel. *Adv. Chem. Phys.*, **67** (1987), 249.

[118] P. Pulay. *Mol. Phys.*, **17** (1969), 197.

[119] F. Duschinsky. *Acta Physicochim URSS*, **7** (1937), 55.

[120] F. T. Chau, J. M. Dyke, E. P. F. Lee, and D. C. Wang. *J. Elec. Spectrosc. Rel. Phenom.*, **97** (1998), 33.

[121] D. K. W. Mok, E. P. F. Lee, F. T. Chau, D. C. Wang, and J. M. Dyke. *J. Chem. Phys.*, **113** (2000), 5791.

[122] S. Carter and N. C. Handy. *J. Chem. Phys.*, **87** (1987), 4294.

[123] J. K. G. Watson. *Mol. Phys.*, **15** (1968), 479.

[124] S. J. Davis, L. Hanko, and P. L. Wolf. *J. Chem. Phys.*, **82** (1985), 4831.

[125] S. J. Davis and M. Woodward. *J. Phys. Chem.*, **95** (1991), 4610.

[126] C. A. Helms, L. Hanko, K. Hager, and G. P. Perram. *J. Appl. Phys.*, **66** (1989), 6093.

[127] A. J. Cormack, A. J. Yencha, R. J. Donovan, K. P. Lawley, A. Hopkirk, and G. C. King. *Chem. Phys.*, **213** (1996), 439.

[128] A. J. Yencha, A. Hopkirk, A. Hiraya, R. J. Donovan, J. G. Goode, R. R. J. Maier, G. C. King, and A. Kvaran. *J. Phys. Chem.*, **99** (1995), 7231.

[129] A. J. Yencha, M. C. A. Lopes, and G. C. King. *Chem. Phys. Lett.*, **325** (2000), 559.

[130] A. J. Yencha, A. E. R. Malins, and G. C. King. *Chem. Phys. Lett.*, **370** (2003), 756.

[131] P. M. Guyon, R. Spohr, W. A. Chupka, and J. Berkowitz. *J. Chem. Phys.*, **65** (1976), 1650.

[132] T. Baer and P. M. Guyon. *J. Chem. Phys.*, **85** (1986), 4765.

[133] D. M. de Leeuw, R. Mooyman, and C. A. de Lange. *Chem. Phys. Lett.*, **54** (1978), 231.

[134] J. M. Dyke, N. Jonathan, and A. Morris. *Int. Rev. Phys. Chem.*, **2** (1982), 3.

[135] J. Berkowitz and G. L. Goodman. *J. Chem. Phys.*, **71** (1979), 1754.

[136] K. P. Huber and G. Herzberg. *Constants of Diatomic Molecules*. van Nostrand Reinhold, New York (1979).

[137] R. A. Durie. *Can. J. Phys.*, **44** (1966), 337.

[138] J. C. McGurk and W. H. Flygare. *J. Chem. Phys.*, **59** (1973), 5742.

[139] J. M. Dyke. *J.C.S. Faraday II*, **83** (1987), 67.

[140] G. C. King, A. Zubeck, P. M. Rutter, and F. H. Read. *J. Phys. E*, **20** (1987), 440.

[141] R. I. Hall, A. McConkey, K. Ellis, G. Dawber, L. Avaldi, M. A. Mac-Donald, and G. C. King. *Meas. Sci. Technol.*, **3** (1992), 316.

[142] J. Berkowitz, C. H. Batson, and G. L. Goodman. *Phys. Rev. A*, **24** (1981), 149.

[143] V. N. Sarma and Y. N. Joshi. *Can. J. Phys.*, **61** (1983), 1434.

[144] L. Minnhagen. *Ark. Fys.*, **21** (1962), 415.

[145] W. C. Martin and C. H. Corliss. *J. Res. Natl. Bur. Stand. (U.S.)*, **64A** (1960), 443.

[146] Y. Y. Gu, A. M. Chojacki, C. J. Zietkiewick, A. A. Senin, and J. G. Eden. *J. Chem. Phys.*, **119** (2003), 12342.

[147] C. Kiess and C. Corliss. *J. Res. Nat. Bur. Stand. Sect. A*, **63** (1959), 1.

[148] B. Ruscic, J. Greene, and J. Berkowitz. *J. Phys. B*, **17** (1984), L79.

[149] B. Ruscic and J. Berkowitz. *Phys. Rev. Lett.*, **50** (1983), 675.

[150] B. Ruscic, J. Greene, and J. Berkowitz. *J. Phys. B*, **17** (1984), 1503.

[151] V. Sarma and Y. Joshi. *J. Phys. B*, **16** (1983), 1671.

[152] S. Pratt. *Phys. Rev. A*, **32** (1985), 928.

[153] S. Pratt. *Phys. Rev. A*, **33** (1986), 1718.

[154] S. Pratt, P. Dehmer, and J. Dehmer. *Chem. Phys. Lett.*, **126** (1986), 12.

[155] C. Caldwell and M. Krause. *Rad. Phys. Chem.*, **70** (2004), 43.

[156] W. J. van der Meer, P. van der Meulen, and C. A. de Lange. *Chem. Phys.*, **115** (1987), 109.

[157] K. Kimura, T. Yamasaki, and Y. Achiba. *Chem. Phys. Lett.*, **58** (1978), 231.

[158] S. Benzaid, M. Krause, A. Menzel, and C. Caldwell. *Phys. Rev. A*, **57** (1998), 4420.

[159] K. Radler and J. Berkowitz. *J. Chem. Phys.*, **70** (1979), 216.

[160] J. Berkowitz. *Adv. Chem. Phys.*,, **72** (1988), 1.

[161] J. Wu, S. Whitfield, C. Caldwell, M. Krause, P. van der Meulen, and A. Fahlman. *Phys. Rev. A*, **42** (1990), 1350.

[162] P. van der Meulen, M. Krause, C. Caldwell, S. Whitfield, and C. de Lange. *Phys. Rev. A*, **46** (1992), 2468.

[163] J. Hansen, R. Cowan, S. Carter, and H. Kelly. *Phys. Rev. A*, **30** (1984), 1540.

[164] E. Brown, S. Carter, and H. Kelly. *Phys. Rev. A*, **21** (1980), 1237.

[165] L. Nahon, L. Duffy, P. Morin, F. Combet-Farnoux, J. Tremblay, and M. Larzilliere. *Phys. Rev. A*, **41** (1990), 4879.

[166] M. Meyer, J. Lacoursiere, P. Morin, and F. Combet-Farnoux. *J. Phys. B*, **27** (1994), 3875.

[167] D. Kennedy and S. Manson. *Phys. Rev. A*, **5** (1983), 227.

[168] E. S. Chang. *What we can learn from angular distribution studies.* Daresbury internal publication, 1990.

[169] W. R. Johnson, K. T. Cheng, K. N. Huang, and M. L. Dourneuf. *Phys. Rev. A*, **22** (1980), 989.

[170] S. T. Manson, A. Msezane, A. F. Starace, and S. Shahabi. *Phys. Rev. A*, **20** (1979), 1005.

[171] F. Combet-Farnoux and M. Ben-Amar. *J. Elec. Spect. Rel. Phenom.*, **41** (1986), 67.

[172] D. S. King, P. K. Schenck, and J. C. Stephenson. *J. Mol. Spectrosc.*, **78** (1979), 1.

[173] C. W. Mathews. *J. Chem. Phys*, **45** (1966), 1068.

[174] C. W. Mathews. *J. Chem. Phys*, **46** (1967), 2355.

[175] P. Venkateswarlu. *Phys. Rev.*, **77** (1950), 676.

[176] A. Charo and F. C. DeLucia. *J. Mol. Spectrosc.*, **94** (1982), 363.

[177] W. H. Kirchoff, D. R. J. Lide, and F. X. Powell. *J. Mol. Spectrosc.*, **47** (1973), 491.

[178] H. B. Qian and P. B. Davies. *J. Mol. Spectrosc.*, **169** (1995), 201.

[179] J. B. Burkholer, C. J. Howard, and P. A. Hamilton. *J. Mol. Spectrosc.*, **127** (1988), 362.

[180] P. B. Davies, P. A. Hamilton, J. M. Elliott, and M. J. Rice. *J. Mol. Spectrosc.*, **102** (1983), 193.

[181] P. B. Davies, W. Lewis-Bevan, and D. K. Russell. *J. Chem. Phys.*, **75** (1981), 5602.

[182] J. P. Booth, G. Cunge, P. Chabert, and N. Sadeghi. *J. Appl. Phys.*, **85** (1999), 3097.

[183] B. A. Cruden, K. K. Gleason, and H. H. Sawin. *J. Appl. Phys.*, **89** (2001), 915.

[184] J. P. Booth, G. Cunge, F. Neuilly, and N. Sadeghi. *Plasma Sources Sci. Technol.*, **7** (1998), 423.

[185] M. Haverlag, E. Stoffels, W. W. S. G. M. W. Kroesen, and F. J. de Hoog. *J. Vac. Sci. Technol. A*, **14** (1996), 384.

[186] J. P. Booth. *Plasma Sources Sci. Technol.*, **8** (1999), 249.

[187] T. J. Buckley, R. D. Johnson, R. E. Huie, Z. Zhang, S. C. Kuo, and R. B. Klemm. *J. Phys. Chem.*, **99** (1995), 4879.

[188] V. Tarnovsky and K. Becker. *J. Chem. Phys.*, **98** (1993), 7868.

[189] F. T. Chau, D. K. W. Mok, E. P. F. Lee, and J. M. Dyke. *ChemPhysChem*, **6** (2005), 2037.

[190] A. Halkier, T. Helgaker, W. Klopper, P. Jorgensen, and A. G. Csaszar. *Chem. Phys. Lett.*, **310** (1999), 385.

[191] J. Wormhoudt, K. E. McCurdy, and J. B. Burkholder. *Chem. Phys. Lett.*, **158** (1989), 480.

[192] C. W. Mathews. *Can. J. Phys.*, **45** (1967), 2355.

[193] O. Suto and J. Steinfeld. *Chem. Phys. Lett.*, **168** (1990), 181.

[194] D. K. W. Mok, E. P. F. Lee, F. T. Chau, and J. M. Dyke. *J. Chem. Phys.*, **120** (2004), 1292.

[195] L. Margules, J. Demaison, and J. E. Boggs. *J. Phys. Chem.*, **103** (1999), 7632.

[196] MOLPRO is a package of *ab initio* programs written by H. J. Werner, P. J. Knowles, R. Lindh, F. R. Manby, M. Schütz, P. Celani, T. Korona, G. Rauhut, R. D. Amos, A. Bernhardsson, A. Berning, D. L. Cooper, M. J. O. Deegan, A. J. Dobbyn, F. Eckert, C. Hampel, G. Hetzer, A. W. Lloyd, S. J. McNicholas, W. Meyer, M. E. Mura, A. Nicklass, P. Palmieri, R. Pitzer, U. Schumann, H. Stoll, A. J. Stone, R. Tarroni, and T. Thorsteinsson (2008).

[197] G. K. Jarvis, K. J. Boyle, C. A. Mayhew, and R. P. Tuckett. *J. Phys. Chem. A*, **102** (1998), 3230.

[198] L. Golob. Ph.D. thesis, University of Southampton (UK) (1975).

[199] S. Eden, P. Limao-Vieira, P. A. Kendall, N. J. Mason, J. Delwiche, M. J. Hubin-Franskin, T. Tanaka, M. Kitajima, H. Tanaka, H. Cho, and S. V. Hoffman. *Chem. Phys.*, **297** (2004), 257.

[200] Z. L. Cai. *Theor. Chim. Acta*, **86** (1993), 249.

[201] K. Sendt and G. B. Bacskay. *J. Chem. Phys.*, **112** (2000), 2227.

[202] R. D'Agostino and D. L. Flamm. *J. Appl. Phys.*, **52** (1981), 162.

[203] D. R. Johnson and F. X. Powell. *Science*, **164** (1969), 950.

[204] F. Seel, E. Heinrich, W. Combler, and R. Budenz. *Chimica*, **23** (1969), 73.

[205] W. H. Kirchoff, D. R. Johnson, and F. X. Powell. *J. Mol. Spectrosc.*, **48** (1973), 157.

[206] Y. Endo, S. Saito, E. Hirota, and T. Chikaraishi. *J. Mol. Spectrosc.*, **77** (1979), 222.

[207] J. C. Deroche, H. Bürger, P. Schulz, and H. Willner. *J. Mol. Spectrosc.*, **89** (1981), 269.

[208] R. J. Glinski and C. D. Taylor. *Chem. Phys. Lett.*, **155** (1989), 511.

[209] R. J. Glinski, C. D. Taylor, and F. Kutzler. *J. Phys. Chem.*, **94** (1990), 6196.

[210] D. M. de Leeuw, R. Mooyman, and C. A. de Lange. *Chem. Phys.*, **34** (1978), 287.

[211] R. D. Johnson and J. W. Hudgens. *J. Phys. Chem.*, **94** (1990), 3273.

[212] Q. Li, J. Shu, Q. Zhang, S. Yu, L. Zhang, C. Chen, and X. Ma. *J. Phys. Chem. A*, **102** (1998).

[213] C. Thomson. *Chem. Phys. Lett.*, **44** (1976), 475.

[214] K. K. Irikura. *J. Chem. Phys.*, **102** (1995), 5357.

[215] E. P. F. Lee, D. K. W. Mok, F. Chau, and J. M. Dyke. *J. Chem. Phys.*, **125** (2006), 104304.

[216] J. M. Dyke, L. Golob, N. Jonathan, and A. Morris. *J.C.S. Faraday II*, **71** (1975), 1026.

[217] D. W. Turner, C. Baker, A. D. Baker, and C. R. Brundle. *Molecular Photoelectron Spectroscopy*. Wiley Interscience (1970).

[218] K. Ellis, R. I. Hall, L. Avaldi, G. Dawber, A. McConkey, L. Andric, and G. C. King. *J. Phys. B*, **27** (1994), 3415.

[219] D. W. Smith and L. Andrews. *J. Chem. Phys.*, **60** (1974), 81.

[220] C. J. Howard. *J. Chem. Phys.*, **67** (1977), 5258.

[221] J. W. C. Johns, A. R. W. McKellar, and M. Riggin. *J. Chem. Phys.*, **68** (1978), 3957.

[222] J. M. Dyke, N. Jonathan, A. Morris, and M. J. Winter. *Mol. Phys.*, **44** (1981), 1059.

[223] C. D. Walther and H. G. Wagner. *Ber. Bunsenges. Phys. Chem.*, **87** (1983).

[224] G. J. Vazquez, R. J. Buenker, and S. D. Peyerimhoff. *Mol. Phys.*, **29** (1986), 291.

[225] M. L. Senent. *Mol. Phys.*, **96** (1999), 1587.

[226] J. M. Robbe, M. Monnerville, G. Chambaud, P. Rosmus, and P. J. Knowles. *Chem. Phys.*, **252** (2000), 9.

[227] Y. Song, M. Evans, C. Y. Ng, C. W. Hsu, and G. K. Jarvis. *J. Chem. Phys.*, **111** (1999), 1905.

[228] R. P. Thorn, L. J. Stief, S. C. Kuo, and R. B. Klemm. *J. Phys. Chem. A*, **103** (1999), 812.

[229] C. A. Taatjes, D. L. Osborn, T. A. Cool, and K. Nakajima. *Chem. Phys. Lett.*, **394** (2004), 19.

[230] M. I. Abbas, J. M. Dyke, and A. Morris. *J. Chem. Soc. Faraday Trans. II*, **72** (1976), 814.

[231] G. Meloni, P. Z. Stephen, S. J. Klippenstein, M. Ahmed, S. R. Leone, C. A. Taatjes, and D. L. Osborn. *J. Am. Chem. Soc.*, **128** (2006), 13559.

[232] A. Febo, C. Perrino, M. Gherardi, and R. Sparapani. *Environ. Sci. Technol.*, **29** (1995), 2390.

[233] L. J. Beckham, W. A. Fessler, and M. A. Kise. *Chem. Rev.*, **48** (1951), 319.

[234] C. A. Taatjes, G. Meloni, T. M. Selby, A. J. Trevitt, D. L. Osborn, C. J. Percival, and D. E. Shallcross. *J. Am. Chem. Soc.*, **130** (2008), 11883.

[235] B. Ruscic and J. Berkowitz. *J. Chem. Phys.*, **98** (1993), 2568.

[236] M. Dampc, M. R. F. Siggel-King, G. C. King, and M. Zubek. *Chem. Phys.*, **359** (2009), 77.

[237] J. V. Hatfield, J. Comer, T. A. York, and P. J. Hicks. *Rev. Sci. Instrum.*, **63** (1992), 792.

[238] N. S. Shuman, W. R. Stevens, K. Lower, and T. Baer. *J. Phys. Chem. A*, **113** (2009), 10710.